Addressing the Low Solubility of Proteolysis Targeting Chimeras Through Solid State Engineering

SCREEN, MARTIN,ANDREW

Addressing the Low Solubility of PROteolysis TArgeting Chimeras Through Solid State Engineering

Author
Martin A. Screen

Supervisor
Prof. Jonathan W. Steed

Co-supervisors
Prof. Clare S. Mahon, Prof. Mark R. Wilson, (Durham University)
Dr James F. McCabe, Dr Sean Askin (AstraZeneca)

A thesis presented for the degree of

Doctor of Philosophy

Department of Chemistry

2025

Abstract

Proteolysis-targeting chimeras (PROTACs) represent a promising drug modality within the beyond Rule of Five (bRo5) chemical space but are hindered by extremely poor aqueous solubility and limited crystallisability, due to their flexible structures consisting of two ligand moieties joined chemically by a linker. While several X-ray structures have been reported of PROTACs in ternary complexes, to date no structures have been published of single-component densely packed PROTACs, from which an understanding of PROTACs' intermolecular interactions, and therefore physical properties, can be developed. This thesis addresses these challenges through solid-state engineering approaches aimed at improving solubility and advancing pre-formulation strategies. The first single-component crystal structures of a cereblon-recruiting PROTAC 'AZ1' are reported, obtained via advanced crystallisation protocols combined with 3D electron diffraction and synchrotron X-ray diffraction. Despite their potential for hydrogen bonding, these structures are dominated by dispersive interactions, forming similar packing motifs across different crystalline forms. Generating amorphous phases of AZ1 by different methods can lead to distinct dissolution behaviours, suggesting that PROTACs can also exhibit pseudo-polyamorphism. Pre-formulation studies show that amorphous solid dispersions (ASDs) of PROTACs with HPMCAS polymer significantly enhance supersaturation upon dissolution compared to the pure amorphous drug, achievable at a relatively high weight-percentage of drug when synthesised via the slurry conversion method. In contrast, co-amorphous systems with small molecule co-formers failed to improve dissolution despite evidence of inter-component hydrogen bonding. Complementary crystallisation studies on lenalidomide, a molecular fragment of AZ1, explore low-solubility co-crystals for pulmonary drug delivery and gel-phase crystallisation to control polymorphism, highlighting novel avenues for managing solid-state properties. Collectively, these findings contribute towards an understanding of how to overcome PROTACs' poor pharmacokinetic properties through tailored solid-state strategies.

Declaration

The work described in this thesis was undertaken in the Department of Chemistry at Durham University (UK) between October 2021 and September 2025, under the supervision of Professor Jonathan W. Steed of Durham University. This work has not been previously submitted for a degree at this or any other university.

All X-ray structures were collected and processed by Dr. Toby J. Blundell. In Chapter 1, the 3D electron diffraction data for AZ1 Form 1 were collected and processed by Dr. Daniel N. Rainer and Prof. Simon J. Coles via the National Electron Diffraction Facility for Nanomaterial Structural Studies; the crystallographic data for AZ1 Form 3 were collected and processed by Dr. Toby J. Blundell using beamline I19 of the Diamond Light Source (DLS) synchrotron; CrysIn calculations on AZ1 crystal structures were performed by Dr. James F. McCabe at AstraZeneca; CrystalExplorer lattice energy calculations on AZ1 crystal structures and the CSD subset were performed by Prof. Aurora J. Cruz-Cabeza; solid-state NMR spectra were acquired by Jamie L. Guest. In Chapter 4, solution-state NMR titrations and DOSY spectra were acquired and interpreted by Dr. Juan A. Aguilar-Malavia; elemental analysis experiments were performed by Dr. Emily Unsworth. All other results are the product of independent work and investigations by the author.

Statement of Copyright

Funding

This work was funded by the Engineering and Physical Sciences Research Council (EPSRC) and AstraZeneca via the Soft Matter and Functional Interfaces Centre for Doctoral Training (EP/S023631/1).

Publications

Chapter 2: M. A. Screen, J. F. McCabe, S. Askin, J. L. Guest, P. Hodgkinson, A. J. Cruz-Cabeza, T. J. Blundell, D. N. Rainer, S. Coles, A. Longcake, M. R. Probert, C. S. Mahon,

M. R. Wilson and J. W. Steed, Crystallising the Un-crystallizable: Insights from Extensive Screening of PROTACs, *J. Am. Chem. Soc.*, 2025, **147**, 31, 28056–28072.

Chapter 3: M. A. Screen, S. Askin, J. F. McCabe, E. Jacobs, A. Anane-Adjei, C. S. Mahon, M. R. Wilson and J. W. Steed, Developing Multi-Component Solid Formulation Strategies for PROTAC Dissolution Enhancement, *Mol. Pharm.*, 2025, **22**, 11, 7052–7067.

Chapter 4: M. A. Screen, G. Tomkinson, J. F. McCabe, S. Askin, C. S. Mahon, M. R. Wilson and J. W. Steed, Designing Lenalidomide Co-crystals with an Extended-Release Profile for Improved Pulmonary Drug Delivery, *New J. Chem.*, 2025, **49**, 6535–6543.

Chapter 5: M. A. Screen, J. A. Aguilar-Malavia, T. J. Blundell, J. F McCabe, S. Askin, C. S. Mahon, M. R. Wilson and J. W. Steed, Non-mimetic Gels Direct Novel Crystallisation Behaviour of Lenalidomide, *Cryst. Growth Des.*, 2025, **25**, 20, 8646–8657.

Table of Contents

Acknowledgements

First and foremost, I would like to express my deepest gratitude to my supervisor, Prof. Jonathan Steed, for his invaluable guidance, encouragement, and patience over the eight years I have been at Durham University. His expertise and insightful feedback have shaped not only this thesis but also my growth as a researcher. I am equally grateful to my Durham co-supervisors, Prof. Clare Mahon and Prof. Mark Wilson, for their support, advice, and enthusiasm, which provided both direction and motivation at crucial stages of my work. This project would never have been possible, of course, without the excellent direction provided by Dr James McCabe and Dr Sean Askin of AstraZeneca, who have both supported me immensely throughout my research journey.

I would also like to thank my collaborators and colleagues in the X-ray Crystallography department at Durham University, the National Electron Diffraction Facility for Nanomaterial Structural Studies, the research group of Prof. Mike Probert at Newcastle University, and the research groups of Prof. Aurora Cruz-Cabeza and Prof. Paul Hodgkinson at Durham University. The discussions, advice, and everyday interactions with such talented scientists made this process both stimulating and enjoyable. Special thanks to Dr Toby Blundell, Dr Daniel Rainer, Dr Juan Aguilar-Malavia and Jamie Guest for their help with experiments, data analysis, and for the many discussions.

I am grateful to the Engineering and Physical Sciences Research Council for financial support, to the Soft Matter and Functional Interfaces Centre for hosting my Centre of Doctoral Training, and to AstraZeneca for the opportunity to work on this project and for providing valuable resources and insight.

On a personal note, I owe immense gratitude to my friends in Durham, inside and outside the Chemistry Department, for their companionship and encouragement which helped me through the trickier chapters of the past four years. In particular, my most heartfelt thanks go to my good friends Libby and David, my fellow bandmates in The Keemons, the research group of Prof. Russell Taylor, Laura and Lucy, Rafa, Megan and James. Their unwavering support and excellent humour will be keenly missed after I move away.

Finally, none of this would have been possible without the love and support of my family, and of course my gorgeous cats Zola and Toby. To my beautiful fiancée Samantha – your encouragement, warmth and love has been unfaltering since I began this adventure, being there for me even when you were going through your own struggles these past few years. This achievement is as much yours as it is mine.

Abbreviations

3D ED	3-Dimensional Electron Diffraction
ADME	Absorption, Distribution, Metabolism and Excretion
AhR	Aryl Hydrocarbon Receptor
API	Active Pharmaceutical Ingredient
ASD	Amorphous Solid Dispersion
bRo5	Beyond Lipinski's Rule-Of-5
CGC	Critical Gelation Concentration
cIAP1	Cellular Inhibitor of Apoptosis Protein 1
CNT	Classical Nucleation Theory
COSMO-RS	Conductor-Like Screening Model for Real Solvents
CRBN	Cereblon
CSP	Crystal Structure Prediction
CSD	Cambridge Structural Database
DCAF15	Ddb1-And Cul5-Associated Factor 15
DFT	Density Functional Theory
DL	Drug Loading
DOSY	Diffusion-Ordered NMR Spectroscopy
DSC	Differential Scanning Calorimetry
DVS	Dynamic Vapor Sorption
EGFR	Epidermal Growth Factor Receptor
ENaCt	Encapsulated Nanodroplet Crystallisation
ER	Estrogen Receptor
ES	Electro-Spray
FaSSIF	Fasted State Simulated Intestinal Fluid
GRAS	Generally Recognised As Safe
HBA	Hydrogen Bond Acceptors
HBD	Hydrogen Bond Donors
HBP	Hydrogen Bonding Propensity
HETCOR	Heteronuclear Correlation
HER2	Human Epidermal Growth Factor Receptor 2
HPMCAS	Hydroxypropyl Methyl Cellulose Acetate Succinate
HS-POM	Hot-Stage Polarised Optical Microscopy
IMHB	Intramolecular Hydrogen Bond
KEAP1	Kelch-Like ECH-Associated Protein 1
KGA	α-Ketoglutaric Acid
LAG	Liquid-Assisted Grinding

LDM	Lenalidomide
LMWG	Low Molecular Weight Gelator
LoC	Limit Of Congruency
LPE	Lipophilic Permeability Efficiency
MD	Molecular Dynamics
MDM2	Mouse Double Minute 2
MGC	Maximum Gelation Concentration
ML	Machine Learning
MOA	Mode Of Action
MW	Molecular Weight
NBA	m-Nitrobenzoic Acid
NMR	Nuclear Magnetic Resonance
OXA	Oxalic Acid
OCC	Open Computational Chemistry
PAA	Poly(Acrylic Acid)
PAMPA	Parallel Artificial Membrane Permeability Assay
PBS	Phosphate Buffered Saline
PEG	Polyethylene Glycol
PM	Physical Mixture
POI	Protein Of Interest
PROTAC	Proteolysis Targeting Chimera
PSA	Polar Surface Area
PVA	Poly(Vinyl Alcohol)
PVPVA	Polyvinylpyrrolidone Vinyl Acetate
RH	Relative Humidity
SC-XRD	Single Crystal X-Ray Diffraction
SEM	Scanning Electron Microscopy
SSNMR	Solid-State Nuclear Magnetic Resonance
TBK1	TANK-Binding Kinase 1
TDP	Targeted Protein Degradation
TGA	Thermogravimetric Analysis
UPLC	Ultra Performance Liquid Chromatography
UPS	Ubiquitin-Proteasome System
VHL	Von Hippel-Lindau
XRPD	X-Ray Powder Diffraction
XPS	X-Ray Photoelectron Spectroscopy

1. Introduction

1.1 Drug Formulation

Targeted protein degradation (TPD) is an emerging therapeutic modality with the potential to tackle disease-causing proteins previously deemed “undruggable” with conventional small molecules. In the 20 years since the conception of a proteolysis targeting chimera (PROTAC), a molecule capable of harnessing the ubiquitin-proteasome system to degrade a target protein, TPD has moved from academia to industry and is attracting substantial interest, with more than 10 PROTACs now in clinical trials.[1] However, PROTACs are very poorly water-soluble and lie in a chemical space outside of that defined by Lipinski’s rule of 5,[2] and as such, face challenges regarding their development into drug products with sufficient bioavailability. Drug formulation strategies employed successfully for other small molecule pharmaceuticals, such as amorphisation, may help to improve their bioavailability. Experimental and computational pre-formulation studies are required first to understand the physicochemical properties of PROTACs before any such strategies can be implemented, since there is currently no literature in the nascent field of PROTACs formulation.

Formulation scientists in the pharmaceuticals industry are responsible for ensuring that drug products are bioavailable, and both physically and chemically stable. In order to do so, the properties of the solid form of the drug substance must be well understood and controlled. At least 50% of active pharmaceutical ingredients (APIs) subjected to industrial screening processes have been found to be polymorphic,[3] meaning that they exist in more than one crystalline form depending on the intermolecular arrangements present. This gives rise to both opportunities and challenges for the pharmaceutical industry;[4] on one hand, it offers the possibility to choose between forms and tailor the properties of a drug substance to meet performance requirements such as bioavailability, but it can also lead to undesirable transformations between solid forms that can adversely affect the drug substance’s function. The solid-state properties can vary greatly between different forms, which include polymorphs, solvates, salts and amorphous phases, and therefore significantly impact their solubility and stability characteristics that are essential for successful drug candidate development.[5] It is therefore imperative to study the solid form landscapes of new drug compounds so that their pharmaceutical properties can be reliably controlled, and discovery of new forms can represent potential intellectual property opportunities.[6,7]

1.1.1 Polymorphism

Polymorphs can arise from different packing arrangements of relatively rigid molecules with little or negligible conformational variance, or from molecules adopting significantly different conformations in the crystal. Both crystal nucleation and growth control the polymorphic outcome under a given set of conditions, and nucleation is the less understood of the two steps. Explanations of its mechanism have been proposed through classical nucleation theory (CNT) where nuclei are assumed to have the same molecular arrangement as a large crystal and grow by one monomer unit at a time, and non-classical theories where the density and crystal structure of the nuclei can fluctuate independently of each other; some such theories include two-step nucleation and the aggregation of pre-nucleation clusters (Figure 1.1).[8,9] While CNT has been used historically to provide good approximations of the critical nuclei radius and the nucleation rate in many cases, including the antiplatelet drug dipyridamole for example,[10] two-step nucleation theory has been more successful in explaining nucleation behaviours in polymorphic systems, where the ability of a solvent to promote aggregation of preassembled growth units greater than single monomers into molecular clusters has been shown to control the polymorphic outcome of a crystallisation.[11] Molecular dynamics (MD) simulations of 5-fluorouracil have illustrated this behaviour, where the aggregation of 5-fluorouracil molecules into doubly hydrogen bonded dimers consistent with the Form II crystal structure was observed in a dry nitromethane solution, but was hindered by strong binding to water in both water solution and wet nitromethane.[12] In these two cases, F-F hydrophobic interactions that feature in the Form I structure were promoted instead. This corroborated the experimental polymorphic outcome, where Form I was obtained from water and wet nitromethane solutions while Form II was obtained only from dry nitromethane.

Solution-mediated polymorphic transformation is particularly important to control in industrial manufacturing processes, where crystals of a metastable form can undergo rearrangement to form a lower energy polymorph through contact with solvent molecules. This process involves three steps; dissolution of the metastable crystals, nucleation of the more stable crystalline phase (often rate-limiting) and its subsequent growth.[13] Spontaneous or temperature-induced transformation between polymorphs is also possible in the solid state, which is of particular concern during the processing and storage of the drug products.[14] A famous example of an undesired polymorphic transformation is the late-appearing form of Abbott Laboratories' HIV inhibitor drug Ritonavir, where a second solid form of the drug (Form II) was discovered for the first time when batches of the drug capsules failed dissolution specifications two years after the product was launched.[15] The physical properties of the more thermodynamically

stable Form II differed substantially from the original Form I, and the product had to be removed temporarily from the market until a new formulation approach was implemented. It is therefore desirable in many cases to isolate the most thermodynamically stable form of a drug compound to ensure reproducible bioavailability of the product over its shelf-life under a variety of real-world storage conditions, but in cases where a faster dissolution rate is required to improve the absorption of a drug, the development of a metastable crystalline or amorphous form with greater solubility may be justified.[4,5] This approach is becoming more common since approximately 70 % of APIs in development are considered to have poor aqueous solubility.[16] These forms are at risk of recrystallising into less soluble polymorphs however, unless stabilised.

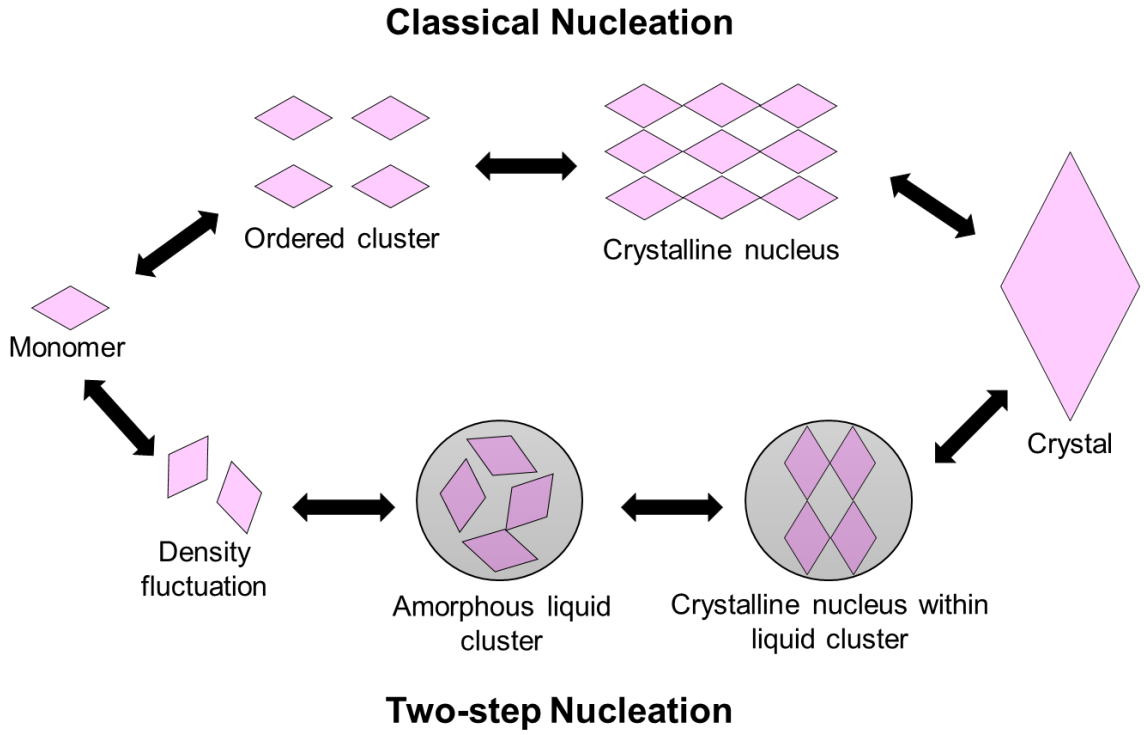

Figure 1.1. Classical and non-classical “two-step” nucleation mechanisms.

The solubility of a given polymorph is closely related to its molecular packing and conformation, where different arrangements of molecules in the solid can give rise to differences in lattice enthalpy, hygroscopicity and packing efficiency. The mechanical properties of drug polymorphs also require investigation to ensure they are adequately processable for scaled-up manufacture, and differ depending on the given polymorph’s crystal structure.[17] Variation in molecular packing also results in drug polymorphs having different relative stabilities.[3] One or more of these many factors may dictate the preference for a given polymorph of a drug, or a particular form may be selected simply for the ease of its reproducibility in the synthetic procedure.[4] Methods used to selectively

crystallise a chosen polymorph in a synthetic process include the use of additives,[18] polymer heteronuclei,[19] engineered surfaces,[20] and crystallisation in gel media, such as the toluene gel of a drug-mimetic gelator compound which can facilitate the direct crystallisation of the thermodynamic red form of ROY compared to the metastable yellow form obtained from toluene solution (Figure 1.2).[21–26]

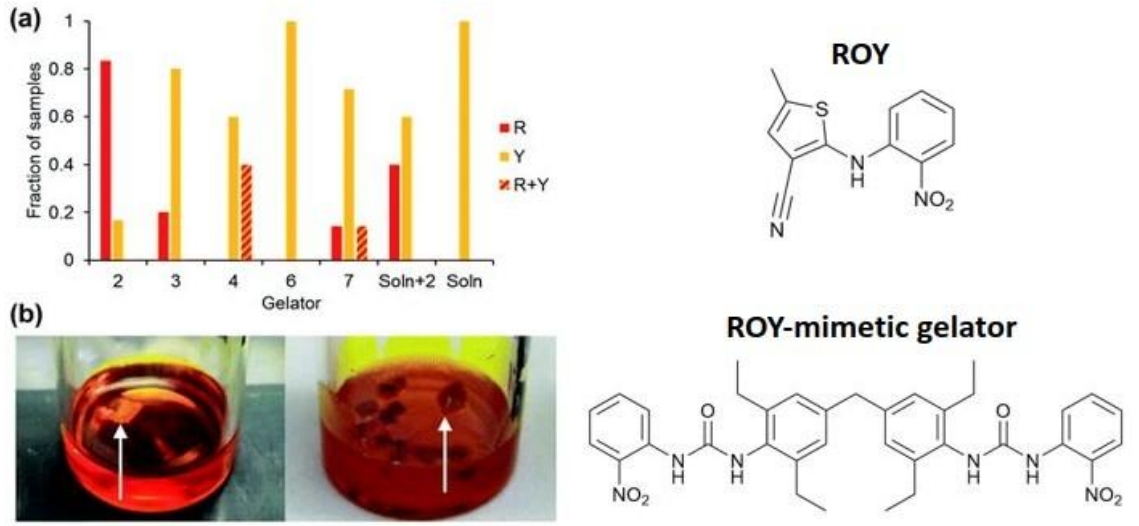

Figure 1.2. Selective crystallisation of the metastable red form of the highly polymorphic drug substance ROY using drug-mimetic supramolecular gels.[23] (a) Collated data comparing the form of ROY obtained from 100 mg mL^{-1} toluene gels of a drug-mimetic gelator (structure shown below graph), non-specific gelators, from toluene solution saturated with the drug-mimetic gelator, and from solution. (b) Crystallisation of the yellow (Y) form of ROY from a toluene gel of a control compound unrelated to ROY (left) and the red (R) form from a toluene gel of the drug-mimetic gelator (right).

There are many experimental methods for discovering and isolating polymorphs as part of the solid-form screening process to identify all of the crystal forms that a compound can adopt, including sublimation, crystallisation from a single solvent, evaporation from binary solvent mixture, vapor diffusion, thermal treatment, crystallisation from the melt, rapidly changing pH, thermal desolvation of crystalline solvates, growth in presence of additives, and grinding.[4] High-throughput crystallisation tools such as the Encapsulated Nanodroplet Crystallisation (ENaCt) protocol have been developed to provide efficient screening of polymorphs using minimal sample.[27,28] Computational tools can also support the screening process, including crystal structure prediction (CSP) - the calculation of a compound's crystal energy landscapes from first principles. CSP has been used to successfully anticipate the discovery of new polymorphs of various pharmaceutical compounds including paracetamol, aspirin and carbamazepine,[29] as well

as confirming the most stable polymorph under storage and production conditions and informing potential experiments to discover practically relevant polymorphs from minima in the crystal energy profile. However, the computational expense of CSP increases non-linearly with larger and more flexible molecules or as the number of crystal components increases,[29] and even if the most stable structure can be calculated, it may not be experimentally accessible due to limitations in its nucleation and growth.[31] Despite these limitations, targeted CSP calculations performed in tandem with empirical data and an understanding of common supramolecular synthons has been used to provide insight for co-crystal and salt formation.[30] Given the limits of time and resources, there is no guarantee that all possible polymorphs of a compound will be discovered and the risk of unwanted transformations will be eliminated entirely after the screening process, but the majority of the thermodynamic and kinetic solid products are aimed to be discovered by exposing the compound to a sufficiently wide range of conditions under which nucleation and growth of API crystallites occurs.[31]

1.1.2 Hydrates and solvates

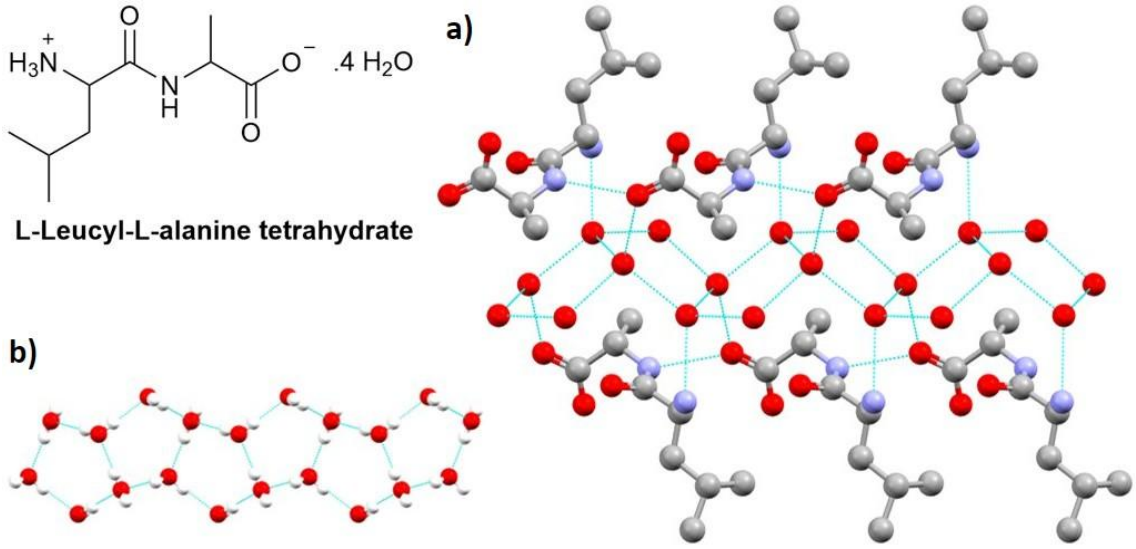

Figure 1.3. a) The crystal structure of L-leucyl L-alanine tetrahydrate, which shows cyclic water pentamers and hydrophobic aggregates of peptide side chains forming separate columns in the crystal respectively (Cambridge Structural Database (CSD) refcode RAVMOQ - hydrogen atoms omitted for clarity).[32] b) The water column from the hydrate structure shown in isolation.

Solvates can arise when solvents are used in the purification of drug substances, and involve solvent molecules either becoming trapped in empty spaces within the crystal structure of a host compound, or interacting with molecules of the crystal via hydrogen bonding or van der Waals forces.[4] The resulting form is referred to as a hydrate when the

solvent is water, and these may form when pharmaceuticals come into contact with water during processing steps (crystallisation, lyophilisation, wet granulation, spray-drying etc.), upon storage in an atmosphere containing water, or upon contact with water contained in their final dosage form. Solvates may exhibit greater stability against decomposition than the anhydrous form of a compound in cases where the solvent molecules increase the crystal lattice energy through favourable interactions to the host, and in some cases the inclusion of even weakly-interacting solvent molecules is necessary to stabilise a structure that may have otherwise decomposed due to empty spaces in the packing arrangement.[33] In the case of hydrates, water can be absorbed in the bulk structure and/or adsorbed to the solid surface, in either stoichiometric or non-stoichiometric ratios. Some unusual stoichiometric hydrates can contain non-integer ratios of water, such as caffeine with 0.8 mol of water per mol caffeine, or brucine which can form a 3.85-hydrate (HyC).[34] Another unusual example is a tetrahydrate of L-leucyl L-alanine which contains columns of solvent in the crystal, where water molecules form cyclic pentamers in an elaborate hydrogen bonding system (Figure 1.3).[32] Solvent molecules within a crystal lattice can affect both the packing arrangement and intermolecular interactions between molecules of the host compound, which can change the solubility, dissolution rate, chemical and physical stability of the compound relative to the anhydrous or non-solvated form.[35] Since these properties may affect the bioavailability and processability of a drug product, it is imperative that hydrate and relevant solvate forms of a drug are studied experimentally. In some cases, a solvate form may even be the desired form for development due to advantages in processibility[36] and other properties such as antimicrobial functionality.[37]

Hydrates are often susceptible to dehydration during drying or storage steps, which can lower the water content or dehydrate the solid completely, sometimes forming an anhydrous polymorph or an amorphous phase.[34] Dehydration of the hydrate may be complex and involve multiple phases, with transformations between hydrate polymorphs.[38] Stoichiometric hydrates possess a different crystal structure to other solid forms of the compound and have a well-defined water content at any given relative humidity, and their dehydration requires significant rearrangement of host molucules.[34] Conversely, non-stoichiometric hydrate structures, where water is often retained in open structural voids such as channels, can be challenging solid forms to process since the water molecules are often relatively weakly bound, and without very precise control of environmental factors such as relative humidity and temperature, the variations in the water content of the solid can lead to substantial errors in dose uniformity or mass-based values such as activity data for biologically active compounds.[34] This type of hydrate may dehydrate fully or only partially as water escapes from the voids without any considerable change to the crystal structure, besides the anisotropic distortion due to the release of

solvent.[39] This results in the formation of isomorphic dehydrates/desolvates that can exhibit reduced chemical or physical stability compared to the original hydrate due to the increase in void space within the crystal.[40] Isomorphic dehydrates are generally very hygroscopic due to their higher energy, metastable nature and reduced packing efficiency.[40]

Hydrates can be obtained in solid form screening procedures by suspending the anhydrous material in water or by exposing the anhydrous powder to a high relative humidity. Solvates can be obtained using similar methods to polymorph screening; crystallisation from single or mixed solvents, or by vapor diffusion. At minimum, screening should be carried out using all of the solvents employed in the synthetic and purification processes for the drug compound, and may also include water, methanol, ethanol, acetone, propanol, isopropanol, acetonitrile, ethyl acetate and appropriate mixtures.[41]

1.1.3 Co-crystals and salts

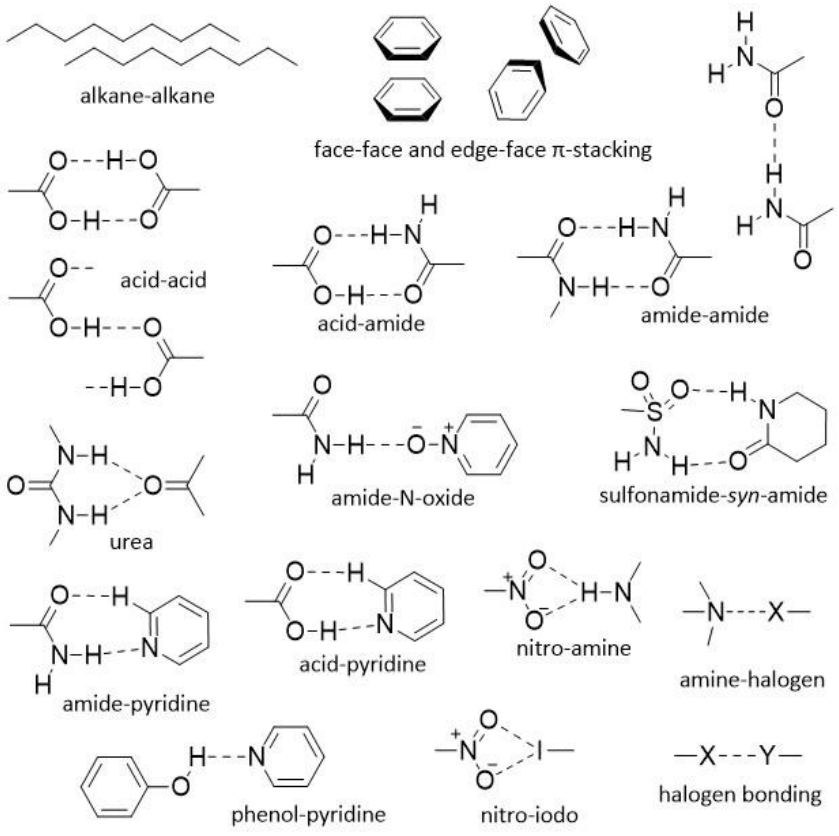

Figure 1.4. Common homo- and hetero-synthons used in crystal engineering.[22,39]

Adding a second component to optimise the chemical, physical and economic characteristics of an API without modifying its chemical structure or pharmacology can be achieved through the development of pharmaceutical salts and co-crystals.[30,42,43]

Pharmaceutical salts have been used for decades to improve the water solubility, toxicity profile and dissolution rate of APIs,[42] and the use of co-crystals has become more commonplace in the last 20 years as their own advantages have become apparent.[44] The presence of non-covalent interactions such as hydrogen bonding, *π*-*π* stacking, van der Waals forces or halogen-bonding between API molecules and co-formers within the crystal lattice affords these altered properties, and an understanding of the possible supramolecular motifs that can form between the different components of the system can provide insight for co-crystal engineering (Figure 1.4).[30,45] The poorly aqueous-soluble anti-epileptic drug lamotrigine is one example of a pharmaceutical where applying the supramolecular synthon approach led to the discovery of new crystal forms, some with enhanced pre-clinical properties (Figure 1.5).[46]

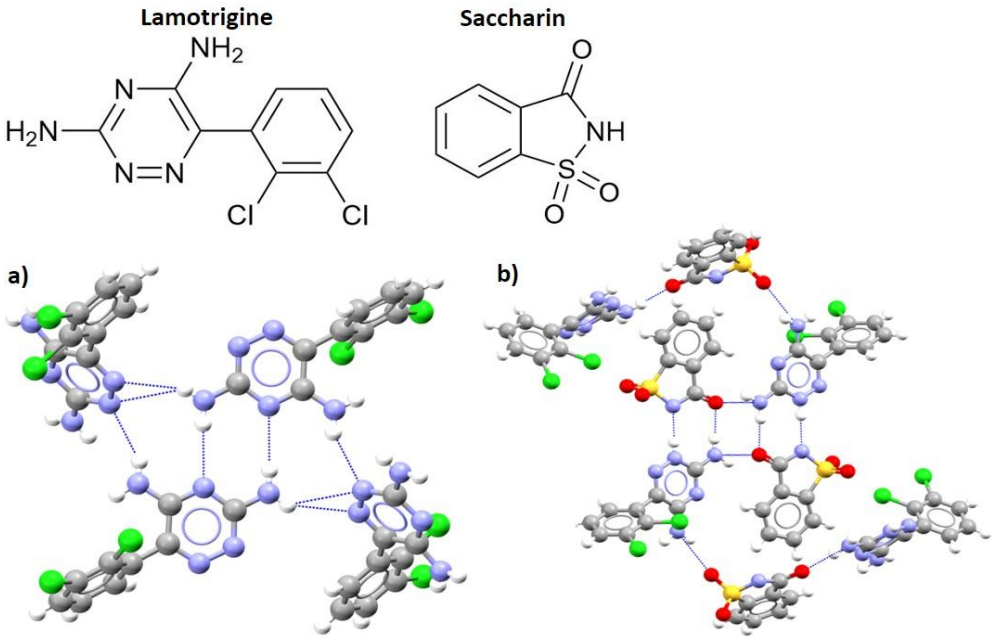

Figure 1.5. a) The crystal structure of the poorly soluble anti-epileptic drug lamotrigine (CSD refcode EFEMUX). b) A novel co-crystal form of lamotrigine discovered through the supramolecular synthon approach, featuring enhanced pre-clinical properties including a 58 % increase in dissolution rate (CSD refcode WUVKOO).[46]

While enhanced processability and/or drug dissolution (and therefore absorption) can be achieved through the use of a salt formulation, some desirable properties come at the expense of others.[43] Increasing the strength of intermolecular interactions in the crystal produces higher-melting salts that are easier to process and generally more chemically stable, but with their increase in lattice enthalpy comes a reduction in their solubility.[43,47] This creates a challenge for chemists to choose the most appropriate salt form, which is generally a semi-empirical process involving the synthesis of various candidates and

comparing them by properties such as stability, hygroscopicity and flowability as well as their cost, ease of crystallisation and yield.[42]

The ΔpKa rule is often used to predict whether a given pair of API and co-former will form a salt or co-crystal. Salt formation is expected in systems where there is a difference in pKa of more than ~3 log units between the conjugate acidic and basic components, while smaller differences (ΔpKa < ~2) are generally considered typical for co-crystal formation; the difference lying in the degree of proton transfer from one component to the other.[30,47] Co-crystallisation of an API is a particularly attractive approach in cases where traditional methods for forming salts fail to produce any solid forms that are viable for development, perhaps where API molecules lack ionisable functional groups, contain moieties that are prone to decomposition and/or racemisation, or are not strongly acidic/basic.[48,49] In addition to being an effective strategy for optimising neutral as well as acidic/basic APIs, the co-crystallisation approach has the advantage of a much greater library of compounds to choose from; around 100 salt formers are available but only around a dozen are preferred due to their toxicity, stability and solubility of the resulting product,[42] whereas the number of potential co-formers is closer to 1000.[47] This large chemical space does present a challenge for industrial scientists, however, and computational tools such as the liquid phase thermodynamics theory COSMO-RS (conductor-like screening model for real solvents) that can predict the success of API - co-former pairs are becoming increasingly useful.[50,5153]

Co-crystallisation improves the solubility and dissolution rate of poorly soluble APIs by generating a long-lived metastable supersaturated state and maintaining it for an extended time (hours) - this is referred to as the “spring and parachute effect” (Figure 1.6).[52] The lifetime of the supersaturation depends on the strength of the bonds between the API and co-former, which are usually hydrogen bonds and therefore dissociate within minutes to an hour in a biological environment, and upon the presence of any precipitation inhibitors to hinder the nucleation and/or growth of API crystals in the supersaturated solution.[53]

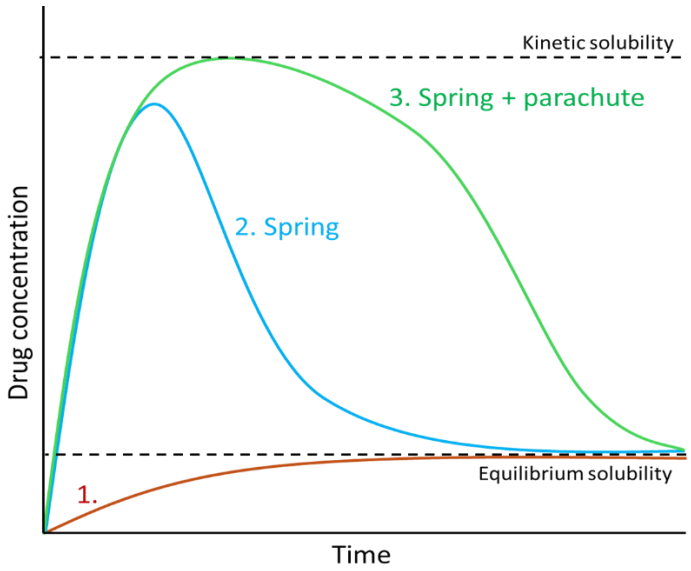

Figure 1.6. Schematic drug dissolution profiles for different drug delivery systems. (1) the dissolution of the most stable crystalline phase up to its equilibrium solubility. (2) the dissolution of a higher energy form of the drug in the absence of precipitation inhibitors, producing a spike in concentration referred to as a "spring". (3) the dissolution of a higher energy form of the drug in presence of precipitation inhibitors, maintaining the high concentration for a greater time period and referred to as a "parachute".[52] The higher energy forms of the drug, e.g. co-crystals, dissolve to a higher but unstable "kinetic" solubility before returning to the equilibrium solubility of the thermodynamic form over time.

1.1.4 Amorphous forms

An amorphous material is characterised as having no clearly defined molecular structure or long-range order and will show a diffuse halo in its X-ray powder diffraction (XRPD) pattern. Above its glass transition temperature (T_g), the amorphous glass will change from a rigid state to a plastic, viscous liquid as molecular mobility increases.[54] The amorphous form of an API generally provides the greatest solubility and dissolution rate advantage since it is the highest energy solid state of a material often with greater molecular motion, and hence it has become of increasing interest to pharmaceutical industry.[55,56] Amorphisation is particularly interesting for poorly aqueous-soluble pharmaceutical compounds administered orally, where there is generally a correlation between dissolution rate and bioavailability.[56] Amorphisation of APIs has been implemented successfully within the pharmaceuticals industry and accounts for approximately 30% of drug products requiring solubility enhancement.[57] Methods to produce amorphous forms of a material include solidification of the melt, rapid precipitation from solution, reduction of particle size via milling, spray-drying, lyophilisation (freeze-drying), desolvation of a solvate or hydrate, and precipitation of

acidic or basic materials by changing pH.[4] Amorphous formulations are generally designed to achieve the spring and parachute effect shown in Figure 1.6, where the rapid dissolution of the amorphous solid initially creates a supersaturated solution that is maintained over a long period of time to afford the greater drug absorption, and hence bioavailability, compared to a crystalline formulation.[58]

Amorphous API formulations are typically thermodynamically unstable however, and prone to recrystallisation unless physically stabilised. Recrystallisation of a formulation upon exposure to a liquid medium negates the benefit gained from the spring and parachute effect as the drug concentration decreases significantly to the equilibrium solubility of the crystal form produced.[56] Furthermore, amorphous solids are often more hygroscopic than their crystalline counterparts since their greater free volume allows water molecules to penetrate them more easily and the uptake of water plasticises the solid, increasing molecular mobility and the likelihood of recrystallisation.[59] Numerous factors govern the physical stability of amorphous solids against recrystallisation; those that depend on molecular structure are the aforementioned molecular mobility (correlated inversely with T_g), the configurational entropic barrier to crystallisation, the enthalpic driving force to produce a solid form with lower configurational enthalpy, and the degree of hydrogen bonding between molecules.[60,61] Factors independent of the molecular structure include the humidity, mechanical stress, temperature and preparation method, since the thermal history of the material can vary the extent of molecular relaxation.[62] Some organic compounds such as triphenyl phosphite can also exhibit polyamorphism, where distinct amorphous phases that vary in their local structures can be formed, often by using different methods to produce the amorphous phase.[63,64] The first pharmaceutically relevant substance in which this behaviour was noted was mannitol which can be prepared as two different amorphous phases at room temperature and pressure, one of which has substantially lower energy and density with a higher T_g.[65] Though rare, polyamorphism adds yet another layer of complexity to the solid-state landscape of a drug that can allow solid-state engineers to further tune the properties and behaviours of an API but equally requires one to characterise the amorphous phases produced in a variety of methods.

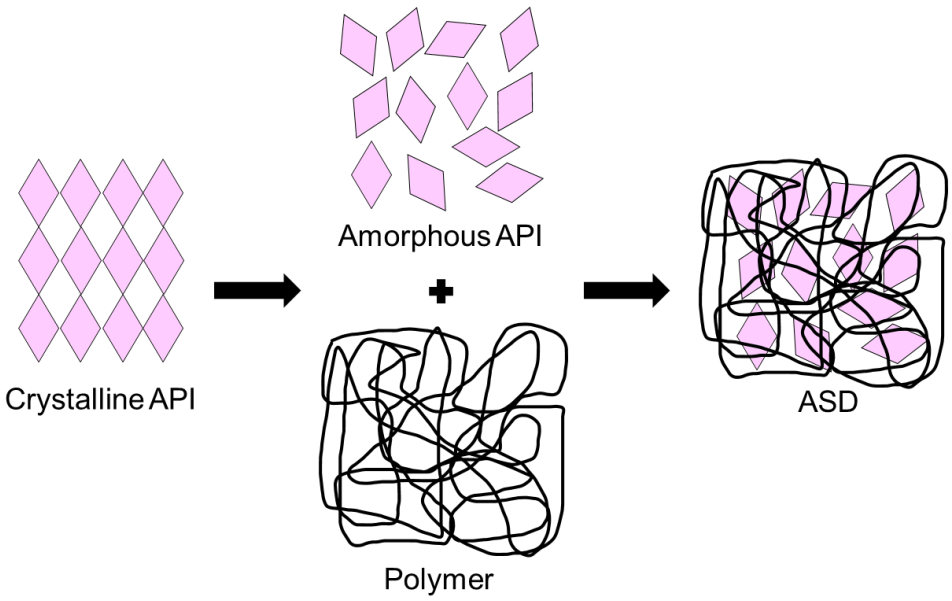

Figure 1.7. A schematic representation of an amorphous solid dispersion, where an amorphous API is stabilised within a polymer matrix.[16]

Recent strategies for physically stabilising amorphous formulations include the use of polymers[66] or low molecular weight co-formers[67] to produce co-amorphous solids, or the confinement of amorphous API within mesoporous silica nanoparticles.[56] Amorphous solid polymer dispersions (ASDs) are one type of co-amorphous form where an API is dispersed within a glassy polymer matrix, and since the miscibility of the API in the polymer is directly related to its stability against crystallisation, the drug and polymer are preferably mixed at the molecular level to produce a glass solution (Figure 1.7).[67] The polymer matrix usually raises the T_g of the ASD compared to the pure amorphous API, inhibiting crystallisation through a reduction of molecular motion to impart greater physical stability,[67] and it has been shown that differences in the types of intermolecular interactions between a given polymer and API affect both the ASD dissolution performance and the maximum drug-loading capacity.[68–70] Rapid dissolution of API from an ASD produces a supersaturated solution with an enhanced free drug concentration that can exceed the amorphous solubility in some systems; in these cases, the drug separates from the bulk aqueous phase via liquid-liquid phase separation to produce colloidal nanoparticles, which act as a reservoir to maintain the elevated drug concentration.[69,70] This behaviour has only been observed in ASDs with low drug loading however, where API and polymer are released congruently at the rate of polymer dissolution. ASDs are also quite often hygroscopic, with water ingress again causing a reduction in T_g that can lead to phase separation and recrystallisation,[71] and they also face manufacturing difficulties. The drug loading of many ASDs is unable to exceed 25

% due to the limited miscibility of the API with polymers, meaning that large volumes of polymer are required to produce the final dosage forms.[70]

Milling with small molecule excipients such as amino acids has also been found to improve the physical stability of poorly water-soluble amorphous APIs including indomethacin and carbamazepine, significantly increasing dissolution rate and T_g relative to the individual drugs in either their pure amorphous or crystalline state.[72] As discussed in section 1.1.3, pharmaceutical salts can be used to improve properties such as aqueous solubility for hydrophobic drugs. When lyophilised for use in an oral dosage form, these salts often lose part or all of their crystallinity through processing and become amorphous. Compared to the freebase equivalent, amorphous salts of an API have been shown to greatly increase the T_g by introducing strong ionic interactions that reduce molecular motion, and the greater the charge density of the ionic species used in the salt formation, the stronger the electrostatic interaction and hence the greater the T_g increase.[73] Salts of amorphous materials can therefore be utilised to enhance physical stability.

1.2 PROTACs

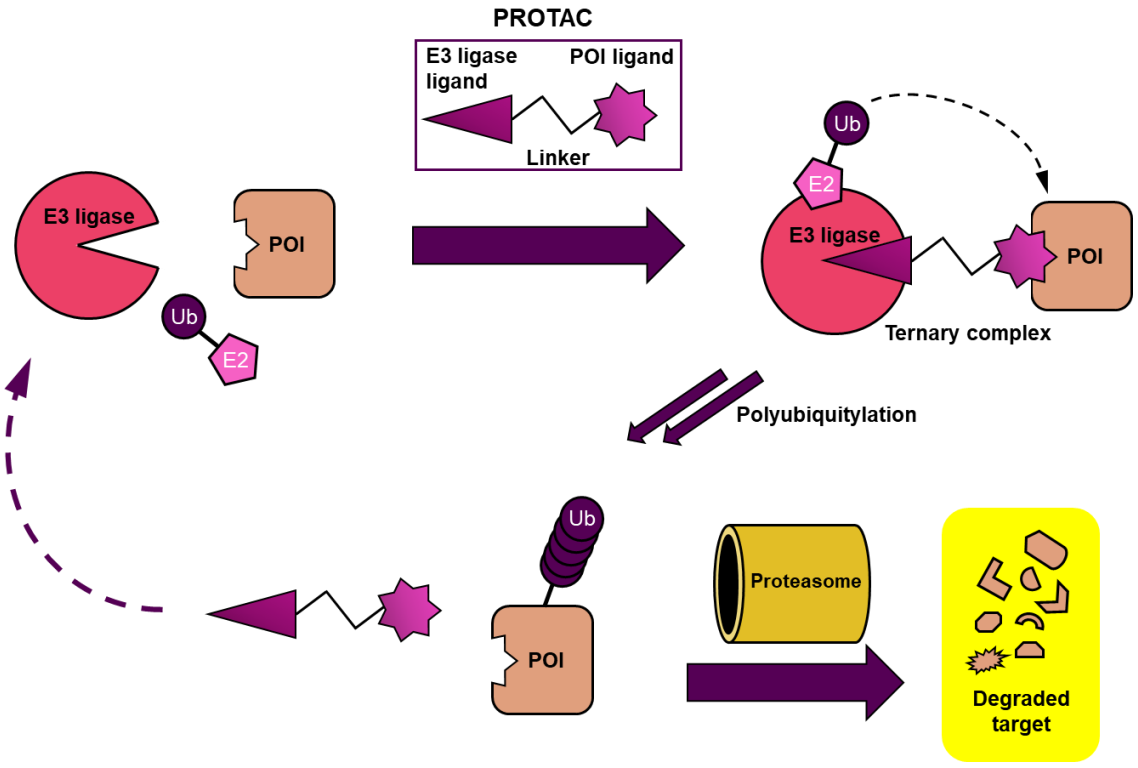

Figure 1.8. The event-driven mode of action of PROTACs. The heterobifunctional PROTAC molecule binds simultaneously to the POI and E3 ligase, forming a ternary complex that facilitates ubiquitylation of the POI and its degradation by the proteasome.

Substantial interest has been raised in targeted protein degradation (TPD) for its potential to enable therapeutical modulation of proteins that have previously proved difficult to target using conventional small molecule approaches.[74] One major TPD strategy emerging in the last two decades employs PROTACs; heterobifunctional molecules using a linker moiety to join two ligands groups that can bind simultaneously to a protein of interest (POI) and an E3 ubiquitin ligase. The formation of this ternary complex by the PROTAC molecule induces ubiquitylation of the POI and subsequently its degradation via the ubiquitin-proteasome system (Figure 1.8).[74–77] Conventional, occupancy-driven protein inhibition using small molecules requires the drug to bind to the target's active site(s), and since the drug efficacy is driven by retaining a high target occupancy, high doses are often required and can cause unwanted side-effects through off-target binding.[78] Diseases such as cancer and bacterial infections may also become resistant to therapeutics using this inhibition mode of action (MOA) in many cases.[79,80] The MOA for PROTACs differs by using an iterative, event-driven pharmacology to induce protein *degradation* and is not reliant on binding specifically to the active site, bypassing the need to block the catalytic activity of the target directly.[81] Reducing the protein concentration in disease tissues through degradation of the targets also affords potential benefits beyond simply inhibiting their function.[75] PROTACs may have the ability to degrade targets previously deemed part of the "undruggable" proteome since they require only target engagement and can bind to "silent" binding pockets,[82] proving advantageous over small molecules which have proved unsuitable for bridging the size and/or shape of the target's active sites, or where the target possesses multiple functional domains.[75,77] Approximately 80% of the human proteome falls into the so-called "undruggable" protein category[83] and many play a critical role in the function of cancers and other major diseases, so are of particular interest to the pharmaceutical industry.[74]

1.2.1 PROTAC Chemistry

The structure of the ternary complex created by the POI, PROTAC and E3 ligase depends strongly on the molecular structure of the PROTAC itself, and the potency of a given PROTAC as a protein degrader is ultimately determined by the stability of the ternary complex it forms, as well the rates of processing the target via the ubiquitin-proteasome system (UPS) and of the target's re-synthesis.[84,85] The structural characteristics of the E3 ligase and POI themselves must be understood in order to design a PROTAC with the best combination of the two ligand warheads and linker moiety, and often a crystal structure of the POI ligand bound to its target is necessary for

designing new degraders.[76] Techniques to complement these studies often include molecular modelling.[86]

Recruiting different E3 ligases to degrade a given target has a distinct impact on the degradation profile.[87] While there are predicted to be more than 600 human E3 ligases, only a distinct few have been used to generate effective PROTACs, with cereblon (CRBN) and von Hippel-Lindau (VHL) ligases the most common to date (Figure 1.9).[76,88] CRBN-based PROTACs are currently one of very few orally-bioavailable degrader classes.[74] However, these E3 ligases show no cell selectivity and can cause uncontrolled protein degradation, meaning that the PROTACs which recruit them can produce toxicity to normal cells through off-target effects.[89] Expansion of the E3 ligase library is highly desirable to introduce/improve cell selectivity, to avoid the emergence of drug resistance to the more frequently used CRBN and VHL ligases, to induce longer-lasting ternary complexes that persist long enough for the E3 ligase to ubiquitinate the substrate, and to develop PROTACs capable of recruiting E3 ligases with specific expression profiles in a given tissue/tumour type or cellular compartment.[81,82] Alternative E3 ligases that have been recruited by PROTACs in recent years include the Mouse double minute 2 homolog (MDM2), Cellular Inhibitor of Apoptosis Protein 1 (cIAP1), kelch-like ECH-associated protein-1 (KEAP1), aryl hydrocarbon receptor (AhR), and Ddb1-and Cul4-associated factor 15/16 (DCAF15/16).[88–91] DCAF15 and DCAF16 are predominantly localised in a single subcellular compartment, and have been shown in at least one case to display clear subcellar selectivity.[92]

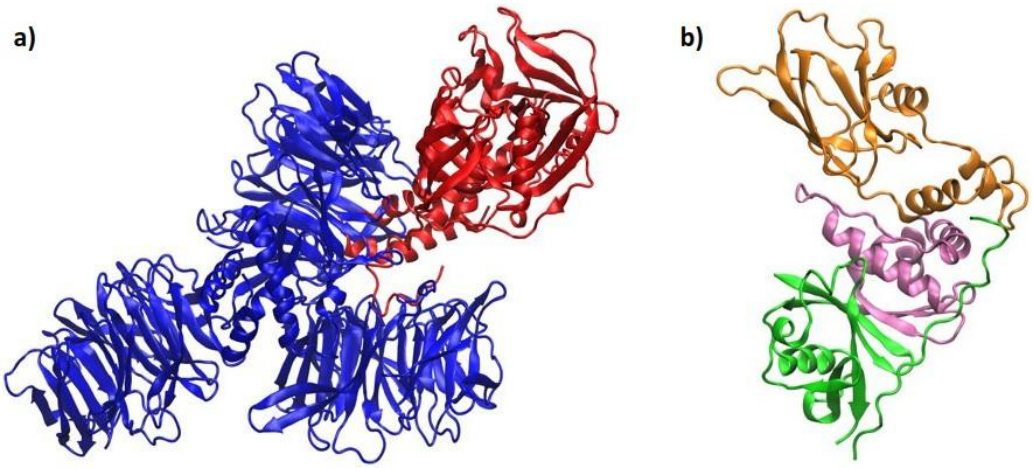

Figure 1.9. a) CRBN (red) and Ddb1 (blue) in the E3 ligase complex (PDB 4CI2).[93] b) VHL (orange), EloC (pink) and EloB (green) in the E3 ligase complex (PDB 3ZRF).[94]

Orienting the E3 ligase and POI closely enough to make favourable protein-protein interactions, and subsequently to allow ubiquitin units to transfer across the ternary

complex, is achieved using an appropriate linker geometry and chemical composition.[76,77,95] PROTACs linkers can range in polarity and flexibility; some of the most flexible are lipophilic alkyl chains which are easy to synthesise but often too hydrophobic to provide sufficient cell permeability,[81,96] so heteroatom-containing polyethylene glycol (PEG) chains are used more often to increase PROTAC solubility.[77,81,95] More rigid linkers can be produced using heterocyclic moieties such as piperidine and piperazine, where the smaller entropic penalty of forming the ternary complexes is thought to explain the effective protein degradation observed for them.[97] It has also been observed that a minimum linker length is required to prevent steric clashing between the E3 ligase and POI ligands that counteracts the PROTAC binding affinity, with one study indicating that TANK-binding kinase 1 (TBK1) PROTACs generated using linkers with fewer than 12 carbon atoms had no measurable degradation activity (Figure 1.10).[98] Conversely, when the linker group is too long, ubiquitylation of the target protein cannot occur.[81,99] Understanding the favoured PROTACs conformations arising from flexibility in the linker under conditions comparable to intracellular compartments is therefore highly advantageous for rational PROTACs design.

The relationship between linker length and PROTAC selectivity appears to be complex, with one study showing that an increase in linker length increased a PROTAC's selectivity from targeting both epidermal growth factor receptor (EGFR) and human epidermal growth factor receptor 2 (HER2) to instead only degrading EGFR,[100] while another study showed that the smaller number of conformations possible for a shorter linker in a CRBN-based PROTAC increased selectivity by reducing flexibility.[101] These results suggest that the selectivity of PROTACS can be modified in a sophisticated manner via linker choice, but a better understanding of the structure-activity relationships is required before PROTACs can be designed with specific linkers to achieve desired selectivity profiles.[76] One paper suggested that initial PROTAC design should employ longer linker groups, before they are systematically shortened to achieve the optimum linker and structure activity relationship.[102]

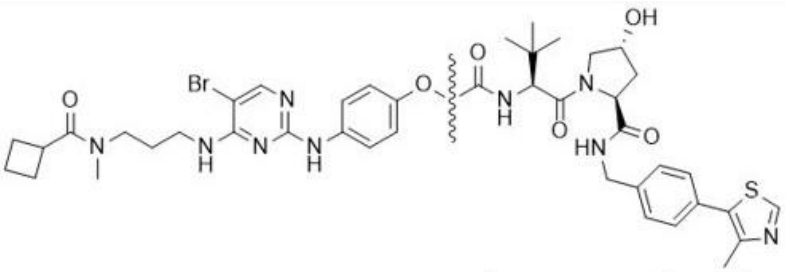

Linker	# of linear non-H linker atoms	DC_{50}	D_{max}	PSA (Å)
	7	>1000	ND	200
	8	>1000	ND	209
	9	>1000	ND	200
	10	>1000	ND	209
	11	>1000	ND	219
	12	88	79	209
	13	71	86	219
	14	103	92	228
	15	12	96	219
	16	95	90	209
	17	29	96	237
	18	6	96	228
	19	25	96	228
	20	34	96	246
	21	3	96	237
	29	292	76	237

Figure 1.10. Degradation activity for a series of TBK1 PROTACs (structure shown above) produced with linkers of different lengths.[98] PROTACs with linkers shorter than 12 carbon atoms have no degradation activity, indicating a minimum linker length is required. ND: not determined. DC_{50}: concentration at which 50 % degradation is observed. D_{max}: maximal degradation observed. Data represent the mean of ≥ 2 determinations. PSA calculations performed with ChemAxon software.

1.2.2 PROTAC Challenges

Solubility and cell permeability are key properties for improving the bioavailability of oral PROTACs such as those based on CRBN,[103] but a poor understanding of the structure-property relationships for PROTACs hampers progress in ensuring that the degraders will reach their intracellular targets.[104] The development of new drug compounds in

general has expanded rapidly into a chemical space beyond Lipinski's rule of 5 (bRo5),[81] a guideline used to assemble high-throughput screening libraries,[74] and the number of poorly water-soluble APIs has greatly increased with PROTACs included.[16] Many physicochemical properties of PROTACs molecules, such as their molecular weight (MW), polar surface area (PSA), numbers of hydrogen bond acceptors and donors (HBAs and HBDs respectively), number of rotatable bonds, lipophilicity, and degree of ionisation, lie in the bRo5 chemical space.[81,105] Membrane permeability is generally inversely proportional to MW and many PROTACS weigh in the range of 900 - 1200 Da,[106] though hydrophobicity and the number of HBDs are argued to have a greater impact on permability.[107,108] A lack of information on how to optimise the absorption, distribution, metabolism and excretion (ADME) profiles of molecules in the bRo5 space complicates PROTACs design and their poor aqueous solubility impedes various stages of the drug development process, including their formulation into drug products.[103] The limited solubility and number of ionisable atoms in PROTACs can also make it difficult to determine their pKa experimentally (via potentiometric titration or spectral gradient analysis for example), and therefore complicate the process of salt and/or co-crystal screening.[109] One example of an optimisation challenge is that while increasing linker length has been shown to increase PROTAC selectivity in some cases (as discussed in section 1.2.1), it is generally accompanied by an increase in one of more of the MW, HBDs or HBAs of the PROTAC and therefore reduces membrane permeability.[107]

The high flexibility and size of PROTACs molecules also increases the conformational space that they can explore. Investigating the solution conformations of a given degrader can help to predict its cell membrane permeability,[104] as well as helping to understand the structure of the ternary complex it forms as discussed in section 1.2.1. Recent work has shown that a high MW and high polarity VHL-based PROTAC exhibits elongated conformations with a greater PSA in polar solvents, but folds up via intramolecular hydrogen bonds and $\pi-\pi$ interactions to reduce its size and PSA in apolar solvents (Figure 1.11).[104] This molecular chameleonicity facilitates the cell permeability of the PROTAC, allowing it to mimic either the exterior and interior of the membrane.[103,104] Other chameleonic bRo5 compounds such as cyclosporin A, a cyclic peptide, have been shown to expose or shield their polarity dynamically to facilitate high permeability and aqueous solubility simultaneously, compared to rigid analogues or those whose properties are insensitive to the molecular conformation,[110] and the ability to dynamically form intramolecular hydrogen bonds (IMHBs) was shown to be particularly effective for providing this property.[111] This is a particularly intriguing result because the interplay between solubility and permeability usually makes their simultaneous optimisation a challenge for bRo5 compounds,[103] where increasing permeability by making the molecule more lipophilic would normally decrease its solubility for example.[16] It is

therefore of interest to assess PROTACs conformations in both polar and nonpolar environments to understand how their structural features and properties are related, and to determine whether any IMHBs that exist are static (persisting in both polar and nonpolar environments) and may be reducing the solubility in aqueous media, or dynamic and instead improving both aqueous solubility and cell permeability. These studies also confirm that many molecular property descriptors conventionally used for Ro5 small molecules, such as size, lipophilicity, and polarity, cannot be applied to bRo5 compounds directly because they are insensitive to the 3D conformation of the molecule and its environment.[81]

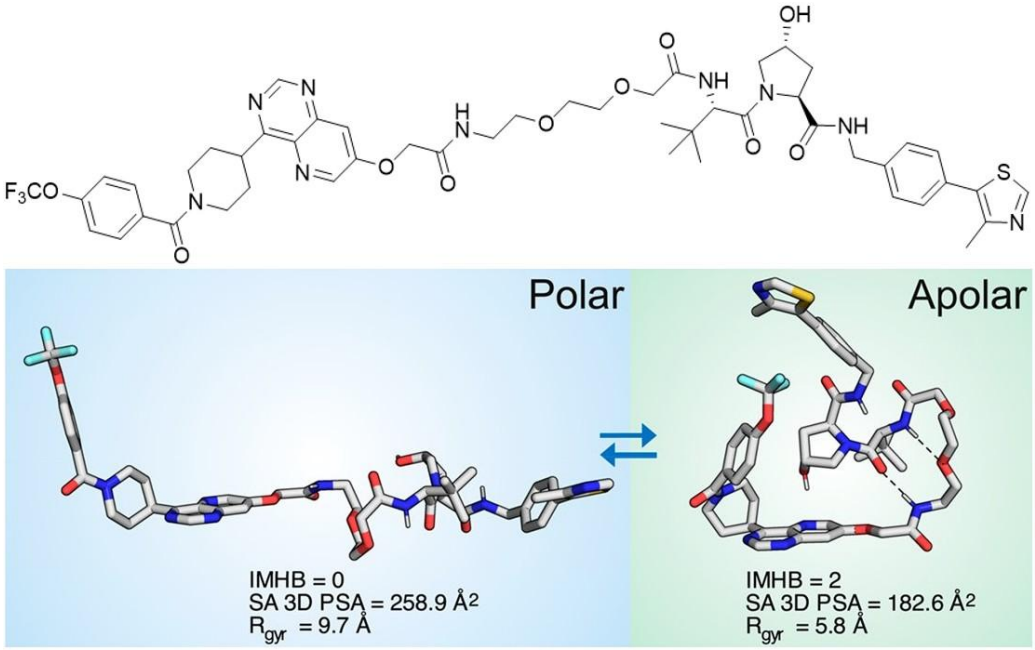

Figure 1.11. A chameleonic PROTAC shown by NMR to exhibit elongated conformations with higher PSA in polar solvents and folded conformations with lower PSA in apolar solvents, allowing it to mimic either the exterior or interior of a cell membrane depending on its environment and thus imparting cell permeability.[104] Reproduced with permission from Professor Jan Kihlberg. Copyright © 2020 American Chemical Society.

Some improved bRo5 physicochemical property descriptors for ionisation, lipophilicity, polarity and chameleonicity have been proposed in recent work,[105] and additional information such as the number of IMHBs and radius of gyration (R_g) of a PROTAC molecule have proven useful for predicting cell permeability and therefore to guide the process of molecular design.[81] Multiple tools can be used in tandem to measure a single property, circumventing the limitations of using only individual methods.[105] Another barrier to understanding PROTACs properties is that many conventional assays are unsuitable for their study. Improving bioavailability for oral PROTACs in particular has largely been associated with molecules having higher lipophilicity, reducing the aqueous

solubility below the limit of assays and encouraging non-specific binding to the labware.[75,112] New methods are being designed to navigate around these issues and provide insight into structure-permeability relationships, with one recent example involving the combination of a parallel artificial membrane permeability assay (PAMPA) with a lipophilic permeability efficiency (LPE) metric to relate permeability data with structural features.[107]

1.2.3 PROTAC Formulation

Poorly water-soluble APIs such as PROTACs typically exhibit poor oral absorption and therefore insufficient bioavailability. Where adaptation of the chemical structure fails to improve oral absorption of PROTACs, formulation approaches may succeed by enhancing aqueous solubility and/or dissolution rate via either the chemical modifications previously discussed such as salts and co-crystals, or physical modifications such as amorphisation and nanocrystallisation.[57,109] As discussed in section 1.1.4, co-amorphous formulations are one route to dosing poorly soluble drugs for further development.[16] While there are no reports in the literature of PROTAC co-amorphous formulations using low molecular weight co-formers, there are several recent examples of successfully applying ASD formulations to enhance the solubility of PROTAC compounds. Pöstges et al. first produced ASD formulations of an initially amorphous androgen-receptor PROTAC 'ARCC-4' at 10 and 20 % DL with hydroxypropyl methyl cellulose acetate succinate (HPMCAS) and Eudragit polymers by vacuum compression moulding, with non-sink dissolution studies showing a pronounced supersaturation enhancement without drug precipitation.[113] Hofmann et al. also demonstrated significant supersaturation enhancements for spray-dried ASDs of an initially amorphous cereblon (CRBN) PROTAC with Soluplus and Eudragit polymers at 10 % DL, compared to the pure amorphous API.[114] Mareczek et al. later demonstrated dissolution enhancements for spray-dried ASDs of both an initially semi-crystalline PROTAC 'ARV-110' and an initially amorphous PROTAC 'SelDeg51' with poly(vinyl alcohol) (PVA) at 30 % DL, indicating that the ASD formulations using the crystalline API were physically stable for at least 4 weeks.[115] Most recently, Zhang et al. studied ASDs of a CRBN PROTAC with HPMCAS, Eudragit and Soluplus prepared at 5, 10 and 20 % DL by solvent evaporation, confirming the presence of drug-polymer hydrogen bonding interactions using FTIR and showing that HPMCAS ASDs could be produced as high as 40 % DL, although ASDs at higher drug loading showed poor dissolution performance.[116] They also showed, however, that the limited dissolution enhancement of the high DL ASDs could be improved greatly by adding sodium dodecyl sulfate as a surfactant to produce a ternary ASD system.[116]

To aid in the design of multi-component PROTAC formulations, a fundamental understanding of the API's physical behaviour must be developed through pre-formulation studies. For the case of PROTACs, examples of work to be carried out may include an investigation of the solid form landscape and the physical, mechanical and chemical properties of each discovered form, including analysis of the conformations the molecule adopts in each form and what types of interactions are dominant between the molecules, and the solubility of each form in a range of solvents. Understanding the nature of the intermolecular interactions in the solid state (i.e. which types of intermolecular interaction dominate the interaction potential energy, or which hydrogen bonding motifs are the most common) is particularly relevant to the ASD formulation strategy, since it can inform the choice of polymer in which to disperse the API and hence improve both the dissolution performance and maximum drug-loading capacity of the ASD,[68–70] and to the co-crystal/salt-forming strategies where a co-former/counter-ion may be selected based on an understanding of the supramolecular synthons that could form between it and the API.[30]

Experimental pre-formulation research can be combined with complementary *in silico* studies to add further support to conclusions from experimental data and/or to validate theoretical models. MD simulations have been used in previous studies to successfully predict miscibility and solubility parameters,[117] T_g and plasticisation effects for pharmaceutical compounds,[118] as well as for modelling PROTACs conformations and calculating energy barriers between them.[119] Computational CSP can also be used to support solid form investigation, as discussed in section 1.1.1. Recent work has also shown that machine learning (ML) techniques can be used to greatly increase the speed of predicting solid-state nuclear magnetic resonance (NMR) chemical shifts from large atomistic MD simulations of amorphous API structures.[120] These predicted shifts can then be correlated with real spectroscopic data to aid in identifying hydrogen bonding motifs and determining their contribution to the intermolecular interaction potential.[120]

1.3 Conclusion

PROTACs are an incipient modality for the treatment of various cancer types, benefitting from an event-driven MOA that results in the degradation of proteins rather than only their inhibition, offering several advantages over conventional small molecule pharmaceuticals. However, like most APIs currently in development, PROTACs generally suffer from poor aqueous solubility. To benefit from their pharmacological advantages, the bioavailability of PROTACs must be improved without making significant alterations to the chemical structure of the compounds. This goal may be achieved through

formulation approaches such as co-crystallisation, amorphisation or combinations thereof, but implementing these strategies may be complicated by the large MW and other bRo5 properties of the PROTAC compounds. Combining conventional experimental procedures with computational modelling may aid in the pre-formulation studies required initially to understand the solid form characteristics of the compounds and inform the formulation strategies going forward.

1.4 Scope and aims of this thesis

Roughly 70 % of breast cancers express estrogen receptor (ER) and/or progesterone receptors, implying the hormone dependence of these tumour cells for growth. Ovarian and endometrial cancers are also thought to be dependent on ER alpha signalling for growth. Currently available therapies such as fulvestrant have had a strongly positive impact on breast cancer treatment, however a considerable number of patients whose tumours express ER display *de novo* resistance to existing ER therapies or develop resistance to those therapies over time.[121] The PROTAC molecule shown in Figure 1.12, referred to henceforth as AZ1, consists of a lenalidomide-based ligand which recruits the E3 ligase cereblon and an ER ligand adjoined via a piperazine/piperidine-based linker moiety. Compounds of this type have been found to possess potent anti-tumour activity and inhibit the uncontrolled cellular proliferation which arises from malignant disease. They selectively degrade ER alpha in a number of different breast cancer cell-lines including MCF-7, CAMA-1 and BT474.[121]

The work in this thesis aims to improve the current understanding of the physical properties of these high MW, flexible and poorly soluble PROTAC compounds including AZ1 by studying their crystallisability, their potential to form stable amorphous phases and their potential to form crystalline or amorphous multi-component solids. An improved knowledge of the role that non-covalent interactions have in crystal packing may aid in the development of a solid formulation approach for oral PROTAC drug products.

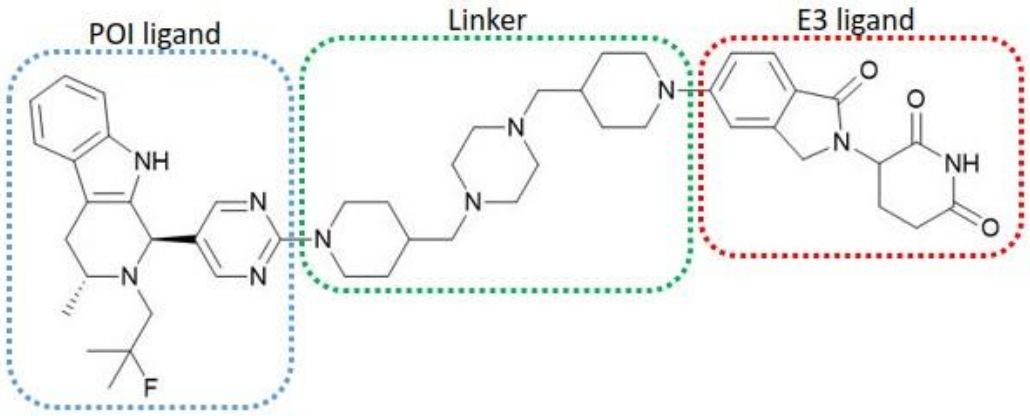

Figure 1.12. The structure of 3-5-[4-(4-[(1-5-[(1R,3R)-2-(2-fluoro-2-methylpropyl)-3-methyl2,3,4,9-tetrahydro-1H-beta-carbolin-1-yl]pyrimidin-2-ylpiperidin-4-yl)methyl]piperazin-1ylmethyl)piperidin-1-yl]-1-oxo-1,3-dihydro-2H-isoindol-2-ylpiperidine-2,6-dione (compound AZ1).

1.5 References

1. A. Mullard, *Nat. Rev. Drug Discov.*, 2021, **20**, 247–250.
2. C. A. Lipinski, F. Lombardo, B. W. Dominy and P. J. Feeney, *Adv. Drug Deliv. Rev.*, 2001, **46**, 3–26.
3. A. J. Cruz-Cabeza, S. M. Reutzel-Edens and J. Bernstein, *Chem. Soc. Rev.*, 2015, **44**, 8619–8635.
4. H. G. Brittain, *Polymorphism in pharmaceutical solids*, Dekker: New York, 1999, vol. 95.
5. M. Saifee, N. Inamdar, D. L. Dhamecha and A. A. Rathi, *Int. J. Health Res.*, 2010, **2**, 291–306.
6. K. Suresh, T. Mehta, V. Thakrar and R. G. Sharma, *Cryst. Growth Des.*, 2025, **25**, 1282–1292.
7. J. Bernstein and J. MacAlpine, *Polymorphism in the Pharmaceutical Industry: Solid Form and Drug Development*, Wiley-VCH, 2019.
8. S. Karthika, T. K. Radhakrishnan and P. Kalaichelvi, *Cryst. Growth Des.*, 2016, **16**, 6663–6681.
9. K. Sugano, *Int. J. Pharm.*, 2009, **378**, 142–145.
10. D. Erdemir, A. Y. Lee and A. S. Myerson, *Acc. Chem. Res.*, 2009, **42**, 621–629.
11. S. Hamad, C. Moon, C. Richard, A. Catlow, A. T. Hulme and S. L. Price, *J. Phys. Chem. B*, 2006, **110**, 3323–3329.
12. M. A. O'Mahony, C. C. Seaton, D. M. Croker, S. Veesler, Å. C. Rasmuson and B. K. Hodnett, *Cryst. Growth Des.*, 2014, **14**, 3967–3974.
13. H. Park, J. S. Kim, S. Hong, E. S. Ha, H. Nie, Q. T. Zhou and M. S. Kim, *J. Pharm. Investig.*, 2022, **52**, 175–194.
14. S. R. Chemburkar, J. Bauer, K. Deming, H. Spiwek, K. Patel, J. Morris, R. Henry, S. Spanton, W. Dziki, W. Porter, J. Quick, P. Bauer, J. Donaubauer, B. A. Narayanan, M. Soldani, D. Riley and K. McFarland, *Org. Process Res. Dev.*, 2000, **4**, 413–417.
15. A. B. Anane-Adjei, E. Jacobs, S. C. Nash, S. Askin, R. Soundararajan, M. Kyobula, J. Booth and A. Campbell, *Int. J. Pharm.*, 2022, **614**, 121387.
16. B. P. A. Gabriele, C. J. Williams, M. E. Lauer, B. Derby and A. J. Cruz-Cabeza, *Cryst. Eng. Comm.*, 2021, **23**, 2027–2033.

17. P. L. Kaskiewicz, I. Rosbottom, R. B. Hammond, N. J. Warren, C. Morton, P. J. Dowding, N. George and K. J. Roberts, *Cryst. Growth Des.*, 2021, **21**, 1946–1958.
18. L. Y. Pfund, C. P. Price, J. J. Frick and A. J. Matzger, *J. Am. Chem. Soc.*, 2015, **137**, 871–875.
19. M. Boyes, A. Alieva, J. Tong, V. Nagyte, M. Melle-Franco, T. Vetter and C. Casiraghi, *ACS Nano*, 2020, **14**, 10394–10401.
20. S. Song, L. Wang, C. Yao, Z. Wang, G. Xie and X. Tao, *Cryst. Growth Des.*, 2020, **20**, 9–16.
21. Y. Diao, K. E. Whaley, M. E. Helgeson, M. A. Woldeyes, P. S. Doyle, A. S. Myerson, T. A. Hatton and B. L. Trout, *J. Am. Chem. Soc.*, 2012, **134**, 673–684.
22. J. A. Foster, K. K. Damodaran, A. Maurin, G. M. Day, H. P. G. Thompson, G. J. Cameron, J. C. Bernal and J. W. Steed, *Chem. Sci.*, 2016, **8**, 78–84.
23. Q. Zhang, Y. Yan, Y. Xu, X. Zhang and J. W. Steed, *J. Colloid Interface Sci.*, 2025, **687**, 582–588.
24. R. Contreras-Montoya, L. Álvarez de Cienfuegos, J. A. Gavira, J. W. Steed, A. Gavira and R. Contreras-Montoya, *Chem. Soc. Rev.*, 2024, **53**, 10604–10619.
25. H. Sharma, B. K. Kalita, D. Pathak and B. Sarma, *Cryst. Growth Des.*, 2024, **24**, 17–37.
26. J. P. Metherall, P. A. Corner, J. F. McCabe, M. J. Hall and M. R. Probert, *Acta Crystallogr. B Struct. Sci. Cryst. Eng. Mater.*, 2024, **80**, 4–12.
27. H. E. Straker, L. McMillan, L. Mardiana, G. R. Hebberd, E. Watson, P. G. Waddell, M. R. Probert and M. J. Hall, *Cryst. Eng. Comm.*, 2023, **25**, 2479–2484.
28. S. L. Price, D. E. Braun and S. M. Reutzel-Edens, *Chem. Commun.*, 2016, **52**, 7065.
29. D. J. Berry and J. W. Steed, *Adv. Drug Deliv. Rev.*, 2017, **117**, 3–24.
30. E. H. Lee, *Asian J. Pharm. Sci.*, 2014, **9**, 163–175.
31. C. H. Görbitz, *Acta Crystallogr. C*, 1997, **53**, 736–739.
32. A. Berziņš, E. Skarbulis, T. Rekis and A. Actiņš, *Cryst. Growth Dev.*, 2014, **14**, 2654–2664.
33. D. E. Braun and U. J. Griesser, *Cryst. Growth Des.*, 2016, **16**, 6111–6121.
34. R. K. Khankari and D. J. W. Grant, *Thermochim. Acta*, 1995, **248**, 61–79.
35. T. Suzuki, T. Araki, H. Kitaoka and K. Terada, *Chem. Pharm. Bull.*, 2012, **60**, 45–55.
36. K. M. Kersten, M. E. Breen, A. K. Mapp and A. J. Matzger, *Chem. Commun. (Camb.)*, 2018, **54**, 9286.
37. D. Raijada, A. D. Bond, F. H. Larsen, C. Cornett, H. Qu and J. Rantanen, *Pharm. Res.*, 2013, **30**, 280–289.
38. U. J. Griesser, *Polymorphism: in the Pharmaceutical Industry*, 2006, 211–233.
39. G. A. Stephenson, E. G. Groleau, R. L. Kleemann, W. Xu and D. R. Rigsbee, *J. Pharm. Sci.*, 1998, **87**, 536–542.
40. S. Byrn, R. Pfeiffer, M. Ganey, C. Hoiberg and G. Poochikian, *Pharm. Res.*, 1995, **12**, 945–954.
41. S. M. Berge, L. D. Bighley and D. C. Monkhouse, *J. Pharm. Sci.*, 1977, **66**, 1–19.
42. P. L. Gould, *Int. J. Pharm.*, 1986, **33**, 201–217.
43. M. Guo, X. Sun, J. Chen and T. Cai, *Acta Pharm. Sin. B*, 2021, **11**, 2537–2564.
44. G. R. Desiraju, P. David, Y. Curtin, P. Lain and C. Paul, *Angew. Chem., Int. Ed. Engl.*, 1995, **34**, 2311–2327.
45. M. L. Cheney, N. Shan, E. R. Healey, M. Hanna, L. Wojtas, M. J. Zaworotko, V. Sava, S. Song and J. R. Sanchez-Ramos, *Cryst. Growth Des.*, 2010, **10**, 394–405.
46. G. Bolla, B. Sarma and A. K. Nangia, *Chem. Rev.*, 2022, **122**, 11514–11603.
47. N. J. Babu and A. Nangia, *Cryst. Growth Des.*, 2011, **11**, 2662–2679.
48. D. P. McNamara, S. L. Childs, J. Giordano, A. Iarriccio, J. Cassidy, M. S. Shet, R. Mannion, E. O'Donnell and A. Park, *Pharm. Res.*, 2006, **23**, 1888–1897.
49. C. Loschen and A. Klamt, *J. Pharm. Pharmacol.*, 2015, **67**, 803–811.
50. Y. A. Abramov, C. Loschen and A. Klamt, *J. Pharm. Sci.*, 2012, **101**, 3687–3697.
51. D. D. Bavishi and C. H. Borkhataria, *Prog. Cryst. Growth Charact. Mater.*, 2016, **62**, 1–8.

52. S. Emami, M. Siahi-Shadbad, K. Adibkia and M. Barzegar-Jalali, *BioImpacts*, 2018, **8**, 305–320.
53. A. Shrivastava, *Introduction to Plastics Engineering*, 2018, 1–16.
54. Q. Shi, F. Li, S. Yeh, S. M. Moinuddin, J. Xin, J. Xu, H. Chen and B. Ling, *AAPS Pharm. Sci. Tech.*, 2022, **23**, 1–19.
55. R. Iyer, V. P. Jovanovska, K. Berginc, M. Jaklič, F. Fabiani, C. Harlacher, T. Huzjak and M. V. Sanchez-Felix, *Pharmaceutics*, 2021, **13**, 1682.
56. L. S. Taylor and G. G. Z. Zhang, *Adv. Drug Deliv. Rev.*, 2016, **101**, 122–142.
57. R. Mizoguchi, H. Waraya and Y. Hirakura, *Mol. Pharm.*, 2019, **16**, 2142–2152.
58. D. Zhou, G. G. Z. Zhang, D. Law, D. J. W. Grant and E. A. Schmitt, *Mol. Pharm.*, 2008, **5**, 927–936.
59. P. J. Marsac, H. Konno and L. S. Taylor, *Pharm. Res.*, 2006, **23**, 2306–2316.
60. C. Bhugra and M. J. Pikal, *J. Pharm. Sci.*, 2008, **97**, 1329–1349.
61. P. H. Poole, T. Grande, C. A. Angell and P. F. McMillan, *Science (1979)*, 1997, **275**, 322–323.
62. A. Ha, I. Cohen, X. Zhao, M. Lee and D. Kivelson, *J. Phys. Chem.*, 1996, **100**, 1–4.
63. M. Zhu, J. Q. Wang, J. H. Perepezko and L. Yu, *J. Chem. Phys.*, 2015, **142**, 24, 244504.
64. C. Leuner and J. Dressman, *Eur. J. Pharm. Biopharm.*, 2000, **50**, 47–60.
65. R. Laitinen, K. Löbmann, C. J. Strachan, H. Grohganz and T. Rades, *Int. J. Pharm.*, 2013, **453**, 65–79.
66. M. G. Van, S. Janssens and G. Van Den Mooter, *J. Pharm. Pharmacol.*, 2010, **61**, 1571–1586.
67. C. Que, A. Deac, D. Y. Zemlyanov, Q. Q. Qi, A. S. Indulkar, Y. Gao, G. G. Z. Zhang and L. S. Taylor, *Mol. Pharm.*, 2021, **18**, 3496–3508.
68. T. N. Hiew, D. Y. Zemlyanov and L. S. Taylor, *Mol. Pharm.*, 2022, **19**, 392–413.
69. A. C. F. Rumondor and L. S. Taylor, *Mol. Pharm.*, 2010, **7**, 477–490.
70. K. Löbmann, H. Grohganz, R. Laitinen, C. Strachan and T. Rades, *Eur. J. Pharm. Biopharm.*, 2013, **85**, 873–881.
71. P. Tong, L. S. Taylor and G. Zografi, *Pharm. Res.*, 2002, **19**, 649–654.
72. M. Békés, D. R. Langley and C. M. Crews, *Nat. Rev. Drug Discov.*, 2022, **21**, 181–200.
73. S. D. Edmondson, B. Yang and C. Fallan, *Bioorg. Med. Chem. Lett.*, 2019, **29**, 1555–1564.
74. C. Cecchini, S. Pannilunghi, S. Tardy and L. Scapozza, *Front. Chem.*, 2021, **9**, 215.
75. M. Pettersson and C. M. Crews, *Drug Discov. Today Technol.*, 2019, **31**, 15–27.
76. A. A. Adjei, *J. Clin. Oncol.*, 2006, **24**, 4054–4055.
77. C. Holohan, S. Van Schaeybroeck, D. B. Longley and P. G. Johnston, *Nat Rev. Cancer*, 2013, **13**, 714–726.
78. J. M. A. Blair, M. A. Webber, A. J. Baylay, D. O. Ogbolu and L. J. V. Piddock, *Nat. Rev. Microbiol.*, 2014, **13**, 42–51.
79. S. He, G. Dong, J. Cheng, Y. Wu and C. Sheng, *Med. Res. Rev.*, 2022, **42**, 1280–1342.
80. L. T. Kramer and X. Zhang, *Curr. Res. Chem. Biol.*, 2022, **2**, 100020.
81. C. M. Crews, *Chem. Biol.*, 2010, **17**, 551–555.
82. D. P. Bondeson, A. Mares, I. E. D. Smith, E. Ko, S. Campos, A. H. Miah, K. E. Mulholland, N. Routly, D. L. Buckley, J. L. Gustafson, N. Zinn, P. Grandi, S. Shimamura, G. Bergamini, M. Faelth-Savitski, M. Bantscheff, C. Cox, D. A. Gordon, R. R. Willard, J. J. Flanagan, L. N. Casillas, B. J. Votta, W. Den Besten, K. Famm, L. Kruidenier, P. S. Carter, J. D. Harling, I. Churcher and C. M. Crews, *Nat. Chem. Biol.*, 2015, **11**, 611–617.
83. I. Churcher, *J. Med. Chem.*, 2018, **61**, 444–452.
84. Y. Westermaier, X. Barril and L. Scapozza, *Methods*, 2015, **71**, 44–57.
85. J. Krönke, C. Steinebach, Y. L. D. Ng, I. Sosič, C. S. Lee, S. Chen, S. Lindner, L. P. Vu, A. Bricelj, R. Haschemi, M. Monschke, E. Steinwarz, K. G. Wagner, G. Bendas, J. Luo and M. Gütschow, *Chem. Sci.*, 2020, **11**, 3474–3486.

86. J. Wei, F. Meng, K. S. Park, H. Yim, J. Velez, P. Kumar, L. Wang, L. Xie, H. Chen, Y. Shen, E. Teichman, D. Li, G. G. Wang, X. Chen, H. Ü. Kaniskan and J. Jin, *J. Am. Chem. Soc.*, 2021, **143**, 15073–15083.
87. C. Pu, Y. Tong, Y. Liu, S. Lan, S. Wang, G. Yan, H. Zhang, D. Luo, X. Ma, S. Yu, Q. Huang, R. Deng and R. Li, *Eur. J. Med. Chem.*, 2022, **236**, 114321.
88. N. Ohoka, G. Tsuji, T. Shoda, T. Fujisato, M. Kurihara, Y. Demizu and M. Naito, *ACS Chem. Biol.*, 2019, **14**, 2822–2832.
89. J. Pei, Y. Xiao, X. Liu, W. Hu, A. Sobh, Y. Yuan, S. Zhou, N. Hua, S. G. Mackintosh, X. Zhang, K. B. Basso, M. Kamat, Q. Yang, J. D. Licht, G. Zheng, D. Zhou and D. Lv, *Cell Chem. Biol.*, 2023, **30**, 2, 203–213.
90. X. Zhang, V. M. Crowley, T. G. Wucherpfennig, M. M. Dix and B. F. Cravatt, *Nat. Chem. Bio.*, 2019, **15**, 737–746.
91. D. Weerakoon, R. J. Carbajo, L. De Maria, C. Tyrchan and H. Zhao, *J. Chem. Inf. Model.*, 2022, **62**, 340–349.
92. X. Sun, H. Gao, Y. Yang, M. He, Y. Wu, Y. Song, Y. Tong and Y. Rao, *Signal Transduct. Target Ther.*, 2019, **4**, 1–33.
93. R. R. Shah, J. M. Redmond, A. Mihut, M. Menon, J. P. Evans, J. A. Murphy, M. A. Bartholomew and D. M. Coe, *Bioorg. Med. Chem.*, 2020, **28**, 115326.
94. X. Han, C. Wang, C. Qin, W. Xiang, E. Fernandez-Salas, C. Y. Yang, M. Wang, L. Zhao, T. Xu, K. Chinnaswamy, J. Delproposto, J. Stuckey and S. Wang, *J. Med. Chem.*, 2019, **62**, 941–964.
95. A. P. Crew, K. Raina, H. Dong, Y. Qian, J. Wang, D. Vigil, Y. V. Serebrenik, B. D. Hamman, A. Morgan, C. Ferraro, K. Siu, T. K. Neklesa, J. D. Winkler, K. G. Coleman and C. M. Crews, *J. Med. Chem.*, 2018, **61**, 583–598.
96. P. Martín-Acosta and X. Xiao, *Eur. J. Med. Chem.*, 2021, **210**, 112993.
97. H. K. Kim, J. E. Seol, S. W. Ahn, S. Jeon, C. S. Park and J. Han, *Pflug. Arch. Eur. J. Phy.*, 2021, **473**, 1695–1711.
98. D. L. Buckley, I. Van Molle, P. C. Gareiss, H. S. Tae, J. Michel, D. J. Noblin, W. L. Jorgensen, A. Ciulli and C. M. Crews, *J. Am. Chem. Soc.*, 2012, **134**, 4465–4468.
99. G. M. Burslem, B. E. Smith, A. C. Lai, S. Jaime-Figueroa, D. C. McQuaid, D. P. Bondeson, M. Toure, H. Dong, Y. Qian, J. Wang, A. P. Crew, J. Hines and C. M. Crews, *Cell Chem. Biol.*, 2018, **25**, 67-77.
100. R. P. Nowak, S. L. Deangelo, D. Buckley, Z. He, K. A. Donovan, J. An, N. Safaee, M. P. Jedrychowski, C. M. Ponthier, M. Ishoey, T. Zhang, J. D. Mancias, N. S. Gray, J. E. Bradner and E. S. Fischer, *Nat. Chem. Biol.*, 2018, **14**, 706–714.
101. M. A. Troy Bemis, J. J. La Clair and M. D. Burkart, *J. Med. Chem.*, 2021, **64**, 8042–8052.
102. D. García Jiménez, M. Rossi Sebastiano, M. Vallaro, V. Mileo, D. Pizzirani, E. Moretti, G. Ermondi and G. Caron, *J. Med. Chem.*, 2022, **65**, 12639–12649.
103. Y. Atilaw, V. Poongavanam, C. Svensson Nilsson, D. Nguyen, A. Giese, D. Meibom, M. Erdelyi and J. Kihlberg, *ACS Med. Chem. Lett.*, 2021, **12**, 107–114.
104. G. Ermondi, M. Vallaro, G. Goetz, M. Shalaeva and G. Caron, *Eur. J. Pharm. Sci.*, 2020, **146**, 105274.
105. T. X. Xiang and B. D. Anderson, *J. Membr. Biol.*, 1994, **140**, 111–122.
106. V. G. Klein, C. E. Townsend, A. Testa, M. Zengerle, C. Maniaci, S. J. Hughes, K.-H. Chan, A. Ciulli and R. S. Lokey, *ACS Med. Chem. Lett.*, 2020, **11**, 1732–1738.
107. M. D. Shultz, *J. Med. Chem.*, 2019, **62**, 1701–1714.
108. C. Cantrill, P. Chaturvedi, C. Rynn, J. Petrig Schaffland, I. Walter and M. B. Wittwer, *Drug Discov. Today*, 2020, **25**, 969–982.
109. M. Rossi Sebastiano, B. C. Doak, M. Backlund, V. Poongavanam, B. Over, G. Ermondi, G. Caron, P. Matsson and J. Kihlberg, *J. Med. Chem.*, 2018, **61**, 4189–4202.
110. P. Matsson, B. C. Doak, B. Over and J. Kihlberg, *Adv. Drug Deliv. Rev.*, 2016, **101**, 42–61.
111. A. Pike, B. Williamson, S. Harlfinger, S. Martin and D. F. McGinnity, *Drug Discov. Today*, 2020, **25**, 1793–1800.

112. F. Pöstges, K. Kayser, J. Appelhaus, M. Monschke, M. Gütschow, C. Steinebach and K. G. Wagner, *Pharmaceutics*, 2023, **15**, 156.
113. N. Hofmann, M. Harms and K. Mäder, *Int. J. Pharm.*, 2024, **650**, 123725.
114. L. Mareczek, L. K. Mueller, L. Halstenberg, T. M. Geiger, M. Walz, M. Zheng and F. Hausch, *Pharmaceutics*, 2024, **16**, 924.
115. H. Zhang, H. Wu, L. Wang, Y. Gao, L. M. Galarza, Y. Zhao, Z. Wang, L. Gao and J. Han, *J. Drug Deliv. Sci. Technol.*, 2025, **107**, 106837.
116. J. Gupta, C. Nunes, S. Vyas and S. Jonnalagadda, *J. Phys. Chem. B*, 2011, **115**, 2014–2023.
117. J. Gupta, C. Nunes and S. Jonnalagadda, *Mol. Pharm.*, 2013, **10**, 4136–4145.
118. M. Cordova, M. Balodis, A. Hofstetter, F. Paruzzo, S. O. Nilsson Lill, E. S. E. Eriksson, P. Berruyer, B. Simões de Almeida, M. J. Quayle, S. T. Norberg, A. Svensk Ankarberg, S. Schantz and L. Emsley, *Nat. Comm.*, 2021, **12**, 1–8.
119. *WIPO Pat.*, Estrogen Receptor Degrading PROTACs, WO2020201080 (A1), 2020.

2. Crystallising the Un-crystallisable: Insights from Extensive Screening of PROTACs

2.1 Introduction

As discussed in section 1.1, formulation scientists in the pharmaceutical industry are responsible for ensuring that the active ingredients in drug products are bioavailable, and both physically and chemically stable. This requires the solid-state properties of the drug substance to be well understood and controlled. At least 50% of active pharmaceutical ingredients (APIs) subjected to industrial screening processes have been found to be polymorphic,[1] meaning that they exist in more than one crystalline form depending on the intermolecular arrangements present. This presents both opportunities and challenges for the pharmaceutical industry: while different forms can be selected to optimise drug properties such as bioavailability, undesired transformations between forms can compromise product performance.[2,3] Properties such as solubility and physical stability can vary greatly between different forms,[4] which include polymorphs, solvates, salts and amorphous phases, so it is imperative to study the solid form landscapes of new drug compounds comprehensively before selecting the final form for drug product development. Identifying solid forms may also provide intellectual property opportunities.[5,6] There are many experimental methods for discovering or isolating polymorphs as part of the screening process, including sublimation, crystallisation from a single or binary solvent mixture, vapor diffusion, thermal treatment, slurrying, crystallisation from the melt, changing pH, thermal desolvation of crystalline solvates, growth in presence of additives, and grinding.[2] Given the limits of time and resources, there is no guarantee that all possible polymorphs of a compound will be discovered or that the risk of unwanted transformations will be eliminated entirely after the screening process, but the majority of the thermodynamic and pharmaceutically relevant kinetic solid products are discovered by exposing the compound to a sufficiently wide range of crystallisation conditions.[7]

As discussed in section 1.1.4, the amorphous form of an API generally provides the greatest solubility and dissolution rate advantage since it is the highest energy solid state of a material often with greater molecular motion, and hence it has become of increasing interest to pharmaceutical industry.[3,8] Amorphisation is particularly interesting for poorly aqueous-soluble pharmaceutical compounds administered orally, where the inherently greater amorphous solubility and increased dissolution rate drive increased concentration within the gastrointestinal lumen.[8] Amorphisation of APIs has been

implemented successfully within the pharmaceuticals industry and accounts for approximately 30% of drug products requiring solubility enhancement.[9] However, amorphous API formulations are typically thermodynamically unstable and without physical stabilisation they are prone to crystallisation, negating any dissolution benefits.[8] Furthermore, amorphous solids are often more hygroscopic than their crystalline counterparts since their greater free volume allows water molecules to penetrate them more easily and the uptake of water plasticises the solid, increasing molecular mobility and the likelihood of recrystallisation.[10] Numerous factors govern the physical stability of amorphous solids against crystallisation; those that depend on molecular structure are the aforementioned molecular mobility (correlated inversely with glass transition temperature T_g), the configurational entropic barrier to crystallisation, the enthalpic driving force to produce a solid form with lower configurational enthalpy, and the degree of hydrogen bonding between molecules.[11,12] Factors independent of the molecular structure include the humidity, mechanical stress, temperature and preparation method, since the thermal history of the material can vary the extent of molecular relaxation.[13] As discussed in section 1.1.4, some organic compounds can also exhibit polyamorphism, which adds yet another layer of complexity to the solid-state landscape of a drug.

Targeted protein degradation (TPD), introduced in section 1.2, is an emerging therapeutic modality with the potential to tackle disease-causing proteins previously deemed 'undruggable' with conventional small molecules, which are typically required to bind to a functional pocket on the protein to have a therapeutic effect. In contrast, TPD harnesses the cell's own degradation machinery to eliminate target proteins, allowing it to modulate proteins regardless of whether they possess a suitable binding site, thereby significantly expanding the druggable proteome. In the 23 years since the conception of a proteolysis targeting chimera (PROTAC), a molecule capable of harnessing the ubiquitin-proteasome system to degrade a target protein, TPD has moved from academia to industry and is attracting substantial interest, with more than 10 PROTACs now in clinical trials.[17] However, PROTACs are very poorly water-soluble and face challenges regarding their development into drug products with sufficient oral bioavailability. Aqueous solubility and cell permeability greatly impact the bioavailability of oral PROTACs in particular, such as those based on the E3 ligase cereblon (CRBN),[18] and a poor understanding of the structure-property relationships for PROTACs makes it difficult to ensure that the degraders will reach their intracellular targets.[19] The development of new drug compounds in general has expanded rapidly into a chemical space beyond Lipinski's rule of 5 (bRo5),[20] a guideline used to determine if a drug is likely to be orally active based on its chemical and physical properties,[21] and the number of poorly water-soluble APIs has greatly increased in recent years with PROTACs included.[22] Many physicochemical properties of PROTAC molecules, such as their

molecular weight (MW), numbers of hydrogen bond acceptors and donors (HBAs and HBDs respectively), and lipophilicity lie in the bRo5 chemical space since they require the functionality of two ligands and a linker group,[4,6] and their poor aqueous solubility impedes various later stages of the drug development process.[18] The high flexibility and size of PROTAC molecules increases the conformational space that they can explore, and most PROTACs are poorly crystalline as a result. While several crystal structures have been solved for ternary complexes between a PROTAC, a target protein and an E3 ligase,[23,24] at the time of writing there are no published crystal structures of PROTACs alone to elucidate the intermolecular interactions between the drug molecules. Establishing pre-formulation data to aid in the development of solid PROTAC formulations such as their affinity for polymorphism, the relative stability of forms and their solvent content, is therefore a major challenge.

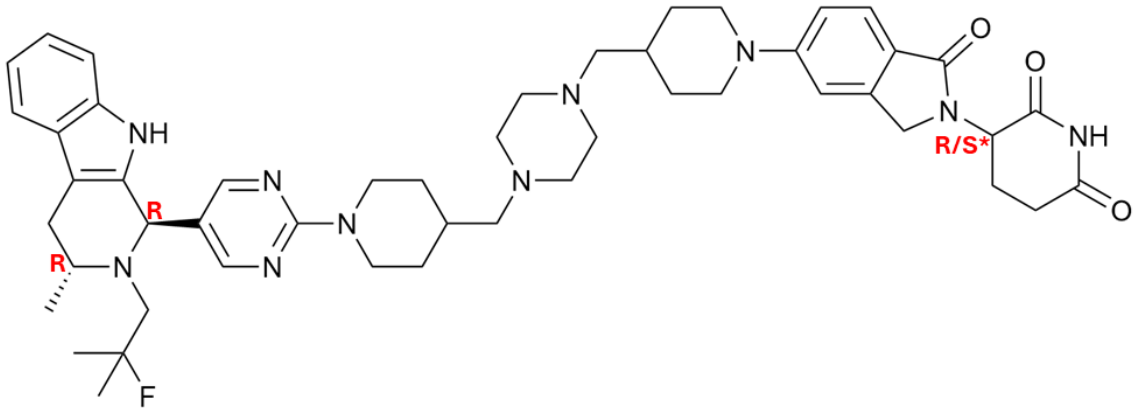

Scheme 2.1. PROTAC compound ‘AZ1’. Different diastereomer compositions of AZ1 are designated as AZ’8612 for a 1:1 mixture of RRR- and RRS- isomers (abbreviated AZ1mix), AZ’9929 for only the RRR- isomer (abbreviated AZ1RRR) and AZ’0163 for only the RRS- isomer (abbreviated AZ1RRS). The indole-containing moiety shown on the left constitutes the estrogen receptor (ER) ligand or “ER-warhead”. The imide-based moiety shown on the right constitutes the “CRBN-ligand”. The two are joined chemically via a piperazine/piperidine-based linker.

Compound ‘AZ1’ is a PROTAC consisting of a lenalidomide-like ligand which recruits CRBN (referred to as the “CRBN-ligand”), and an estrogen receptor (ER) ligand (referred to as the “ER-warhead”) adjoined via a piperazine/piperidine-based linker moiety (Scheme 2.1). Compounds of this type selectively degrade ER alpha in several different breast cancer cell-lines including MCF-7, CAMA-1 and BT474.[25] AZ1 is one of a PROTAC class that may provide greater ER degradation compared to current therapies and may be suitable for oral use as well as parenteral administration. The crystallisability, polymorphism and the stability of the amorphous form of AZ1 must be understood prior

to developing a formulation approach. In this chapter, the difficulty in applying conventional and high-throughput polymorph screening techniques to a cereblon PROTAC is demonstrated and the first PROTAC crystal structures in the literature are presented, alongside characterisation of several other solid forms including potential *pseudo*-polyamorphs. This approach to understanding the solid forms landscape of AZ1 is the first PROTAC pre-formulation study of its type and illustrates the way in which solid form screening strategies need to be adapted using state of the art methodologies for this extreme bRo5 class of compound.

2.2 Experimental

Materials and general methods. PROTAC compounds AZ'8612 ($AZ1_{mix}$), AZ'9929 ($AZ1_{RRR}$) and AZ'0163 ($AZ1_{RRS}$) were supplied by AstraZeneca. All other chemicals and solvents were available from commercial sources and used without further purification. Infrared spectra were recorded between 4000 and 550 cm^{-1} using a Perkin Elmer 100 FT-IR spectrometer with a μATR attachment. Powder X-ray diffraction (XRPD) patterns were collected at room temperature using a Bruker AXS D8 Advance GX003410 diffractometer with a Lynxeye Soller PSD detector, using Cu Kα radiation at a wavelength of 1.5406 Å and collecting from $2° \leq 2\theta \leq 40°$. Solution-phase ^1H NMR spectra (400.20 MHz, DMSO-d_6) were recorded at room temperature on a Bruker Neo-400 spectrometer, with chemical shifts reported in ppm relative to residual solvent signals (δ 2.50 for DMSO-d_6).

Crystal screening of AZ1. Crystallisation of AZ1 was first attempted by heating $AZ1_{mix}$ in single solvents to produce supersaturated solutions upon cooling. The solubility of $AZ1_{mix}$ at 1% w/v was assessed in 38 solvents spanning a broad range of polarity and boiling points. For solvents in which AZ1 was soluble at 1% w/v without requiring heat, the concentration was doubled by addition of powder until heat was required to dissolve (a full list of approximate solubility data is included in Appendix A, Table A1). Solutions at 1% w/v that required heat to dissolve but were stable for at least 4 hours after heating were left undisturbed for 3 weeks. For solvents in which heat was required to dissolve AZ1 at 1% w/v but the resulting solutions were not stable for at least 4 hours before precipitation, the concentration was halved by addition of solvent until solutions produced by heating were stable for at least 4 hours. The concentrations of AZ1 required to produce such solutions was recorded. No dilutions were attempted in solvents which were insoluble even with heat at 1% w/v. All solutions were cooled passively to room temperature after heating. If no solid material was observed after 3 weeks, multiple repeats of the crystallisation experiment were performed with different methods: cooling

in a fridge or freezer, slow solvent evaporation, addition of anti-solvent in 50 µL aliquots until translucent followed by reheating to dissolve and passive cooling, and anti-solvent addition by vapour diffusion using diethyl ether. Solvents that produced crystalline material, identified by cross-polarised optical microscopy and XRPD, were studied further by controlled cooling experiments from 5 °C below boiling to -20 °C at 0.05 °C/min using a Cambridge Reactor Design Polar Bear Plus; slow evaporation of solvent from seeded solutions; and anti-solvent layering in an NMR tube. Experiments that produced crystalline solids of $AZ1_{mix}$ were also repeated using pure isomer samples of $AZ1_{RRR}$ and $AZ1_{RRS}$ to study their individual crystallisability.

Encapsulated Nanodroplet Crystallisation (ENaCt) protocol. Stock solutions of $AZ1_{mix}$, $AZ1_{RRS}$ and $AZ1_{RRR}$ in a range of 16 solvents varying in polarity and boiling point were prepared at near-saturated concentrations. In solutions with lower than 5.2 mg/mL solubility, the supernatant was used. Crystallisation experiments were completed using an STP LabTech mosquito® liquid handling robot using 96-well glass plates (SWISSCI LCP Modular, 100 µm spacer) and sealed with a 175 µm glass cover slip. An appropriate volume (typically 200 nL) of each oil was first dispensed onto the 96-well plates (aspirate 1.0 mm/min, dispense 1.0 mm/min), after which 50 nL of AZ1 solution was injected into each oil droplet (aspirate 20 mm/min, dispense 20 mm/min). Plates were then sealed with a glass cover slip, stored in the dark at room temperature for 14 days and inspected for crystal growth at regular intervals. Visualization of the experiment wells was carried out with a Nikon SMZ1000 microscope fitted with a cross polariser. Photographs were taken with a GXCAM-U3-5 5.1MP camera. Full plate readouts are shown in Appendix A, Tables A2 and A3.

Preparation of Form 1. A slurry of $AZ1_{mix}$ (20 mg) in acetonitrile (5 mL) was stirred on an Expondo roller mixer at 100 rpm for 7 days, before the suspension was filtered and the isolated solid of Form 1 was obtained and characterised by XRPD, elemental analysis, FTIR, NMR, DSC, TGA and solid-state NMR. This form matches the powder pattern of $AZ1_{RRS}$ as synthesised, which was also fully characterised.

Preparation of Form 2. $AZ1_{mix}$ (56 mg) was added to dichloromethane (0.5 mL) and heated to dissolve before cooling passively. After 3 weeks, needle crystals of Form 2 were afforded and characterised by XRPD, elemental analysis, FTIR, NMR, DSC, TGA and solid-state NMR. Isostructural needle crystals can also be produced by the same method but using $AZ1_{RRS}$, with the same XRPD pattern, IR spectrum and DSC thermogram. Another isostructural sample of needle crystals can be prepared using the same cooling method from a chloroform solution.

Preparation of single crystals of Form 3. $AZ1_{mix}$ (5 mg) was added to p-xylene (0.5 mL) and heated to boiling before cooling passively. The sample did not dissolve and was left undisturbed for 11 months. One single crystal of Form 3 was afforded in a droplet of solvent on the vial wall.

Electron diffraction (3D ED). 3D electron diffraction data for Form 1 were collected on a Rigaku Synergy-ED (LaB_6, 200 kV), equipped with a HyPix-ED hybrid pixel area array detector. The sample was gently ground between glass slides and a lacey carbon coated copper TEM grid (200 mesh; Agar Scientific, UK) dabbed in the solid. The grid was then plunged into liquid nitrogen and mounted on a Gatan Elsa cryogenic holder (model 698) and introduced into the column using cryo-transfer at 175(5) K. Data collections were conducted at 175(5) K in continuous rotation mode using a selected area aperture (~2 µm diameter in the image plane) using CrysAlisPRO (version 1.171.44.78a). A range of particles was surveyed and a single data collection chosen for structure determination. The data were indexed, integrated and scaled using CrysAlisPRO (version 1.171.44.79a) without absorption correction to allow for dynamical refinement. The structure was solved using SHELXD[26] and refined dynamically using olex2.refine (N-beam) implemented in the Olex2 (version 1.5-ac7-014)[27] employing electron scattering factors.[28] After initial refinement using the kinematical approximation, the obtained model was used as a starting model for dynamical refinement. All non-hydrogen atoms were refined using anisotropic atom displacement parameters, while hydrogen atoms were placed and refined based on geometry and using a riding model with distances fixed to neutron X-H bond lengths.[29] Two reflections were omitted from the final refinement as they were considered untrustworthy based on their errors and disagreement with the general spread of reflections in the F_{obs} vs F_{calc} plot. Crystal data for Form 1: $C_{49}H_{63}FN_{10}O_3$, M_r = 859 g/mol, space group *I*2, *a* = 9.4516(8) Å, *b* = 6.2776(4) Å, *c* = 75.233(16) Å, α = 90 °, β = 92.476(10) °, γ = 90 °, *V* = 4459.7(10) Å^3, R_1 (I > 2s(I)) = 0.1539, wR_2 (all data) = 0.4140. Absolute structure was assessed using the Z-score method[30] as implemented in Olex2, which gave Z-score values of 17.40 (noise-adjusted) and 9.19 (raw). Full crystallographic data, parameters of refinement and the hydrogen bonding distances and angles are listed in Appendix A, Tables A4 and A5. Complete experimental and refinement information are contained in the deposited CIF along with structure factors and embedded .RES file. This structure is deposited in the CSD with CCDC reference code CCDC 2445862.

Single crystal X-ray Diffraction (SC-XRD). Single-crystal X-ray diffraction data for Form 3 was collected at 100.0(2) K on the I-19 beamline (Dectris Pilatus 2M pixel-array photon-counting detector, undulator, graphite monochromator, λ = 1.0402 Å) at the Diamond Light Source, Oxfordshire and processed using Xia2/DIALS. The structure was

solved by direct methods and refined by full-matrix least squares on F^2 for all data using Olex2[27] and SHELXTL.[36] All non-hydrogen atoms were refined with anisotropic displacement parameters. Hydrogen atoms were located on the difference map and refined isotropically on a riding model unless otherwise specified. The platon SQUEEZE routine was used to remove 0.75 solvent *p*-xylene molecules per asymmetric unit that could not be sensibly modelled due to disorder. Positional disorder was also observed for the lenalidomide end group atoms C1-5, N1, N2 O1 and O2 and refined to a ratio of 0.884(4):0.116(4) for the *R*- and *S*- enantiomers respectively. Crystal data for Form 3: $C_{55}H_{70.5}FN_{10}O_3$, M_r = 938.71, space group $P2_1$, a = 12.0183(5) Å, b = 6.2727(2) Å, c = 33.8422(11) Å, α = 90 °, β = 99.389(3) °, γ = 90 °, V = 2517.09(16) Å^3, R_1 (I > 2s(I)) = 0.0492, wR_2 (all data) = 0.1188. Full crystallographic data, parameters of refinement and the hydrogen bonding distances and angles are listed in Appendix A, Tables A6 and A7. This structure is deposited in the CSD with CCDC reference code CCDC 2448039.

Preparation of amorphous solids. Amorphous form A can be prepared by adding $AZ1_{mix}$ or $AZ1_{RRS}$ to a 5 mL stainless steel grinding jar with one stainless steel grinding ball (6.4 mm diameter) and grinding with a Retsch MM200 Mixer Mill at 20 Hz for 15 minutes. The resulting solid has the same thermal and dissolution characteristics as $AZ1_{RRR}$, which is amorphous as synthesised. Amorphous form B was prepared by heating Form 2 to 150 °C in an oven for 2 hours to remove the solvent. Amorphous solids were characterised by FTIR, XRPD, DSC and TGA.

Scanning electron microscopy (SEM). SEM samples were prepared by adding solid powders to polycarbonate wafers and coating with 25 nm of platinum using a Cressington 328 Ultra High-Resolution EM Coating System. The images were obtained using a Carl Zeiss Sigma 300 VP FEG SEM microscope, operated at 5 kV using an in-lens detector.

CrysIn analysis. The AstraZeneca in-house developed Crystal Interaction (CrysIn) tool[37] was used for quantification and comparison of static interactions between molecules in the Form 1 and Form 3 crystal structures. For each molecule in the asymmetric unit of the investigated crystal structure, all intermolecular pair (synthon) interaction energies within its first coordination shell were calculated using counterpoise corrected B3LYP-D3/6-31G(d,p) molecular energies as implemented in Gaussian 16.[38] This is a comparable approach as used in, for example, energy framework calculations in CrystalExplorer[39] or PIXEL[40] calculations.

Cambridge Structural Database (CSD). The single component drug predefined hitlist was retrieved from the CSD (version 5.45, Nov 23). The list contains 2388 refcode entries and contains redeterminations. Removing structural redeterminations within that list resulted into a subset of 1040 unique crystal structures. To facilitate computations, the

set was further refined by removing structures with Z' values other than one, and zwitterionic structures. This led to our final subset of 592 structures referred to as "CSD-drugs$_{NZ1,1}$" throughout the manuscript. To summarise, the CSD-drugs$_{NZ1,1}$ subset contains unique crystal structures (no redeterminations) of single component drugs crystallising with Z'=1 and only non-zwitterionic compounds. This subset was used for further computational investigations.

Lattice energy calculations for the CSD-drugs$_{NZ1,1}$ subset. Lattice (or cohesive) energy calculations were calculated for all structures in the CSD-drugs$_{NZ1,1}$ subset using the Open Computational Chemistry (OCC) software.[41–43] CIF files for the CSD-drugs$_{NZ1,1}$ structures were retrieved from the CSD using a custom-made Python script which checks for hydrogen atom coordinates and adds them if missing with the method implemented in the CSD Python API. CIF files were used as input files for the OCC calculation. For each OCC calculation, the electron density of the drug compound is first calculated by retrieving its geometry from the CIF file and performing a single point energy calculation at the B3LYP/6-31 G** level of theory in the gas-phase.[44,45] The electron density of the drug compound is then used to compute all drug-drug pairwise interactions within 30 Å of a reference molecule in the crystal structure. An overall lattice energy (E_{latt}) is then computed by adding up all dimer interactions and dividing by two. Whilst this is a simple way of estimating lattice energies and it certainly does not account for intramolecular energy penalties, it has been shown to reproduce benchmark DFT-d methods within 6.6 kJ/mol on average.[46] Energies were computed successfully for 592 structures in the CSD-drugs$_{NZ1,1}$ subset.

Thermal analysis. Differential scanning calorimetry (DSC) samples were prepared using Tzero standard pans and lids with pin-holes, and analysed using a TA Instruments Q2000 differential scanning calorimeter by first equilibrating at 25 °C and heating to 400 °C at 10 °C/min. Amorphous samples were also analysed at a heating rate of 50 °C/min. Samples analysed in a heat-cool-heat cycle were first equilibrated at 25 °C, heated to 200 °C at 10 °C/min, cooled to 25 °C at 10 °C/min, and then heated to 400 °C at 10 °C/min. Modulated DSC samples were first equilibrated at 25 °C then heated to 200 °C, cooled to 25 °C and reheated to 400 °C using a modulated method with a scanning speed of 3 °C/min, an amplitude of ± 1 °C and a period of 60 s. The instrument was calibrated using indium standard prior to analysis, with a melting point onset of 156.89 °C and a heat capacity of 33.971 J/g. Thermogravimetric analysis (TGA) samples were analysed using platinum pans and a TA Instruments Discovery thermogravimetric analyser, heating from 25 °C to 400 °C at 10 °C/min.

Solid-state Nuclear Magnetic Resonance (SSNMR). Carbon-13 spectra were recorded at 125.72 MHz using a Bruker Avance III HD spectrometer and a 4.0 mm (rotor

o.d.) magic-angle spinning probe. The spectra were obtained using cross-polarization, with a 4 ms contact time for CPTOSS experiments, at a sample spin-rate of 10 kHz. SPINAL-64 decoupling was performed on ^{1}H with a 3 μs 90° pulse, for both CPTOSS and HETCOR experiments. Spectral referencing was with respect to tetramethylsilane (carried out by setting the high-frequency signal from adamantane to 38.5 ppm). The (indirect) ^{1}H dimension for the HETCOR experiments was referenced by setting the high-frequency cross peak of glycine to 8.4 ppm, and scaling using the default for FSLG decoupling sequence.

Hot stage polarised optical microscopy (HS-POM). Thermomicroscopy analysis was performed using a polarised microscope (BX53, Olympus) coupled with the LTS420 hot stage (Linkam). Samples were heated from room temperature up to 190 °C and cooled back to 30 °C at a rate of 10 °C/min.

Ultra Performance Liquid Chromatography (UPLC) analysis. The concentrations of AZ1 were determined using a Waters ARC UPLC -MC206 system with an ACQUITY UPLC BEH C18 column (130 Å, 1.7 μm, 2.1 mm X 50 mm, Waters Corporation, UK) and a UV detection wavelength of 300 nm. The mobile phase of acetonitrile/water was varied in a gradient method from 95/5 v/v to 5/95 v/v at a flow rate of 1 mL/min.

AZ1 solubility. The thermodynamic solubility of AZ1 Form 1 in fasted state simulated intestinal fluid (FaSSIF) was determined by adding an excess of Form 1 powder to 1 mL of solvent and stirring at 1,000 rpm for 24 hours. The samples were then centrifuged for 30 minutes at 31,000 × *g* and the supernatant was diluted appropriately to maintain absorbance readings within the UPLC standard curve. The concentration of AZ1 was determined by UPLC analysis, converting peak area values to concentrations via a calibration curve. No difference in solubility between Form 1 prepared using $AZ1_{mix}$ or $AZ1_{RRS}$ was detected.

Non-sink powder dissolution measurements. Dissolution experiments were performed in triplicate for each sample. The powders were sieved using standard mesh sieves to remove particles larger than 150 μm. Vessels were charged with accurately weighed masses (approximately 1.3 mg) of the various crystalline and amorphous solids before adding the correct volume (approximately 10 mL) of pre-warmed FaSSIF at 37 °C such that all slurries were accurately at ten times the measured solubility limit of Form 1. Slurries were stirred at 400 rpm for 2 hours. Aliquots of the slurries were removed at each time point, centrifuged for 30 minutes at 31,000 × *g*, and the neat supernatant was analysed to maintain absorbance readings within the UPLC standard curve. The concentrations of AZ1 were determined by UPLC analysis, converting peak area values to concentrations via a calibration curve. The pH of each dissolution slurry was recorded

at the end of the experiment to confirm that it had not varied outside of the specification of the buffer.

2.3 Results and Discussion

AZ1 crystallisation

Table 2.1. A summary of the structure and compositions of AZ1 solid forms, and their method of preparation. AZ1 solids may be composed of different isomers: RRR- only (AZ'9929, abbreviated $AZ1_{RRR}$), RRS- only (AZ'0163, abbreviated $AZ1_{RRS}$) or a 1:1 mixture of both (AZ'8612, abbreviated $AZ1_{mix}$). Structures such as Form 1, Form 2 etc. are distinguished by their X-ray powder patterns, thermal and spectral analysis.

Structure	Composition	Preparation
Form 1	$AZ1_{RRS}$	As synthesised
	$AZ1_{mix}$	Slurry in MeCN
Form 2	$AZ1_{RRS}$	Cooling crystallisation in DCM
	$AZ1_{mix}$	Cooling crystallisation in DCM
Form 3	$AZ1_{mix}$	Cooling crystallisation in p-xylene
Amorphous type A	$AZ1_{RRS}$	Milling Form 1
	$AZ1_{RRR}$	As synthesised
	$AZ1_{mix}$	Milling Form 1
Amorphous type B	$AZ1_{mix}$	Desolvating Form 2

AZ1 contains three chiral carbon atoms, however in the present study, only the carbon atom denoted by an asterisk (*) in Scheme 2.1 may differ in configuration while the other two are fixed as R- configuration. AZ1 therefore comprises three distinct isomeric compositions: RRR-only (AZ'9929, abbreviated $AZ1_{RRR}$), RRS-only (AZ'0163, abbreviated $AZ1_{RRS}$), and a 1:1 mixture of both diastereomers (AZ'8612, abbreviated $AZ1_{mix}$), all synthesised separately. X-ray powder diffraction (XRPD) analysis (Figure 2.1a) reveals that $AZ1_{RRS}$ is crystalline with a powder pattern referred to henceforth as Form 1, while $AZ1_{RRR}$ is amorphous. XRPD and solid-state ^{13}C NMR (Appendix A, Figure A2) show that $AZ1_{mix}$ matches the Form 1 structure of the $AZ1_{RRS}$ sample but with broader powder pattern peaks and a slight hump in the baseline, yet a relatively crystalline NMR spectrum[47] showing only slightly more disorder than the $AZ1_{RRS}$ sample. This suggests that although both diastereomers are able to arrange in the Form 1 crystal structure, the presence of random stereoisomers and/or the small size of the crystal particles results

in poor X-ray diffraction. Since $AZ1_{mix}$ was by far the most abundant PROTAC sample available, most of the crystal screening was carried out using this sample and the separate RRS- and RRR- diastereomers were only screened using high-throughput methods that require low sample masses or in select experiments with a higher likelihood of success.

A thorough crystal screening process using a broad range of solvents and techniques was employed to attempt to grow single crystals of AZ1 and to study its potential polymorphism. At first, conventional crystallisation techniques such as cooling of saturated solutions, slow solvent evaporation and anti-solvent addition were attempted using $AZ1_{mix}$. The high-throughput Encapsulated Nanodroplet Crystallisation (ENaCt) protocol,[48] which has been used successfully to grow single crystals of pharmaceutical compounds such as nifedipine,[49] felodipine and cannabidiol,[50] was also employed in the polymorph screening of $AZ1_{mix,}$ $AZ1_{RRS}$ and $AZ1_{RRR}$. Nanolitre droplets of AZ1 stock solutions in 16 solvents were dispensed inside of larger droplets of four inert, viscous oils and allowed to evaporate slowly alongside control droplets of stock solutions without oil.[48] However, the only crystalline material isolated using the ENaCt method were two microcrystalline particles that did not diffract strongly enough for single crystal analysis using X-ray techniques, amongst hundreds of samples that were identified as amorphous residues based on a lack of birefringence and well-defined morphology. Eventually larger scale crystallisation methods proved to be the only effective approach. Conventional crystallisation experiments that produced crystalline samples of $AZ1_{mix}$ were repeated using pure isomer samples of $AZ1_{RRR}$ and $AZ1_{RRS}$. Including the ENaCt experiments, a total of over 1,800 individual crystallisation attempts were performed but fewer than 10 of these experiments produced a crystalline solid, with conventional passive cooling of supersaturated solutions and slurry in single solvents as the only successful techniques. Of these crystalline samples, only one was suitable for single crystal analysis using X-ray techniques.

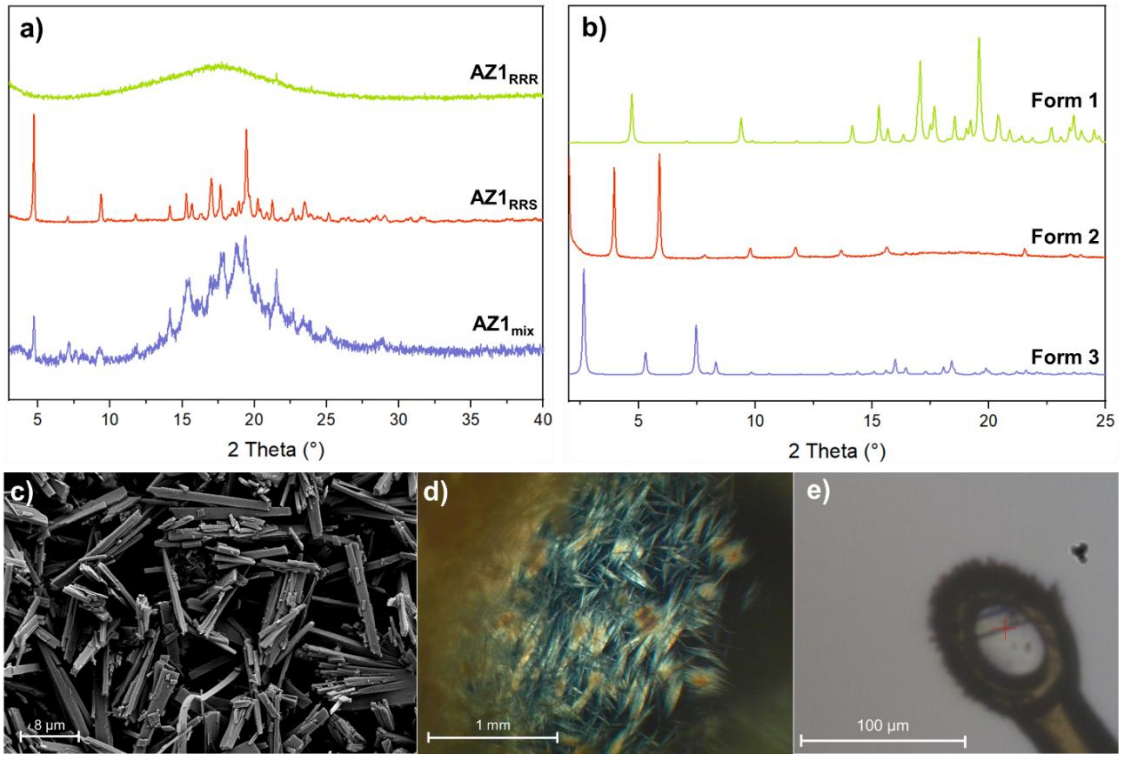

Figure 2.1. a) XRPD patterns of $AZ1_{mix}$, $AZ1_{RRS}$ and $AZ1_{RRR}$ as synthesised. b) XRPD patterns of Form 1 (anhydrous), Form 2 (dichloromethane solvate) and Form 3 (p-xylene solvate). The powder pattern for Form 3 was simulated from SC-XRD data since there was not enough material to characterise by XRPD. c) SEM image of Form 1 ($AZ1_{RRS}$). d) Optical microscope image of Form 2 ($AZ1_{mix}$). e) Diffractometer microscope image of Form 3.

Three distinct crystalline forms were identified from the crystalline solids produced: anhydrous AZ1 (Form 1 as previously described), which in addition to the as-synthesised $AZ1_{RRS}$ material, can be produced as a crystalline powder by slurry of the initially semi-crystalline $AZ1_{mix}$ in acetonitrile; a dichloromethane solvate obtained as crystalline needles by cooling crystallisation of $AZ1_{mix}$ or $AZ1_{RRS}$ from dichloromethane (Form 2); and just one crystal of a second solvate form obtained by cooling crystallisation of $AZ1_{mix}$ from p-xylene (Form 3) as shown in Figure 2.1e. The Form 3 sample took almost a year to grow but proved to be suitable for single crystal X-ray diffraction (SC-XRD). A sample that appears to be isostructural with Form 2 was also grown as needle-like crystals by cooling crystallisation of $AZ1_{mix}$ in chloroform. While Form 1 could be reproduced easily from either $AZ1_{mix}$ or $AZ1_{RRS}$, Forms 2 and 3 crystallised in only rare cases, proving the difficulty in exploring these compounds' potential polymorphism and solvatomorphism.

SEM images reveal that the most crystalline Form 1 sample ($AZ1_{RRS}$ as-synthesised) has a well-defined narrow plate morphology with particles ranging from approximately 10 – 15 µm in length and around 2 µm in width (Figure 2.1c). Optical microscope images of Form 2 crystals (Figure 2.1d) obtained from either $AZ1_{RRS}$ or $AZ1_{mix}$ reveal a needle-

like morphology with a high aspect ratio and approximate length of 0.5 – 1 mm, however even the sample with the most crystalline powder pattern did not diffract X-rays well enough for structure determination even by synchrotron-source X-ray diffraction, and samples ground gently to a powder were unsuitable for analysis by electron diffraction, meaning that no structure solution was possible for Form 2. Since only one crystal of Form 3 was grown (Figure 2.1e), with a similar plate-like morphology to that of Form 1 but at a larger scale of 0.089 × 0.008 × 0.002 mm, any characterisation beyond SC-XRD was not possible. Efforts to reproduce this form by numerous cooling and slurry crystallisation experiments at a range of temperatures were unsuccessful. Slurries of Form 1 or Form 2 in p-xylene using magnetic stirring bars or impellers produced only amorphous powders within hours, whereas crystalline samples could be obtained by stirring slurries of Form 1 more gently using a roller mixer which produces much lower shear forces that grind the fragile crystalline particles into amorphous powder. However, XRPD analysis shows that after roller-mixing for several hours, days or months, only the form initially added or amorphous solid could be detected. Attempts to gradually cycle the temperature of a slurry containing Form 1 between room temperature and near boiling point, intending to reproduce similar conditions to the original experiment but with accelerated mass transport, produced no evidence of Form 3. Hence from the limited data available, it is hypothesized that Form 3 is a metastable solvate in p-xylene. This demonstrates the poor crystallisability of PROTAC compounds and the difficulty not only in discovering new forms, but in reproducing them for characterisation.

Crystal Structure Analysis

Structure solution by 3D electron diffraction (3D ED) was possible for the as-synthesised $AZ1_{RRS}$ crystalline powder. The crystal structure of Form 1 shows that AZ1 molecules form discrete hydrogen bonded dimers aligned with the *a* axis via head-to-tail N9-H9•••O1 interactions and aliphatic stacking (Figure 2.2). The dimers then stack along the *b* axis by numerous dispersive short contacts, and similarly along the *a* axis but to a lesser extent. The only interactions apparent along the *c* axis arise from close contacts between hydrophobic end-groups of neighbouring AZ1 molecules. There is only one hydrogen bond linking neighbouring AZ1 molecules despite the availability of two hydrogen bond donors and three carbonyl acceptors, leaving two that are involved only in weak interactions with C-H groups in adjacent molecules. Full interaction map analysis in Mercury[51] (Appendix A, Figure A3) shows that all but one pair of potential hydrogen bond donor and acceptor groups in the AZ1 molecule are not involved in interactions predicted by the map, suggesting that the crystal conformation and/or packing is unable to satisfy the hydrogen bonding potential of all these moieties at once. XRPD analysis of

the bulk sample is consistent with the calculated XRPD pattern from the single crystal data, confirming bulk solid form purity (Appendix A, Figure A4).

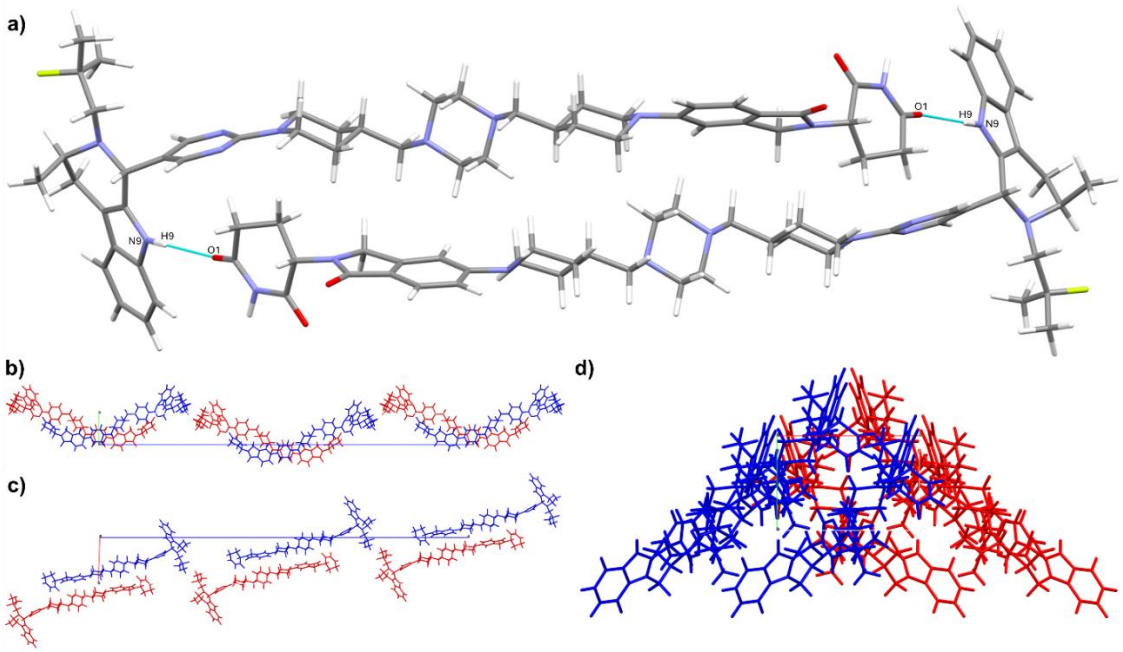

Figure 2.2. Form 1 crystal structure. a) Dimer interaction between AZ1 molecules involving a head-to-tail N9-H9•••O1 interaction. b-d) Views down crystallographic *a*, *b* and *c* axes respectively. Data were collected and processed by the National Electron Diffraction Facility for Nanomaterial Structural Studies and Dr. Toby J. Blundell.

Pairwise intermolecular interactions were evaluated using Crystal Interaction (CrysIn), a tool developed by AstraZeneca to quantify static interactions between molecules in the crystal using density functional theory (DFT).[37] For each pairwise interaction between the asymmetric unit and its neighbouring molecules, the interaction energy and its percentage contribution to the total lattice energy are calculated as well as a dispersive ratio, indicating the extent to which the interaction is dispersive or electrostatic in nature (a ratio of 1 describes a fully dispersive interaction, while 0.7 indicates some significant contribution of electrostatic attraction as well). The results of the calculation and the three pairwise interactions contributing the most to the Form 1 lattice energy are depicted in Figure 2.3, with the remaining pairwise interactions depicted in Appendix A, Figure A5. The results show that approximately 84% of the lattice energy can be attributed to four pairwise interactions with the greatest contribution from the formation of AZ1 dimers (d006, Figure 2.3b), through an interaction that is predominantly dispersive despite the presence of a hydrogen bond. These dimers then pack along the *b* axis via dispersive aliphatic stacking interactions (d000/d001, Figure 2.3c). The next two strongest pairwise

interactions consist of further dispersive stacking along the *a* and *b* axes, with only around 5% of the remaining lattice energy accounted for by interactions aligned with the *c* axis including an interaction between fluorinated moieties with slightly greater electrostatic contribution. This distribution of the lattice energy into interactions aligned with the three crystallographic axes is reflected in the plate-like BFDH morphology predicted by Mercury,[51] where the longest crystal dimension is aligned with the crystallographic *b* axis, followed by the *a* then *c* axes, which is also in good agreement with the morphology observed by SEM. CrysIn analysis shows overall that besides the one hydrogen bond present in the AZ1 dimer interaction, the crystal structure is dominated by the sum of many dispersive, aliphatic stacking interactions with little contribution from directional hydrogen bonding or aromatic stacking interactions. The poor crystallisability of AZ1 may then be explained by the lack of strong and directional interactions that could guide the molecules into adopting the crystal conformation and pack into the three-dimensionally ordered structure, favouring instead an amorphous solid where the molecular conformation is less constrained and molecules may be able to make stronger local interactions at the expense of long-range order.

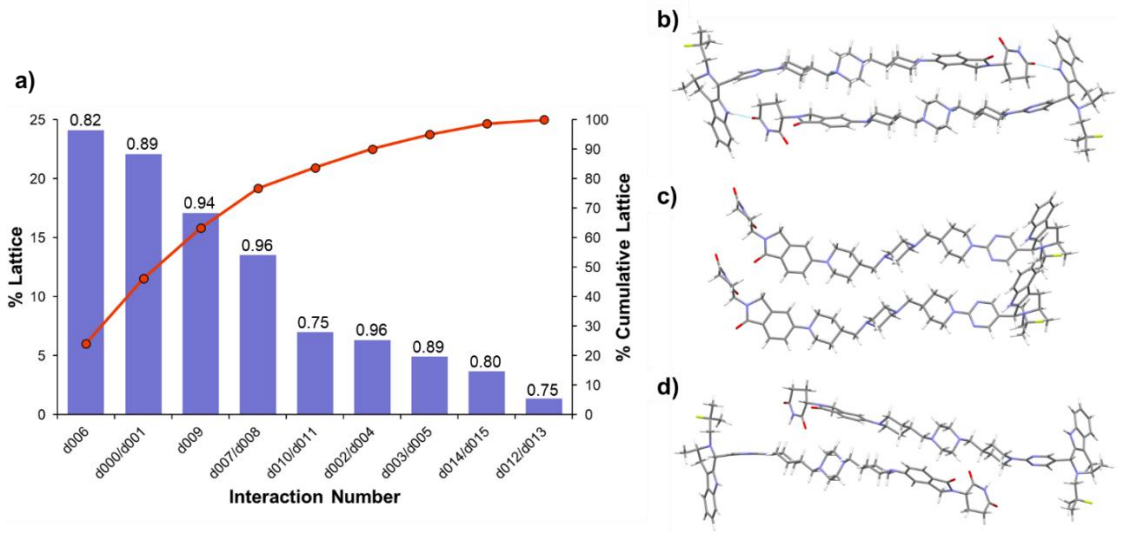

Figure 2.3. a) CrysIn analysis of Form 1. The bar chart shows the percentage contribution of each pairwise interaction type to the total lattice energy. The line chart shows the cumulative lattice energy accounted for as pairwise interactions are summed together. The numbers above each bar chart are the dispersive ratios for each pairwise interaction, where a ratio of 1 indicates a fully dispersive interaction with no electrostatic contribution. b-d) The three pairwise interactions that contribute the most to the Form 1 lattice energy by CrysIn analysis. From top to bottom: the AZ1 dimer interaction (d006); aliphatic stacking interactions along the *b* axis (d000/d001); aliphatic stacking interactions along the *a* axis (d009). The remaining six pairwise interactions are shown in Appendix A, Figure A5. CrysIn calculations were performed by Dr James F. McCabe.

Only one crystal of Form 3 large enough for synchrotron-source SC-XRD was obtained via a cooling crystallisation of $AZ1_{mix}$ from p-xylene, in which AZ1 has very low solubility even at the solvent boiling point of 138 °C. Undissolved material at the bottom of the vial was identified as poorly crystalline Form 1 with a significant quantity of amorphous content, while Form 3 crystallised within a droplet of solvent high up on the side of the vial after approximately 11 months. One hypothesis is that gradual mass transport up the sides of the vial and/or slow solvent evaporation over many months allowed a small quantity of AZ1 to recrystallise in this droplet on the vial wall. Structure solution of Form 3 reveals that it is a channel solvate with a 1 : 0.75 ratio of AZ1 to p-xylene, with the contribution of severely disordered p-xylene solvent which was removed from the structure solution using the SQUEEZE algorithm[52] (Figure 2.4). The disorder in the CRBN-ligand of the AZ1 molecule (Figure 2.5a) arises from the presence of both RRR- and RRS- diastereomers in different unit cells since both isomers can pack into the same crystal structure, likely because the overall shape of the molecule is relatively similar for both configurations of this chiral atom, and because the intermolecular interactions are predominantly dispersive and isotropic in nature, unlike hydrogen bonds, and so are not affected significantly by the difference in configuration. The RRR- and RRS- isomers were present in a ratio of 88% to 12% respectively in the crystal analysed, despite beginning the crystallisation experiment from a 1:1 ratio of the isomers. Hence, interestingly, the predominant diastereomer in Form 3 is different to the RRS isomer analysed in the 3D ED structure of Form 1. It is unknown whether RRS-enriched crystals were also present in the sample since only one Form 3 crystal was suitable for analysis. However, the presence of other crystals consisting mostly of RRS- rather than RRR- seems plausible given that the most crystalline samples of Forms 1 and 2 produced in other crystallisation experiments were grown using $AZ1_{RRS}$ rather than $AZ1_{mix}$. AZ1 molecules in Form 3 produce a hydrogen bonded stack aligned with the *b* axis via head-to-tail N9-H9•••O1 interactions. Along the *a* and *c* axes, AZ1 molecules interact only via dispersive short contacts. Like Form 1, the crystal predominantly consists of dispersive interactions with only one hydrogen bond linking neighbouring AZ1 molecules, despite the availability of two hydrogen bond donors and three carbonyl acceptors. Full interaction map analysis (Appendix A, Figure A6) shows again that the molecular packing does not satisfy the hydrogen bonding potential of all the available moieties.

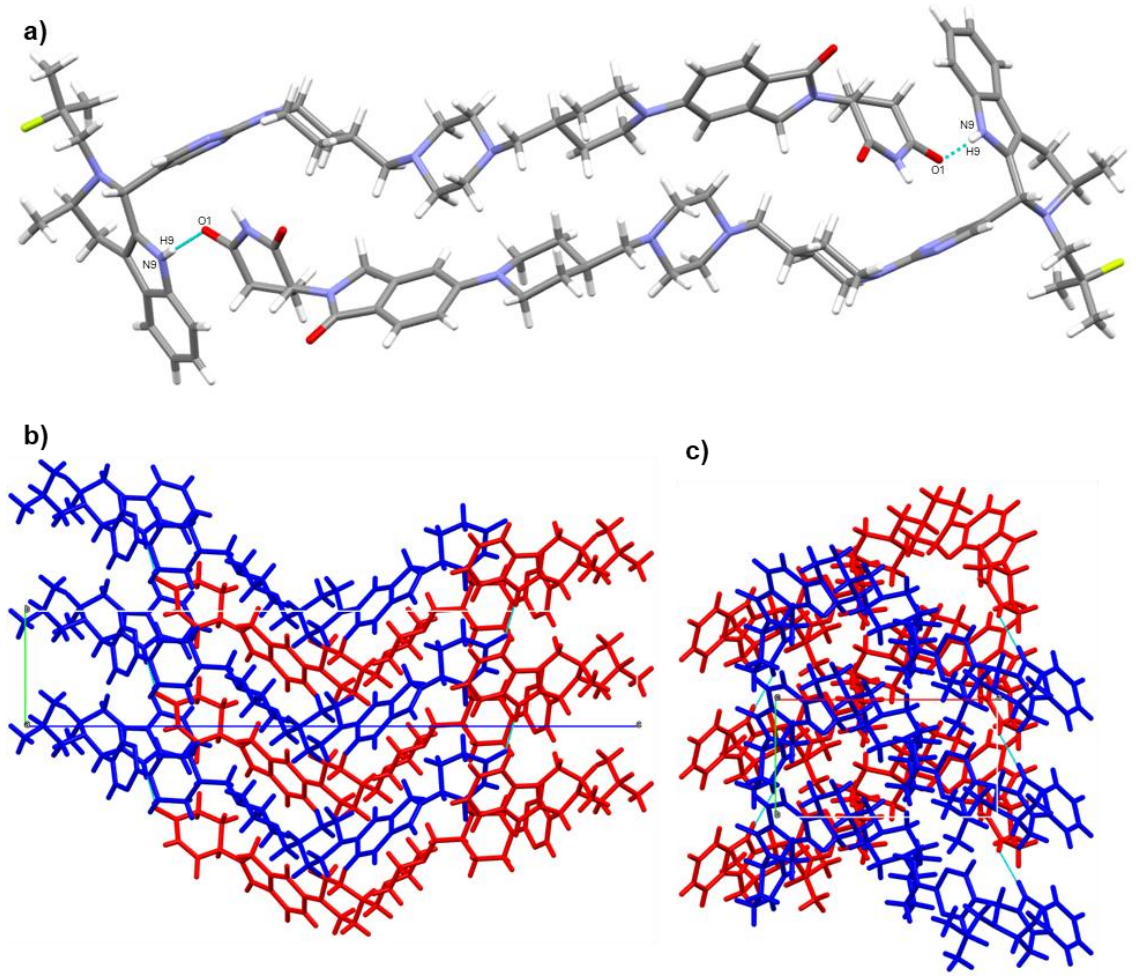

Figure 2.4. The crystal structure of AZ1 Form 3 with the disordered p-xylene solvent removed via the SQUEEZE algorithm. a) The unit cell of Form 3 with a single hydrogen bond between the two AZ1 molecules, viewed down the *b* axis. b) The view down the *a* axis. c) The view down the *c* axis. Data were collected and processed by Dr. Toby J. Blundell.

The solvent channels (Figure 2.5b) account for 14.7% of the unit cell volume (371.05 / 2517.09 Å^3) and each unit cell contains 1.5 p-xylene molecules. The channel walls are hydrophobic in nature, consisting mostly of flexible alkyl groups and the faces of planar aromatic sub-units of AZ1, such as the indole- and pyrimidine-like moieties in the ER-warhead. The Form 3 structure was also analysed by CrysIn, noting the limitation that the p-xylene solvent is not explicitly included in the model and hence any contributions to the lattice energy from interactions between AZ1 and p-xylene are neglected. The 12% component of the RRS- isomer present as modelled disorder was also removed prior to the calculation, leaving only the RRR- major component. CrysIn analysis shows that approximately 85% of the lattice energy is accounted for by three pairwise interactions that are mostly dispersive in nature based on their dispersive ratio (Figure 2.6), with the remaining pairwise interactions depicted in Appendix A, Figure A7. The strongest interaction is dimer-like as in Form 1, showing a relatively high dispersive ratio again despite the presence of a hydrogen bond. Unlike in Form 1 where the dimer interaction

accounts for ~24% of the lattice energy at -114.39 kJ/mol, in Form 3 the dimer accounts for ~38% at -143.18 kJ/mol, with only a small difference between the dispersive ratios (0.82 in Form 1 compared to 0.78 in Form 3). The N9-H9•••O1 interaction is roughly 0.1 Å shorter in the Form 3 structure but at a less linear N-H-O bond angle of 130 ° compared to 166 ° in Form 1. The stronger dimer interaction in Form 3 ($AZ1_{RRR}$) compared to Form 1 ($AZ1_{RRS}$) may result from an inherent difference in the ability of the two isomers to densely pack in the solid state. Like Form 1, stacking interactions aligned with the *b* axis dominate the Form 3 lattice energy. This demonstrates that despite containing mostly the RRR- diastereomer rather than the RRS- present in the Form 1 structure, the crystal structures are built from very similar intermolecular interactions.

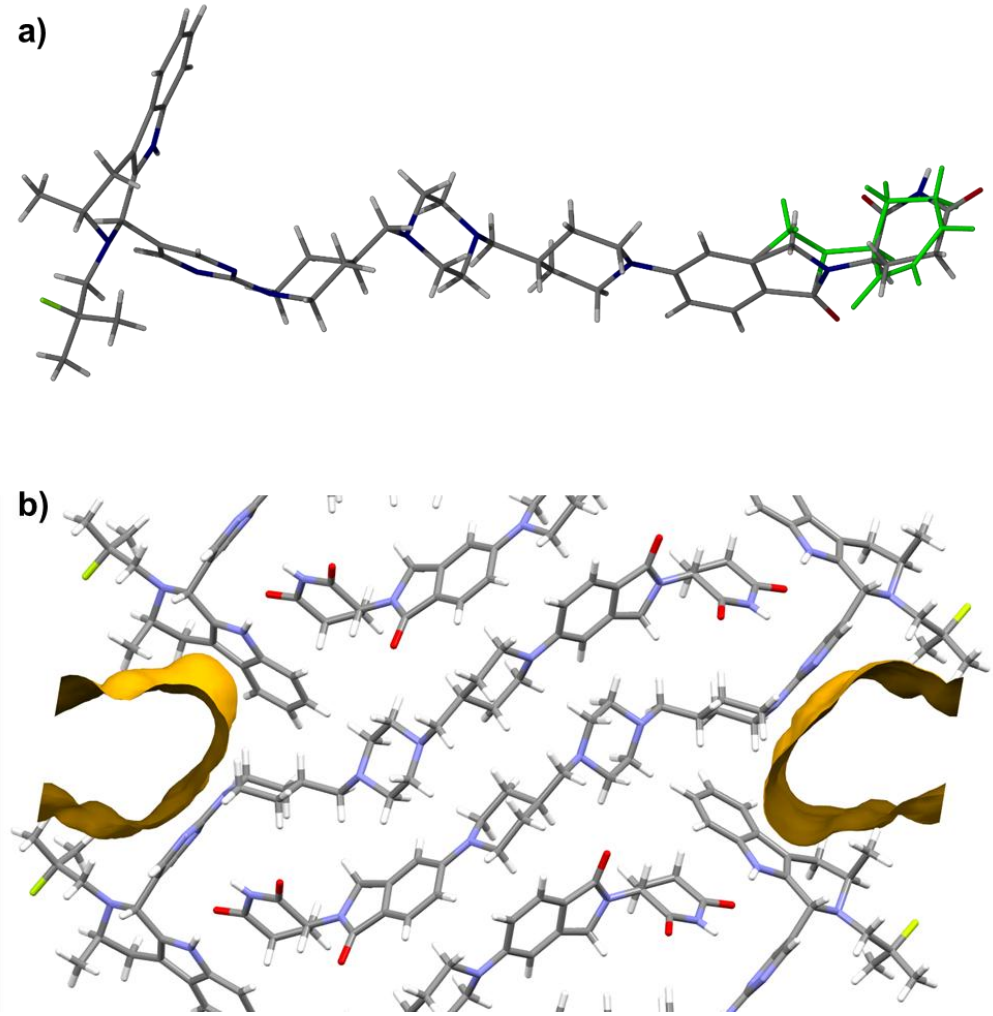

Figure 2.5. a) Disorder in the CRBN ligand of AZ1 arising from the presence of both RRR- and RRS- diastereomers in an 88:12 ratio in the crystal structure of Form 3. The RRS- minor component is highlighted in green. b) Solvent accessible voids in the crystal structure of AZ1 Form 3, depicted using Mercury.[51]

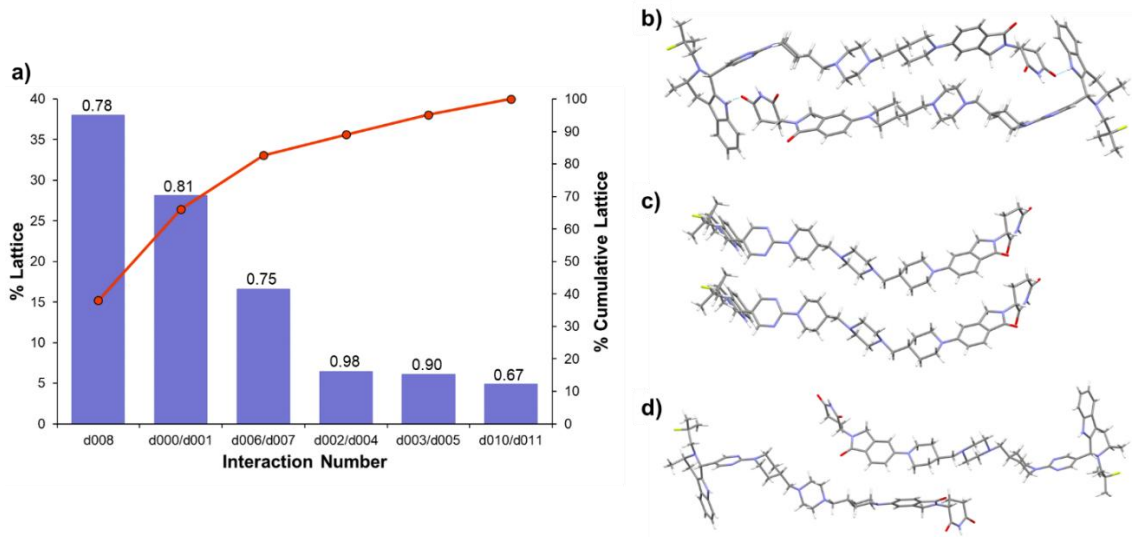

Figure 2.6. a) CrysIn analysis of Form 3. The bar chart shows the percentage contribution of each pairwise interaction type to the total lattice energy. The line chart shows the cumulative lattice energy accounted for as pairwise interactions are summed together. The numbers above each bar chart are the dispersive ratios for each pairwise interaction, where a ratio of 1 indicates a fully dispersive interaction with no electrostatic contribution. b-d) The three pairwise interactions of AZ1 molecules that contribute the most to the lattice energy of the Form 3 crystal structure. These three dispersive interactions cumulatively account for 84% of the lattice energy. From top to bottom: AZ1 dimer interaction (d008); aliphatic stacking interactions along the *b* axis (d000/d001); aliphatic stacking interactions in the *ac* plane (d006/d007). The remaining three pairwise interactions are shown in Appendix A, Figure A7. CrysIn calculations were performed by Dr James F. McCabe.

The crystal conformation of AZ1 appears to be similar between Forms 1 and 3 regardless of the difference in diastereomer (Figure 2.7), adopting an elongated shape in both structures that allows a greater surface area of the molecules to stack closely in three dimensions, unlike a folded or C-shaped conformation that would impede the formation of many short dispersive contacts. As a large and relatively flexible bRo5 molecule with multiple rotatable bonds in its linker moiety, there is probably a considerable entropic penalty for AZ1 to adopt only the elongated crystal conformation present in either crystal. Coupled with a lack of strong, directional interactions such as hydrogen bonds or aromatic stacking interactions in either crystal that could guide the molecule into adopting one conformation from the many available, the overall driving force for packing AZ1 into either of these crystal structures appears to be very weak. This explains the generally poor crystallinity observed in even the most crystalline samples obtained through the screening process, most of which were unsuitable for analysis by diffraction methods, and why many of the crystallisation experiments using methods such as ENaCt, where solid material often precipitates within 2 weeks, were unsuccessful. The formation of only

one diffraction-quality crystal of Form 3, eleven months after the initial cooling crystallisation experiment was begun, further exemplifies these particularly slow crystal growth kinetics.

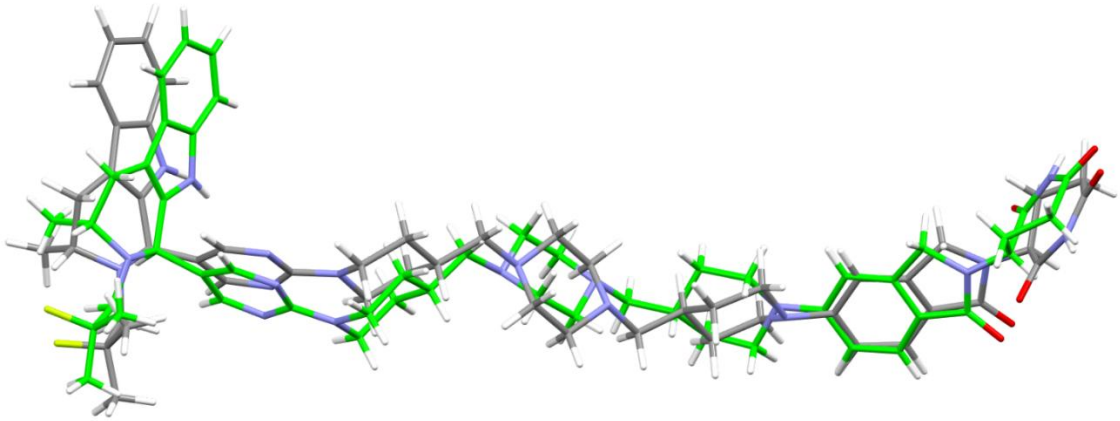

Figure 2.7. Comparison of AZ1 crystal conformations in Form 1 (full colour) and Form 3 (green highlight). Only the major RRR- isomer component of the Form 3 crystal structure is shown. Only the RRS- isomer is present in Form 1.

Comparison to crystalline drugs in the CSD

The Cambridge Structural Database contains published solid forms of more than 785 unique drug molecules,[53] providing the opportunity to compare the available PROTAC crystal structures of AZ1 Forms 1 and 3 with a broad range of API compounds for which crystal data already exists. The CSD search protocol is described in the experimental section and produced a subset of 738 single component crystal structures with Z'=1 from the 2388 available entries, designated "CSD-drugs$_{NZ1,1}$". The experimental also describes a computational method to calculate lattice energies and pairwise interaction energies for all structures including Forms 1 and 3. As with the CrysIn analysis, it should be noted that the removal of disordered p-xylene solvent and the minority AZ1 diastereomeric component will affect the computed energies in the Form 3 structure.

The computed lattice energies of the crystals containing drug compounds in the CSD (CSD-drugs$_{NZ1,1}$ subset) are shown in Figure 2.8. Typically, the lattice energies of the non-zwitterionic drugs become more stabilizing the larger the compound. Remarkably, Form 1 has lower lattice energy (-373.6 kJ/mol) than all CSD-drugs$_{NZ1,1}$ compounds with Form 3 being only about 8 kJ/mol less stable (-365.3 kJ/mol), not including any further stabilisation from interactions between AZ1 and the un-modelled p-xylene solvent. This suggests that the particularly low aqueous solubility of AZ1, and potentially other

PROTACs, is due to not only their lipophilicity but also their very strong lattice energies, giving them some degree of both “brick-dust” and “grease-ball” solubility characteristics. It should also be noted that only one structure in the CSD-drugs$_{NZ1,1}$ subset contains a drug molecule larger than AZ1; this corresponds to the drug compound sirolimus, also known as rapamycin.[54] Of the crystal structures with a lattice energy lower than -300 kJ/mol and/or containing a compound with >100 atoms, all but one are structures of bRo5 molecules (with ganciclovir as the exception, CSD refcode UGIVAI01). This group of structures consists of the drug compounds digoxin, diosmin, lapatinib, cyclohexane-1,2,3,4,5,6-hexayl hexakis(pyridine-3-carboxylate), lactitol, rapamycin, rifampicin, clarithromycin and erythromycin. In contrast to PROTAC compound AZ1, these compounds generally show much greater diversity of solid forms – particularly the large compounds rifampicin, clarithromycin and erythromycin which contain 117–121 atoms compared to 126 in AZ1. These compounds can also be crystallised far more readily than AZ1, for example from cooling of aqueous solutions. The only notable exception to this is lapatinib, where single crystals of the anhydrous freebase form (-341 kJ/mol lattice energy, 66 atoms) could only be produced via an unexpected method using wire as a nucleation device.[55] Unlike AZ1, however, lapatinib exhibits two anhydrous polymorphs and the commercially available ditosylate salts are highly polymorphic.[56] This suggests that PROTAC AZ1 stands alone within this subset of structures as being particularly difficult to crystallise yet producing crystal structures with particularly strong lattice energies.

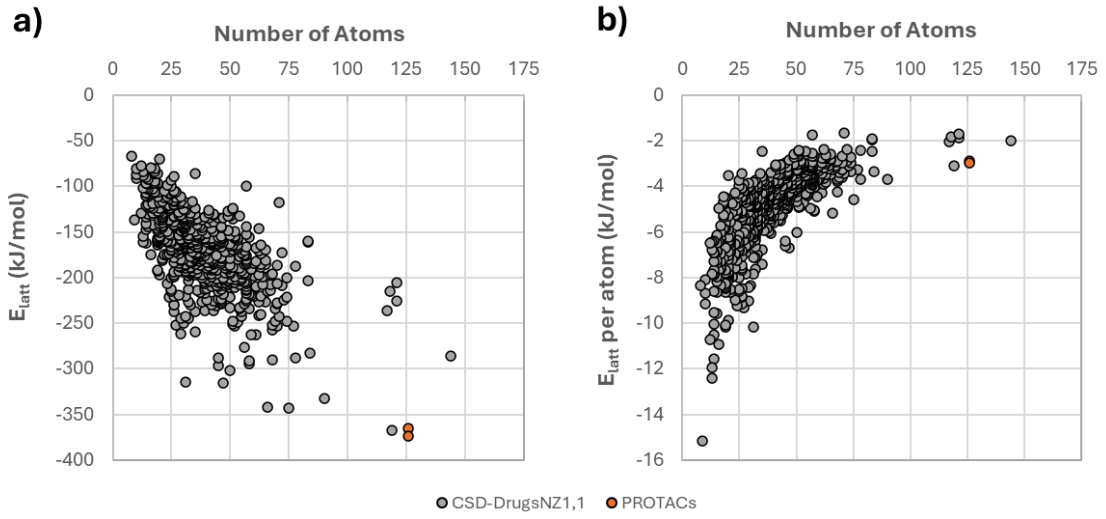

Figure 2.8. Dependence of the a) lattice energy (E_{latt}) and b) lattice energy per atom with the number of atoms of the crystallising compound for the CSD-drugs$_{NZ1,1}$ subset (grey), and AZ1 forms 1 and 3 structures reported in this work (orange). Lattice energy calculations on CSD-drugs$_{NZ1,1}$ were performed by Prof. Aurora J. Cruz-Cabeza.

The lattice energies per atom are shown in Figure 2.8b for the CSD-drugs$_{NZ1,1}$ subset and AZ1 Forms 1 and 3. The lattice energy per atom becomes less stabilizing the larger the drug compound becomes, converging towards -2 kJ/molatom at large compound sizes. Smaller compounds (<25 atoms) crystallise with significantly more stabilizing lattice energies per atom (between -15 to -4 kJ/molatom) than larger compounds. This trend suggests that drug compounds are less able to optimise directional intermolecular interactions such as hydrogen bonds as they become larger, with a greater lattice energy contribution from dispersion. Since the molecular weight of AZ1 falls roughly in the middle of the average range for PROTAC compounds at 859 g/mol,[57] it is likely that the low lattice energies per atom observed for AZ1, at -3.0 kJ/molatom and -2.9 kJ/molatom for Forms 1 and 3 respectively, are representative of many similar bRo5 compounds. Interestingly, 50% of the crystal structures containing larger compounds (with >69 atoms) contain structural voids which could potentially contain solvent, as observed in Form 3. This observation suggests that the poor ability of the larger compounds to crystallise often results in structures which must include solvent to densely pack. Just like AZ1, three of the large compounds in the CSD-drugs$_{NZ1,1}$ subset, namely probucol (HAXHET and HAXHET01), cabergoline (SUPBEK and SUPBEK03) and difluprednate (IHOZOW01 and IHOZOW02), crystallise in both a close packed structure and one containing structural voids.

Comparison of AZ1 bulk forms

Thermal analysis and solution NMR spectroscopy (Appendix A, Figure A8-9) reveal that Form 1 is anhydrous, with a melt onset at 256 °C or 262 °C depending on whether obtained from AZ1$_{mix}$ or AZ1$_{RRS}$ respectively. This aligns with the observation that Form 1 containing only AZ1$_{RRS}$ has a slightly more crystalline powder pattern than the sample produced by slurrying AZ1$_{mix}$ in acetonitrile, and the high melting points of both samples are commensurate with the high calculated lattice energy of Form 1. The FTIR spectra for both samples are indistinguishable (Appendix A, Figure A10). Thermal and spectral characterisation (Appendix A, Figure A12-14) also reveal that Form 2 is a non-stoichiometric solvate form containing dichloromethane, obtained as needles by cooling crystallisation. A sample obtained from a cooling crystallisation in chloroform appears to be isostructural with Form 2 based on XRPD analysis, thermal data and FTIR data (Appendix A, Figure A14-16). Unlike Form 1, the crystallisation of Form 2 was very challenging to reproduce and so only a few tens of milligrams of sample could be generated, mostly derived from AZ1$_{mix}$ which was used for all the following

characterisation. The slightly humped baseline in the XRPD pattern (Figure 2.1b) and broad signals in both the FTIR (Appendix A, Figure A16) and solid-state NMR spectra (Appendix A, Figure A2) of this sample reveal that it is disordered. A miniscule quantity of Form 2 produced using $AZ1_{RRS}$ had an identical XRPD pattern but slightly sharper FTIR features suggesting less disorder. Thermal analysis shows that Form 2 undergoes a gradual solvent loss of roughly 1.3 % mass between 25 and 100 °C (0.13 molar eq. of dichloromethane) followed by a sharper solvent loss of 2.4 % starting at roughly 150 °C (0.25 molar eq. of dichloromethane), for a combined total stoichiometry of 1 : 0.38. Given the volatility of the solvent, it is possible that a greater molar ratio of solvent is present in Form 2 before the crystals are filtered and analysed. A single T_g at 159 °C is observed by DSC on the second heating of the sample, indicating the collapse of the desolvated crystal structure into an amorphous phase. This is supported by hot-stage polarised optical microscopy (Appendix A, Figure A13) which shows the disappearance of all birefringent particles and the needle-like morphology above 170 °C and upon subsequent cooling to 30 °C. The high T_g of the resulting amorphous phase indicates that molecular mobility is low and the phase is very kinetically stable, likely due to a sum of many weak dispersive interactions between large molecules as observed in the crystalline phases, but perhaps also because the molecules are not constrained to a single conformation as they are in the crystal and can therefore optimise directional interactions such as hydrogen bonds at a local scale at the expense of long-range ordering. A small sample of Form 2 heated to 150 °C in an oven for 2 hours produces a solid with a fully amorphous powder diffraction pattern and a T_g at 159 °C (Appendix A, Figure A17). However, the FTIR spectrum appears not to change compared to the starting material (Appendix A, Figure A18). This could be because the desolvated solvate structure is very similar to the crystalline Form 2 structure.

FTIR analysis (Figure 2.9) shows significant differences in the carbonyl region (1600-1750 cm-1) and N-H region (3100-3500 cm-1) of AZ1 between Forms 1 and 2. Form 1 contains three carbonyl bands compared to at least four broad bands in Form 2, suggesting that the structures differ in the degree of hydrogen bonding to the three carbonyl moieties within AZ1. Coupled with the broader and less defined N-H region of Form 2, this suggests that the N-H donors and C=O acceptors in the AZ1 molecules are involved in more and/or stronger hydrogen bonds in the Form 2 structure compared to Form 1, potentially arising from a more favourable crystal conformation that can only pack densely when supported by solvent molecules such as dichloromethane. The FTIR spectra of Forms 1 and 2 differ also by shifts of 5 – 10 cm^{-1} in at least ten features between 750 – 1550 cm^{-1}. Two-dimensional ^{1}H-^{13}C FSLG HETCOR NMR analysis (Appendix A, Figure A21) reveals no direct evidence for hydrogen bonding in either sample since these spectra are dominated by intramolecular correlations, but the

differences observed in the carbonyl region (above 165 ppm) between the two crystal forms are consistent with the differences in hydrogen bonding observed via FTIR. The HETCOR analysis of Form 2 shows that the carbonyl peaks produce only a single weak contact at short contact times, most likely corresponding to the intramolecular correlation between the carbonyl carbon atoms and the NH hydrogen atom in the imide moiety of AZ1. This interaction appears stronger at longer contact times (Appendix A, Figure A22) with longer distance dipolar interactions also observed in both crystal forms that can be attributed to correlations between the carbonyl carbon atoms and neighbouring alkyl hydrogen atoms.

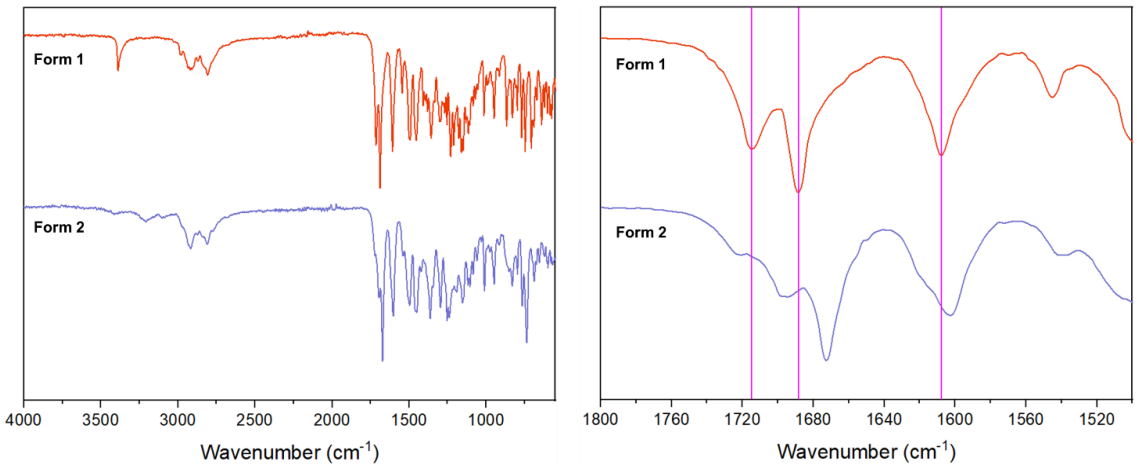

Figure 2.9. FTIR spectra comparing AZ1 Form 1 and 2. There are differences in the peak breadth and wavenumber in the 1600-1750 cm^{-1} and 3100-3500 cm^{-1} regions, suggesting differences in the type and/or degree of hydrogen bonding.

Since Forms 2 and 3 both present a lamellar-like X-ray powder pattern dominated by a series of strong, evenly spaced peaks that correspond to (00*l*) reflections in the case of Form 3, it is possible that Form 2 possesses a similar channel solvate structure where the main difference is the diameter or spacing of the solvent voids, causing the structural differences along the *c* axis that would cause the (00*l*) reflections to shift uniformly in angle. Applying Bragg's law to the first four (00*l*) reflections of the Form 3 powder pattern gives an average *d* spacing of 22.6 Å, which is approximately the distance between solvent channels along the *c* axis. Applying Bragg's law to the first three reflections of the Form 2 powder pattern, and assuming the first peak detected at 1.9 ° is the (001) reflection, gives a higher *d* spacing of 29.8 Å. This suggests that either the solvent channels are larger in Form 2 than in Form 3, or that the hypothetical AZ1 dimers in Form 2 are more closely aligned with the *c* axis and cause a greater separation of the solvent

channels, compared to the somewhat diagonal alignment of AZ1 dimers with the *c* axis observed in Form 3.

The ^{13}C NMR spectra (Appendix A, Figure A2) for Form 1 samples derived from either $AZ1_{mix}$ or $AZ1_{RRS}$ are very similar and the mixed isomer samples show only slightly more disorder, suggesting that the Form 1 structure is capable of accommodating both diastereomers in the same packing arrangement. The mixed isomer Form 1 crystals may grow as solid solutions like the single crystal of Form 3 analysed by SC-XRD, giving good diffraction with some disorder from the presence of random isomers. Meanwhile the NMR spectrum of Form 2, derived from $AZ1_{mix}$, is significantly more disordered by comparison and since both NMR and XRPD analysis shows it contains only a single crystalline phase, the disorder likely arises because the Form 2 structure cannot accommodate both isomers as well as Form 1, leading to greater local variation in chemical environments and a more disordered crystal.

The observation that AZ1 has a propensity to form solvates is commensurate with the findings from the CSD analysis that bRo5 compounds are less able to pack densely as pure solids compared to smaller drug molecules, and the available thermal, spectral and diffraction data suggests that the Form 2 structure may be a similar channel solvate to Form 3 but with a greater importance of hydrogen bonding interactions. The difficulty in drawing conclusions from the limited data on Form 2 illustrates the challenge faced by the pharmaceutical industry in identifying all solid forms of PROTACs. Solvate forms are another challenge for drug development since many solvents used in synthesis are toxic to humans, and because their desolvation behaviour can raise challenges regarding their stability, solubility and mechanical properties. While crystallisation experiments of $AZ1_{mix}$ that produced Form 1 and Form 2 were reproducible using $AZ1_{RRS}$ and with similar crystallinity, attempts to crystallise pure $AZ1_{RRR}$ consistently produced amorphous solids. This indicates that $AZ1_{RRR}$ is prone to amorphisation in the absence of $AZ1_{RRS}$, yet in $AZ1_{mix}$ it appears capable of forming crystalline solid solutions with $AZ1_{RRS}$ in at least Forms 1 and 3 based on spectroscopic and crystallographic data. These findings also suggest that neither stereoisomer impedes the crystal growth of the other.

Amorphous solids

Amorphous phases of AZ1 can be produced easily, since the compound is poorly crystallizable. Grinding any AZ1 sample in a ball mill at 20 Hz for as little as 5 minutes results in an amorphous powder by XRPD analysis, and thermal analysis of the amorphous as-synthesised $AZ1_{RRR}$ material as well as milled samples of $AZ1_{mix}$ and $AZ1_{RRS}$ all show a T_g value around 157 – 161 °C (Appendix A, Figure A23-25) and

broadening of spectral bands in the FTIR spectrum, resembling the amorphous desolvated solvate produced by heating Form 2 to remove the dichloromethane. The high T_g values suggest that all of these amorphous phases are likely to be very stable with respect to recrystallisation at room temperature, forming robust glasses. The milled $AZ1_{RRS}$ solid appears to differ from the others slightly in the sharpness and position of its carbonyl bands between 1680 and 1720 cm^{-1} and between 1600 and 1620 cm^{-1} (Figure 2.10), potentially indicating differences in the degree of hydrogen bonding to the carbonyl groups within its local structure. The desolvated Form 2 solid also has a slightly sharper feature at 1672 cm^{-1} compared to 1684 cm^{-1} for the others, and two missing bands at 1175 cm^{-1} and 867 cm^{-1} suggesting similar local structure differences may be present in this phase. It is possible that greater free volume and fewer conformational restrictions in amorphous form allow AZ1 molecules to form more and/or stronger hydrogen bonding interactions, broadening the C=O and N-H regions of the FTIR spectra compared to the crystalline phases and resulting in highly stable glasses characterised by a high T_g.

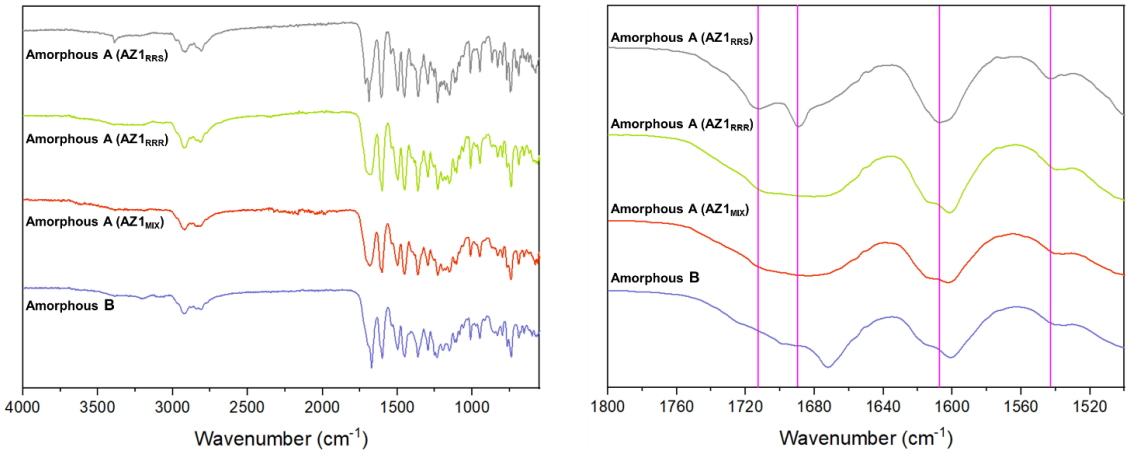

Figure 2.10. FTIR spectra of AZ1 amorphised by grinding Form 1 in a ball mill (amorphous form A) or by desolvating Form 2 (amorphous form B).

While these spectral differences appear to be relatively minor, a comparison of the dissolution profiles for the amorphous solids produced by milling the anhydrous Form 1 (amorphous form A) and those produced by desolvating the Form 2 solvate (amorphous form B) reveal a much more significant 4-fold difference in apparent solubility. Figure 2.11a shows non-sink dissolution profiles over 2 hours in fasted state simulated intestinal fluid (FaSSIF) at 37 °C, comparing amorphous forms A and B to crystalline Form 1, with all samples produced using $AZ1_{mix}$. To reduce the impact of particle size differences between the samples produced by ball milling or otherwise, the un-milled samples were ground gently in a pestle and mortar and all powders were sieved to remove particles

larger than 150 µm. SEM images (Figure 2.12) confirm that all samples consisted of particles in the range of 1 – 10 µm in length with similar dispersity and show a consistent particle morphology. Despite this, amorphous form A showed a considerable apparent solubility increase compared to the crystalline Form 1 whereas amorphous form B showed a far lower solubility, almost matching the crystalline Form 1. Since the FTIR comparison of crystalline Forms 1 and 2 appears to indicate more and/or stronger hydrogen bonds in the latter form, it is possible that amorphous form B also contains more and/or stronger hydrogen bonds than amorphous form A, that stabilise it against dissolution. This greater stabilisation of the amorphous phase via molecular interactions is not evident from thermal analysis however, with all amorphous solids presenting a very similar T_g. This demonstrates that while amorphous forms of AZ1 prepared by different methods may appear similar by standard characterisation techniques, potential differences in their local structure cause their dissolution behaviour to vary significantly.

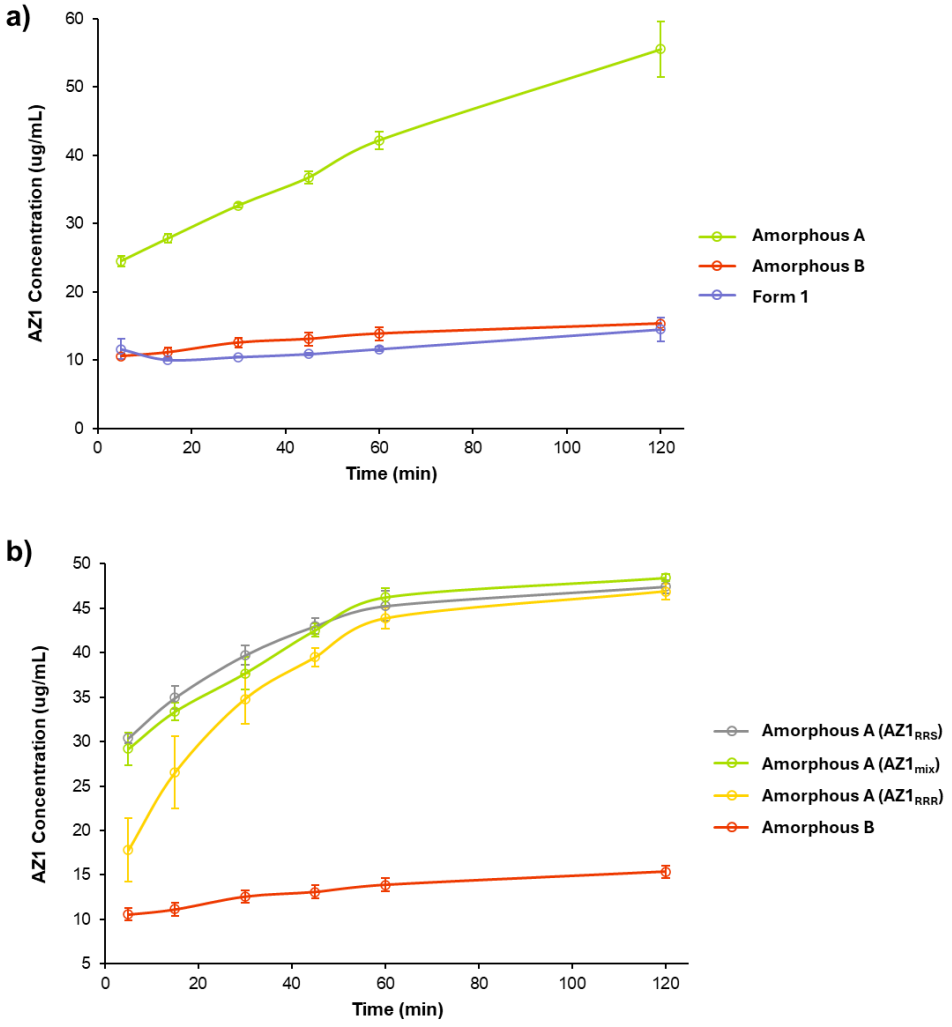

Figure 2.11. Non-sink dissolution profiles over 2 hours in fasted state simulated intestinal fluid (FaSSIF) at 37 °C, using a 10-fold non-sink condition relative to the crystalline solubility (Form 1). a) Dissolution profiles of AZ1 Form 1 crystals, amorphous form A and amorphous form B, with all

three samples prepared using $AZ1_{mix}$. b) Dissolution profiles of amorphous form A samples produced separately from $AZ1_{mix}$, $AZ1_{RRR}$ and $AZ1_{RRS}$ as well as amorphous form B. $AZ1_{mix}$ and $AZ1_{RRS}$ were milled to produce amorphous form A while $AZ1_{RRR}$ was used as synthesised without milling. Average concentrations and error bars indicating standard deviations of the mean are shown for time-points acquired in triplicate for both plots. Dissolution data points reflect a time constant due to 30 minutes of centrifugation as detailed in section 2.2, during which further dissolution may have occurred.

The dissolution profiles of amorphous form A produced by ball-milling $AZ1_{mix}$ or $AZ1_{RRS}$ were compared to the as-synthesised amorphous $AZ1_{RRR}$ (un-milled) and amorphous form B (Figure 2.11b). Again, the un-milled $AZ1_{RRR}$ samples were ground gently by hand and sieved to partially control for particle size differences. The two milled and the un-milled $AZ1_{RRR}$ samples of amorphous form A have a similar dissolution profile reaching approximately the same apparent solubility, with the initially slower dissolution of $AZ1_{RRR}$ likely arising from a more polydisperse particle size since it was not ball-milled. Indeed, SEM images (Figure 2.12c) show that this sample contains some larger particles. This may also explain the greater variation between individual repeats in the early time-points. After 30 minutes of dissolution, the $AZ1_{RRR}$ sample began to overlap with the dissolution profiles of the other two amorphous form A solids and the independent repeats become much more similar. Again, amorphous form B has a much flatter dissolution profile and much lower solubility than all the others. This behaviour may well be an example of *pseudo*-polyamorphism in which different amorphous forms, prepared in different ways, exhibit different physical properties without an observed first order phase transition in between them.[58] This type of phenomenon has been observed for the antibiotic roxithromycin (four different amorphous forms distinguishable by their particle morphology, thermodynamics and dissolution behaviour[59]), simvastatin (cryo-milling and quench-cooling of the melt[60]), the diuretic hydrochlorothiazide (three distinct amorphous forms prepared by spray-drying, quench-cooling and ball milling[61]) and the antihypertensive drug valsartan (two amorphous forms distinguished by solid-state NMR and dissolution tests[62]). In contrast, amorphous celecoxib prepared in different ways gives materials exhibiting similar physicochemical properties.[63] The existence of polyamorphism represents both a challenge and an interesting opportunity in pharmaceutical intellectual property and further highlights the complexity of the solid forms landscape of PROTACs.[64]

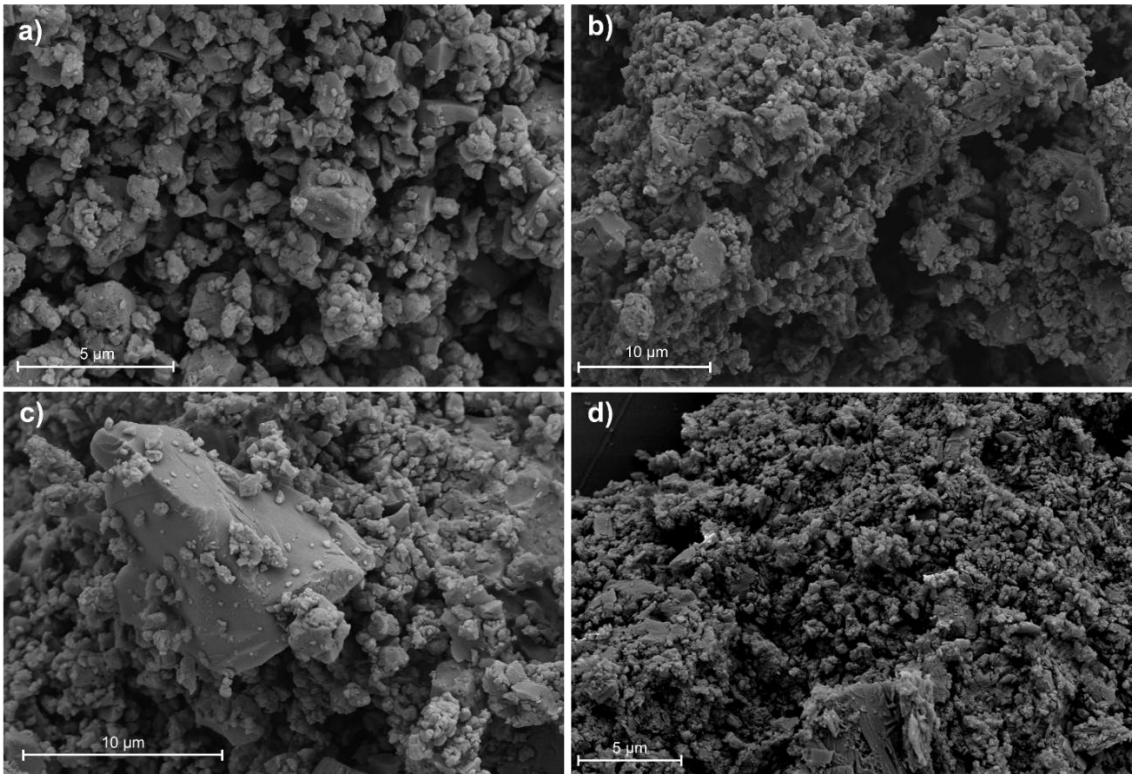

Figure 2.12. SEM images of a) $AZ1_{MIX}$ ball-milled, b) $AZ1_{RRS}$ ball-milled, c) $AZ1_{RRR}$ as synthesised and d) desolvated Form 2. While the milled samples are very similar with most particles between 1 – 5 µm in length, $AZ1_{RRR}$ shows greater polydispersity with the presence of larger particles above 10 µm.

2.4 Conclusion

PROTAC compounds such as AZ1 are poorly crystallizable and their slow crystal growth kinetics hinder the discovery of crystalline forms, even by high-throughput crystallisation techniques. When AZ1 crystals were obtained by larger scale crystallisation techniques, only one crystal was suitable for structural analysis using synchrotron-source X-ray diffraction and another microcrystalline powder was suitable only for analysis using electron diffraction. These analyses revealed two AZ1 crystal structures built almost entirely on dispersive interactions such as aliphatic stacking with very low importance of hydrogen bonding, and with similarly elongated crystal conformations to maximize surface area for dispersive interactions. The generally poor crystallisability and slow growth kinetics of AZ1 can be explained by the lack of strong, directional interactions present and the reliance instead on the sum of many weak, non-directional interactions. AZ1 Forms 1 and 3 have two of the highest lattice energies in the CSD-drugs subset yet have among the lowest lattice energy per atom in the same subset of structures, reflecting their inability to optimise strong, directional interactions and explaining why they have poor solubility and high melting points. Like similarly large drugs in the subset,

AZ1 crystallises in two solvate forms of which at least one is a channel solvate containing voids, exemplifying the poor ability of bRo5 compounds to densely pack in the crystalline phase. Thermal and spectral characterisation suggest that Form 2 may have a similar channel solvate structure to Form 3, and that not all forms are equally capable of accommodating different stereoisomers. AZ1 may also exhibit *pseudo*-polyamorphism, with amorphous solids produced by desolvating Form 2 crystals displaying very different dissolution characteristics to those produced by milling the anhydrous Form 1 crystals. This study demonstrates how standard solid-form screening approaches for small-molecule drugs may be insufficient for more complex bRo5 compounds such as PROTACs. Given their crystallisation challenges, the pharmaceutical industry may need to recalibrate its expectations around the time and effort required to explore these compounds' solid form landscapes, and more advanced methods that combine the efficiency of high-throughput screening with the control of conventional crystallisation may be essential for developing PROTAC drug products.

2.5 References

1. A. J. Cruz-Cabeza, S. M. Reutzel-Edens and J. Bernstein, *Chem. Soc. Rev.*, 2015, **44**, 8619–8635.
2. H. G. Brittain, *Polymorphism in pharmaceutical solids*, Dekker: New York, 1999, vol. 95.
3. B. C. Hancock and M. Parks, *Pharm. Res.*, 2000, **17**, 397–404.
4. M. Saifee, N. Inamdar, D. L. Dhamecha and A. A. Rathi, *Int. J. Health Res.*, 2010, **2**, 291–306.
5. K. Suresh, T. Mehta, V. Thakrar and R. G. Sharma, *Cryst. Growth Des.*, 2025, **25**, 1282–1292.
6. J. Bernstein and J. MacAlpine, *Polymorphism in the Pharmaceutical Industry: Solid Form and Drug Development*, Wiley-VCH, 2019.
7. E. H. Lee, *Asian J. Pharm. Sci.*, 2014, **9**, 163–175.
8. Q. Shi, F. Li, S. Yeh, S. M. Moinuddin, J. Xin, J. Xu, H. Chen and B. Ling, *AAPS PharmSciTech*, 2022, **23**, 1–19.
9. R. Iyer, V. P. Jovanovska, K. Berginc, M. Jaklič, F. Fabiani, C. Harlacher, T. Huzjak and M. V. Sanchez-Felix, *Pharmaceutics*, 2021, **13**, 1682.
10. R. Mizoguchi, H. Waraya and Y. Hirakura, *Mol. Pharm.*, 2019, **16**, 2142–2152.
11. D. Zhou, G. G. Z. Zhang, D. Law, D. J. W. Grant and E. A. Schmitt, *Mol. Pharm.*, 2008, **5**, 927–936.
12. P. J. Marsac, H. Konno and L. S. Taylor, *Pharm. Res.*, 2006, **23**, 2306–2316.
13. C. Bhugra and M. J. Pikal, *J. Pharm. Sci.*, 2008, **97**, 1329–1349.
14. P. H. Poole, T. Grande, C. A. Angell and P. F. McMillan, *Science*, 1997, **275**, 322–323.
15. A. Ha, I. Cohen, X. Zhao, M. Lee and D. Kivelson, *J. Phys. Chem.*, 1996, **100**, 1–4.
16. M. Zhu, J. Q. Wang, J. H. Perepezko and L. Yu, *J. Chem. Phys.*, 2015, **142**, 244504.
17. A. Mullard, *Nat. Rev. Drug Discov.*, 2021, **20**, 247–250.
18. D. García Jiménez, M. Rossi Sebastiano, M. Vallaro, V. Mileo, D. Pizzirani, E. Moretti, G. Ermondi and G. Caron, *J. Med. Chem.*, 2022, **65**, 12639–12649.

19. Y. Atilaw, V. Poongavanam, C. Svensson Nilsson, D. Nguyen, A. Giese, D. Meibom, M. Erdelyi and J. Kihlberg, *ACS Med. Chem. Lett.*, 2021, **12**, 107–114.
20. S. He, G. Dong, J. Cheng, Y. Wu and C. Sheng, *Med. Res. Rev.*, 2022, **42**, 1280–1342.
21. M. Békés, D. R. Langley and C. M. Crews, *Nat. Rev. Drug Discov.*, 2022, **21**, 181–200.
22. A. B. Anane-Adjei, E. Jacobs, S. C. Nash, S. Askin, R. Soundararajan, M. Kyobula, J. Booth and A. Campbell, *Int. J. Pharm.*, 2022, **614**, 121387.
23. R. P. Nowak, S. L. Deangelo, D. Buckley, Z. He, K. A. Donovan, J. An, N. Safaee, M. P. Jedrychowski, C. M. Ponthier, M. Ishoey, T. Zhang, J. D. Mancias, N. S. Gray, J. E. Bradner and E. S. Fischer, *Nat. Chem. Biol.*, 2018, **14**, 706–714.
24. M. S. Gadd, A. Testa, X. Lucas, K. H. Chan, W. Chen, D. J. Lamont, M. Zengerle and A. Ciulli, *Nat. Chem. Biol.*, 2017, **13**, 514–521.
25. *WIPO Pat.*, Estrogen Receptor Degrading PROTACs, WO2020201080 (A1), 2020.
26. G. M. Sheldrick, *Acta Crystallogr. A*, 2008, **64**, 112–122.
27. O. V. Dolomanov, L. J. Bourhis, R. J. Gildea, J. A. K. Howard and H. Puschmann, *J. Appl. Crystallogr.*, 2009, **42**, 339–341.
28. A. Saha, S. S. Nia and J. A. Rodríguez, *Chem. Rev.*, 2022, **122**, 13883–13914.
29. F. H. Allen and I. J. Bruno, *Acta Cryst. B*, 2010, **66**, 380–386.
30. P. B. Klar, Y. Krysiak, H. Xu, G. Steciuk, J. Cho, X. Zou and L. Palatinus, *Nat. Chem.*, 2023, **15**, 848–855.
31. P. Evans, *Acta Crystallogr. D Biol. Crystallogr.*, 2006, **62**, 72-82.
32. P. R. Evans, and G. N. Murshudov, *Acta Crystallogr. D Biol. Crystallogr.*, 2013, **69**, 1204-1214.
33. M. D. Winn, C. C. Ballard, K. D. Cowtan, E. J. Dodson, P. Emsley, P. R. Evans, R. M. Keegan, E. B. Krissinel, A. G. W. Leslie, A. McCoy, S. J. McNicholas, G. N. Murshudov, N. S. Pannu, E. A. Potterton, H. R. Powell, R. J. Read, A. Vagin, K. S. Wilson, *Acta Crystallogr. D Biol. Crystallogr.*, 2011, **67**, 235-242.
34. G. Winter, *J. Appl. Cryst.,* 2010, **43**, 186-190.
35. G. Winter, D. G. Waterman, J. M. Parkhurst, A. S. Brewster, R. J. Gildea, M. Gerstel, L. Fuentes-Montero, M. Vollmar, T. Michels-Clark, I. D. Young, N. K. Sauter, G. Evans, *Acta Crystallogr. D Struct. Biol.*, 2018, **74**, 85-97.
36. G. M. Sheldrick, *Acta Crystallogr. C Struct. Chem.*, 2015, **71**, 3–8.
37. A. Halme, M. J. Quayle, S. O. Nilsson Lill, A. Pettersen, M. Fransson and C. Boissier, *Cryst. Growth Des.*, 2019, **19**, 3670–3680.
38. M. J. Frisch et al., Gaussian 16 Revision C.01, 2016, Gaussian Inc., Wallingford CT
39. P. R. Spackman, M. J. Turner, J. J. McKinnon, S. K. Wolff, D. J. Grimwood, D. Jayatilaka and M. A. Spackman, *J. Appl. Crystallogr.*, 2021, **54**, 1006–1011.
40. A. Gavezzotti, *Z. Kristallogr.*, 2005, **220**, 499–510.
41. P. R. Spackman, A. J. Walisinghe, M. W. Anderson and J. D. Gale, *Chem. Sci.*, 2023, **14**, 7192–7207.
42. C. F. Mackenzie, P. R. Spackman, D. Jayatilaka and M. A. Spackman, *IUCrJ*, 2017, **4**, 575–587.
43. S. P. Thomas, P. R. Spackman, D. Jayatilaka and M. A. Spackman, *J. Chem. Theory Comput.*, 2018, **14**, 1614–1623.
44. A. D. Becke, *J. Chem. Phys.*, 1993, **98**, 5648–5652.
45. B. P. Pritchard, D. Altarawy, B. Didier, T. D. Gibson and T. L. Windus, *J. Chem. Inf. Model.*, 2019, **59**, 4814–4820.
46. P. R. Spackman, M. A. Spackman and J. D. Gale, *IUCrJ*, 2023, **10**, 754–765.
47. D. C. Apperley, R. K. Harris and P. Hodgkinson, *Solid-State NMR: Basic Principles and Practice*, Momentum Press, New York, 2012.
48. A. R. Tyler, R. Ragbirsingh, C. J. McMonagle, P. G. Waddell, S. E. Heaps, J. W. Steed, P. Thaw, M. J. Hall and M. R. Probert, *Chem*, 2020, **6**, 1755–1765.
49. J. P. Metherall, P. A. Corner, J. F. McCabe, M. J. Hall and M. R. Probert, *Acta Crystallogr. B Struct. Sci. Cryst. Eng. Mater.*, 2024, **80**, 4–12.

50. H. E. Straker, L. McMillan, L. Mardiana, G. R. Hebberd, E. Watson, P. G. Waddell, M. R. Probert and M. J. Hall, *Cryst. Eng. Comm.*, 2023, **25**, 2479–2484.
51. C. F. Macrae, I. Sovago, S. J. Cottrell, P. T. A. Galek, P. McCabe, E. Pidcock, M. Platings, G. P. Shields, J. S. Stevens, M. Towler and P. A. Wood, *J. Appl. Cryst.*, 2020, **53**, 226–235.
52. A. L. Spek, *Acta Cryst.*, 2015, **71**, 9–81.
53. M. J. Bryant, S. N. Black, H. Blade, R. Docherty, A. G. P. Maloney and S. C. Taylor, *J. Pharm. Sci.*, 2019, **108**, 1655–1662.
54. D. C. Neil Swindells, P. S. White, and J. A. Findlay, *Can. J. Chem.*, 1978, **56**, 2491–2492.
55. G. L. B. de Araujo, M. Zeller, D. Smith, H. Nie, S. R. Byrn, *Cryst. Growth Des.,* 2016, **16**, 10, 6122–6130
56. *WIPO Pat.*, Quinazoline anhydrate forms, WO2009079547 (A1), 2009.
57. T. K. Neklesa, J. D. Winkler and C. M. Crews, *Pharmacol. Ther.*, 2017, **174**, 138–144.
58. D. P. Elder, J. E. Patterson and R. Holm, *J. Pharm. Pharmacol.*, 2015, **67**, 757–772.
59. M. Milne, W. Liebenberg and M. E. Aucamp, *Int. J. Pharm.*, 2016, **498**, 304–315.
60. K. A. Graeser, C. J. Strachan, J. E. Patterson, K. C. Gordon and T. Rades, *Cryst. Growth Des.*, 2008, **8**, 128–135.
61. I. C. B. Martins, A. S. Larsen, A. I. Madsen, O. A. Frederiksen, A. Correia, K. M. Ø. Jensen, H. S. Jeppesen and T. Rades, *Chem. Sci.*, 2023, **14**, 11447–11455.
62. M. Skotnicki, D. C. Apperley, J. A. Aguilar, B. Milanowski, M. Pyda and P. Hodgkinson, *Mol. Pharm.*, 2016, **13**, 211–222.
63. M. Wang, O. Aalling-Frederiksen, A. Madsen, K. M. Ø. Jensen, M. R. V. Jørgensen, J. Gong, T. Rades and I. C. B. Martins, *Int. J. Pharm.*, 2024, **661**, 124470.
64. B. Gellie, *Disordered Pharmaceutical Materials*, Wiley-VCH, Weinheim, 2016.

3. Developing Multi-Component Solid Formulation Strategies for PROTAC Dissolution Enhancement

3.1 Introduction

Multicomponent solids, which can offer advantageous chemical and physical characteristics compared to a pure active pharmaceutical ingredient (API) without modifying its chemical structure or pharmacology,[1–4] usually consist of two molecular components bonded by non-covalent interactions such as hydrogen bonding, π-π stacking, van der Waals forces or halogen-bonding, and as such they are often designed using an understanding of the possible supramolecular motifs that can form between the two components.[1] The resulting solids can be either crystalline or amorphous, as introduced in sections 1.1.3 and 1.1.4. The latter possess no long-range order but often show improved solubility and/or dissolution rate compared to their co-crystalline counterpart through their higher free energy.[4–6] Compared to an inherently unstable pure amorphous drug, co-amorphous formulations are often less likely to recrystallise into the crystalline drug form and lose their dissolution advantage.[7] The glass transition temperature (T_g) of the resulting amorphous solid is usually between that of the two compounds, which would suggest greater molecular mobility and lower kinetic stability than the single component with the higher T_g, however the co-amorphous phase is usually further physically stabilised by intermolecular interactions between components. This is in part because the formation of strong heterodimer interactions can disrupt short-range molecular ordering of one component, where the formation of homodimers often precedes recrystallisation and the loss of the dissolution advantage provided by the co-amorphous phase.[8] Strong intermolecular interactions between components in a co-amorphous solid can usually be identified by the T_g value deviating from the theoretical T_g calculated via the Gordon-Taylor equation,[9–12] which predicts the T_g of a homogeneous co-amorphous solid assuming no specific interactions between components (ideal mixing) and ideal free volume additivity of the two components.[8] The greater physical stability that they impart allows the more soluble and faster dissolving amorphous solid to persist for a longer duration in contact with solution, maintaining supersaturation of the API for a longer duration before crystallisation. This type of dissolution kinetics is often referred to as a “spring and parachute”. In some systems, such as co-amorphous naproxen/cimetidine, heterodimer formation involving hydrogen bonds has also been

shown to cause synchronous dissolution of the individual components as well as enhancing the dissolution rate.[13] Hence, producing a co-amorphous formulation involving strong non-covalent bonds between a poorly soluble drug that has a low dissolution rate and a more soluble co-former may facilitate dissolution improvement of the low-solubility API, even compared to its own pure amorphous form.

Co-amorphous formulations using low molecular weight excipients can include non-pharmaceutically active, generally-recognised-as-safe (GRAS) compounds. Alternatively, a second drug molecule can be used to provide a dual-action pharmaceutical formulation, such as co-amorphous indomethacin / paracetamol,[14] naproxen / cimetidine,[13] and indomethacin / naproxen,[15] which all show greater physical stability and enhanced dissolution rates as well as evidence of intermolecular interactions between components. Other drug-drug co-amorphous solids such as simvastatin / glipizide[16] and ritonavir / indomethacin[17] show dissolution and stability improvements without any evidence of specific intermolecular interactions. However, in both these cases, while the dissolution rate of one drug component was increased compared to its pure amorphous form, the second component did not see such an increase due to the lack of synchronous dissolution. Co-amorphous formulations containing polymer excipients instead of small molecules are usually referred to as amorphous solid dispersions (ASDs), in which the stabilisation of the amorphous API depends on its solubility in the carrier polymer.[18] Below the miscibility limit, the drug is molecularly dispersed and stabilised against recrystallisation by physical separation of the drug molecules between polymer chains.[18] The polymer matrix usually raises the T_g of the ASD compared to the pure amorphous drug, inhibiting crystallisation through a reduction of molecular motion to impart greater physical stability,[19] and it has been shown that differences in the types of intermolecular interactions between a given polymer and drug affect both the ASD dissolution performance and the maximum drug-loading (DL) capacity.[5,19,20] Rapid dissolution of drug from an ASD produces a supersaturated solution with an enhanced free drug concentration that can exceed even the amorphous API solubility in some systems; in these cases, the drug separates from the bulk aqueous phase via liquid-liquid phase separation to produce colloidal nanoparticles, which act as a reservoir to maintain the elevated drug concentration.[4,20,21] This behaviour is generally at lower drug loadings where drug and polymer are released congruently at the rate of polymer dissolution – the limit of this congruent release is referred to as the “LoC” of the ASD formulation. The method used to prepare ASDs with acidic polymers has been shown to have a strong impact on the degree of proton transfer between drug and polymer, particularly for combinations of drug and polymer that differ in pK_a by several log units, where the greater charge separation between drug and polymer causes greater aqueous solubility.[22] ASDs of the malaria drug lumefantrine and poly(acrylic acid) (PAA)

produced by slurry conversion showed 70 % protonation of the drug by the polymer in the resulting solid, whereas the same ASDs prepared by melt quenching showed only 20 % protonation and had sixfold lower apparent solubility in simulated gastric fluid.[22] On the downside, ASDs are also quite often hygroscopic and with water ingress can cause a reduction in T_g (plasticisation) that can lead to phase separation of the co-amorphous solid and drug recrystallisation.[23] Furthermore, the DL of many ASDs is unable to exceed 25 % w/w due to the limited miscibility of the drug with polymers, meaning that large volumes of polymer are required to produce the final dosage forms. Co-amorphous formulations with low molecular weight excipients are usually produced at a 1:1 molar ratio, by comparison.[24] Designing an ASD formulation with optimised polymer selection and drug loading also relies solely on experimental information and cannot currently benefit from *in silico* screening protocols such as COSMOtherm[25] which aid in the development of low molecular-weight multi-component solids.[26]

While there are no reports in the literature of PROTAC co-amorphous formulations using low molecular weight co-formers, there are several recent examples of successfully applying ASD formulations to enhance the solubility of PROTAC compounds. Pöstges et al. first produced ASD formulations of an initially amorphous androgen-receptor PROTAC 'ARCC-4' at 10 and 20 % DL with hydroxypropyl methyl cellulose acetate succinate (HPMCAS) and Eudragit polymers by vacuum compression moulding, with non-sink dissolution studies showing a pronounced supersaturation enhancement without drug precipitation.[27] Hofmann et al. also demonstrated significant supersaturation enhancements for spray-dried ASDs of an initially amorphous cereblon (CRBN) PROTAC with Soluplus and Eudragit polymers at 10 % DL, compared to the pure amorphous API.[28] Mareczek et al. later demonstrated dissolution enhancements for spray-dried ASDs of both an initially semi-crystalline PROTAC 'ARV-110' and an initially amorphous PROTAC 'SelDeg51' with poly(vinyl alcohol) (PVA) at 30 % DL, indicating that the ASD formulations using the crystalline API were physically stable for at least 4 weeks.[29] Most recently, Zhang et al. studied ASDs of a CRBN PROTAC with HPMCAS, Eudragit and Soluplus prepared at 5, 10 and 20 % DL by solvent evaporation, confirming the presence of drug-polymer hydrogen bonding interactions using FTIR and showing that HPMCAS ASDs could be produced as high as 40 % DL, although ASDs at higher drug loading showed poor dissolution performance.[30] They also showed, however, that the limited dissolution enhancement of the high DL ASDs could be improved greatly by adding sodium dodecyl sulfate as a surfactant to produce a ternary ASD system.[30] However, these studies did not show how the dissolution enhancement of a given PROTAC ASD varied with the ASD preparation method used, and with the exception of work by Mareczek et al., whether the selected preparation method could be applied successfully to more than one PROTAC compound. Furthermore, the previous studies

have not investigated the slurry conversion method for producing ASDs, which was shown by Neusaenger et al. to produce lumefantrine–PAA ASDs with the highest degree of drug protonation and therefore the greatest aqueous dissolution enhancement compared to other methods.[22] In this chapter, the dissolution behaviour of co-amorphous formulations of a CRBN PROTAC 'AZ1' using either small-molecule or polymeric excipients are compared, and the nature of non-covalent interactions between drug and excipient components is investigated. The effects of polymer selection, DL and ASD preparation methods on the dissolution performance of AZ1 ASDs are also investigated and the generality of the ASD formulation procedure across four structurally distinct CRBN PROTACs is established.

3.2 Experimental

Materials and general methods. PROTAC compounds 'AZ1-4' were supplied by AstraZeneca and were prepared according to previously published methodology.[31] AZ1 amorphous form A was prepared by neat milling of AZ1 powder as synthesised using a Retsch MM200 Mixer Mill for 20 mins at 20 Hz in a stainless-steel milling jar. Hydroxypropyl methyl cellulose acetate succinate (HPMCAS-LG – AQOAT®) was supplied by Shin-Etsu Chemicals (Tokyo, Japan). Polyvinylpyrrolidone vinyl acetate (PVPVA – Kollidon VA64) was supplied by BASF Corporation (Ludwigshafen, Germany). All other chemicals and solvents were available from commercial sources and used without further purification. Infrared spectra were recorded between 4000 and 550 cm^{-1} using a Perkin Elmer 100 FT-IR spectrometer with a μATR attachment. Unless otherwise specified, X-ray powder diffraction (XRPD) patterns were collected at room temperature using a Bruker AXS D8 Advance GX003410 diffractometer with a Lynxeye Soller PSD detector, using Cu Kα radiation at a wavelength of 1.5406 Å and collecting from $2° \leq 2\theta \leq 40°$.

COSMOconf and COSMOtherm calculations. COSMOconf and COSMOtherm (version 23.0.0) were used to calculate excess enthalpy/mixing enthalpy of the interaction between drug and co-formers, using up to ten of the lowest energy conformers generated by COSMOconf. Drug and co-formers were entered in SMILES notation to calculate the sigma profiles. The optimised geometries of the structures were obtained using the TZVP-FINE parametrization to obtain the necessary COSMO files. Calculation of the interaction between drug and co-former components was performed using COSMO (conductor-like screening model) software using BP_TZVPD_FINE_19 parametrization. The polar and hydrogen bond interaction energies between the components are quantified based on the surface screening charge densities, which result

from a quantum chemical continuum solvation calculation using COSMO.[24,32] The strength of interactions between the two components, as compared with that of the pure reactants, is estimated via mixing enthalpy. Mixing enthalpy is a rough approximation to the free energy of interaction. The greater (more negative) the mixing enthalpy, the greater the hetero (drug – co-former) interactions, and the greater the probability of co-crystal formation.

Mechanochemical milling of PROTACs. PROTAC compounds AZ1-4 were amorphised and reduced to smaller, homogeneous particles for dissolution studies by adding PROTAC powder to a 5 mL agate grinding jar with one agate grinding ball (6.4 mm diameter) and grinding with a Retsch MM200 Mixer Mill at 20 Hz for 20 minutes. The resulting solids were characterised by XRPD, modulated DSC (mDSC), TGA, FTIR and SEM.

AZ1 co-crystal screening. AZ1 (5 mg) and co-formers were mixed in an equimolar ratio in HPLC vials and ethyl acetate (5 µL) was added before liquid-assisted grinding for 1 hour at 600 rpm with one stainless steel ball bearing in a Fritsch Pulverisette 7 planetary ball mill. The resulting solids were analysed by XRPD using a Rigaku SmartLab diffractometer with Cu Kα radiation at a wavelength of 1.5406 Å and collecting from 3° ≤ 2θ ≤ 40°. Fully amorphous solids were analysed further by mDSC.

Preparation of AZ1 co-amorphous salts. Salts of AZ1 with oxalic acid, m-nitrobenzoic acid and α-ketoglutaric acid were prepared by adding AZ1 and co-former (50 mg total mass) in an equimolar ratio to a 5 mL stainless steel grinding jar with one stainless steel grinding ball (6.4 mm diameter) and liquid-assisted grinding with a Retsch MM200 Mixer Mill at 20 Hz for 20 minutes. The resulting solids were analysed by XPRD, heat-cool-heat mDSC, TGA and FTIR.

Preparation of ASDs by slurry conversion. Powders of PROTAC compounds AZ1-4 and polymers were mixed in a vial at the intended DL (% w/w) and dichloromethane-ethanol (1:1 v/v) was added to the powder at a solid/liquid ratio of 1:4 w/w. Each batch contained approximately 50 – 60 mg of PROTAC compound. The slurries were stirred magnetically for 5 minutes at 70 °C in a water bath and dried under vacuum at room temperature for 24 hours. The solid products were added to a 5 mL agate grinding jar with one agate grinding ball (6.4 mm diameter) and ground with a Retsch MM200 Mixer Mill at 20 Hz for 20 minutes. The resulting solids were characterised by XRPD, mDSC, TGA, FTIR and SEM.

Preparation of ASDs by mutual solvent evaporation. AZ1 ASDs using HPMCAS and PVPVA were generated by dissolving both polymer and PROTAC components in dichloromethane-ethanol (4:1 v/v) before evaporating the solvent in an oven at 70 °C

overnight, producing ASDs at 10, 20, 30 and 40% w/w DL. Powder masses and solvent volumes were used such that all ASDs contained the same mass of AZ1 and had the same surface area, varying in the total ASD mass.

Thermal analysis. Differential scanning calorimetry (DSC) samples were prepared using Tzero standard pans and lids with pinholes and analysed using a TA Instruments Q2000 differential scanning calorimeter. Single-ramp modulated DSC samples were first equilibrated at 25 °C then heated to 200 °C using a modulated method with a scanning speed of 3 °C/min, an amplitude of ± 1 °C and a period of 60 s. Heat-cool-heat mDSC samples were heated from 20 °C to 200 °C, cooled to 25 °C and re-heated to 200 °C. The instrument was calibrated using indium standard prior to analysis, with a melting point onset of 156.89 °C and a heat capacity of 33.971 J/g. Thermogravimetric analysis (TGA) samples were analysed using platinum pans and a TA Instruments Discovery thermogravimetric analyser, heating from 25 °C to 200 °C at 20 °C/min.

Scanning electron microscopy (SEM). SEM samples were prepared by adding solids to polycarbonate wafers and coating with 25 nm of platinum using a Cressington 328 Ultra High-Resolution EM Coating System. The images were obtained using a Carl Zeiss Sigma 300 VP FEG SEM microscope, operated at 5 kV using an in-lens detector.

Ultra Performance Liquid Chromatography (UPLC) analysis. The concentrations of PROTAC compounds were determined using a Waters ARC UPLC -MC206 system with an ACQUITY UPLC BEH C18 column (130 Å, 1.7 µm, 2.1 mm X 50 mm, Waters Corporation, UK) and a UV detection wavelength of 300 nm. The mobile phase of acetonitrile/water varied in a gradient method from 95/5 v/v to 5/95 v/v at a flow rate of 1 mL/min.

PROTAC solubility. The thermodynamic solubilities of amorphous PROTACs AZ1-4 in fasted state simulated intestinal fluid (FaSSIF) were determined by adding an excess of amorphous PROTAC to 1 mL of solvent and stirring at 1,000 rpm for 24 hours. The samples were then centrifuged for 30 minutes at 31,000 × *g* and the supernatants were diluted appropriately to maintain absorbance readings within the UPLC standard curve. The concentration of PROTAC was determined by UPLC analysis, converting peak area values to concentrations via a calibration curve. Solid residues were taken from each slurry after 24 hours and analysed by XPRD to confirm that the PROTACs were still amorphous.

Non-sink powder dissolution measurements. Dissolution experiments were performed in duplicate for each sample. The powders were sieved using standard mesh sieves to remove particles larger than 150 µm. Vessels were charged with accurately weighed masses of the amorphous PROTAC and ASD solids before adding the correct

volume (approximately 10 mL) of pre-warmed FaSSIF at 37 °C such that all slurries were accurately at ten times the measured solubility limit of the amorphous PROTAC. Slurries were stirred at 400 rpm for 2 hours. Aliquots of the slurries were removed at each time point, centrifuged for 30 minutes at 31,000 × *g*, and the neat supernatant was analysed to maintain absorbance readings within the UPLC standard curve. The concentrations of PROTAC were determined by UPLC analysis, converting peak area values to concentrations via a calibration curve. The pH of each dissolution slurry was recorded at the end of the experiment to confirm that it had not varied outside of the specification of the buffer. Solid residues were taken from each slurry at the end of the dissolution experiment and analysed by XRPD to confirm that the samples had not recrystallised during the experiment.

ASD conditioning. Samples of ASDs found to provide a dissolution advantage over the pure drug substance were conditioned in a desiccator at 40 °C and 75% relative humidity (RH) using a saturated NaCl solution,[34] and the resulting solids were analysed by XRPD, modulated DSC, and TGA.

3.3 Results and Discussion

In Chapter 2 it was shown that PROTAC compound AZ1 is able to crystallise in an anhydrous form and two solvate forms; however, it is very difficult to grow these crystals, and the vast majority of crystallisation attempts yielded amorphous material.[31,34] Amorphous solids prepared by either milling an AZ1 anhydrous phase or desolvating a solvate crystal also exhibit very different dissolution behaviour. In this work, only the amorphous “form A” produced by milling the anhydrous solid will be considered; a form characterised by a broad halo in the X-ray powder diffractogram and a high T_g of 160 °C. This amorphous solid has an equilibrium solubility of 48.4 ± 2.6 µg/mL in fasted state simulated intestinal fluid (FaSSIF) at 37 °C. Co-amorphous formulations of this compound with low molecular weight and polymeric excipients are compared herein. PROTAC compounds AZ2, AZ3 and AZ4 consist of the same ligand moieties as AZ1 but with different linker groups (Scheme 3.1), and are all amorphous in their as-synthesised form[31] with even higher T_g values around 170 – 174 °C. The equilibrium solubilities of AZ2, AZ3 and AZ4 in FaSSIF at 37 °C are 28.1 ± 5.2 µg/mL, 34.5 ± 7.7 µg/mL and 17.3 ± 1.6 µg/mL, respectively. Since these compounds are available in much lower quantities, only the most effective co-amorphous formulation strategy for dissolution enhancement of AZ1 was taken forward to study these PROTACs.

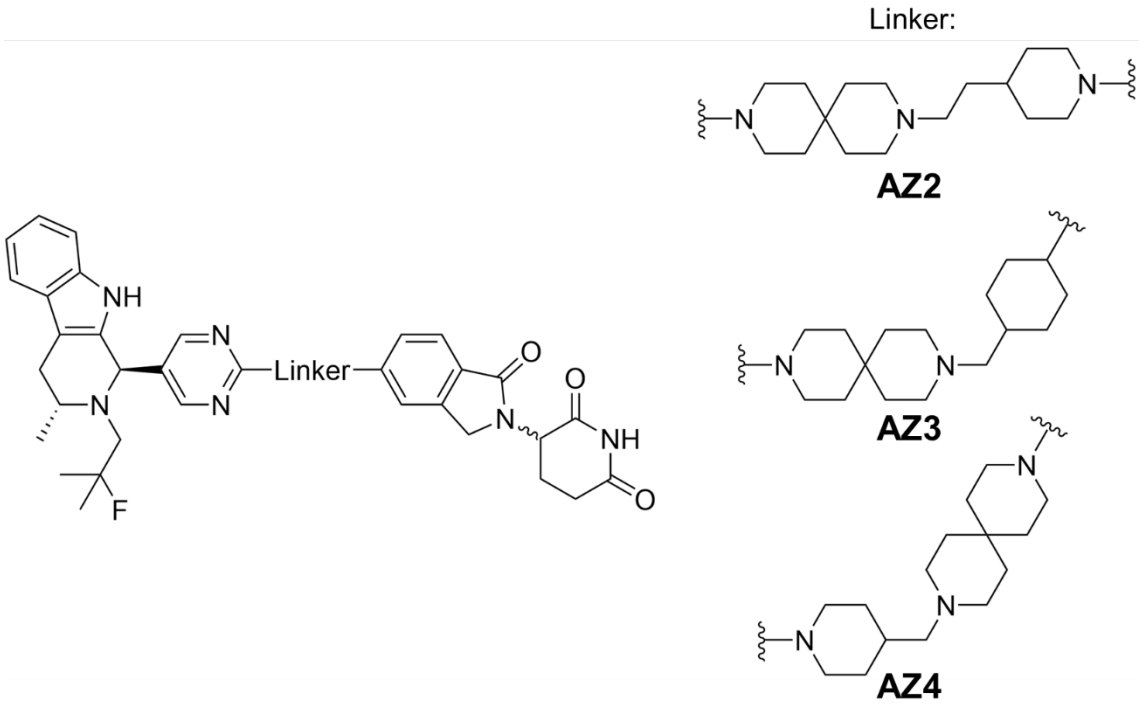

Scheme 3.1. PROTAC compounds AZ2, AZ3 and AZ4. Molecules differ from each other and AZ1 only by the structure of the linker moiety.

A list of 48 small molecules was chosen for a co-crystal screen with AZ1 based on a combination of *in silico* predictions and consideration of potential supramolecular synthons between components. Molecules previously shown to co-crystallise with lenalidomide, a drug compound that structurally resembles the CRBN-ligand moiety of AZ1, were also included in the co-crystal screen with AZ1.[35–40] The solids produced by liquid-assisted grinding (LAG) of each co-former with AZ1 in the presence of ethyl acetate were analysed by XRPD, which showed that all samples containing crystalline material of any kind contained only separate phases of the original components, either as a convolution of the powder patterns for the two starting materials or as the crystalline pattern of one component convoluted with a broad amorphous halo from the second component. All samples that produced a completely amorphous powder pattern were analysed further by modulated DSC to determine whether the amorphous solid consisted of separate, physically mixed amorphous components or a single co-amorphous phase. The presence of only one glass transition temperature (T_g) at a lower temperature than for pure AZ1 indicates that the sample is a single co-amorphous phase rather than a physical mixture of components. Nine of the forty-eight LAG experiments produced amorphous solids with a single T_g varying in breadth between the samples, indicating different degrees of heterogeneity depending on the co-former (Appendix B, Figure B1-S2).

Three of the nine co-amorphous solids with α-ketoglutaric acid (KGA), m-nitrobenzoic acid (NBA) and oxalic acid (OXA) as co-formers were chosen for scaled-up synthesis and non-sink dissolution comparison against pure AZ1 based on a combination of three criteria. Since the T_g values of AZ1 and other PROTACs are often high due to low molecular mobility and high physical stability of the amorphous phase and may be correlated to their poor dissolution performance, co-amorphous solids with the lowest T_g were favoured. The physical stability of the solids after three months was assessed by XRPD (Appendix B, Figure B3), with samples that had recrystallised into separate components over this duration deemed physically unstable and unsuitable for further study. Finally, the co-amorphous solids were ranked by the aqueous solubility of the pure co-former, based on the hypothesis that if strong intermolecular bonds can form between the co-former and PROTAC and enable synchronous dissolution, a more soluble co-former may produce a co-amorphous solid with a greater dissolution advantage over the pure API. It should be noted that a more rapidly dissolving co-former is less likely to destabilise the amorphous phase and lead to the recrystallisation of poorly crystallizable PROTACs as it would for smaller conventional drugs.[18] AZ1 has a calculated pK_a of approximately 10, while NBA, the least acidic of the three co-formers, has a pK_a of 3.5, therefore these three solids may exist in the form of co-amorphous salts, assuming that the "ΔpK_a rule" used to predict the formation of co-crystalline materials also holds true for amorphous solids. This rule states that where there is a difference of more than 2-3 log units between the pK_a of the acid and protonated base components salt formation is likely in the resulting two-component solid.[41–43] While other AZ1 co-amorphous solids such as those of saccharin and salicylic acid had a significantly lower T_g than AZ1-OXA and AZ1-KGA, the co-formers recrystallised from the solids within days. This is likely because the lower T_g indicates greater molecular mobility, and even if stabilised by drug – co-former intermolecular interactions, these amorphous glasses appear less kinetically stable overall.

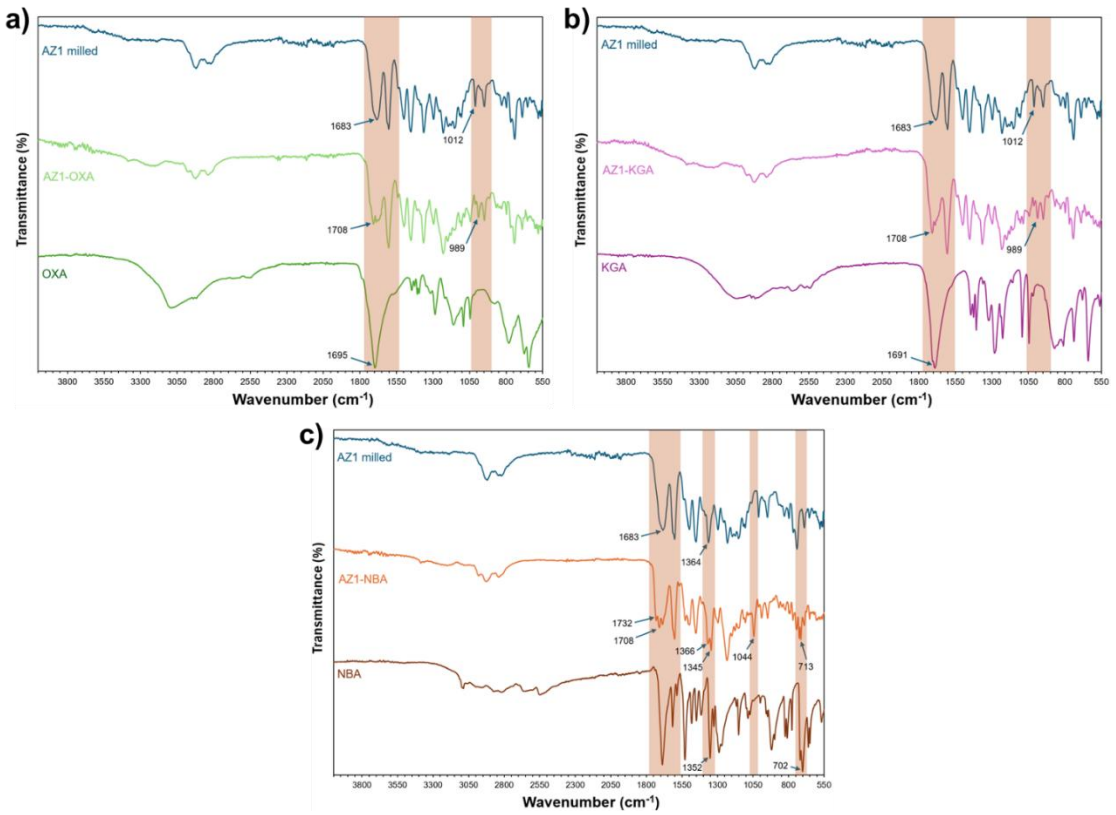

Figure 3.1. FTIR spectra of AZ1 co-amorphous solids with a) OXA, b) KGA and c) NBA compared to the pure components.

FTIR analysis (Figure 3.1) shows that despite the presence of both components in an equimolar ratio in all three co-amorphous solids, the spectra are all dominated by signals from AZ1 due to its much greater number of atoms. There are some small differences in the spectra for the AZ1-OXA and AZ1-KGA solids compared to amorphous AZ1 with relative growth in intensity and sharpening of the carboxylic acid $\nu_{(C=O)}$ band at 1708 cm^{-1} compared to the band at 1683 cm^{-1} and a change in the relative strengths of bands at 1012 and 989 cm^{-1} in the alkene $\nu_{(C=C)}$ bending region. However, the spectrum of AZ1-NBA contains many more features that are shifted relative to the pure components. The presence of a new carboxylic acid $\nu_{(C=O)}$ band at 1732 cm^{-1}, shifts of 3 – 20 cm^{-1} in both directions for the nitro $\nu_{(N-O)}$ stretches and shifts of 6 – 14 cm^{-1} in both directions for the alkene $\nu_{(C=C)}$ bending modes suggest that the molecules may be engaged in hydrogen bonding interactions via both the carboxylic acid and nitro moieties of NBA, most likely with the carbonyl and imide moieties in AZ1. There is no strong evidence to suggest that intermolecular interactions form between AZ1 and OXA or KGA, with these two co-amorphous solids having very similar spectra to each other.

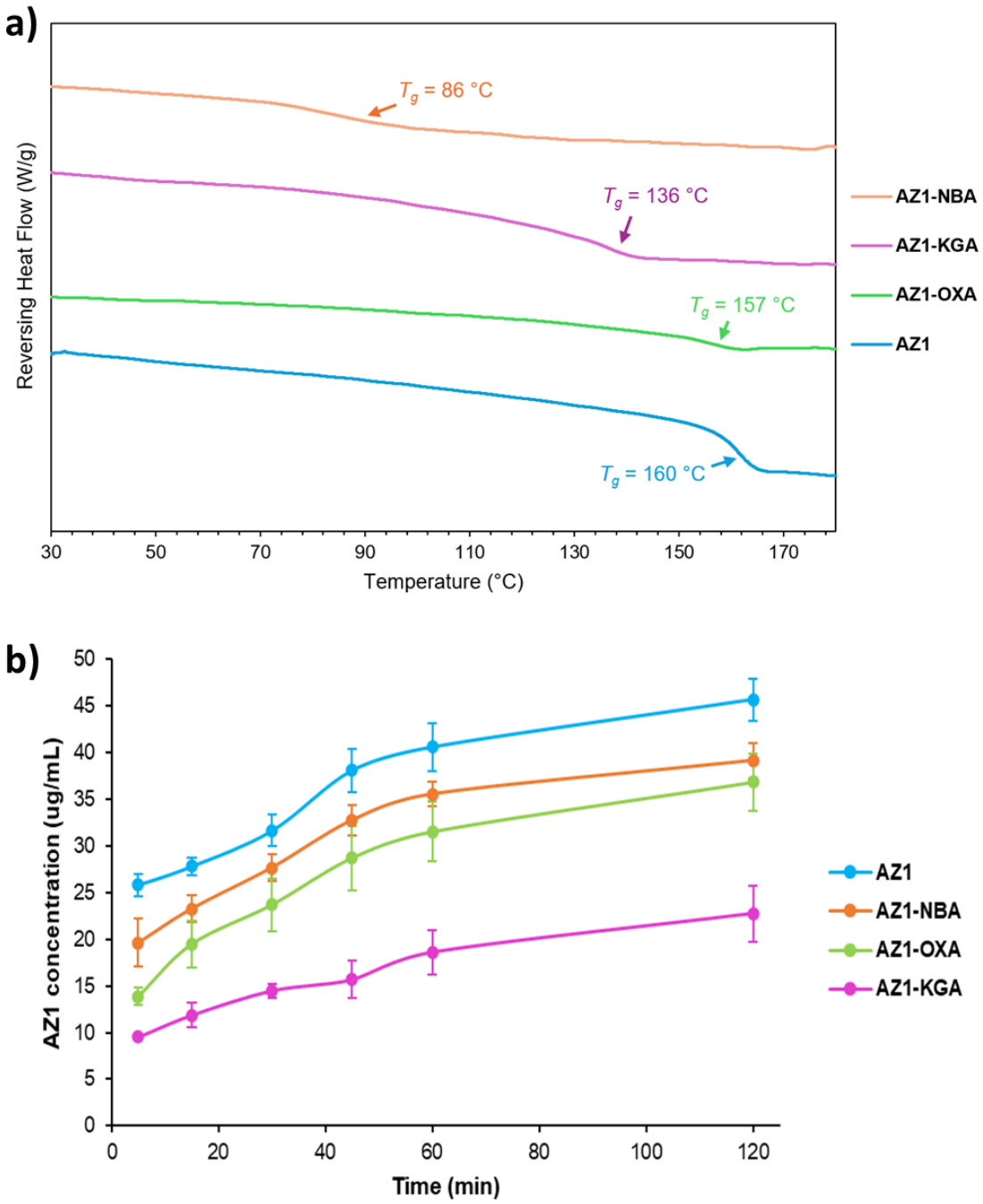

Figure 3.2. a) Modulated DSC thermograms for AZ1 and its co-amorphous salts with OXA, NBA and KGA. The T_g of AZ1-KGA and AZ1-NBA are significantly reduced compared to the pure drug. b) Non-sink dissolution profiles of amorphous AZ1 and co-amorphous salts with NBA, OXA and KGA over 2 hours in fasted state simulated intestinal fluid (FaSSIF) at 37 °C, using a 10-fold non-sink condition compared to the amorphous solubility. Dissolution experiments were run in duplicate with average concentrations plotted and error bars showing the range of concentrations measured at each time point.

Modulated DSC (Figure 3.2a) shows that AZ1-NBA, AZ1-KGA and AZ1-OXA have T_g values of 86 °C, 136 °C and 157 °C respectively, with AZ1-NBA showing a relatively

broad glass transition event. While AZ1-OXA does not have a significantly lower T_g than pure AZ1, the solubility of the co-former and the physical stability of the co-amorphous solid over 3 months made it a suitable candidate for dissolution studies. AZ1-NBA, on the other hand, shows a very significant difference in T_g compared to the pure API. TGA (Appendix B, Figure B4) shows that all three solids are dry with no significant mass loss up to 120 °C, followed by gradual mass loss totalling approximately 5 % upon heating from 120 °C to 200 °C. This is likely due to samples degrading as they exceed T_g.

Non-sink dissolution profiles for amorphous AZ1 and the three co-amorphous salts over 2 hours in FaSSIF at 37 °C are shown in Figure 3.2b, allowing for discrimination between the dissolution profiles of the pure API and the co-amorphous formulations. AZ1 powder was milled via the same method used to produce the co-amorphous phases, except that no ethyl acetate solvent was used, to reduce and homogenise the particle size, and all solid samples were sieved to remove particles larger than 150 μm. For this profile and for all others presented in this chapter, dissolution data points reflect a time constant due to 30 minutes of centrifugation as detailed in section 3.2, during which further dissolution may have occurred. All three co-amorphous salts have a similar dissolution profile shape to amorphous AZ1 but at lower apparent solubilities over the 2-hour range, with AZ1-KGA exhibiting the lowest solubility at approximately 40 % of the concentration of AZ1 in solution at every timestep. This may be partly due to their larger particle sizes of roughly 10 – 60 μm as observed by SEM (Appendix B, Figure B5), being more comparable to the ripened AZ1 particles after 24 hours of slurry rather than the smaller particles initially produced by the milling process (Appendix B, Figure B6), and also because in the cases of AZ1-OXA and AZ1-KGA there are no strong drug – co-former interactions to enable synchronous dissolution despite the high aqueous solubilities of the co-formers. AZ1-NBA has the best dissolution performance of the three co-amorphous salts, which may be related to the presence of stronger intermolecular interactions between components as observed by FTIR analysis. However, even in this example, the interactions are too weak to confer a dissolution advantage compared to the pure amorphous API. Despite the relative ease of production, co-amorphous formulations with small molecule co-formers do not appear to be an effective strategy for PROTAC dissolution enhancement.

Amorphous Solid Dispersions of AZ1

Five commercial polymers commonly used in pharmaceutical products[44] were selected for preliminary screening of ASD formation with AZ1; hydroxypropyl methyl cellulose (HPMC), hydroxypropyl methyl cellulose acetate succinate (HPMCAS), poly(acrylic acid) (PAA), poly(vinyl pyrrolidone) (PVP) and poly(vinyl pyrrolidone)/vinyl acetate (PVPVA).

Small-scale ASDs were produced directly within DSC and TGA pans by solvent evaporation of drug-polymer solutions to achieve a drug loading (DL) of 10 – 40 % w/w prior to thermal analysis. HPMCAS and PVPVA reliably formed ASDs with clearly measurable T_g values, while the others produced lower quality thermal data, often with undetectable T_g events. HPMCAS and PVPVA were therefore taken forward to investigate the effects of polymer selection on the drug loading and dissolution advantage that can be achieved by ASD formulations of AZ1. HPMCAS is substituted with acetyl and succinoyl groups, resulting in an approximate pK_a of 5, while PVPVA is much less acidic with a pK_a similar to protonated AZ1 at around 9.5, providing the opportunity to study the role of polymer acidity in ASD formation and performance. The slurry conversion and solvent evaporation methods of preparing these ASDs were also compared, since the ASD preparation method has been shown to affect the degree of proton transfer between drug and polymer and therefore impact aqueous dissolution.[22]

Slurry conversion amorphous solid dispersions

All ASDs of both polymers from 10 – 40 % w/w DL prepared by the slurry conversion method showed a single T_g and an amorphous X-ray powder pattern (Appendix B, Figure B7), indicating the formation of a single co-amorphous phase. TGA (Appendix B, Figure B8-9) shows that the HPMCAS ASDs contain 0.5 % w/w residual solvent on average, even after drying. PVPVA ASDs contain even more residual solvent, with 1 – 3 % weight loss observed between 20 – 80 °C. Both HPMCAS and PVPVA ASDs show a roughly linear positive correlation between DL and T_g observed by mDSC (Figure 3.3), trending upwards towards the T_g of pure AZ1. While the measured T_g values of the PVPVA ASDs match the values calculated using the Fox relation (a simplified form of the Gordon-Taylor equation[45]) to within 1 – 2 °C, the T_g values measured for the HPMCAS ASDs are all 4 °C higher than the predicted values from 10 – 30 % DL before matching the prediction exactly at 40% DL (Appendix B, Table B1). The Fox equation assumes ideal mixing, with no excess enthalpy or entropy. A positive deviation in T_g values, such as this, is likely indicative of stronger intermolecular drug-polymer interactions in the HPMCAS ASDs up to 30 % DL, while the PVPVA ASDs behave more like ideal mixtures across the 10 – 40 % DL range. This may arise from stronger interactions between the basic API and the more acidic HPMCAS polymer compared to PVPVA. While these strong interactions may enhance dissolution performance compared to the PVPVA ASDs, work by the Taylor group has shown that they can also be correlated with a lower LoC and therefore greater potential pill burden.[5,45]

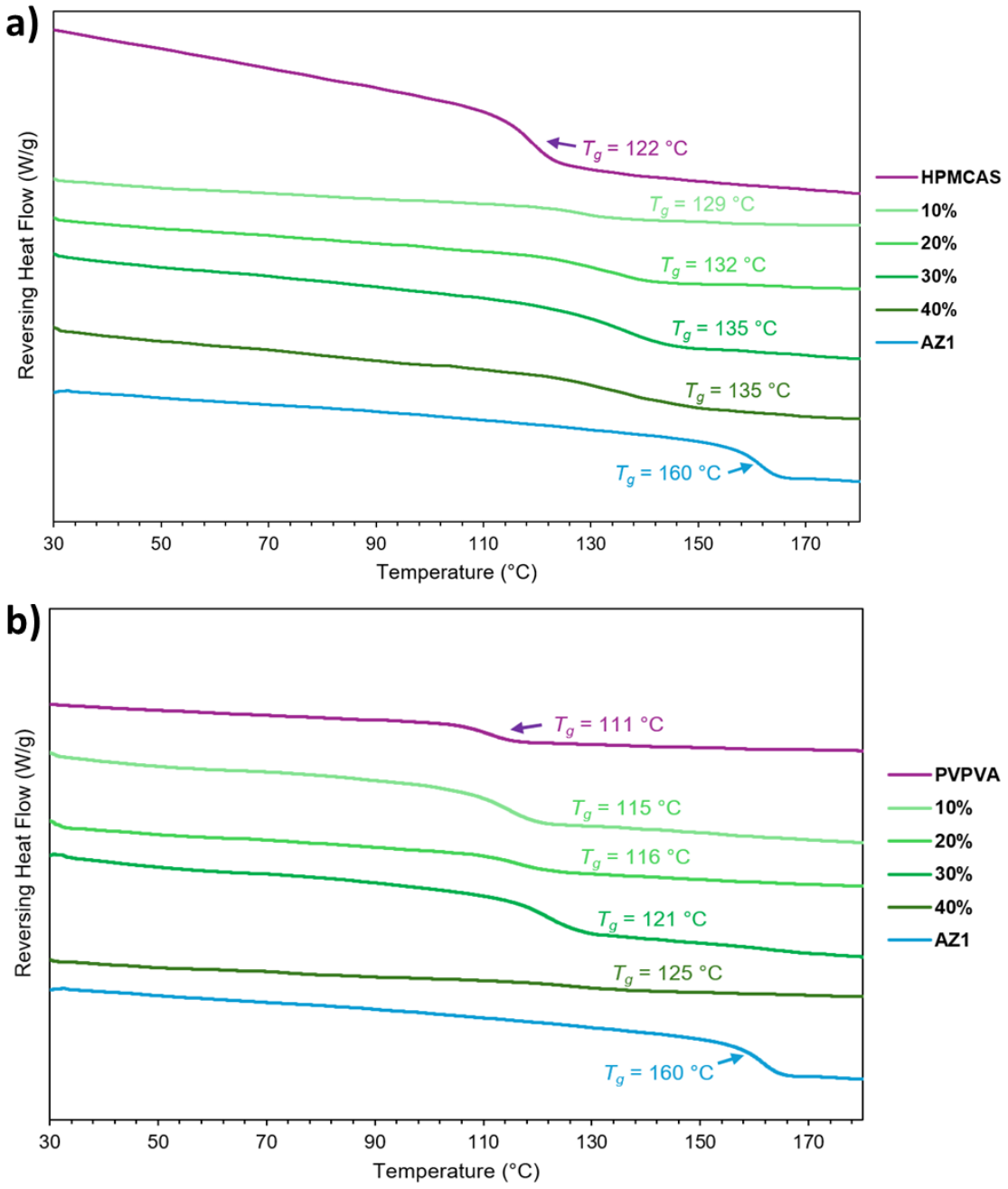

Figure 3.3. Modulated DSC thermograms for AZ1 and its ASDs from 10 – 40 % DL with a) HPMCAS and b) PVPVA, prepared by slurry conversion. A trend towards higher T_g is observed as DL increases.

The FTIR spectra (Appendix B, Figure B10-11) of all ASDs are dominated by the polymer signals at low DL with very little change as DL increases, except for the growth of the AZ1 carboxylic acid $\nu_{(C=O)}$ bands at 1613 and 1683 cm^{-1}, which are not shifted relative to the pure drug substance. This suggests that there is no hydrogen bonding interaction between components, although it does not rule out dispersive forces such as aliphatic stacking interactions, which have been shown in previous work to dominate the lattice energy of AZ1 crystal forms[34] and could be present between drug and polymer chains.

While X-ray photoelectron spectroscopy (XPS) was used by Neusaenger et al. to determine the degree of salt formation in amorphous lumefantrine-poly(acrylic acid) dispersions prepared by slurry conversion,[22] the presence of ten distinct nitrogen atoms in AZ1 makes it unfeasible to measure the degree of drug protonation by the same method, and there is no spectral evidence for drug-polymer proton transfer.

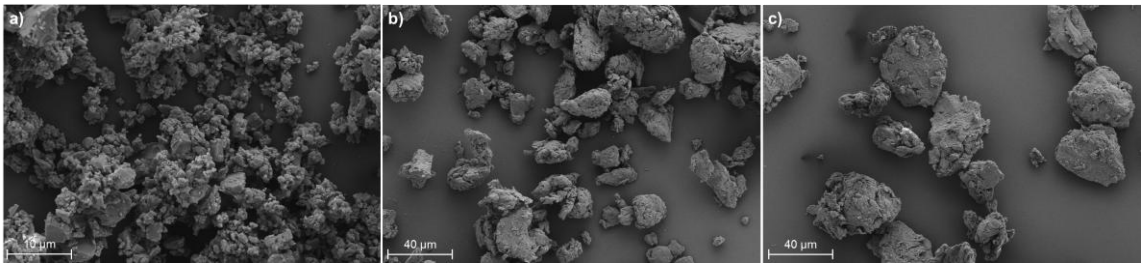

Figure 3.4. SEM images of a) milled AZ1, b) AZ1 HPMCAS ASD (10% DL) and c) AZ1 PVPVA ASD (10% DL).

Milling the ASDs to homogenise and reduce the particle sizes prior to dissolution studies produced smooth particles with a roughly flat-spherical or plate-like shape. Longer and/or faster milling did not reduce the particle size significantly further. While SEM (Figure 3.4) shows that milling the pure AZ1 powder produced particles ranging from approximately 1 – 5 µm, the ASD particles were larger at 10 – 50 µm.

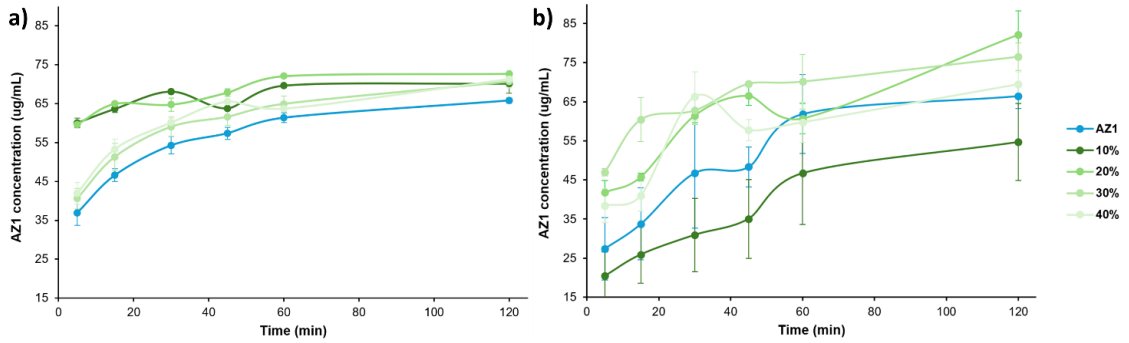

Figure 3.5. Non-sink dissolution profiles of amorphous AZ1 and a) HPMCAS ASDs or b) PVPVA ASDs of AZ1 prepared from 10 – 40 % DL by slurry conversion, over 2 hours in FaSSIF at 37 °C and using a 10-fold non-sink condition compared to the amorphous solubility. Dissolution experiments were run in duplicate, with average concentrations plotted. Error bars indicate the range of concentrations measured at each time point.

Non-sink dissolution profiles for amorphous AZ1 and the HPMCAS and PVPVA ASDs over 2 hours in FaSSIF at 37 °C are shown in Figure 3.5. The milled amorphous AZ1

dissolves at a higher apparent solubility of approximately 65 µg/mL compared to the equilibrium solubility at 48 µg/mL measured over 24 hours in FaSSIF, likely because the micronised particles have a higher surface area and may dissolve quickly before re-precipitating on larger particles over 24 hours. This Ostwald ripening of amorphous particles has been exemplified with felodipine by Olsson and coworkers,[46] and was confirmed in this case by SEM analysis of the particles before and after 24 hours of slurry, showing that the particles had grown from an initial 1 – 5 µm up to 25 – 50 µm (Appendix B, Figure B6). All the HPMCAS ASDs show further increases in apparent solubility compared to AZ1, with the ASDs at 10 and 20 % DL showing almost double the solubility in the first 5 minutes and a sustained dissolution increase over the full 2-hour duration, maintaining at least 10 % higher solubility after 2 hours. However, HPMCAS ASDs at 30 and 40 % DL follow the same profile as pure AZ1, indicating that the limit of congruency (LoC) for these ASDs is between 20 and 30 %, but the presence of some polymer in solution may be the cause of the slightly enhanced dissolution compared to the pure drug. This LoC is reasonably high, given that the deviations in T_g compared to predicted values would suggest strong interactions between components.[5,47] The dissolution profiles of all HPMCAS ASD samples are also relatively consistent between repeats. This shows that despite the particles being roughly an order of magnitude larger than pure AZ1, the HPMCAS ASD formulations at 10 % and 20 % DL are capable of dissolving AZ1 to a higher concentration and more quickly than the pure drug powder alone. By contrast, none of the PVPVA ASDs showed a different shape of dissolution profile to pure AZ1, although ASDs at 20 – 40 % DL appear to have slightly higher apparent solubility over the first 45 minutes of dissolution compared to pure AZ1. However, there was also much greater variance in the profiles between repeated measurements of the same PVPVA samples, suggesting sample inhomogeneity despite the milling process.

These results indicate PROTAC ASD formulations produced by the slurry conversion method can have a significant dissolution enhancement when using the correct polymeric excipient – in this case, HPMCAS appears to be a much more effective excipient than PVPVA, likely due to its greater acidity compared to the drug substance. This mirrors findings by the Taylor group that HPMCAS ASDs generally display higher drug release compared to PVPVA dispersions,[48] and that the formation of drug-rich nanodroplets via liquid-liquid phase separation is observed for high-releasing ASD formulations when the drug concentration exceeded the amorphous solubility.[48–52] It is proposed that HPMCAS is better at stabilizing these nanodroplets compared to PVPVA,[47] creating a drug reservoir from which the high drug supersaturation can be maintained.[49–52]

Solvent evaporation amorphous solid dispersions

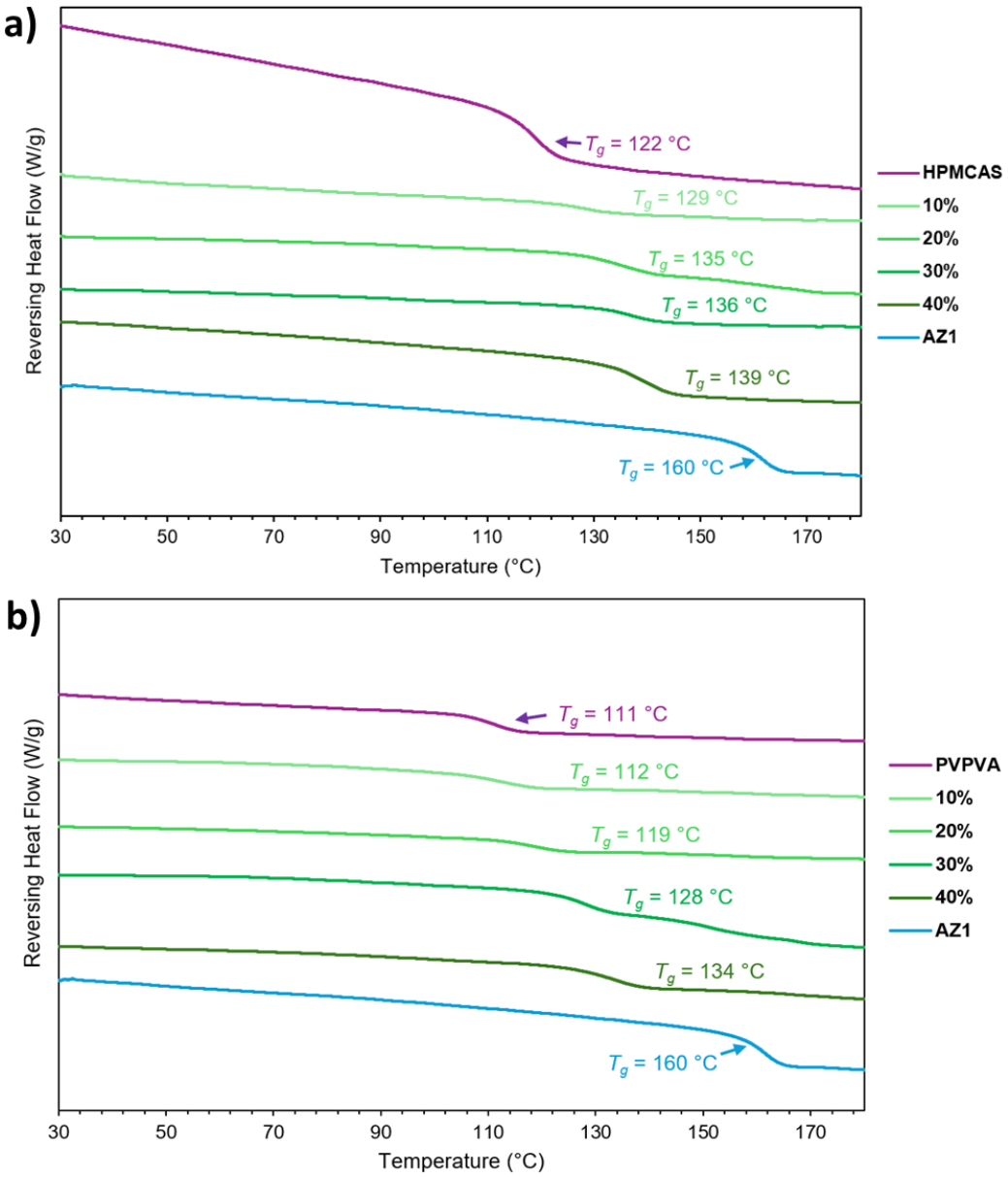

Figure 3.6. Modulated DSC thermograms for AZ1 and its ASDs from 10 – 40 % DL with a) HPMCAS and b) PVPVA, prepared by solvent evaporation. A trend towards higher T_g is observed as DL increases.

ASDs were also prepared by evaporation of a volatile solvent from a solution of AZ1 and polymer, producing thin films that contained no traces of crystalline material by XRPD analysis (Appendix B, Figure B12). The FTIR spectra (Appendix B, Figure B13-14) for ASDs of both polymers also closely matched the equivalent slurry conversion ASDs, showing no evidence of intermolecular interactions. The measured T_g values for the HPMCAS ASDs (Figure 3.6) were 4 – 7 °C higher than the calculated values, similar to the ASDs prepared by slurry conversion. The measured T_g values for the PVPVA ASDs

ranged from 3 °C lower than the predicted value at 10 % DL up to 8 °C higher than the predicted value at 40 % DL, unlike those prepared by slurry conversion which all matched the predicted values, suggesting that there are much stronger drug-polymer interactions present in the ASDs produced by this method. TGA analysis shows that HPMCAS ASDs contain slightly more residual solvent than when prepared by slurry conversion with an average 1 % weight loss up to 60 °C, and PVPVA ASDs contain slightly less with 0.6 % weight loss on average (Appendix B, Figure B15-16). This is likely because the thin films produced were still slightly plasticised with solvent even after holding at 70 °C in an oven overnight.

Solvent evaporation ASDs were prepared such that the surface area of the ASDs produced with a given polymer would be constant, as well as containing a constant mass of AZ1 such that each dissolution experiment would contain a concentration of AZ1 at ten times the solubility limit measured for amorphous AZ1 in FaSSIF (10-fold non-sink condition). However, since pure AZ1 could not be manufactured as a thin film by the same method, the dissolution profiles measured for these ASDs are presented in comparison to that of AZ1 as a powder and are therefore not directly comparable, unlike for the slurry conversion ASDs.

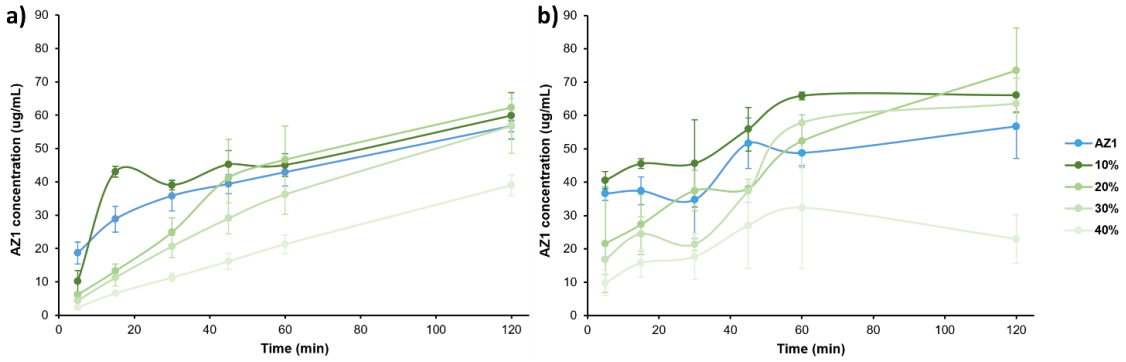

Figure 3.7. Non-sink dissolution profiles of amorphous AZ1 and a) HPMCAS ASDs or b) PVPVA ASDs of AZ1 prepared from 10 – 40 % DL by solvent evaporation, over 2 hours in FaSSIF at 37 °C and using a 10-fold non-sink condition compared to the amorphous solubility. Dissolution experiments were run in duplicate, with average concentrations plotted and error bars showing the range of concentrations measured at each time point.

Non-sink dissolution profiles for amorphous AZ1 and the HPMCAS and PVPVA ASDs prepared by solvent evaporation over 2 hours in FaSSIF at 37 °C are shown in Figure 3.7. Only the 10 % ASDs of both polymers show a consistent increase in apparent solubility over pure AZ1, noting again that the ASDs were prepared as thin films, whereas AZ1 was a free-flowing powder. ASDs prepared at 20 % DL or higher with either polymer

show no apparent solubility increase or have even a lower solubility than pure AZ1. While all PVPVA ASDs follow the same type of dissolution profile as AZ1, the 10 % HPMCAS ASD demonstrates a spring in solubility in the first 15 minutes compared to the other samples, boosting approximately 33 % higher than pure AZ1 before coming back down to follow the same profile as the pure drug. This is a considerably smaller dissolution improvement over pure AZ1 compared to the same ASD produced by slurry conversion, and it appears that the LoC for ASDs prepared by this method is also lower at less than 20 %. Any intermolecular interactions between AZ1 and PVPVA that were implied from the deviation of measured T_g values from the predicted values do not appear to have enhanced the drug dissolution.

Regardless of preparation method, the HPMCAS shows significantly more promise than PVPVA for producing PROTAC ASD formulations with a dissolution advantage over the pure drug. This is likely because of stronger drug-polymer intermolecular interactions evidenced by a positive deviation in T_g compared to predicted values, and possibly also because the greater difference in pK_a between the two components facilitates a greater extent of proton transfer, producing a more strongly charge-separated solid which boosts aqueous solubility. It also appears that this can be achieved to a greater extent via the slurry conversion method rather than by mutual solvent evaporation, suggesting that the former method may facilitate greater separation of the drug within the polymer matrix, or greater proton transfer between components.

Applicability to other PROTAC compounds

The generality of the dissolution advantage provided by HPMCAS ASDs of a PROTAC produced via the slurry conversion method was tested by applying the same ASD formulation protocol to three other PROTAC compounds AZ2-4 (Scheme 3.2). These compounds have the same ligand moieties but vary in the linker moiety and are all amorphous without milling, unlike AZ1. ASDs were prepared only as high as 30 % DL since the highest LoC for AZ1 ASDs had been observed between 20 and 30 %, and due to limited available material for these additional PROTAC compounds. For the same reason, a comparison between polymers and/or ASD preparation methods was not possible for AZ2-4.

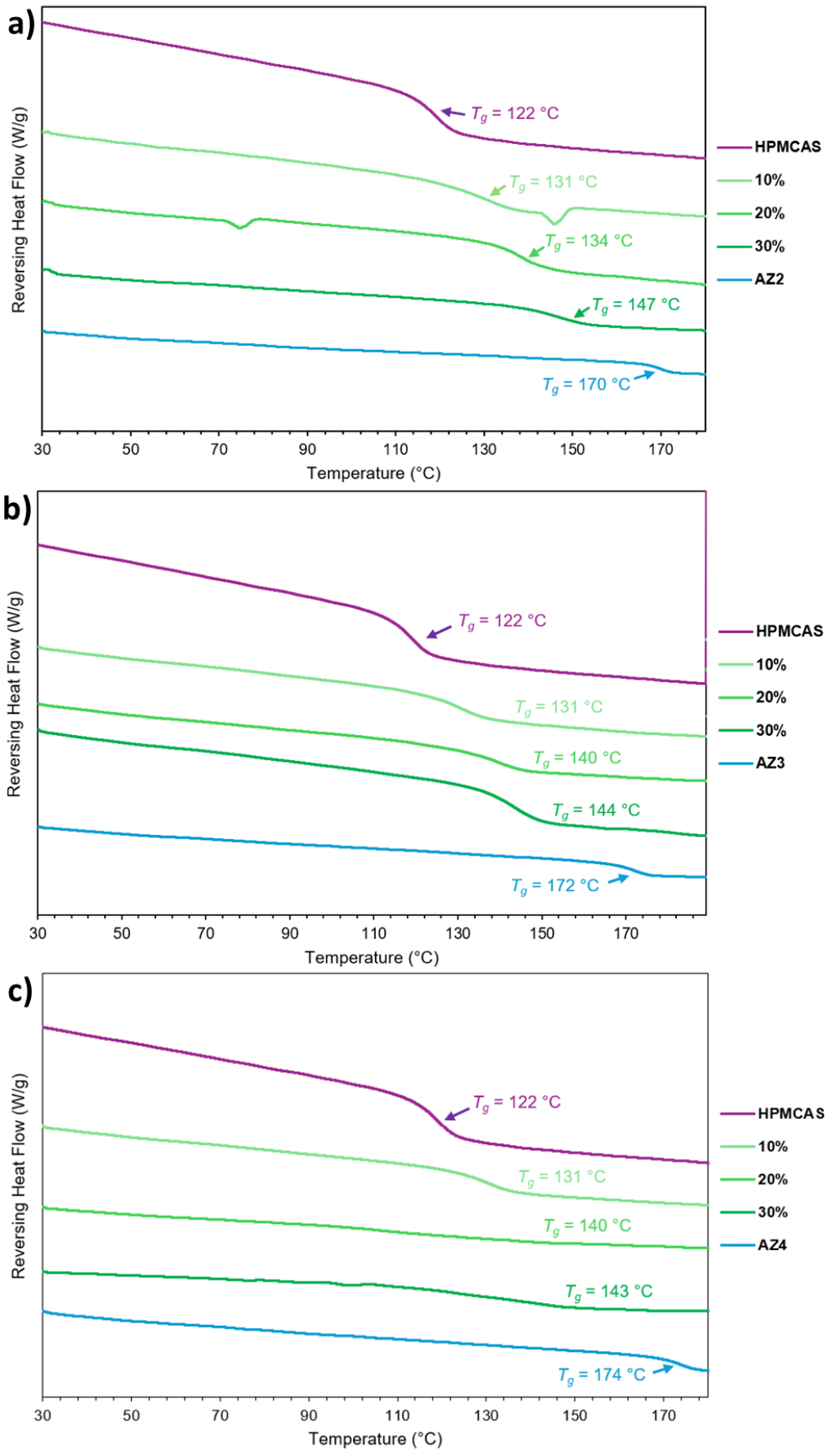

Figure 3.8. DSC thermograms of HPMCAS ASDs of a) AZ2, b) AZ3 and c) AZ4 prepared by slurry conversion.

As for ASDs of AZ1, XRPD (Appendix B, Figure B17) shows that all are amorphous. FTIR analysis of AZ2 ASDs (Appendix B, Figure B18) shows downward shifts in the carboxylic acid $\nu_{(C=O)}$ band from 1730 cm^{-1} to 1724 cm^{-1} for the 10 % ASD, shifting incrementally upward with increasing DL back to 1730 cm^{-1} in the 30 % ASD. The 10 % ASD also has a narrower carboxylic acid $\nu_{(C=O)}$ band at 1705 cm^{-1}. This seems to indicate the most/strongest hydrogen bonding between AZ2 and HPMCAS at lower DL, decreasing towards higher DL. FTIR analysis of the AZ3 and AZ4 ASDs (Appendix B, Figure B19-20) shows much less difference between the ASDs and pure components, with no discernible differences in the carbonyl region suggesting an absence of hydrogen bonding interactions between drug and polymer. TGA (Appendix B, Figure B21-23) shows that the AZ2 and AZ3 ASDs contain ~0.3 % residual solvent on average with broad mass loss between 20 – 80 °C, with gradual mass loss totalling ~1.5 % over the remaining temperature range above 80 °C. AZ4 ASDs appeared to be dry below 80 °C but show a steady mass loss between 120 – 200 °C of as much as 3 %. DSC analysis (Figure 3.8) shows that for all three PROTACs, the ASDs increase in T_g with increasing DL trending towards the respective pure PROTAC T_g values. Steeper trends in T_g with DL are observed in these samples compared to those of AZ1, since all three PROTACs have a higher T_g than AZ1 by 10 – 15 °C. The measured T_g values of all three sets of ASDs also show more significant positive deviations from the calculated T_g values, ranging from 5 – 14 °C higher than the predicted values. This suggests that there are stronger drug-polymer interactions in all three sets of ASDs compared to those of AZ1.

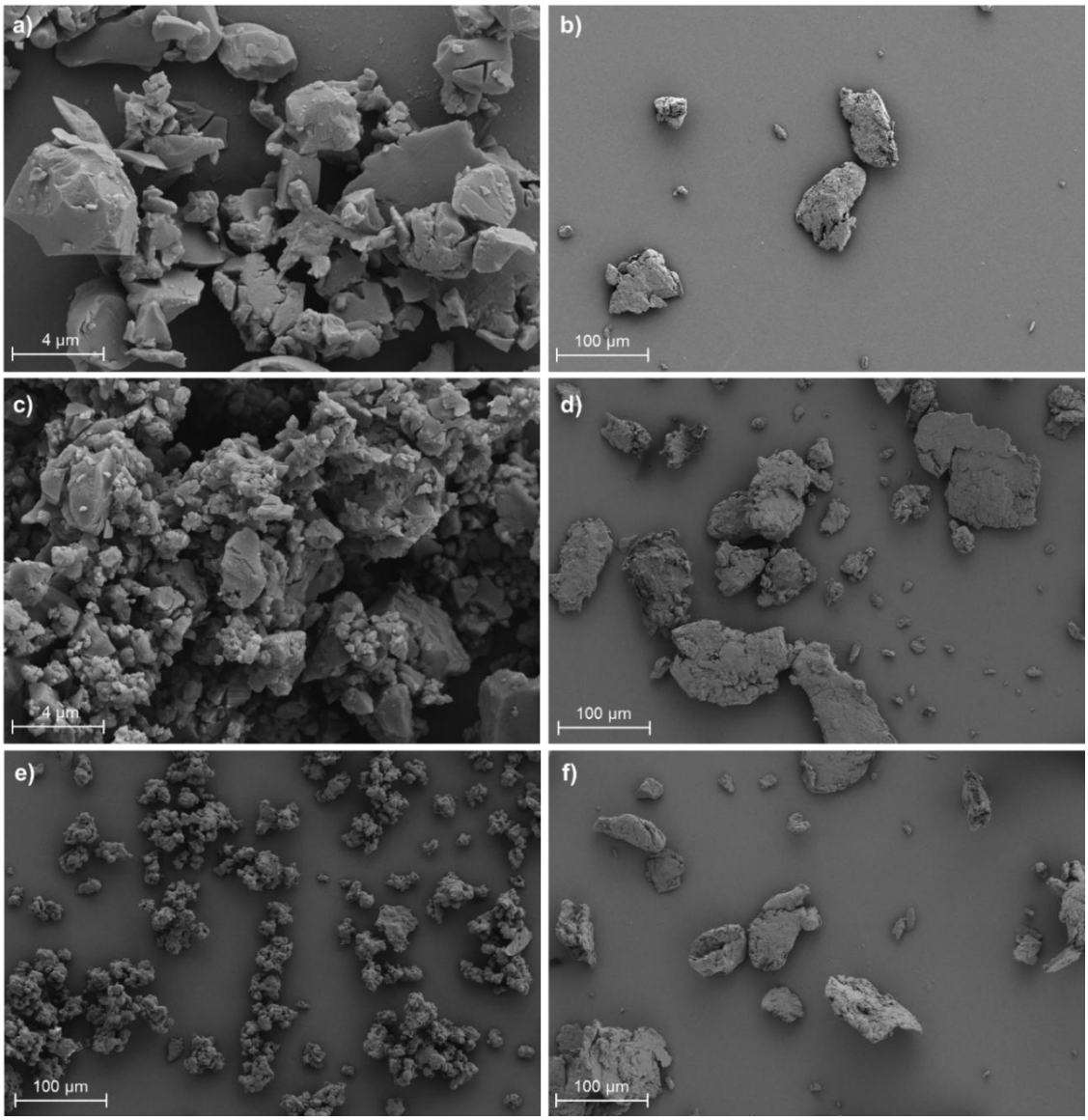

Figure 3.9. SEM images of a) milled AZ2, b) AZ2 HPMCAS ASD, c) milled AZ3, d) AZ3 HPMCAS ASD, e) milled AZ4 and f) AZ4 HPMCAS ASD. All ASDs are at 10% DL.

SEM (Figure 3.9) shows that milled AZ2 and AZ3 particles are approximately 1 – 5 µm, while milled AZ4 particles are 10 – 30 µm in size and appear to clump together more strongly. This is unlikely to be caused by a greater quantity of water adsorbed into the pure AZ4 drug substance, since TGA shows that AZ4 contains less water than either AZ2 or AZ3 (Appendix B, Figures B21-23). ASD particles for all three PROTACs range from approximately 20 – 100 µm.

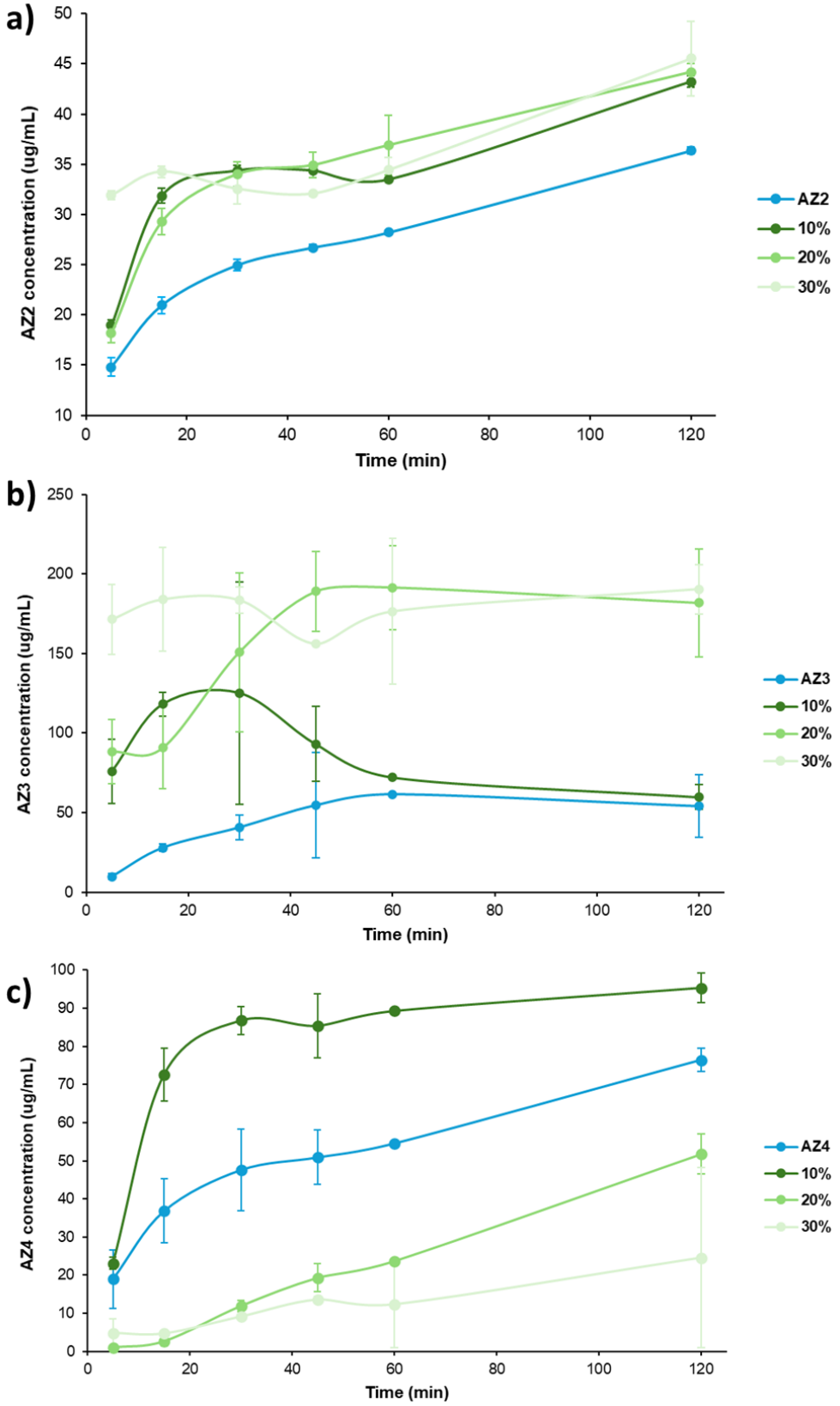

Figure 3.10. Non-sink dissolution profiles of amorphous PROTACs and HPMCAS ASDs of a) AZ2, b) AZ3 and c) AZ4 prepared from 10 – 30 % DL by slurry conversion, over 2 hours in FaSSIF at 37 °C and using a 10-fold non-sink condition compared to the amorphous solubilities of each PROTAC. Dissolution experiments were run in duplicate with average concentrations plotted and error bars showing the range of concentrations measured at each time point.

Non-sink dissolution profiles for amorphous AZ2, AZ3 and AZ4 and their ASDs over 2 hours in FaSSIF at 37 °C are shown in Figure 3.10. All ASDs from 10 – 30 % DL of both AZ2 and AZ3 show an increase in apparent solubility to varying extents, while only the 10 % ASD of AZ4 shows such an increase with 20 and 30 % ASDs falling considerably lower in apparent solubility. This suggests that the LoC values of AZ2 and AZ3 ASDs may be even higher than 30 %, with no limit detected in this study – these are far higher than expected given the considerable deviations in T_g from the predicted values. All three ASDs of AZ2 consistently show an approximate 50 % boost in apparent solubility after 15 minutes and sustain a higher dissolution profile by no less than 15 % across the full 2-hour duration, with a significant spring in the first 30 minutes compared to pure AZ2. Interestingly, the highest DL sample at 30 % shows the greatest spike in AZ2 concentration at 5 minutes, consistently between repeats. A similarly unexpected trend is observed for ASDs of AZ3, where increasing DL leads to greater overall apparent solubility although with different profiles in each case. The 10 % ASD exhibits an initial spring boosting to four times the drug concentration produced by pure AZ2, before falling back down to roughly the same profile as the pure drug after 1 hour. The 20 % ASD also starts with a significantly higher concentration after only 5 minutes but rather than springing up and falling back down, the concentration increases to four times the apparent solubility of AZ2 and is sustained for the remainder of the dissolution experiment. The 30% ASD was by far the most soluble overall, measuring at over seventeen times the apparent solubility of AZ2 after the first 5 minutes, but has a flat dissolution profile compared to the other ASDs. The variation in the dissolution profiles for repeats of the AZ3 ASDs is also much greater, and the concentrations measured are much higher overall since AZ3 is the most soluble of the PROTAC compounds studied. Meanwhile, ASDs of AZ4 all follow a similar dissolution profile to each other, with only the 10 % ASD providing a spring in apparent solubility to approximately double the concentration of AZ4 compared to the pure drug substance after 15 – 30 minutes and sustaining no less than a 25 % solubility boost compared to the pure drug over the 2-hour range. ASDs at 20 and 30 % consistently provide a 2 – 3 times lower concentration of AZ4 compared to the pure API across the dissolution experiment. The LoC for this system is clearly between 10 and 20 % DL. The relatively poorer dissolution performance of AZ4 ASDs compared to the pure API contradicts the relatively lower difference in particle size between the pure and formulated samples, suggesting that it is more likely a result of weaker drug-polymer interactions. Alternatively, if drug-rich nanodroplets are formed by these ASD formulations, it may be that the HPMCAS polymer is less stabilizing of the AZ4 nanodroplets than for AZ2 or AZ3.

Overall, the dissolution advantage provided by the ASD formulations for AZ2-4 was much more significant than for AZ1 and this formulation approach appears to be effective for increasing kinetic solubility of this type of PROTAC compounds in general, despite the ASD particles being considerably larger than the pure drug powders. ASD formulations may be able to provide some dissolution/solubility benefit for PROTAC compounds, but the design of the ASD is crucially important, and the relative level of dissolution enhancement is modest compared to more conventional drugs.[53,54] However, further improvements such as hierarchical ASD formulation, where the particle surfaces are modified with an additional polymer coating, may lead to even greater dissolution behaviour and improved wettability.[55,56] This strategy may be particularly effective if achieved via the slurry conversion method of ASD preparation which has been shown here to produce ASDs of superior dissolution capability. The data presented here are also not always fully consistent with the current LoC theory (noting for example the behaviour of ASDs of AZ2 and AZ3), indicating that other mechanisms may be involved. This highlights the technical formulation challenge presented by PROTAC compounds.

ASD conditioning

The physical stabilities of all ASDs that provided a dissolution improvement compared to the pure drug substance were assessed by XRPD and thermal analysis after conditioning the samples for 1 month at 75 % relative humidity and 40 °C, simulating a storage environment that may accelerate drug recrystallisation. XRPD (Appendix B, Figure B24) shows that no ASD samples begin to recrystallise over this time period, which is particularly of interest for AZ1 which is known to crystallise under certain conditions.[34] The T_g values measured by a single-ramp mDSC protocol (Table 3.1) showed also very little deviation from the pre-conditioned samples, indicating that any plasticization of the ASDs by water within the humid conditioning environment does not have a significant effect on molecular mobility. TGA analysis (Appendix B, Figure B25) shows that most of the conditioned ASDs lost between 0.1 – 0.7 % weight up to 100 °C, suggesting a relatively low quantity of adsorbed moisture, followed by gradual mass loss of up to 1 % between 100 – 180 °C as the samples exceed T_g. AZ3 ASDs at 10 and 20 % DL and AZ2 ASD at 20 % DL were slightly wetter than the others with around 0.5 % greater mass loss up to 100 °C compared to the other samples, and the AZ4 ASD at 10 % DL contained considerably more residual solvent at approximately 1.5 %. However, the generally low moisture uptake of the conditioned samples is commensurate with HPMCAS ASDs typically showing less hygroscopicity than other polymeric carriers used in the pharmaceutical industry,[57] and suggests that the ASDs shown to provide a dissolution

enhancement in this study are likely to be stable against plasticization and phase separation for months.

Table 3.1. T_g values of ASD samples before and after conditioning for 1 month at 75 % RH and 40 °C. “E” and “SC” refer to evaporation and slurry conversion methods of ASD preparation, respectively. All ASDs of AZ2, AZ3 and AZ4 were prepared by slurry conversion.

Sample	Pre-conditioned T_g (°C)	Conditioned T_g (°C)
AZ1 HPMCAS E 10%	129	130
AZ1 HPMCAS SC 10%	129	129
AZ1 HPMCAS SC 20%	132	128
AZ2 10%	131	132
AZ2 20%	134	139
AZ2 30%	147	147
AZ3 10%	131	132
AZ3 20%	140	139
AZ3 30%	144	144
AZ4 10%	131	131

3.4 Conclusion

In this work, it is shown that aqueous dissolution can be enhanced for a CRBN PROTAC using HPMCAS as a carrier polymer up to a drug loading of 20 % w/w whereas dissolution is not improved by using PVPVA, indicating the importance of ASD polymer selection. It is also shown that the slurry conversion method produces PROTAC ASDs with a higher limit of congruency and better dissolution performance compared to the solvent evaporation method. Co-amorphous formulations using low molecular weight co-formers do not show any dissolution improvement by comparison, despite spectral evidence of drug – co-former hydrogen bonds. While such interactions are not detected in the ASDs, positive deviations in measured T_g values compared to predicted values suggest that strong drug-polymer interactions may be present and could be dispersive in nature. Despite these strong interactions, the limits of congruency were higher than 30% w/w in some cases, suggesting that additional mechanisms may be involved in the dissolution behaviour of these compounds compared to conventional poorly soluble drugs. The most effective formulation approach of preparing ASDs using HPMCAS as a carrier polymer via the slurry conversion method was applied successfully to three other CRBN PROTAC compounds, showing even greater dissolution enhancements

compared to the pure amorphous drugs and proving the general application of the formulation strategy. All ASD samples are stable against plasticization and phase separation after 1 month of storage under elevated humidity and temperature. This work reveals that while formulation approaches using small molecule excipients may not be as suitable for enhancing the dissolution of PROTACs as they are for conventional small molecule drugs, ASD formulations prepared using an informed polymer selection and manufacturing method may be a robust approach for the pharmaceutical industry to produce commercializable solid forms of PROTACs for oral dosage units. It is also evident that general rules and understanding from ASD formulation of conventional drugs, such as the relationship between drug loading and LoC, do not necessarily apply to PROTAC ASDs and that screening must be performed for more PROTACs before general principles can be developed.

3.5 References

1. D. J. Berry and J. W. Steed, *Adv. Drug Deliv. Rev.*, 2017, **117**, 3–24.
2. S. M. Berge, L. D. Bighley and D. C. Monkhouse, *J. Pharm. Sci.*, 1977, **66**, 1–19.
3. P. L. Gould, *Int. J. Pharm.*, 1986, **33**, 201–217.
4. R. Iyer, V. P. Jovanovska, K. Berginc, M. Jaklič, F. Fabiani, C. Harlacher, T. Huzjak and M. V. Sanchez-Felix, *Pharmaceutics*, 2021, **13**, 1682.
5. C. Que, A. Deac, D. Y. Zemlyanov, Q. Q. Qi, A. S. Indulkar, Y. Gao, G. G. Z. Zhang and L. S. Taylor, *Mol. Pharm.*, 2021, **18**, 3496–3508.
6. J. Aaltonen and T. Rades, *Dissolution Technol.*, 2009, **16**, 2, 47–54.
7. B. C. Hancock and G. Zografi, *J. Pharm. Sci.*, 1997, **86**, 1–12.
8. S. J. Dengale, H. Grohganz, T. Rades and K. Löbmann, *Adv. Drug Deliv. Rev.*, 2016, **100**, 116–125.
9. J. A. Baird and L. S. Taylor, *Adv. Drug Deliv. Rev.*, 2012, **64**, 396–421.
10. W. Brostow, R. Chiu, I. M. Kalogeras and A. Vassilikou-Dova, *Mater. Lett.*, 2008, **62**, 3152–3155.
11. C. T. Moynihan, *J. Am. Ceram. Soc.*, 1993, **76**, 1081–1087.
12. P. C. Painter, J. F. Graf and M. M. Coleman, *Macromolecules*, 1991, **24**, 5630–5638.
13. M. Allesø, N. Chieng, S. Rehder, J. Rantanen, T. Rades and J. Aaltonen, *J. Contr. Release*, 2009, **136**, 45–53.
14. H. Fael and A. L. Demirel, *Int. J. Pharm.*, 2021, **600**, 120448.
15. K. Löbmann, R. Laitinen, H. Grohganz, K. C. Gordon, C. Strachan and T. Rades, *Mol. Pharm.*, 2011, **8**, 1919–1928.
16. K. Löbmann, C. Strachan, H. Grohganz, T. Rades, O. Korhonen and R. Laitinen, *Eur. J. Pharm. Biopharm.*, 2012, **81**, 159–169.
17. S. J. Dengale, O. P. Ranjan, S. S. Hussen, B. S. M. Krishna, P. B. Musmade, G. Gautham Shenoy and K. Bhat, *Eur. J. Pharm. Sci.*, 2014, **62**, 57–64.
18. R. Laitinen, K. Löbmann, C. J. Strachan, H. Grohganz and T. Rades, *Int. J. Pharm.*, 2013, **453**, 65–79.
19. S. Janssens and G. Van den Mooter, *J. Pharm. Pharmacol.*, 2010, **61**, 1571–1586.
20. T. N. Hiew, D. Y. Zemlyanov and L. S. Taylor, *Mol. Pharm.*, 2022, **19**, 392–413.
21. P. D. Nunes, J. F. Pinto, J. Henriques and A. M. Paiva, *Mol. Pharm.*, 2022, **19**, 51–66.
22. A. L. Neusaenger, X. Yao, J. Yu, S. Kim, H. W. Hui, L. Huang, C. Que and L. Yu, *Mol. Pharm.*, 2023, **20**, 1347–1356.

23. A. C. F. Rumondor and L. S. Taylor, *Mol. Pharm.*, 2010, **7**, 477–490.
24. M. Luo, A. Chen, S. Shan, M. Guo and T. Cai, *Mol. Pharm.*, 2025, **22**, 6, 3401–3413.
25. C. Loschen and A. Klamt, *Ind. Eng. Chem. Res.*, 2012, **51**, 14303–14308.
26. A. B. Anane-Adjei, E. Jacobs, S. C. Nash, S. Askin, R. Soundararajan, M. Kyobula, J. Booth and A. Campbell, *Int. J. Pharm.*, 2022, **614**, 121387.
27. F. Pöstges, K. Kayser, J. Appelhaus, M. Monschke, M. Gütschow, C. Steinebach and K. G. Wagner, *Pharmaceutics*, 2023, **15**, 156.
28. N. Hofmann, M. Harms and K. Mäder, *Int. J. Pharm.*, 2024, **650**, 123725.
29. L. Mareczek, L. K. Mueller, L. Halstenberg, T. M. Geiger, M. Walz, M. Zheng and F. Hausch, *Pharmaceutics,* 2024, **16**, 924.
30. H. Zhang, H. Wu, L. Wang, Y. Gao, L. M. Galarza, Y. Zhao, Z. Wang, L. Gao and J. Han, *J. Drug Deliv. Sci. Technol.*, 2025, **107**, 106837.
31. *WIPO Pat.*, Estrogen Receptor Degrading PROTACs, WO2020201080 (A1), 2020.
32. A. Klamt, *Wiley Interdiscip. Rev. Comput. Mol. Sci.*, 2011, **1**, 699–709.
33. A. Wexler and S. Hasegawa, *J. Res. Natl. Bur. Stand.*, 1954, **53**, 19–26.
34. M. A. Screen, J. F. McCabe, S. Askin, J. L. Guest, P. Hodgkinson, A. J. Cruz-Cabeza, T. J. Blundell, D. N. Rainer, S. J. Coles, A. Longcake, M. R. Probert, C. S. Mahon, M. R. Wilson and J. W. Steed, *J. Am. Chem. Soc.*, 2025, **147**, 31, 28056–28072.
35. J. X. Song, J. M. Chen and T. B. Lu, *Cryst. Growth Des.*, 2015, **15**, 4869–4875.
36. J. X. Song, Y. Yan, J. Yao, J. M. Chen and T. B. Lu, *Cryst. Growth Des.*, 2014, **14**, 3069–3077.
37. L. Wang, Y. Yan, X. Zhang and X. Zhou, *Int. J. Pharm.*, 2022, **613**, 121394.
38. *WIPO Pat.*, Crystalline forms of lenalidomide, WO 2019/064222 A1, 2019
39. *US Pat.*, Novel crystalline forms of 3-(4-amino-1-oxo-1.3 dihydro-isoindol-2-yl)-piperidine-2,6-dione, US 2014/0296291 A1, 2014.
40. M. A. Screen, G. Tomkinson, J. F. McCabe, S. Askin, C. S. Mahon, M. R. Wilson and J. W. Steed, *New J. Chem.*, 2025, **49**, 6535–6543.
41. S. L. Childs, G. P. Stahly and A. Park, *Mol. Pharm.*, 2007, **4**, 3, 323–338.
42. A. J. Cruz-Cabeza, *Cryst. Eng. Comm.*, 2012, **14**, 6362–6365.
43. W. Q. Tong and G. Whitesell, *Pharm. Dev. Technol.*, 1998, **3**, 215–223.
44. S. W. Shalaby, Y. Ikada, R. Langer and J. Williams, *Polymers of Biological and Biomedical Significance*, American Chemical Society, Washington, DC, 1993, vol. 540.
45. P. J. Skrdla, P. D. Floyd and P. C. Dell'Orco, *Phys. Chem. Chem. Phys.*, 2017, **19**, 20523–20532.
46. L. Lindfors, P. Skantze, U. Skantze, M. Rasmusson, A. Zackrisson and U. Olsson, *Langmuir*, 2006, **22**, 906–910.
47. A. Deac, Q. Qi, A. S. Indulkar, Y. Gao, G. G. Z. Zhang and L. S. Taylor, *Mol. Pharm.*, 2023, **20**, 2217–2234.
48. R. Yang, A. K. P. Mann, T. Van Duong, J. D. Ormes, G. A. Okoh, A. Hermans and L. S. Taylor, *Mol. Pharm.*, 2021, **18**, 2066–2081.
49. A. S. Indulkar, J. E. Waters, H. Mo, Y. Gao, S. A. Raina, G. G. Z. Zhang and L. S. Taylor, *J. Pharm. Sci.*, 2017, **106**, 1998–2008.
50. M. J. Jackson, U. S. Kestur, M. A. Hussain and L. S. Taylor, *Mol. Pharm.*, 2016, **13**, 223–231.
51. D. E. Alonzo, Y. Gao, D. Zhou, H. Mo, G. G. Z. Zhang and L. S. Taylor, *J. Pharm. Sci.*, 2011, **100**, 3316–3331.
52. A. S. Indulkar, Y. Gao, S. A. Raina, G. G. Z. Zhang and L. S. Taylor, *Mol. Pharm.*, 2016, **13**, 2059–2069.
53. A. S. Indulkar, X. Lou, G. G. Z. Zhang and L. S. Taylor, *Mol. Pharm.*, 2019, **16**, 1327–1339.
54. F. Tres, M. M. Posada, S. D. Hall, M. A. Mohutsky and L. S. Taylor, *Int. J. Pharm.*, 2018, **543**, 29–37.
55. T. N. Hiew, M. A. Solomos, P. Kafle, H. Polyzois, D. Y. Zemlyanov, A. Punia, D. Smith, L. Schenck and L. S. Taylor, *J. Pharm. Sci.*, 2025, **114**, 1, 289–303.

56. T. N. Hiew, S. Saboo, D. Y. Zemlyanov, A. Punia, M. Wang, D. Smith, M. Lowinger, M. A. Solomos, L. Schenck and L. S. Taylor, *J. Pharm. Sci.*, 2023, **112**, 8, 2057–2068.
57. A. Butreddy, *Eur. J. Pharm. Biopharm.*, 2022, **177**, 289–307.

4. Designing Lenalidomide Co-crystals with an Extended-Release Profile for Improved Pulmonary Drug Delivery

4.1 Introduction

As previously discussed in section 1.1.3, pharmaceutical co-crystals are used to improve the chemical, physical and economic characteristics of an active pharmaceutical ingredient (API) without modifying its chemical structure or pharmacology, by crystallising it with at least one other component or "co-former".[1–3] Unlike pharmaceutical salts, which have been used for decades to improve physicochemical properties such as the water solubility, toxicity profile and dissolution rate of APIs,[2] co-crystals consist of neutral components interacting non-covalently via hydrogen bonds, π-π stacking, van der Waals forces and halogen bonds without electrostatic attraction between oppositely charged ions. Use of these interactions potentially allows new pharmaceutical solids with desirable physicochemical properties to be designed via a crystal engineering approach, using an understanding of possible supramolecular motifs between two or more components.[1,4] This "supramolecular synthon" approach to co-crystal design has proven effective for improving the pre-clinical properties of numerous poorly soluble drugs such as the anti-epileptic agent lamotrigine,[5] the anti-bacterial drug norfloxacin[6] and the anti-inflammatory drug indomethacin.[7] Solubility enhancement is not the only application for co-crystal formation, however. Work by Aakeroy, for example, has shown that solubility reduction by co-crystal formation can be highly effective in slow-release formulations such as agrochemicals.[8]

Lenalidomide (LDM; Scheme 4.1a) is a drug compound often used as the structural basis for the E3 ligase ligand of cereblon PROTACs such as AZ1, alongside pomalidomide and thalidomide depending on the PROTAC in question. As discussed in Chapter 3, selecting potential co-former molecules to screen for co-crystals and co-amorphous solids of PROTACs can be done using a combination of computational tools such as COSMOtherm and by screening co-formers known to co-crystallise with smaller fragments of the molecule. Expanding the known co-crystal library of LDM may therefore identify more potential co-formers of the structurally related AZ1 PROTAC. LDM itself is an immunomodulatory drug primarily used for the treatment of multiple myeloma in an oral formulation where bioavailability can be improved by enhancing solubility.[9] LDM can also be used to treat pulmonary fibrosis,[10] where a lower solubility is often advantageous

for producing lower and flatter drug dissolution profiles in the lungs.[11] As well as the commercially available hemihydrate Form B, LDM can crystallise as the anhydrous Form A, the dihydrate Form E and several metastable anhydrous polymorphs accessible by different methods of dehydrating Form B or Form E.[12,13] The commercial form, marketed as Revlimid®, is designated as BCS Class 3 by the FDA with poor oral bioavailability resulting from a low permeability,[14] and the API has an approximate aqueous solubility of 0.5 mg/mL at neutral pH. The imide moiety within its structure makes LDM a promising candidate for the design of co-crystals with amide-, carboxylic acid- and hydroxyl-containing co-formers via hydrogen bonding synthons involving N-H···O=C and C=O···H-O interactions. At least one of these synthons is present in each of the single crystal X-ray diffraction (XRD) structures of the five LDM co-crystals in the Cambridge Structural Database (CSD).[15,16] A total of eighteen co-crystal forms (including their hydrates), three solvates and five salts of LDM have been reported after extensive screening with generally recognised as safe (GRAS) compounds.[15–19] Co-crystals with 3,5-dihydroxybenzoic acid were shown to have approximately 40% higher maximum solubility in 0.2 M phosphate buffer at pH 6.8 and 37 °C compared to Form B, reaching the maximum solubility within 3 minutes before slowly decreasing over 24 hours as per the “spring and parachute effect” as introduced in section 1.1.3.[16] A co-crystal with nicotinamide was also synthesised following its prediction using a model of hydrogen bond propensity (HBP) to screen for potential LDM co-crystals. Not only does the co-crystal show a dissolution and solubility improvement over the pure API, but similar results were obtained for a physical mixture of the API and co-former, indicating the formation of a 1:1 complex in the dissolution media.[17] The co-formers used in these examples all have aqueous solubilities one to three orders of magnitude greater than LDM.

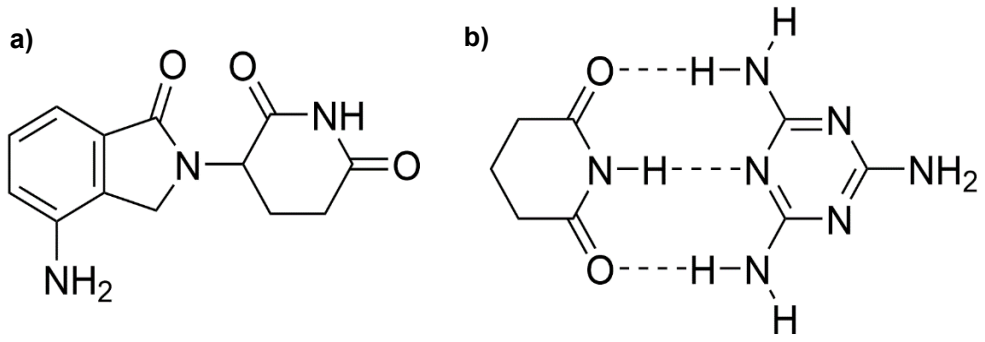

Scheme 4.1. Chemical structures of a) lenalidomide (LDM) and b) a $2R_2^2(8)$ triple hydrogen bonding synthon[20] with melamine (MEL).

Compared to other non-parenteral administration methods, pulmonary drug delivery systems benefit from targeted delivery, reduced side effects and improved bioavailability due to the rate of absorption into the systemic circulation.[21] Inhaled drugs first dissolve in the aqueous lung lining fluid before they can translocate into the blood, lymph and cells, but if the diffusion is too rapid then the duration of pulmonary exposure and total pharmacological effect is diminished.[11] Extending the retention time of drug particles in the lungs is therefore favourable to reduce the frequency of doses that a patient is required to take. Poorly water-soluble drugs such as fluticasone propionate and several sex steroids and antifungal drugs exhibit slow absorption rates from the lungs because they dissolve slowly in the aqueous lung lining fluid, leading to prolonged drug exposure.[11,21,22] For particularly insoluble drugs, however, formulation as multicomponent solids with a highly soluble co-former has been demonstrated as an effective strategy for increasing drug dissolution rates and enhancing pulmonary drug release. Micronised co-crystals of the highly insoluble (<1 μg/mL) antifungal drug itraconazole with succinic acid and L-tartaric acid displayed up to 10-times higher intrinsic dissolution rates and pulmonary absorption profiles in rats compared to the amorphous spray-dried formulation and crystalline form of the pure drug with comparable particle sizes,[23] and the first co-crystal developed of RNA antiviral drug remdesivir with salicylic acid displayed an approximate 15-fold increase in drug release compared to the pure drug after 2 hours of dissolution in simulated lung fluid.[24] In contrast, a typical LDM dose of 10 mg/day for pulmonary therapy[25] may dissolve quickly in the 10 – 30 mL volume of lung fluid usually present in humans,[26] therefore reducing the solubility and absorption rate of the drug in the lungs by formulating as a multicomponent solid with a low-solubility co-former may reduce the reported symptoms of coughs and fever arising from LDM toxicity,[25] potentially improving its effectiveness as a treatment for pulmonary fibrosis.

The imide group in LDM consists of two carbonyl hydrogen bond acceptors (A) separated by an N-H hydrogen bond donor (D) in an A-D-A configuration, making it complementary to a molecule with a D-A-D configuration. An intuitive choice for a low-solubility co-former with a D-A-D configuration is melamine (MEL), a compound that is safe to use at low concentrations (<0.2 mg/kg) in humans,[28,29] with a reported aqueous solubility of 3.2 mg/mL.[30] This relatively low solubility coupled with the anticipated strong ADA-DAD hydrogen bonding pairing might be anticipated to give rise to a reduced solubility LDM co-crystal. The triple hydrogen bonding synthon between MEL and imide-containing cyanuric acid has already been exemplified in work by Seto and Whitesides[31] and by Wang et al. in the crystal structure of the MEL cyanuric acid complex (1:1) trihydrochloride.[32] It has also been used in the sonochemical preparation of hydrogels with uric acid.[33] Unlike all previously reported co-formers of LDM which contain alcohol, carboxylic acid, pyridyl and/or amide moieties as hydrogen bond donors and acceptors,

MEL contains three primary amine hydrogen bond donors as well as three pyridyl nitrogen atom acceptors. In this chapter, the design, preparation and properties of a reduced solubility co-crystal between LDM and MEL are reported. This co-crystal serves as a model exemplar of the way in which co-crystal engineering could be used to lower drug solubility for improved pulmonary therapy.

4.2 Experimental

Materials and general methods. Lenalidomide (as the hemihydrate Form B[12]) and all co-formers were purchased from Merck. Form A was obtained by drying Form B in an oven at 150 °C for 6 hours and characterised by XRPD. Infrared spectra were recorded between 4000 and 550 cm^{-1} using a Perkin Elmer 100 FT-IR spectrometer with a uATR attachment. Unless otherwise specified, powder X-ray diffraction (XRPD) patterns were collected at room temperature using a Bruker AXS D8 Advance GX003410 diffractometer with a Lynxeye Soller PSD detector, using Cu Kα radiation at a wavelength of 1.5406 Å and collecting from $2° \leq 2\theta \leq 40°$.

Preparation of lenalidomide melamine non-stoichiometric hydrate (1). LDM Form B (278 mg, 1.00 mmol) and MEL (240 mg, 1.90 mmol) were added in excess to water (40 mL) such that the undissolved solid contained a 1:1 molar ratio of the two components and stirring overnight. The resulting solid was filtered and dried to afford co-crystal **1** as a white powder (300 mg, 0.728 mmol, 73 %). Co-crystal **1** can also be prepared by manual grinding of LDM Form B and MEL in a pestle and mortar (Appendix C, Figure C1).

Preparation of lenalidomide melamine methanol hemihydrate (2). LDM Form B (230 mg, 0.857 mmol) and MEL (108 mg, 0.857 mmol) were added to methanol (350 mL), stirred to dissolve, and the solvent was slowly evaporated to afford lenalidomide melamine methanol hemihydrate (co-crystal **2**) as blue-green needles (225 mg, 0.528 mmol, 62 %). Co-crystal **2** can also be prepared using a liquid-assisted grinding (LAG) method, by mixing LDM Form B and MEL in a 1:1 molar ratio with 2 drops of methanol in a 5 mL stainless steel grinding jar with one stainless steel grinding ball (6.4 mm diameter) and grinding with a Retsch MM200 Mixer Mill at a frequency of 20 Hz for 30 minutes. The resulting solid was analysed by IR spectroscopy and XRPD (Appendix C, Figure C2).

Single crystal X-ray diffraction (SC-XRD). Single-crystal X-ray diffraction data for co-crystal **2** was collected at 120 K using Mo Kα radiation at a wavelength of 0.71073 Å on a Bruker D8 Venture 3-circle diffractometer. The structure was solved by direct methods

and refined by full-matrix least squares on F^2 for all data using Olex2[34] and SHELXTL.[35] All non-hydrogen atoms were refined in anisotropic approximation, while hydrogen atoms were placed in the calculated positions and refined in riding mode. Crystal data for **2**: $C_{17}H_{24}N_9O_{4.5}$, M_r = 426.45, space group $P\bar{1}$, *a* = 7.9402(3) Å, *b* = 10.2062(3) Å, *c* = 12.5527(4) Å, α = 93.5640(10) °, β = 94.6780(10) °, γ = 111.0870(10) °, *V* = 941.39(5) Å^3, R_1 (I > 2s(I)) = 0.0800, wR_2 (all data) = 0.1816. Full crystallographic data, parameters of refinement and the hydrogen bonding distances and angles are listed in Appendix C, Tables C1 and C2. The structure was deposited in the CCDC under Deposition Number 2402673.

Thermal analysis. Differential scanning calorimetry (DSC) samples were prepared using Tzero standard pans and lids and analysed using a TA Instruments Q2000 differential scanning calorimeter by first equilibrating at 25 °C and then heating to 400 °C at 10 °C/min. Heat-cool-heat DSC samples were heated first to 220 °C, cooled back down to 25 °C, then heated again to 400 °C. Modulated DSC samples were first equilibrated at 25 °C then heated to 350 °C using a modulated method with a scanning speed of 3 °C/min, an amplitude of ± 1 °C and a period of 60 s. The instrument was calibrated using an indium standard prior to analysis, with a melting point onset of 156.89 °C and a heat capacity of 33.971 J/g. Thermogravimetric analysis (TGA) samples were analysed using platinum pans and a TA Instruments Discovery thermogravimetric analyser, heating from 25 °C to 400 °C at 10 °C/min.

Variable Temperature X-ray Diffraction (VT-XRD). VT-XRD powder patterns were obtained using a Bruker D8 Advance A25 diffractometer with a Lynxeye detector and an Anton Paar HTK 1200N furnace, using Cu Kα radiation at a wavelength of 1.5406 Å and collecting from 4° ≤ 2θ ≤ 40°.

Dynamic Vapor Sorption (DVS). Vapor sorption isotherms were measured by dynamic vapor sorption (DVS) at 25 °C using a Dynamic Vapor Sorption Resolution instrument (Surface Measurement System, UK). The relative humidity (RH) was then increased in increments of 10% RH, starting from 40% RH up to 90% RH, returning to 0% RH, increasing again to 90% RH, and finally returning to 0% RH. The waiting time for 0.001% weight change was set to 30 min and the further step was increased or decreased automatically.

Ultra Performance Liquid Chromatography (UPLC) Analysis. The concentrations of LDM were determined using a Waters ARC UPLC -MC206 system with an ACQUITY UPLC BEH C18 column (130 Å, 1.7 µm, 2.1 mm X 50 mm, Waters Corporation, UK) and a UV detection wavelength of 305 nm. The mobile phase of acetonitrile/water was varied in a gradient method from 95/5 v/v to 5/95 v/v at a flow rate of 1 mL/min.

LDM solubility. The thermodynamic solubility of LDM Form A in phosphate buffered saline (PBS) was determined by adding an excess of Form A solid to 1 mL of solvent and stirring at 1,000 rpm for 24 hours. The samples were then centrifuged for 30 minutes at 31,000 × *g* and the supernatant was diluted appropriately to maintain absorbance readings within the UPLC standard curve. The concentration of LDM was determined by UPLC analysis, converting peak area values to concentrations via a calibration curve.

Non-sink dissolution measurements. Co-crystal **1** and LDM Form A were ground to powders and consistent particle sizes were confirmed by optical microscopy. A physical mixture of Form A and MEL was prepared by stirring the two powders together in a 1:1 molar ratio without grinding and characterised by XRPD prior to dissolution. Dissolution experiments were run in triplicate for each sample. Vessels were charged with approximately 5 mL of pre-warmed PBS at 37 °C before accurately weighed masses of each sample were added such that all slurries were at ten times the measured solubility limit of LDM. Slurries were stirred at 350 rpm for 24 hours. Aliquots of the slurries were removed at each time point, centrifuged for 30 minutes at 31,000 × *g*, and the supernatant was diluted appropriately to maintain absorbance readings within the UPLC standard curve. The concentrations were determined by UPLC analysis, converting peak area values to concentrations via a calibration curve. The solids obtained by centrifugation of the 2-hour and 24-hour aliquots were dried and analysed by XRPD.

Scanning electron microscopy (SEM). SEM samples were prepared by adding solid powders to polycarbonate wafers and coating with 25 nm of platinum using a Cressington 328 Ultra High-Resolution EM Coating System. The images were obtained using a Carl Zeiss Sigma 300 VP FEG SEM microscope, operated at 5 kV using an in-lens detector.

Micronization and conditioning. Co-crystal **1** was milled both alone and at 20% w/w with α-lactose in a 5 mL stainless steel grinding jar with one stainless steel grinding ball (6.4 mm diameter) using a Retsch MM200 Mixer Mill at a frequency of 20 Hz for 30 minutes. The resulting solids were analysed by XRPD, modulated DSC and SEM. The samples were then conditioned in a desiccator at 50 °C and 75% RH using a saturated NaCl solution,[36] and the resulting solids were analysed again by XRPD, modulated DSC and SEM.

4.3 Results and Discussion

A hydrated lenalidomide melamine co-crystal (**1**) can be prepared by mechanochemical methods such as grinding LDM Form B and MEL by hand in a pestle and mortar or in a ball mill without addition of solvent, or by slurrying LDM Forms A or B and MEL in water.

Mechanochemical grinding of the anhydrous LDM Form A with MEL, however, fails to produce a co-crystal and results in a physical mixture of the two components. This indicates the importance of hydration in the formation of stable co-crystal **1**. While single crystals of **1** could not be obtained, single crystals can be grown of a closely related LDM MEL co-crystal as a mixed methanol and water solvate (**2**) by slow evaporation from methanol. The same mixed solvate form can also be obtained as a powder by liquid-assisted grinding of LDM Form B and MEL in the presence of methanol. The XRPD patterns of co-crystals **1** and **2** are identical indicating that the two forms are isostructural, and XRPD and ^{1}H NMR analysis (Appendix C, Figures C3 and C4 respectively) shows that a slurry of co-crystal **2** in water leads to the removal of methanol from the co-crystal to give **1** without affecting the crystal structure. Leaving co-crystal **2** in open air for several days also allows all the methanol to evaporate from the crystals without affecting the X-ray powder pattern. Co-crystals **1** and **2** contain a 1:1 ratio of LDM and MEL even though a 3:1 co-crystal might be expected based on the three-fold symmetry of MEL with a D-A-D hydrogen bonding motif available on each face. Grinding both components together in either a 1:1 or 3:1 molar ratio gives the same solvated 1:1 co-crystal structure. This may be because the putative 3:1 hydrogen bonded unit of LDM and MEL packs poorly in the crystalline phase compared to the 1:1 co-crystal where interactions with solvent satisfy the hydrogen bonding capacity of the remaining MEL donors and acceptors (Figure 4.1).

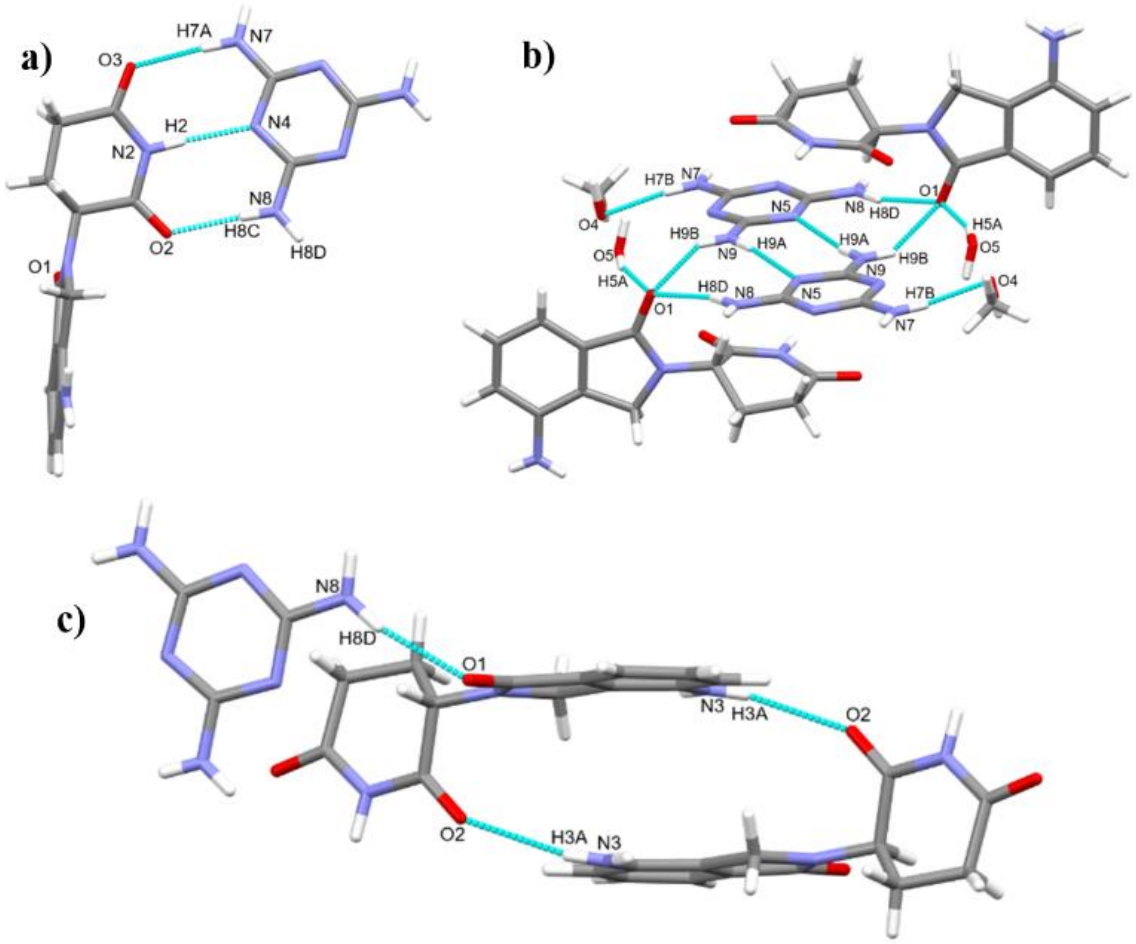

Figure 4.1. The hydrogen bonding motifs that comprise the 3-dimensional structure of **2**. a) A $2R_2^2(8)$ triple hydrogen bonding synthon links LDM and MEL in chains along the *a* axis with an N7···O3 distance of 3.007(3) Å and an N8···O2 distance of 2.924(3) Å. b) Neighbouring anti-parallel chains are connected along the *b* axis by interactions between MEL molecules and with solvent in channels aligned with the *a* axis. The majority component of the disordered methanol solvent is shown. c) LDM molecules interact with each other and with MEL via hydrogen bonds along the *c* axis, as well as forming π···π interactions between LDM molecules aligned with the *b* axis. Data were collected and processed by Dr Toby J. Blundell.

Single crystal X-ray structure determination of co-crystal **2** shows it to be a mixed solvate of the 1:1 LDM MEL co-crystal, containing one mole of methanol and 0.5 moles of water. LDM and MEL molecules are linked by a triple hydrogen bonding synthon N2-H2···N4, N8-H8C···O2 and N7-H7A···O3, and form a chain along the crystallographic *a* axis. Neighbouring antiparallel chains along *a* are connected along the *b* axis by $R_2^2(8)$ synthons between MEL molecules from opposing chains (N9-H9A···N5), N9-H9B···O1 interactions linking MEL and LDM molecules from opposing chains, and N3-H3A···O5 interactions between LDM and water altogether producing a 2D sheet. The 2D structure is further supported through π···π interactions between LDM molecules in neighbouring

antiparallel chains, with a centroid-centroid distance of 3.60 Å. Along the *c* axis, MEL interacts with LDM via N8-H8D···O1 and with methanol via N7-H7B···O4 interactions and LDM molecules are linked via N3-H3A···O2, generating a 3D structure. The methanol and water molecules occupy channels that run along the *a* axis, and the methanol molecules are disordered. XRPD analysis of the bulk sample is consistent with the calculated XRPD pattern from the single crystal data, confirming bulk solid form purity (Figure 4.2). This powder pattern also matches with co-crystal **1**, containing no methanol.

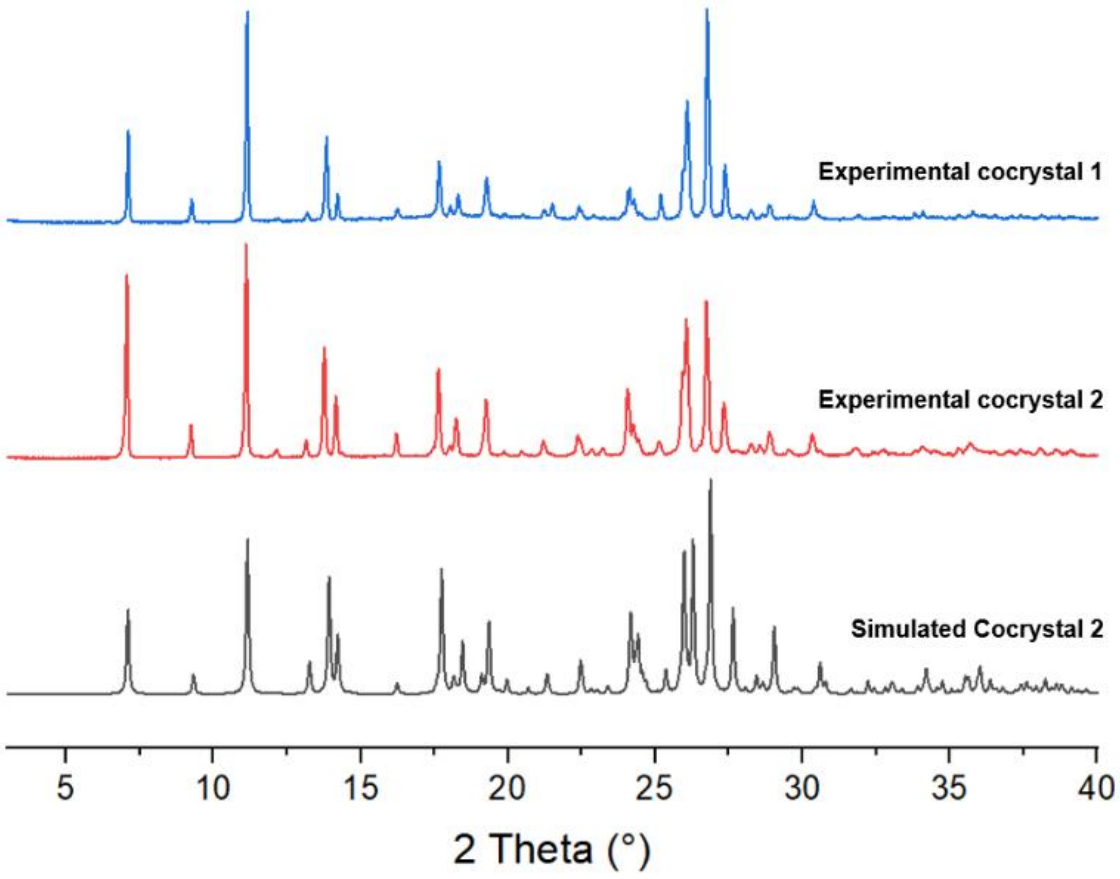

Figure 4.2. XRPD pattern simulated from the SC-XRD structure of **2** compared to the bulk experimental samples of co-crystals **1** and **2**.

While methanol is included in the channel solvate structure upon recrystallizing **2** by slow evaporation from methanol, it is not present in the isostructural crystal **1** produced by grinding or slurry of LDM Form B and MEL in water, indicating that it is not necessary for the stability of the co-crystal and can be replaced with water without disrupting the rest of the structure. This is crucial for the pharmaceutical developability of the co-crystal, since methanol solvates are classified as having inherent toxicity.[37] The remainder of this work is concerned only with co-crystal **1**, although full thermal characterisation of co-crystal **2** is included in Appendix C, Figures C5-C8. Furthermore, a hypothetical

pulmonary therapy dose of co-crystal **1** containing 10 mg of LDM active ingredient[24] would only contain approximately 5 mg of MEL, which is safe for once-daily consumption in humans weighing at least 25 kg based its tolerable daily intake.[27,28]

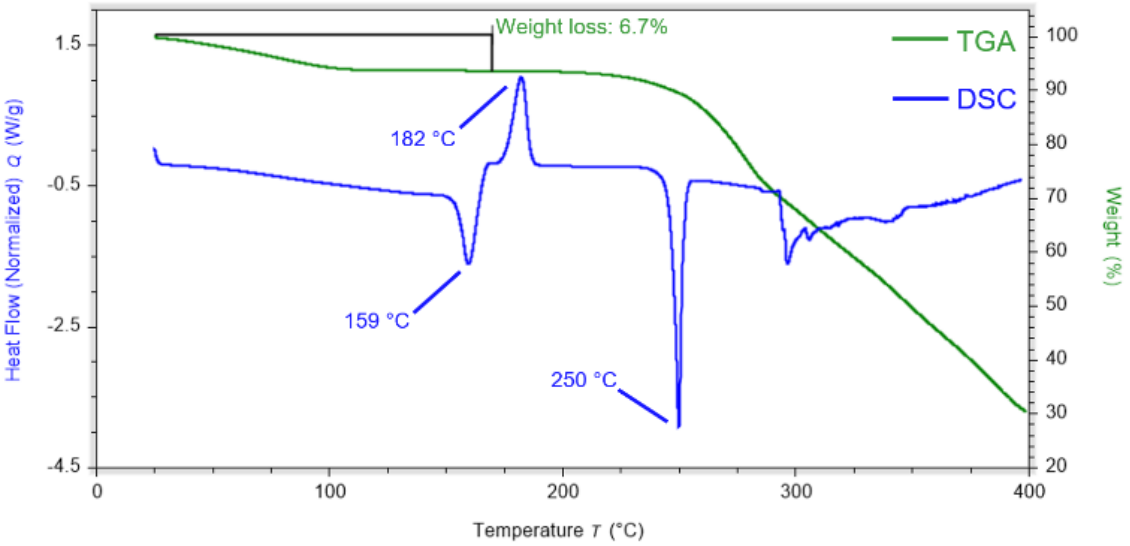

Figure 4.3. DSC and TGA thermograms for **1** showing a broad solvent loss endotherm up to approximately 110 °C followed by the melt of the resulting dehydrated co-crystal at 159 °C, its subsequent recrystallisation into LDM Form A at 182 °C and the melt of Form A with an onset temperature of 246 °C and a peak at 250 °C. MEL appears to decompose at approximately 300 °C.

A broad and shallow endotherm up to 110 °C in the DSC thermogram (Figure 4.3) corresponds to a 6.7% change in mass in the TGA trace, suggesting that the water in co-crystal **1** is relatively labile and is initially present in a molar ratio of approximately 1.5 : 1 with LDM, indicating that **1** is a non-stoichiometric hydrate. The dehydrated co-crystal appears to melt at 159 °C before recrystallizing into LDM Form A at 182 °C, followed by the melt of Form A at 250 °C, as supported by VT-XRD analysis (Figure 4.4**)**. While Form A typically melts at 270 °C,[12] the presence of MEL as an impurity in the LDM sample as well as the likelihood of poor-quality crystals forming *in situ* are potential causes of the observed melting point depression. MEL appears to be amorphous after the recrystallisation of LDM given the absence of its characteristic peaks in the VT-XRD patterns above 180 °C, however no glass transition is observed between 25 and 220 °C in the heat-cool-heat DSC experiment (Appendix C, Figure C9). A glass transition for amorphous MEL was observed, however, at 137 °C for the analogous heat-cool-heat DSC experiment on co-crystal **2** (Appendix C, Figure C7). DVS analysis (Appendix C, Figure C10) shows that **1** loses 6.8 % mass when decreasing from 40 to 0 % RH, closely matching the solvent loss observed by TGA and indicating that below 10 % RH, **1**

becomes a fully dehydrated solvate. An increase of 3.9 % mass when ramping up from 40 to 90 % RH indicates that additional water can pack into the solvent channels at high humidity, leading to a structure of **1** with a 2.5 : 1 molar ratio of water in the asymmetric unit. The absence of hysteresis in the DVS isotherm indicates that the co-crystal structure remains intact throughout the sorption and desorption cycles and is consistent with the channel solvate structure observed in the X-ray structure determination of **2**.

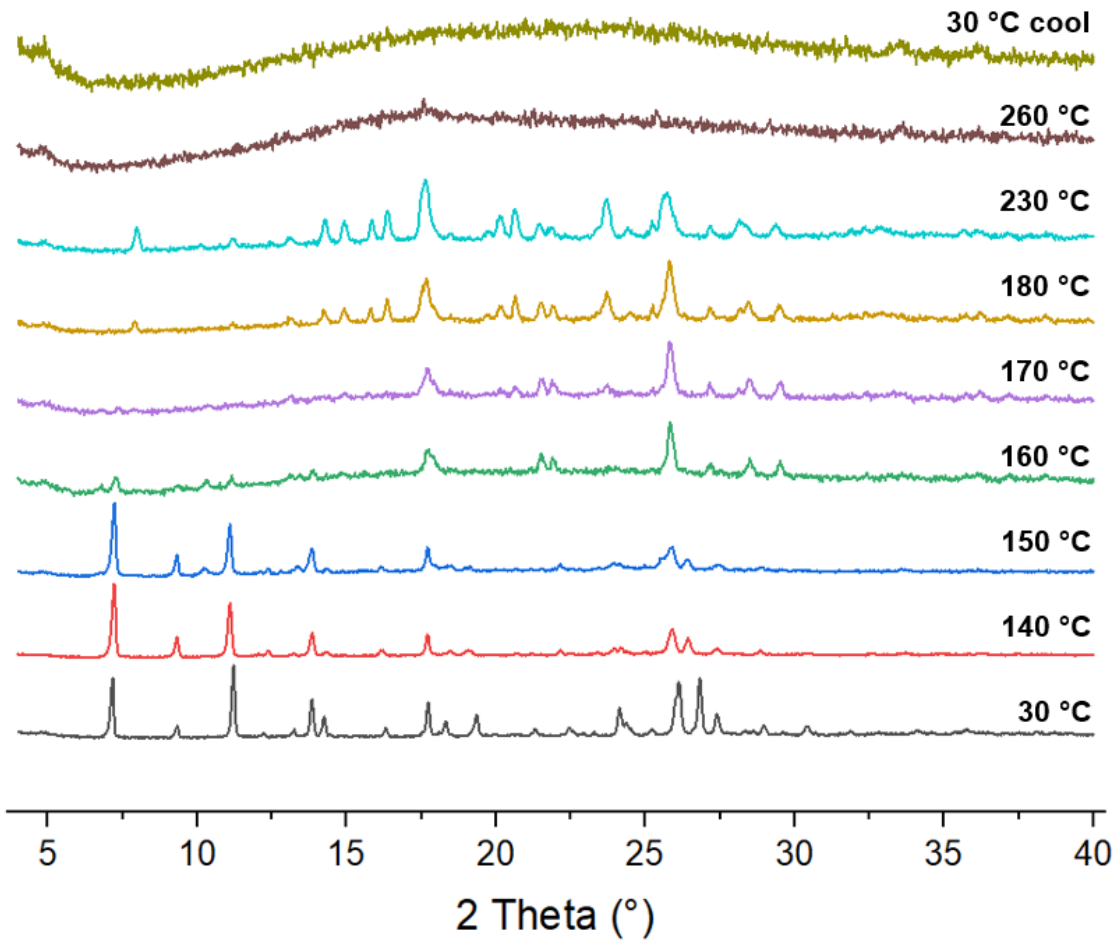

Figure 4.4. VT-XRD patterns for **1** showing recrystallisation into LDM Form A above 150 °C, which melts to leave amorphous material at 260 °C.

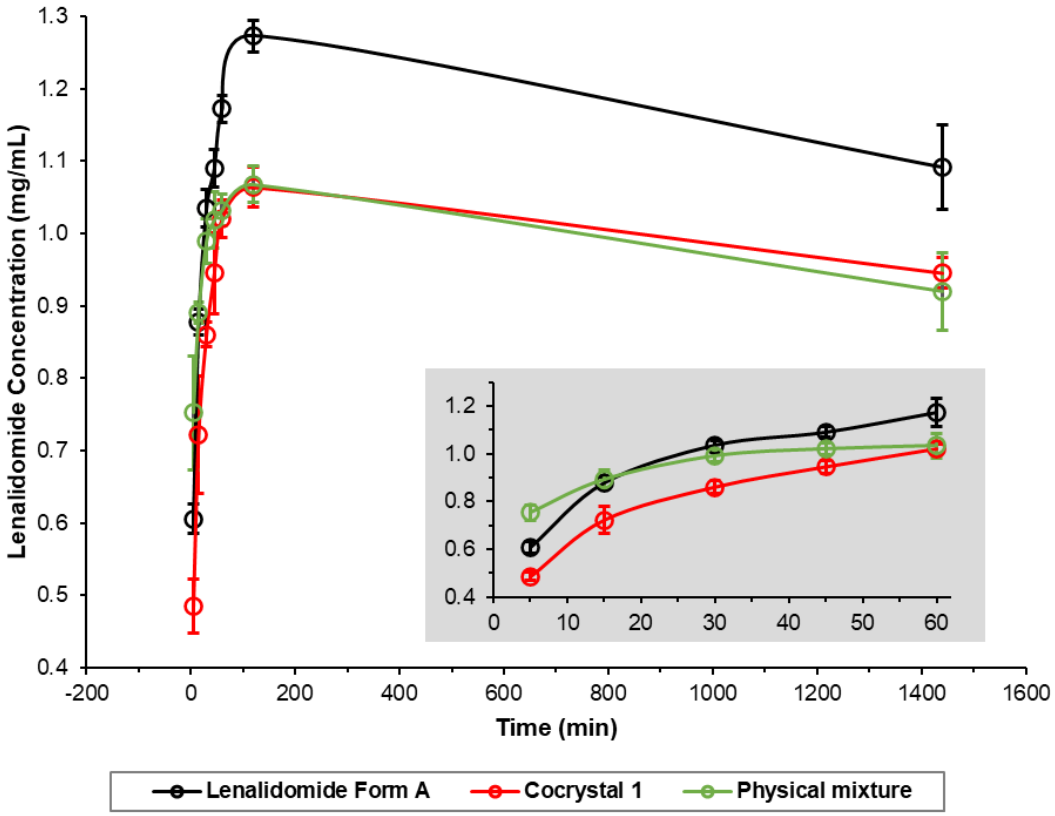

Figure 4.5. Non-sink powder dissolution profiles of LDM Form A, **1** and a physical mixture of Form A and MEL (PM) over 24 hours in PBS at 37 °C. The inlaid plot shows the first hour of the dissolution profile. Average concentrations and error bars indicating standard deviations of the mean are shown for time-points acquired in triplicate. Dissolution data points reflect a time constant due to 30 minutes of centrifugation as detailed in section 4.2, during which further dissolution may have occurred.

Figure 4.5 shows non-sink dissolution profiles for **1** in phosphate buffered saline (PBS) compared to LDM Form A, which quickly converts to Form B in aqueous solution and has a similar dissolution profile,[38] and a physical mixture of Form A with MEL (PM). PBS is a common dissolution medium employed in research studies focusing on pulmonary drug delivery.[39,40] All three samples reach their maximum solubility value between 1 – 2 hours. The maximum solubility value for **1** is approximately 20% lower than Form A, which may indicate that it has a greater lattice energy and therefore a greater thermodynamic barrier to dissolution, and/or because it is a hydrate, which typically have lower water solubility than anhydrous forms.[12,38] The significant decrease in the Form A solubility between 2 and 24 hours can also be attributed to the partial conversion of Form A into the dihydrate Form E in aqueous suspension, confirmed by XRPD analysis of solids removed at the 2- and 24-hour timepoints (Figure 4.6). The PM samples begin with a similar dissolution profile to the pure Form A sample but the solubility plateaus within the first hour and then follows the same dissolution profile as **1**. XRPD analysis

(Figure 4.6c) shows that the PM samples contain mostly **1** with traces of Form B after 2 hours and remain the same until the 24-hour timepoint. This demonstrates the strength of the interactions in the co-crystal and how quickly this co-crystal form can be obtained by slurrying in aqueous solution. XRPD analysis shows that co-crystal **1** is stable over the 24-hour period, including the PM samples where **1** is produced *in situ*. The lower solubility and greater physical stability against recrystallisation of **1** may be advantageous for inhaled formulations of LDM for the treatment of pulmonary fibrosis since these properties extend the duration of pulmonary exposure and increase the overall pharmacological effect,[11] while reducing unwanted side effects such as irritancy. While not relevant to pulmonary drug delivery, the same dissolution behaviour is observed over 24 hours of the same dissolution experiment in fasted state simulated intestinal fluid (FaSSIF) where the maximum solubility of **1** is approximately 60% lower than LDM Form A, indicating that these results are general across more than one bio-relevant medium (Appendix C, Figure C11).

Dry powder inhalable drug formulations require particle sizes between 1 – 5 μm to reach the alveolar region of the lungs and have their optimum therapeutic effect. To assess the feasibility of using co-crystal **1** as an inhalable drug, the co-crystal was micronised on its own and separately in the presence of α-lactose (lactose monohydrate), the most common excipient in pulmonary drug delivery.[41] A 20% w/w loading of co-crystal **1** was used such that the resulting micronised mixture with lactose would contain 12.5% w/w of the lenalidomide API. The micronised powders were characterised by XRPD before and after 24 hours of conditioning in a desiccator at 50 °C and 75% RH to emulate a typical industrial procedure. The powder diffractograms (Figure 4.7) show that co-crystal **1** is considerably amorphised after milling, but its crystallinity is at least partially restored after conditioning. This is confirmed by modulated DSC (Appendix C, Figure C12) which shows a glass transition (T_g) at 143 °C followed by a recrystallisation event and the melt of lenalidomide, as before in Figure 4.3**.** The sample containing α-lactose shows hardly any peaks corresponding to co-crystal **1** between milling and conditioning since it is only present at 20% w/w and considerably amorphised, but some small peaks are more prominent after conditioning. The modulated DSC thermograms of the lactose-containing samples (Appendix C, Figure C13) are dominated by the dehydration and degradation endotherms of α-lactose, obscuring any thermal events corresponding to co-crystal **1**.

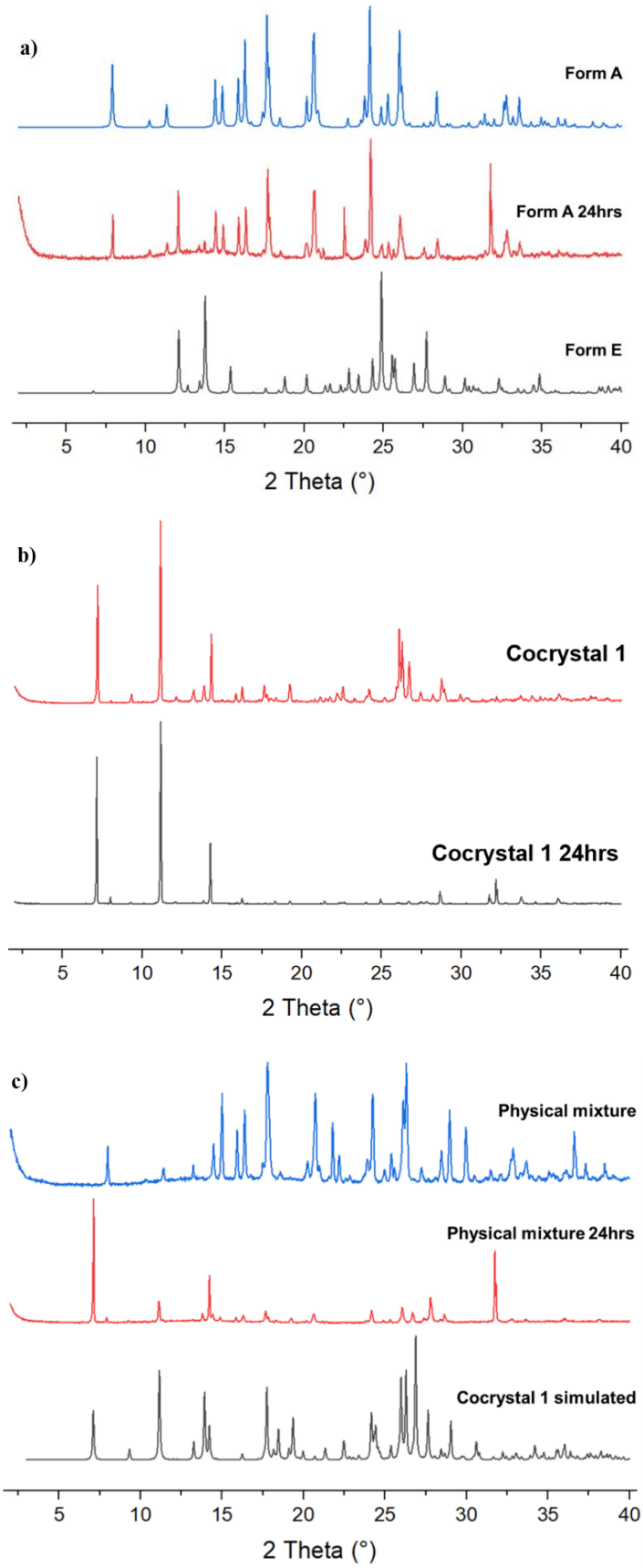

Figure 4.6. XRPD patterns comparing the powder samples before and after 24 hours of dissolution in PBS at 37 °C. **a)** Form A converts partially into Form E over 24 hours. **b) 1** remains the same form over 24 hours. **c)** A physical mixture of Form A and MEL converts into **1** over 24 hours.

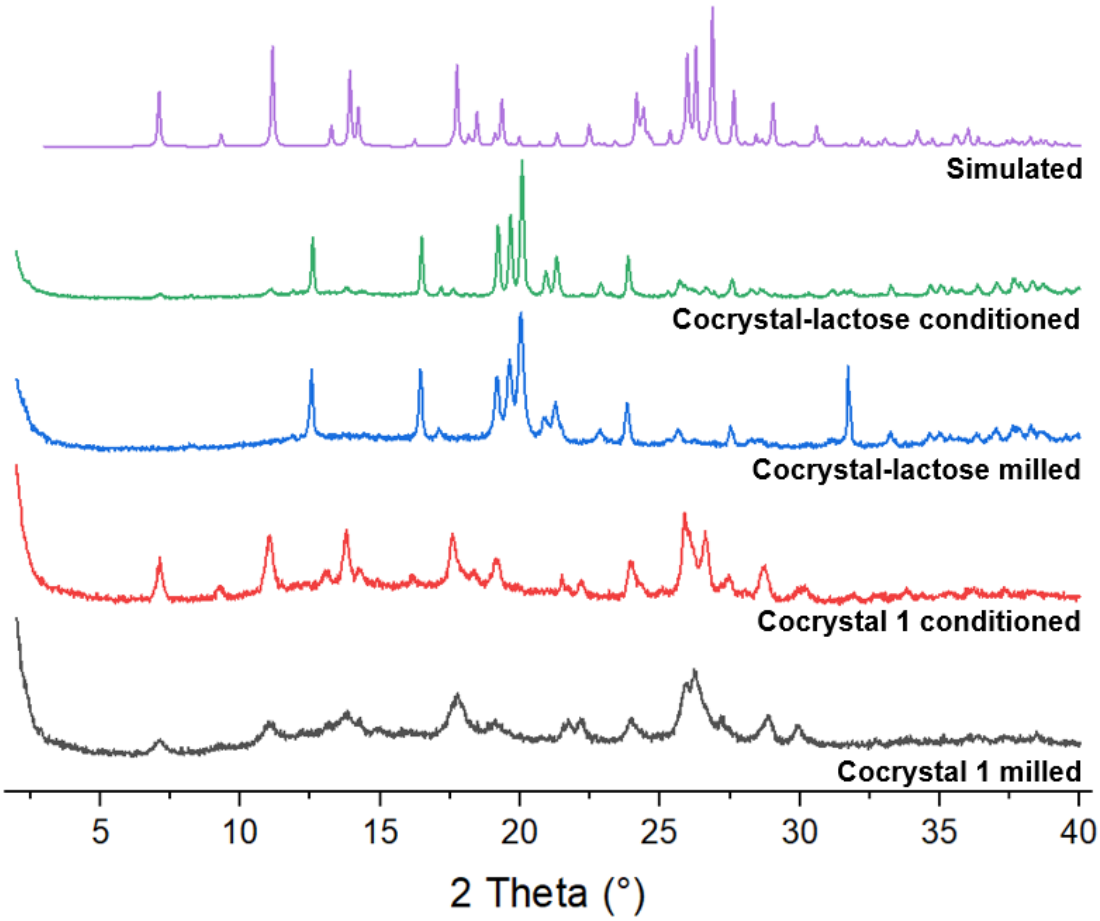

Figure 4.7. XRPD patterns comparing co-crystal **1** after micronization by milling with and without α-lactose as a model excipient, and after a subsequent 24-hour conditioning step at 50 °C and 75 % RH. The stronger peaks observed in the co-crystal-lactose samples correspond to α-lactose. The crystallinity of co-crystal **1** appears to decrease significantly after milling but is partially restored after conditioning. The simulated diffractogram is that of co-crystal **1** from the single crystal structure.

The micronised co-crystal **1**, which still contains the water present from the hydrate crystals that were milled, does not appear to recrystallise over 7 days in the same way if left open to air, indicating that the elevated temperature in the conditioning step is likely to be the critical factor in the recrystallisation of co-crystal **1**. SEM images (Figure 4.8) show that the particles of co-crystal **1** micronised alone are mostly 5 – 20 μm in diameter, although some particles appear to be clumps of agglomerated particles as small as 1 μm and some single particles are as large as 50 μm, which are an order of magnitude too large for pulmonary delivery. It is unclear whether the particles have agglomerated before or during the platinum coating process to prepare the SEM samples. Particles of co-crystal **1** micronised with α-lactose are similarly sized although the surfaces of larger particles appear to be coated with much finer particles, some of which are under 1 μm. Agglomeration is also observed in the lactose-containing samples. This demonstrates

that producing particles of co-crystal **1** and a model excipient within the appropriate size range for use in an inhalable formulation is feasible by simply milling, although the milling process would have to be optimised to reduce the size of the largest particles which would be at risk of impacting the mouth and the walls of the higher airways.[42] Furthermore, it is not obvious whether the residual amorphous material observed by XRPD and DSC is heterogeneously dispersed as separate amorphous particles amongst the crystalline particles, or whether it uniformly coats the exterior of each crystalline particle. In the latter case, the stickier and more hygroscopic amorphous surfaces can increase bridging between particles and lead to the formation of larger and less inhalable agglomerates.[43] Recrystallisation of the amorphous solid coating the particles may also cause them to grow beyond the desirable size range.

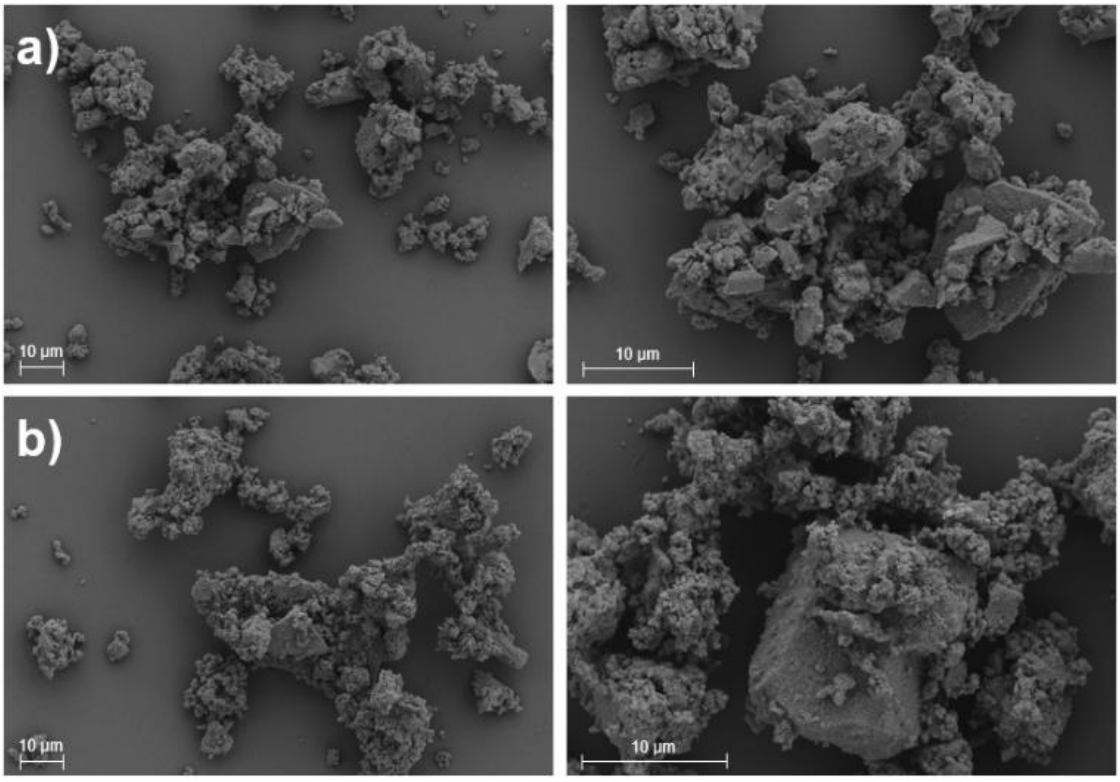

Figure 4.8. SEM images of co-crystal **1** after milling for 30 minutes and conditioning at 50 °C and 75% RH for 24h a) API alone and b) with α-lactose at 20% w/w of the co-crystal.

Non-sink dissolution profiles of co-crystal **1** before and after the micronization and conditioning step were measured in PBS at 37 °C using the same procedure as to compare co-crystal **1** with LDM Form A (Appendix C, Figure C14). The profiles for both samples are indistinguishable, suggesting that like the physical mixture of Form A and MEL in Figure 4.5, the amorphous solid rapidly recrystallises into co-crystal **1** within the aqueous slurry.

4.4 Conclusions

A co-crystal of lenalidomide and melamine was designed by the supramolecular synthon approach and synthesised. The co-crystal is based on the triple hydrogen bond ADA-DAD synthon anticipated between lenalidomide and melamine but forms a 1:1 co-crystal rather than 3:1, with additional channel-included solvent. Thermal and dynamic vapor sorption analysis show that the channel solvent is labile and a dehydrated co-crystal is stable at low humidity and room temperature, but is unstable at elevated temperature in the DSC, converting to lenalidomide Form A. Co-crystal **1** has a lower maximum solubility than Form A by approximately 20 % in PBS and 60 % in FaSSIF and is stable against recrystallisation into lenalidomide or its hydrates over a 24-hour dissolution experiment. A preliminary study shows that simply grinding **1** with α-lactose in a ball mill can produce particles of a size within the appropriate order of magnitude for use in an inhalation device, without irreversibly destroying the crystal structure or affecting the dissolution properties. Designing co-crystals of drugs with lower solubility co-formers via the supramolecular synthon approach may be a useful strategy for improving inhalable formulations of lenalidomide for treating pulmonary fibrosis.

4.5 References

1. D. J. Berry and J. W. Steed, *Adv. Drug Deliv. Rev.*, 2017, **117**, 3–24.
2. S. M. Berge, L. D. Bighley and D. C. Monkhouse, *J. Pharm. Sci.*, 1977, **66**, 1–19.
3. P. L. Gould, *Int. J. Pharm.*, 1986, **33**, 201–217.
4. G. R. Desiraju, P. David, Y. Curtin, P. Lain and C. Paul, *Angew. Chem., Int. Ed. Engl.*, 1995, **34**, 2311–2327.
5. M. L. Cheney, N. Shan, E. R. Healey, M. Hanna, L. Wojtas, M. J. Zaworotko, V. Sava, S. Song and J. R. Sanchez-Ramos, *Cryst. Growth Des.*, 2010, **10**, 394–405.
6. S. Basavoju, D. Boström and S. P. Velaga, *Cryst. Growth Des.*, 2006, **6**, 2699–2708.
7. S. Basavoju, D. Boström and S. P. Velaga, *Pharm. Res.*, 2008, **25**, 530–541.
8. B. Sandhu, A. S. Sinha, J. Desper and C. B. Aakeröy, *Chem. Comm.*, 2018, **54**, 4657–4660.
9. D. V. Bhalani, B. Nutan, A. Kumar and A. K. Singh Chandel, *Biomedicines*, 2022, **10**, 9.
10. Z. Luo, L. Ji, H. Liu, Y. Sun, C. Zhao, X. Xu, X. Gu, X. Ai and C. Yang, *AAPS PharmSciTech*, 2023, **24**, 1–14.
11. Y. Guo, H. Bera, C. Shi, L. Zhang, D. Cun and M. Yang, *Acta Pharm. Sin. B*, 2021, **11**, 2565.
12. *US Pat.*, Polymorphic forms of 3-(4-amino-1-oxo-1,3 dihydro-isoindol-2-yl)-piperidine-2,6-dione, US 7,465,800 B2, 2008.
13. L. Jia, Z. Li and J. Gong, *Pharm. Dev. Technol.*, 2019, **24**, 1175–1180.
14. *WIPO Pat.*, Lenalidomide immediate release formulations, WO 2019/081749 A1, 2019.
15. J. X. Song, J. M. Chen and T. B. Lu, *Cryst. Growth Des.*, 2015, **15**, 4869–4875.
16. J. X. Song, Y. Yan, J. Yao, J. M. Chen and T. B. Lu, *Cryst. Growth Des.*, 2014, **14**, 3069–3077.
17. L. Wang, Y. Yan, X. Zhang and X. Zhou, *Int. J. Pharm.*, 2022, **613**, 121394.

18. *WIPO Pat.*, Crystalline forms of lenalidomide, WO 2019/064222 A1, 2019.
19. *US Pat.*, Novel crystalline forms of 3-(4-amino-1-oxo-1,3 dihydro-isoindol-2-yl)-piperidine-2,6-dione, US 2014/0296291 A1, 2014.
20. M. C. Etter, *Acc. Chem. Res.*, 1990, **23**, 120–126.
21. J. S. Patton and P. R. Byron, *Nat. Rev. Drug Discov.*, 2007, **6**, 67–74.
22. J. Winkler, G. Hochhaus and H. Derendorf, *Proc. Am. Thorac. Soc.*, 2004, **1**, 356–363.
23. M. Karashima, N. Sano, S. Yamamoto, Y. Arai, K. Yamamoto, N. Amano and Y. Ikeda, *Eur. J. Pharm. Biopharm.*, 2017, **115**, 65–72.
24. S. N. Wong, K.-H. Low, Y. L. Poon, X. Zhang, H. W. Chan and S. F. Chow, *Int. J. Pharm.*, 2023, **640**, 122983.
25. K. Amraoui, K. Belhadj, B. Maître, C. Jannière-Nartey and J. Dupuis, *European Respiratory Review*, 2013, **22**, 93–95.
26. J. S. Patton, J. D. Brain, L. A. Davies, J. Fiegel, M. Gumbleton, K.-J. Kim, M. Sakagami, R. Vanbever and C. Ehrhardt, *J. Aerosol Med. Pulm. Drug Deliv.*, 2010, **23**, 71–87.
27. J. A. Tolman and R. O. Williams, *Drug Dev. Ind. Pharm.*, 2010, **36**, 1–30.
28. Melamine in Tableware Questions and Answers, https://www.fda.gov/food/economically-motivated-adulteration-food-fraud/melamine-tableware-questions-and-answers, (accessed August 2024).
29. EFSA cuts melamine TDI by 60 per cent, https://www.feednavigator.com/Article/2010/04/15/EFSA-cuts-melamine-TDI-by-60-per-cent, (accessed August 2024).
30. S. H. Yalkowsky, Y. He and P. Jain, *Handbook of Aqueous Solubility Data*, CRC Press, Boca Raton, 2nd edn., 2010.
31. C. T. Seto and G. M. Whitesides, *J. Am. Chem. Soc.*, 1993, **115**, 905–916.
32. Y. Wang, B. Wei and Q. Wang, *J. Crystallogr. Spectrosc. Res.*, 1990, **20**, 79–84.
33. K. M. Anderson, G. M. Day, M. J. Paterson, P. Byrne, N. Clarke and J. W. Steed, *Angew. Chem. Int. Ed.*, 2008, **47**, 1058–1062.
34. O. V. Dolomanov, L. J. Bourhis, R. J. Gildea, J. A. K. Howard and H. Puschmann, *J. Appl. Crystallogr.*, 2009, **42**, 339–341.
35. G. M. Sheldrick, *Acta Crystallogr. C Struct. Chem.*, 2015, **71**, 3–8.
36. A. Wexler, S. Hasegawa, *J. Res. Natl. Bur. Stand.*, 1954, **53**, 1, 19–26.
37. Food and Drug Administration, *Q3C-Tables and List Guidance for Industry 1*, U.S. Department of Health and Human Services, United States, 2018.
38. *US Pat.*, Polymorphic forms of 3-(4-amino-1-oxo-1, 3 dihydro-isoindo1-2-yl)-piperidine-2,6-dione, US 7,977,357 B2, 2011.
39. Y.-J. Son, M. Horng, M. Copley and J. T. McConville, *Dissolution Technol.*, 2010, **17**, 2, 6–13.
40. S. May, B. Jensen, C. Weiler, M. Wolkenhauer, M. Schneider and C.-M. Lehr, *Pharm. Res.*, 2014, **31**, 3211–3224.
41. G. A. Hebbink, M. Jaspers, H. J. W. Peters and B. H. J. Dickhoff, *Adv. Drug Deliv. Rev.*, 2022, **189**, 114527.
42. P. C. L. Kwok and H. K. Chan, *Ther. Deliv.*, 2013, **4**, 877–878
43. P. H. M. Janssen, L. M. N. Bisharat and M. Bastiaansen, *Int. J. Pharm. X*, 2023, **6**, 100216.

5. Non-mimetic Gels Direct Novel Crystallisation Behaviour of Lenalidomide

5.1 Introduction

While conventional solution-phase crystallisation remains the predominant approach used in industry, crystallisation in gels has also proven effective in directing and controlling drug polymorphic outcomes.[1,2] Gel-phase crystallisation approaches can produce different polymorphic or morphology outcomes to solution-phase methods in the same solvents because the gel network inhibits convection and sedimentation, allowing the diffusion-limited growth of the crystallisation substrate.[1,3,4] The gel fibres themselves may also act as an active surface for heterogeneous secondary nucleation, where the underlying periodicity of the gel fibres arising from aggregation may directly influence the growth of the crystal.[5] This has allowed the discovery of new solid forms and unique crystal morphologies,[2,5,6] as well as preventing concomitant crystallisation and enabling the selective growth of desired polymorphs.[4,7–11] Gel-phase crystallisation may also offer an alternative route to isolate solid forms of hard-to-crystallise bRo5 compounds such as PROTACs.

Supramolecular gels are comprised of low molecular weight gelators (LMWGs) that form gel fibres via self-assembly.[12–15] Bis(urea) compounds are some of the most explored LMWGs since they are cheap, easy to prepare and can gel a wide range of solvents, providing a greater variety of gel phases in which drug crystallisation can be screened in comparison to conventional polymeric hydrogels.[2,16,17] LMWGs such as these form physical gels reversibly via non-covalent interactions such as hydrogen bonding, π-stacking, van der Waals forces, charge transfer interactions, electrostatic interactions, and metal coordination, meaning that many supramolecular gels are stimuli responsive and can be re-dissolved *in situ* by addition of anions, change in pH, sonication or exposure to light to enable simple isolation of the crystallised substrate.[18–24] Bis(urea) gelation in particular is driven by molecular recognition of the self-complementary urea moiety, where the ability to simultaneously donate hydrogen bonds through two NH protons and accept hydrogen bonds through lone pairs on the carbonyl oxygen allows the formation of bifurcated intermolecular hydrogen bonds between urea groups, known as a urea α-tape motif.[25] The structure of LMWGs can also be designed to mimic the crystallisation substrate by including similar moieties in the gelator end-group functionalities: there are numerous examples of drug-mimetic bis(urea) gelators capable of producing unique crystallisation outcomes that could not be obtained from the

equivalent solution phase, nor from gel-phase crystallisation where the gelator was non-mimetic. Previous work by the Steed group has shown that the metastable red form of ROY can be crystallised within gels of a drug-mimetic bis(urea) compound whereas only the thermodynamic stable yellow form could be obtained from solution or using non-mimetic gelators and proposed that the red form may have been templated by conformational matching with the gelator in the fibres.[3] The concomitant crystallisation of thalidomide Forms α and β, and of barbital Forms I, III and V, observed by crystallisation in either the solution-phase or within gels of non-mimetic gelators could only be prevented by crystallizing within gels of drug-mimetic bis(urea) gelators, indicating that the drug-mimetic structure was responsible for the crystallisation control rather than the viscous gel media itself.[4] Mimetic gels have also revealed a new dimethylacetamide solvate of cisplatin and given rise to a new crystal habit of the known dimethylformamide solvate by crystallisation in bis(urea) gelators, where the only crystals suitable for analysis by single crystal X-ray diffraction (SC-XRD) were obtained using the drug-mimetic gelator.[5] Similarly, the crystal habit of metronidazole crystals can be controlled within gels of a drug-mimetic gelator, yet not in those of a non-mimetic gelator.[6] The thermodynamic polymorph of flufenamic acid can be obtained by crystallisation within gels of a pH-responsive drug-mimetic bis(amide) gelator, whereas only the metastable form can be obtained from solution-phase crystallisation.[7] Finally, the highest energy Form 2 of mexiletine hydrochloride, usually only stable at high temperature, can be crystallised within gels of a drug-mimetic bis(urea) gelator and the metastable Form 3 can be produced selectively in gels over the concomitant mixture with Form 1.[8]

As discussed in Chapter 4, lenalidomide (LDM) is an immunomodulatory drug used for the treatment of multiple myeloma and pulmonary fibrosis, similar in structure to thalidomide and pomalidomide, and a molecular fragment of PROTAC AZ1. Celgene originally reported eight polymorphic and solvate forms of LDM termed Forms A – H; including the commercially available hemihydrate, Form B, marketed under the trade name Revlimid®.[26] In 2017, Chennuru et al. reported the single crystal structures of seven polymorphs, hydrates, and solvates termed Forms 1 – 7 of which Forms 1, 2 and 7 are the same as Celgene Forms A, B and E (Table 5.1).[26–28] In addition, a further three forms termed α, β and DH have been reported, although not structurally characterised, and it is not clear whether these represent genuinely new materials.[29] There are also reports of co-crystals with urea, 3,5-dihydroxybenzoic acid, acesulfamate, nicotinamide and melamine.[30–34] Despite the rich solid form landscape already revealed through several extensive solid-form screening studies, it is possible that new crystalline forms of LDM may be accessible from gel-phase crystallisation or that hard-to-access polymorphs such as the metastable Form 4, which can only be accessed by dehydrating one of the LDM hydrate forms, could be crystallised directly within gel media. In this

chapter, the gel-phase crystallisation of LDM within gels of both a drug-mimetic gelator and a non-mimetic gelator is presented to study the importance of structural resemblance between drug and gelator in determining the crystallisation outcome. Gel systems capable of controlling LDM crystallisation were then taken forward to PROTAC crystallisation studies, in order to test the principle while minimizing the consumption of valuable and limited PROTAC sample.

Table 5.1. Nomenclature and details of LDM crystal forms with structures in the CSD. Forms 1-7 are designated by Chennuru et al.,[27] whereas the original patents used lettering A-H to distinguish between forms.[26,28]

LDM crystal form	Details
Form 1, Form A	Anhydrous, thermodynamic
Form 2, Form B	Hemihydrate
Form 3	DMF solvate
Form 4	Anhydrous, metastable
Form 5	DMSO solvate
Form 6, Form C	Acetone solvate
Form 7, Form E	Dihydrate

5.2 Experimental

Materials and general methods. Lenalidomide (LDM, racemic form), L-alanine methyl ester hydrochloride, triethylamine, 1,6-diisocyanatohexane, D,L-aminoglutethimide and 4,4′-methylenebis(2,6-diethylphenyl isocyanate) were purchased from Merck. All other chemicals and solvents were available from commercial sources and used without further purification. FTIR spectra were recorded between 4000 and 550 cm^{-1} using a Perkin Elmer 100 FT-IR spectrometer with a μATR attachment. Powder X-ray diffraction (XRPD) patterns were collected at room temperature using a Bruker AXS D8 Advance GX003410 diffractometer with a Lynxeye Soller PSD detector, using Cu Kα radiation at a wavelength of 1.5406 Å and collecting from $2° \leq 2\theta \leq 40°$. Nuclear Magnetic Resonance (NMR) spectra were recorded on a Bruker Neo-400 spectrometer with operating frequencies of 400.20 MHz for ^{1}H and 100.63 MHz for ^{13}C unless otherwise specified. Mass spectrometry was performed using a Waters Acquity SQD machine running in positive electron spray (ES) mode. Elemental analysis was performed using an Exeter Analytical Inc. CE-400 elemental analyser.

Gelator syntheses. Gelators were prepared using the previously published procedures for non-mimetic gelator G1[35] and imide-mimetic gelator G2[4] respectively. Full procedures and characterisation are provided in Appendix D.

Gel screening. The gelation behaviour of compounds G1 and G2 was analysed in a range of solvents suitable for crystallizing LDM. Gelator solids and solvents were added to vials and gently heated to dissolve them at an initial concentration of 1% w/v. Gel formation was typically observed several minutes after cooling to room temperature, confirmed in the first instance by a qualitative vial inversion test. Some samples formed only weak gels or viscous liquids on cooling which failed the inversion test but produced gels after heating again to re-dissolve followed by 30 seconds of sonication. Samples that dissolved but precipitated upon cooling were repeated at 0.5% w/v. Insoluble samples at 1% w/v were not studied further. Samples that formed gels were repeated at progressively lower concentrations in 0.1% w/v increments until only a partial gel formed, characterised either by the gel being too weak to pass the inversion test or by the presence of some un-gelled solvent remaining, to determine the critical gelation concentration (CGC). Samples increasing in concentration by the same 0.1% w/v increments were also produced to determine the maximum gelation concentration (MGC).

Crystallisation studies of LDM. The solubility of LDM in a range of 24 solvents varying in polarity and boiling point was assessed at room temperature using a gravimetric method. An excess of LDM powder was stirred as a slurry in each solvent for 24 hours using an Expondo roller mixer at 100 rpm, before filtering and transferring an accurately measured volume of supernatant (1 mL) to a pre-weighed vial and leaving to evaporate in an oven at 200 °C overnight before weighing again to determine the dissolved concentration of LDM. Solubility data are listed in Appendix D, Table D1. The crystallisation of LDM was then studied in a range of ten solvents in which LDM has a solubility of at least 1 % w/v and which can be gelled by gelator G1 and/or G2, by passive cooling of hot solutions prepared at 1.2 times the measured solubility of LDM at room temperature. Polymorphic outcome and phase purity were assessed by XRPD and SC-XRD, and crystal growth time and morphology were assessed by optical microscopy.

Gel-phase crystallisation studies of LDM and AZ1. Gel-phase recrystallisation experiments were conducted by adding LDM or AZ1 powder and gelator powder to vials followed by dilution with solvents such that the resulting concentration of the drug was at 1.2 times the measured drug solubility at room temperature, and the resulting concentration of gelator was at either the CGC or MGC for each solvent. Control crystallisation experiments of each drug in the absence of gelator were set up at the same time. The samples were left undisturbed for 2 weeks prior to XRPD and SC-XRD

analysis, or until crystals were visible. XRPD slides were prepared by transferring samples of the gel-crystal mixtures using a spatula and leaving them to dry by evaporation prior to analysis. Where possible, polymorphic outcome was confirmed with unit cell determination by single crystal X-ray diffraction. Gel-phase crystallisation experiments that differed in outcome from the control experiment were repeated in triplicate. Crystallisation experiments of LDM within blended gels were also conducted using the same method but consisting of varying molar ratios of both G1 and G2 (molar ratios of 2:8, 4:6, 6:4 and 8:2) in both dioxane and cyclopentanone.

Rheometry. Cyclopentanone gels of G1 and G2, at both CGC and MGC, and both with and without LDM crystals, were analysed by oscillatory rheometry. G1 gels of dioxane and nitrobenzene containing AZ1 were also analysed. Rheological experiments were performed using an advanced rheometer AR 2000 from TA Instruments equipped with a chiller and using a stainless steel 20 mm parallel plate geometry. Samples of the gels were transferred on to the center of the rheometer plate using a spatula. The oscillatory stress sweep measurements were performed in the range of 0.1 – 100 Pa at a constant frequency of 1 Hz. Frequency sweep measurements were performed in the range of 1 – 10 rad/s at a constant oscillatory stress of 0.5 Pa, within the linear viscoelastic region of the gels analysed.

Scanning electron microscopy (SEM). SEM samples of G1 and G2 cyclopentanone xerogels, both with and without LDM crystals, were prepared by adding solid powders to polycarbonate wafers and coating with 5 nm of platinum using a Cressington 328 Ultra High-Resolution EM Coating System. The images were obtained using a Carl Zeiss Sigma 300 VP FEG SEM microscope, operated at 5 kV using an in-lens detector.

Single crystal X-ray Diffraction (SCXRD). Single-crystal X-ray diffraction data for LDM Form 8 and G1 Form B were collected at 120 K using Mo Kα radiation at a wavelength of 0.71073 Å on a Bruker D8 Venture 3-circle diffractometer. The structures were solved by direct methods and refined by full-matrix least squares on F^2 for all data using Olex2[36] and SHELXTL.[37] All non-hydrogen atoms were refined in anisotropic approximation, while hydrogen atoms were placed in the calculated positions and refined in riding mode unless otherwise specified. Crystal data for LDM Form 8: $C_{15.5}H_{17}N_3O_{3.5}$, M_r = 301.32, space group $P\bar{1}$, a = 11.1851(7) Å, b = 12.1666(8) Å, c = 12.6313(8) Å, α = 62.187(2) °, β = 78.555(2) °, γ = 66.633(2) °, V = 1395.46(16) Å^3, R_1 (I > 2s(I)) = 0.0574, wR_2 (all data) = 0.1243. Full crystallographic data, parameters of refinement and the hydrogen bonding distances and angles are listed in Appendix D, Tables D2 and D3. The structure was deposited in the CCDC under Deposition Number 2453375. Crystal data for G1 Form B: $C_{16}H_{30}N_4O_6$, M_r = 374.44, space group $P1$, a = 4.6439(4) Å, b = 6.0527(5) Å, c = 17.9322(15) Å, α = 95.476(3) °, β = 94.920(3) °, γ = 108.854(3) °, V = 471.17(7) Å^3, R_1

(I > 2s(I)) = 0.0521, wR_2 (all data) = 0.1231. Full crystallographic data, parameters of refinement and the hydrogen bonding distances and angles are listed in Appendix D, Tables D4 and D5. The structure was deposited in the CCDC under Deposition Number 2453376.

NMR titrations. ^{1}H NMR spectra were recorded on a Varian DD2-500 spectrometer with an operating frequency of 499.53 MHz. Gelator solutions at a concentration of 1.4 mg/mL (below CGC) in dioxane-d_8 were analysed at 90 °C before sequentially adding aliquots of a lenalidomide solution in dioxane-d_8 and re-acquiring the spectra such that the concentration of lenalidomide doubled between consecutive ^{1}H spectra. This was repeated until eight scans had been acquired for each gelator, ranging from a gelator : drug molar ratio of 1 : 0.04 up to 4.5 : 1, near the solubility limit of LDM in dioxane. Chemical shifts for lenalidomide and the gelators were monitored throughout the titration.

Diffusion-ordered NMR spectroscopy (DOSY). A 600 MHz Varian spectrometer equipped with an Agilent OneNMR Probe able to deliver a maximum pulsed field gradient of 62 G cm^{-1} was used to conduct diffusiometry studies (^{1}H Diffusion-Ordered SpectroscopY or DOSY) using a convection-compensated pulse sequence based on a combination of a double stimulated echo and bipolar pulsed gradients. The pulse sequence, Dbppstee_cc, is part of the VNMJ 4.2 pulse sequence library.[38,39] Twenty gradient amplitudes ranging from 1.95 to 29.25 G cm^{-1} spaced in equal steps of gradient squared were used. Thirty-two transients were collected. Thirty-two steady-state transients were used. The number of complex data points was 21,406, covering 6.3 kHz. The diffusion-encoding pulsed gradient duration (d) was 2.0 ms. The diffusion time was (D) 200 ms. The gradient stabilisation delay was 2.0 ms. The repetition time was 6.4 s, of which 3.4 s comprised the acquisition time. The unbalancing factor was 0.15. The results were analysed with VNMRJ 4.2 using mono-exponential fittings. The effects of non-uniform field gradients were accounted for using methods developed by G.A. Morris.[40]

5.3 Results and Discussion

Gel screening and characterisation

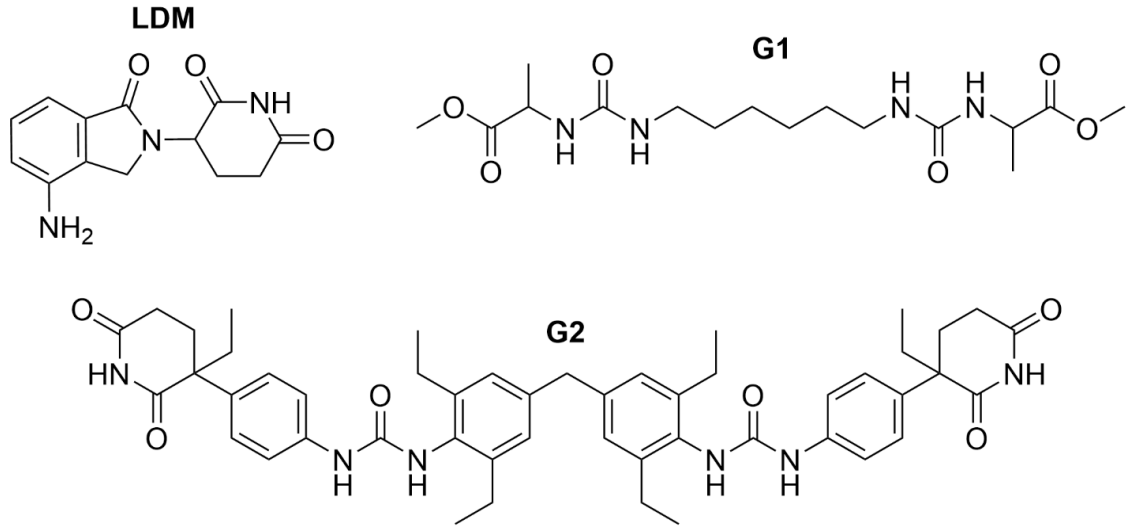

Scheme 5.1. Chemical structures of lenalidomide (LDM) and gelators **G1** and **G2**. The structure of **G1** is unrelated to LDM whereas **G2** contains imide moieties in its end groups that mimic the imide moiety in LDM.

Two bis(urea) gelator compounds, **G1** and **G2** (Scheme 5.1), were chosen for gel-phase crystallisation studies of lenalidomide (LDM). **G1** is a representative non-mimetic gelator bearing no structural resemblance to LDM, whereas **G2** is an imide-based drug-mimetic gelator shown previously to control the concomitant crystallisation of thalidomide, which is closely related to LDM.[4,35] Comparing the crystallisation behaviour of LDM within gels of these two compounds provides an opportunity to understand how important drug-gelator structural similarity is for controlling drug crystallisation in the gel phase. **G1** and **G2** were synthesised via the previously reported methodologies. The observed gelation behaviour of **G1** and **G2** differs somewhat from our previously reported results, particularly for **G2,** which appears to gel fewer solvents than originally reported. This may be caused by trace impurities from synthesis, differences in moisture content or because the reagents were obtained from different suppliers. Table 5.2 shows the gelation results along with critical gelation concentrations (CGCs) and maximum gelation concentrations (MGCs) for **G1** and **G2** in a range of organic solvents. **G1** is capable of gelling eight solvents with CGCs between 0.5 – 1 % w/v, while **G2** is capable of gelling six solvents with CGCs between 0.1 – 2 % w/v. Cyclopentanone, nitrobenzene and 1,4-dioxane can be gelled by both compounds at similar gelator concentrations, allowing for a direct comparison of the gel-phase recrystallisation of LDM between three gel-phase systems differing only in the composition of the gelator.

Table 5.2. Gelation results in good solvents of LDM, as well as CGC and MGC (% w/v) for gelators **G1** and **G2**. IS: insoluble; P: precipitates on cooling; G: gel; G*: gels with sonication. Alcoholic solvents labelled "+DMSO" had a few drops of DMSO added to improve the dissolution of the gelator, as previous work has shown it to improve the solubility of **G2** and enable gelation of alcoholic solvents.[4]

Solvent	G1	CGC	MGC	G2	CGC	MGC
Methanol	IS	-	-	IS	-	-
Ethanol	G	0.7	1.0	IS	-	-
Propanol	P	-	-	IS	-	-
1-Butanol	P	-	-	IS	-	-
2-Butanol	P	-	-	IS	-	-
Cyclopentanone	**G**	**0.5**	**2.0**	**G***	**1.5**	**2.0**
Cyclohexanone	P	-	-	P	-	-
Acetone	G	1.0	2.0	IS	-	-
Acetonitrile	G	0.4	1.0	IS	-	-
Nitrobenzene	**G**	**0.2**	**2.0**	**G**	**0.1**	**2.0**
Nitromethane	IS	-	-	IS	-	-
1,4-Dioxane	**G**	**1.0**	**2.0**	**G**	**1.0**	**2.0**
THF	G	0.5	1.0	P	-	-
Methanol +DMSO	IS	-	-	G	2.0	2.5
Ethanol +DMSO	P	-	-	P	-	-
Propanol +DMSO	P	-	-	P	-	-
1-Butanol +DMSO	P	-	-	G	1.5	1.8
2-Butanol +DMSO	P	-	-	G	0.5	2.5

Representative gels of **G1** and **G2** in cyclopentanone at both CGC and MGC were characterised by oscillatory rheometry. Shear stress sweeps (Figure 5.1a-b) show that both gels have considerably larger storage and loss moduli at MGC compared to CGC, along with a higher yield stress, indicating the formation of stronger gels at higher gelator concentration. Frequency sweeps (Appendix D, Figure D1) corroborate these findings, showing that the gels have a constant viscosity over a range of frequencies when exposed to a shear stress within the linear viscoelastic region (LVR). SEM images (Figure 5.1c-e) show the structure of xerogels produced by drying the cyclopentanone gels of **G1** and **G2**. The gels at their MGC generally comprise linear ribbon-like fibres

approximately 500 nm in width, forming a physically entangled network. By contrast, the gel at CGC has a less well-defined fibrous network, explaining the difference in mechanical strength.

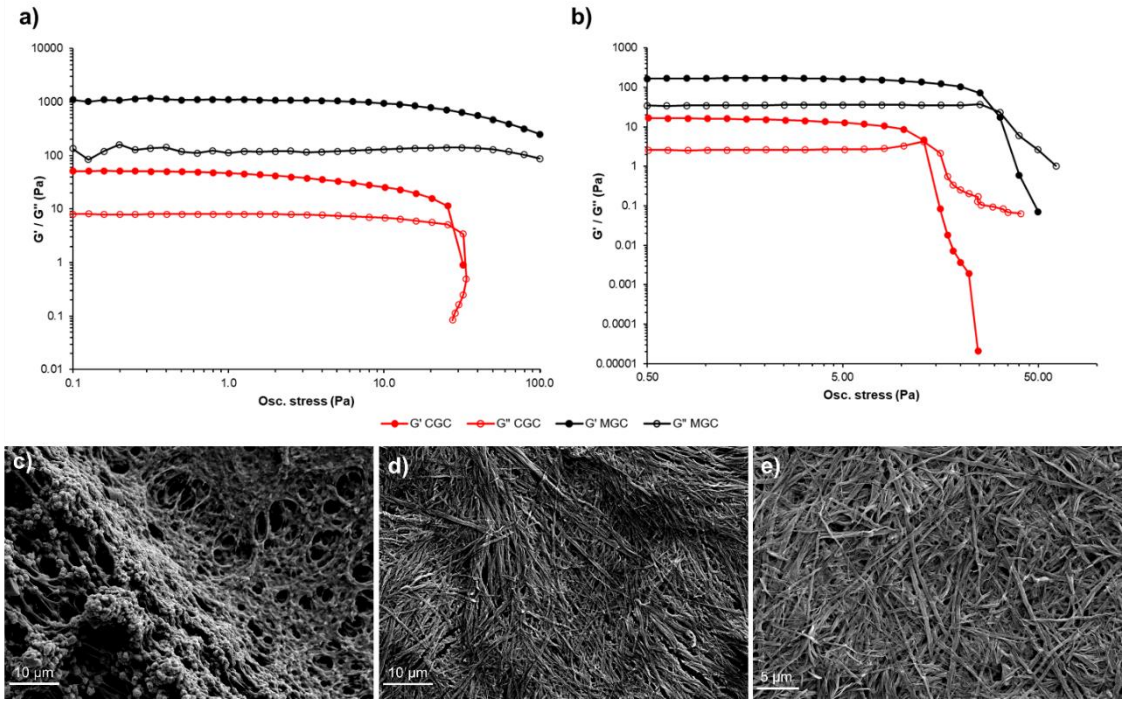

Figure 5.1. a-b) Oscillatory stress-sweep rheological analysis of cyclopentanone gels of a) **G1** and b) **G2** at both CGC and MGC as representative examples, measured at a constant frequency of 1 Hz. Gels are characterised by a G' that is approximately an order of magnitude greater than G" up to the yield stress. Both gel systems have considerably larger storage and loss moduli at MGC compared to CGC. c-d) SEM images of xerogels produced from gels of c) **G1** cyclopentanone (CGC), d) **G1** cyclopentanone (MGC) and e) **G2** cyclopentanone (CGC).

Gel-phase crystallisation of LDM

Gel-phase recrystallisation experiments were performed at a consistent supersaturation of LDM in each solvent, at both the CGC and the MGC of the gelator separately. The crystals grown within gel media are difficult to characterise by optical microscopy due to the opacity of most **G1** and **G2** gels, but in general, they appear to grow at a similar rate to the solution-phase control experiments and were small – in some cases only visible by SEM (Figure 5.2). Not all experiments produced crystals of sufficient size and quality for unit cell determination by SC-XRD analysis, but all samples could be analysed by XRPD. However, attempts to dissolve the **G1** and **G2** gels by addition of anions,[23,24,35] sonication, stirring or heating were unsuccessful, meaning that the crystals could only be transferred to XRPD slides by removing them with a spatula. As a result, in most cases, the powder patterns of the LDM crystals are convoluted with the dried **G1** or **G2** xerogels.

A combination of XRPD and SC-XRD was used, where possible, to determine the polymorphic outcome of each experiment, and the results for gel-phase crystallisation experiments at both CGC and MGC are shown alongside the solution-phase control experiments in Table 5.3. The presence of LDM crystals has varying effects on the strength of the resulting **G1** and **G2** gels, as observed by rheometry (Appendix D, Figure D3). While the presence of crystals appears to weaken gels of **G1** and **G2** in cyclopentanone at their CGC and MGC respectively with decreased storage and loss moduli and a lower yield stress, the **G1** cyclopentanone gel at MGC is relatively unaffected, and the **G2** cyclopentanone gel at CGC is stronger and higher yielding. If the drug crystals grow before or at the same time as the gel fibres, this indicates that depending on the gel system, the presence of crystals may either inhibit the growth and entanglement of gel fibres to form a strong 3-dimensional network or instead make the fibrous network stronger and more rigid, perhaps through inclusion of small crystalline particles within the gel fibres themselves. Alternatively, if the gel network forms before any drug crystals grow, it suggests that interactions between the growing fibres and the drug in solution has an effect on the resulting fibrous network. Qualitative assessment via a vial inversion test indicates that the gels form within several minutes of sonication in most cases, however due to the opacity of the resulting samples, it is unclear how rapidly the LDM crystals grow within the gel media.

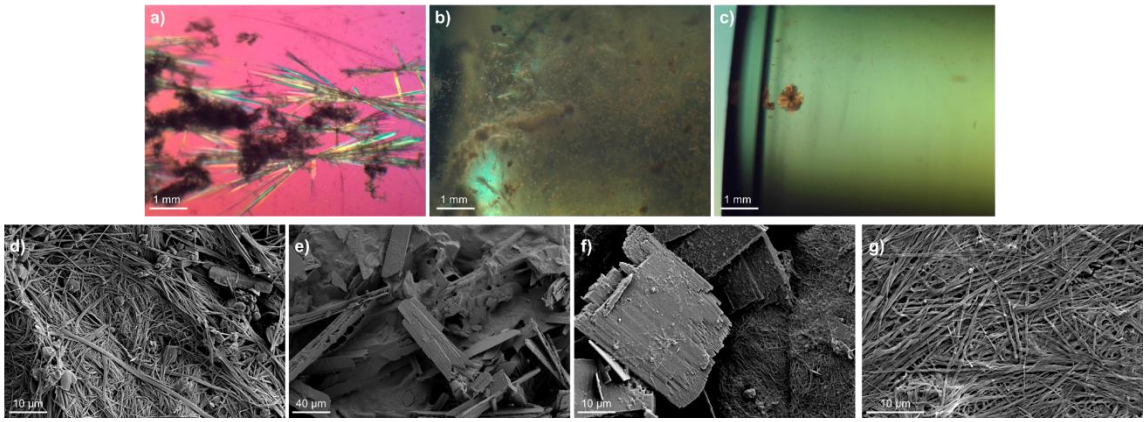

Figure 5.2. Polarised optical microscopy images of LDM crystals grown inside gels of a) **G1** ethanol, b) **G1** cyclopentanone and c) **G2** nitrobenzene all at CGC. SEM images of crystals grown inside gels of d) **G1** dioxane, e) **G1** cyclopentanone (CGC), f) **G1** cyclopentanone (MGC) and g) **G2** cyclopentanone (MGC). LDM crystals grown within gel media were typically of insufficient size and quality for unit cell determination by SC-XRD analysis, with SEM images showing crystals of approximately 20 – 150 µm in length depending on the xerogel sample.

Table 5.3. Polymorphic outcome from gel-phase LDM recrystallisation experiments, determined from a combination of XRPD and SC-XRD analysis. LDM Form 8 refers to a novel cyclopentanone hemi-solvate discovered by SC-XRD analysis of the gel-crystal mixture. Unless otherwise specified, **G1** crystallised in the previously reported Form A structure.[35]

Gelator	Solvent	Crystallisation outcome		
		CGC	MGC	Control
1	EtOH	Form 4 + **G1**	Form 4 + **G1**	Form 1
1	Dioxane	Form 1	Form 1	Forms 1 + 2
1	Acetone	**G1**	**G1**	Form 6
1	MeCN	**G1**	**G1**	Forms 1 + 2
1	Nitrobenzene	Form 4 + **G1**	Amorphous	Form 4
1	Cyclopentanone	Form 8 + **G1**	Form 1 + **G1**	Form 1
1	THF	Form 1 + **G1** Forms A + B	Form 1 + **G1**	Form 1
2	MeOH+DMSO	Amorphous	Amorphous	Form 4
2	Dioxane	Form 2 + **G2**	Form 2 + **G2**	Forms 1 + 2
2	Nitrobenzene	Amorphous	**G2**	Form 4
2	Cyclopentanone	Form 1	Form 1	Form 1
2	1-BuOH+DMSO	Amorphous	Amorphous	Forms 1 + 5
2	2-BuOH+DMSO	Form 5	**G2**	Form 5

While many gel-phase recrystallisation experiments using **G1** produce the same polymorphic outcome as the control experiments (Appendix D, Figure D4), LDM crystallisation within gels of **G1** in three solvents differs from the control experiments in the absence of gelator (Appendix D, Figure D5). XRPD and SC-XRD analysis show that while the control crystallisation of LDM from ethanol produces a pure phase of Form 1, **G1** gels reproducibly contain crystals of the metastable anhydrous Form 4 phase instead, alongside crystals of the **G1** gelator (Figure 5.3a). This indicates that the metastable Form 4 can be grown directly from the gel phase as opposed to the previously reported methods of dehydrating Forms 2 or 7,[29] offering a direct route to crystallizing this polymorph. XRPD analysis of the **G1** dioxane gel-phase recrystallisation experiment at CGC revealed a unique powder pattern, similar to but distinct from the **G1** dioxane control gel containing no LDM, unlike the same experiment at MGC, which matches the control gel (Figure 5.3b). SC-XRD analysis on both samples revealed crystals of LDM Form 1 but not LDM Form 2, which both grow concomitantly from the control crystallisation in the solution phase. While this may be evidence that the **G1** gels of

dioxane could prevent the concomitant crystallisation of LDM Forms 1 and 2 and produce only Form 1, the presence of Form 2 within the gel cannot be ruled out.

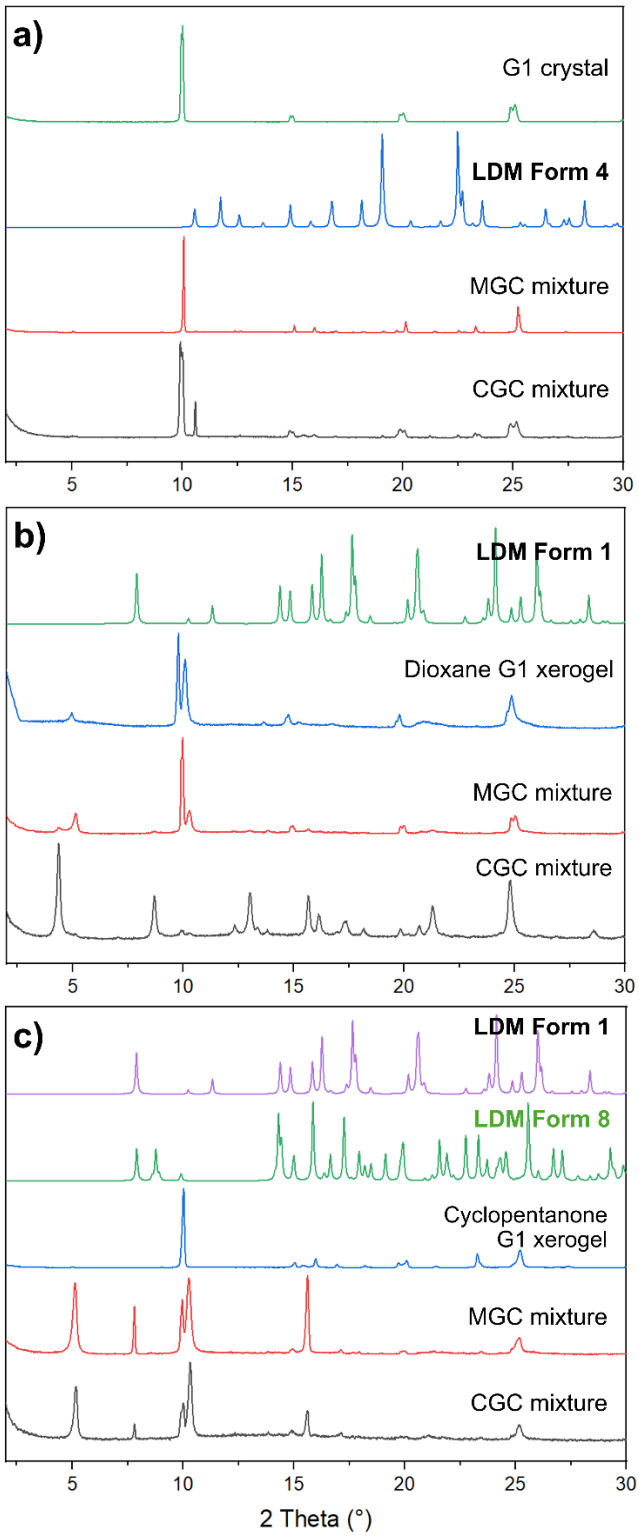

Figure 5.3. XRPD patterns of gel-crystal mixtures analysed from LDM recrystallisation experiments in **G1** gels of a) ethanol, b) dioxane and c) cyclopentanone. Gel-crystal mixtures obtained from experiments at both CGC and MGC are compared. In b) and c), a control gel of **G1** containing no LDM was also analysed as a dried xerogel for comparison. This data was used in

combination with single-crystal XRD to determine the polymorphic outcome from crystallisation within **G1** gels. The powder pattern for LDM polymorphs and solvates, including Form 8 (cyclopentanone hemi-solvate) were simulated from the SC-XRD data and shown in bold. Overlay plots comparing the experimental gel-crystal mixture patterns and simulated LDM crystal patterns are presented in Appendix D, Figure D5.

Most notably, crystallisation within **G1** gels of cyclopentanone affords crystals of a novel cyclopentanone hemi-solvate of LDM (referred to henceforth as LDM Form 8), and the structure was determined by SC-XRD (Figure 5.4). Form 8 contains 1.0 mole of LDM and 0.5 moles of cyclopentanone, with two molecules of LDM and one molecule of cyclopentanone in the asymmetric unit. One molecule of each LDM enantiomer is present in the asymmetric unit, with each enantiomer involved in a different intermolecular hydrogen bonding arrangement. Separate enantiomers make homodimer interactions via $R_2^2(10)$ hydrogen bonded ring motifs[41] consisting of two N103-H103•••O103 or N203-H203•••O202 interactions for the R- and S- enantiomers respectively, with N•••O distances of 2.919(3) Å and 2.826(3) Å respectively. The R-enantiomers also form head-to-tail interactions along the *b* axis via N102-H10A•••O103 interactions. R- and S- enantiomers interact with each other via N202-H20A•••O101 interactions with an N202•••O101 distance of 2.976(4) Å. The LDM S- enantiomers interact with cyclopentanone molecules via N202-H20B•••O1 interactions with an N202•••O1 distance of 3.058(8) Å. The XRPD pattern (Figure 5.3c) of the gel-crystal mixture sampled from the experiment is dominated by the xerogel peaks and a pure phase could not be obtained by dissolving the gel. Attempts to reproduce this crystal by cooling crystallisation or slurry of LDM (starting as Form 1 or 2) in cyclopentanone in the absence of gel for 2 weeks were unsuccessful, yielding only LDM Form 1 (Appendix D, Figure D6). This may indicate that LDM Form 8 can only be obtained by gel-phase crystallisation.

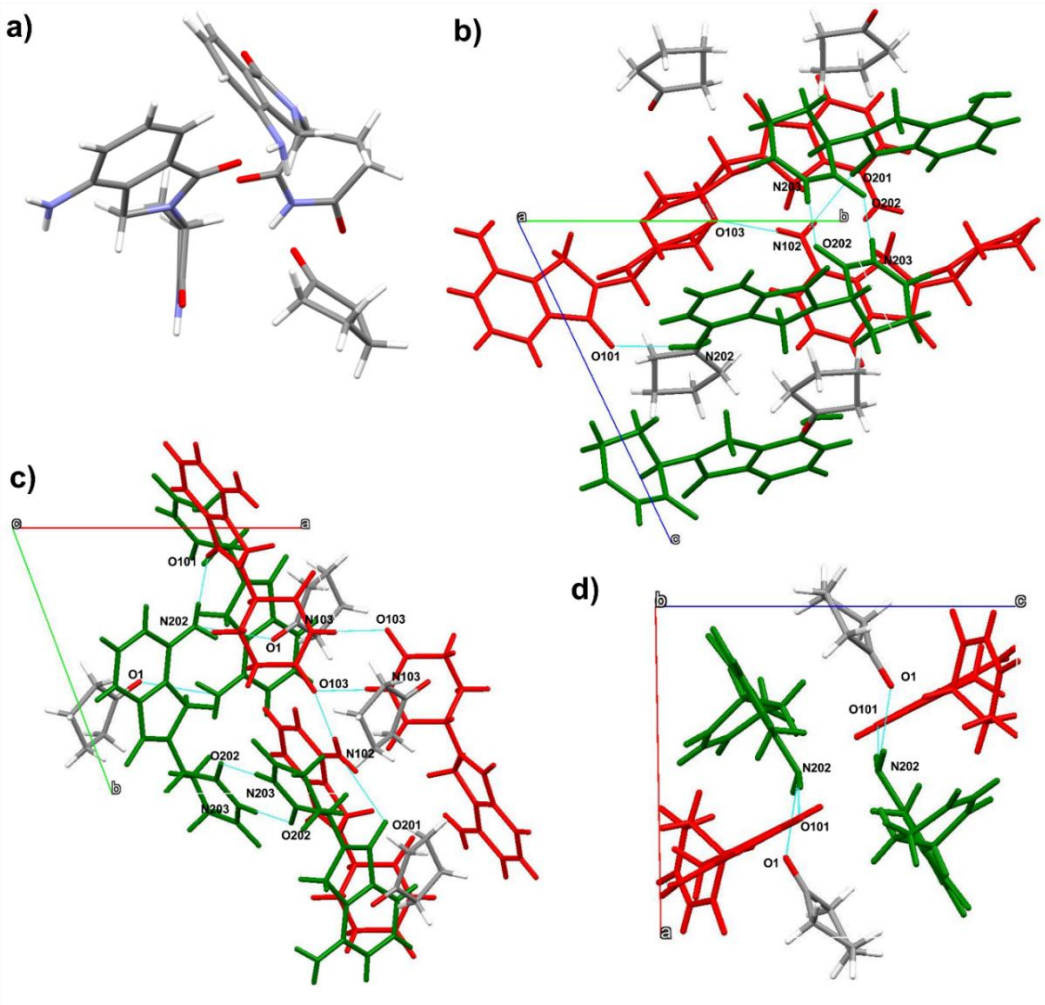

Figure 5.4. The crystal structure of LDM Form 8 (cyclopentanone hemi-solvate). Views of a) the asymmetric unit containing two enantiomers of LDM and one molecule of cyclopentanone, b-d) views down unit cell axes, with LDM enantiomers R- and S- shown in green and red respectively. c) Each LDM enantiomer makes homodimer interactions via $R_2^2(10)$ hydrogen bonded ring motifs consisting of two N103-H103•••O103 or N203-H203•••O202 interactions for the R- and S- enantiomers respectively, with N•••O distances of 2.919(3) Å and 2.826(3) Å respectively. R- and S- enantiomers interact with each other via N202-H20A•••O101 interactions with an N202•••O101 distance of 2.976(4) Å. The LDM S- enantiomers interact with cyclopentanone molecules via N202-H20B•••O1 interactions with an N202•••O1 distance of 3.058(8) Å. Data were collected and processed by Dr Toby J. Blundell.

A new polymorph of the gelator **G1** (referred to henceforth as **G1** Form B) was also discovered upon analysis of the gel-phase recrystallisation experiments from the **G1** tetrahydrofuran gels, in which LDM Form 1 grows alongside gelator crystals at both CGC and MGC. The structure of **G1** Form B was solved via single crystal X-ray diffraction (Figure 5.5a-c), revealing similar features to the originally reported Form A, such as the $R_2^1(6)$ urea α-tape hydrogen bonding motif.[35] The powder pattern of Form B simulated

from the SC-XRD data is very similar to that of Form A, obtained directly from synthesis (Figure 5.5d).

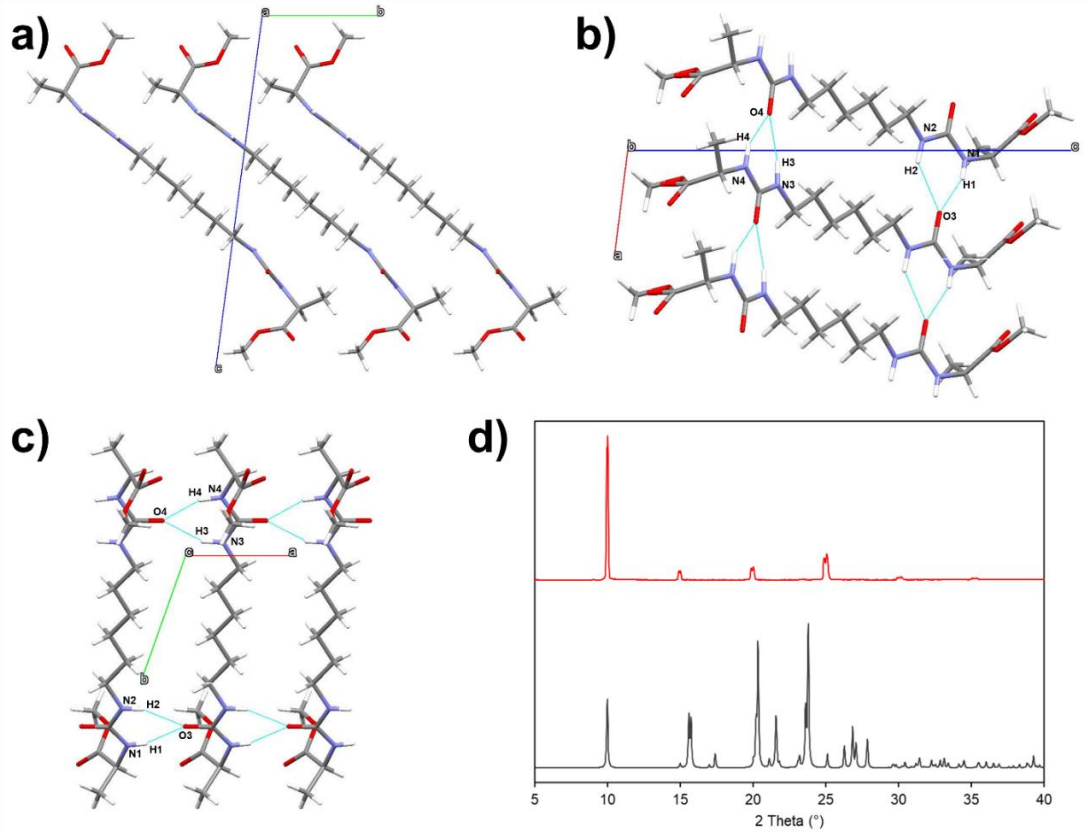

Figure 5.5. a-c) Views down the unit cell axes of the crystal structure of **G1** Form B. b-c) Similarly to Form A,[35] the **G1** molecules stack via a pair of $R_2^1(6)$ urea α-tape hydrogen bonding motifs via N1-H1•••O3, N2-H2•••O3, N4-H4•••O4 and N3-H3•••O4 interactions. d) XRPD diffractograms of **G1** Form A obtained from synthesis (top) compared to Form B powder pattern simulated from SCXRD data (bottom). Data were collected and processed by Dr Toby J. Blundell.

By contrast, the results in Table 5.3 show that crystallisation within **G2** gels does not change the polymorphic outcome compared to the solution-phase control experiments in all solvents except dioxane. As for the **G1** dioxane gels, the gel-phase crystallisation experiments in **G2** dioxane gels at both CGC and MGC produce a different XRPD pattern compared to the **G2** dioxane control gel containing no LDM (Appendix D, Figure D7), and unit cell determination by SC-XRD analysis finds only LDM Form 2, unlike the analogous **G1** gel-phase crystallisation experiments, where only Form 1 is found. However, the XRPD patterns cannot confirm the phase purity of the Form 2 crystals identified by SC-XRD due to the broad and intense xerogel peaks, therefore concomitant crystallisation of Form 1 cannot be ruled out as for the analogous **G1** case. The challenge in analysing the polymorphic outcome of these samples is compounded by the generally

poor crystallinity of LDM grown within the **G2** gels, with some samples found to be completely amorphous by XRPD. Crystallisation experiments in **G2** cyclopentanone gels produce only Form 1, with no amount of the novel Form 8 detected. These results contrast to previously reported examples where the drug-mimetic gelator exerted control over the polymorphic outcome of the crystallizing API, whereas non-mimetic gelators had no such effect.[3,4,6] In the present case, the non-mimetic **G1** gelator has been used to discover a new LDM solvate and is capable of growing the metastable anhydrous form rather than the thermodynamic form in certain solvent systems, while the drug-mimetic gelator has not. This is particularly interesting since the same **G2** gelator was previously shown to be capable of affecting the crystallisation behaviour of the very similar API thalidomide.

Gel-phase crystallisation experiments were also conducted in gel blends of **G1** and **G2** in varying molar ratios, in both cyclopentanone and dioxane. Given the considerable structural differences between the **G1** and **G2** molecules, in particular the difference in linker, it is likely that the blended gels consist of two independent, non-interacting fibrous networks where **G1** and **G2** fibres grow orthogonally,[35] although it is possible that they entangle with each other to form a 3-dimensional network. XRPD analysis of the resulting gel-crystal mixtures (Appendix D, Figure D8) is complicated by the presence of strong gelator signals and poor crystallinity of the LDM crystals, but in cyclopentanone it appears that the novel LDM Form 8 can grow from gels composed of any composition containing at least 20 % w/w of **G1** (Appendix D, Table D6). This suggests that simply the presence of some **G1** fibres within the gel network is sufficient to induce the growth of LDM Form 8, and the presence of **G2** has a neutral effect. XRPD analysis of the dioxane gels show that xerogel signals dominate the diffractogram at all gelator ratios and the LDM is poorly crystalline, although it appears that Form 2 may crystallise at higher ratios of **G1**. Since the pure **G1** gels previously analysed appeared to contain only Form 1 instead of the concomitant mixture, this evidence suggests that these gels probably do not prevent the concomitant crystallisation of Forms 1 and 2.

LDM-gelator interactions

It is unclear whether interactions between drug and gelator are responsible for the previously reported examples of supramolecular gelators controlling API crystallisation outcome. If the drug and gel fibres interact strongly, these interactions may be detectable when the drug and gelator are in solution. Suitable methods to study these interactions are titration and diffusiometry. Solutions of **G1** and **G2** at 1.4 mg/mL (below CGC) in dioxane-d_8 contain gelatinous precipitates at room temperature, which can be dissolved

to produce clear solutions suitable for solution-state NMR analysis at 90 °C. Dioxane-d_8 solutions of LDM were titrated into these hot gelator solutions to study potential drug-gelator interactions in the resulting solution, increasing from a 25-fold excess of gelator to a 4.5-fold excess of drug (Figure 5.6). In both samples, the LDM integrals increase concomitantly with the addition of LDM. In the **G1** sample (Figure 5.6a), very few signals corresponding to either drug or gelator change in chemical shift with increasing LDM concentration, aside from a small increase of 0.02 – 0.03 ppm in the **G1** urea-NH signals at approximately 5.0 and 5.1 ppm, and an increase of 0.05 ppm in the LDM NH signals at 9.5 and 10.4 ppm corresponding to the amine and imide groups respectively. These NH signals are particularly sensitive to water content, NH-water exchange, inter- and intra-molecular interactions and viscosity. Because of this, changes in only the NH signals and no other signals are insufficient evidence of strong intermolecular interactions between LDM and **G1** or self-association of either component. In the **G2** sample (Figure 5.6b), there are more signals that change chemical shift upon addition of LDM, including several **G2** aromatic-region signals from both the linker and the end groups, and the NH moieties in **G2** (urea and imide), all increasing in chemical shift by around 0.05 – 0.07 ppm. This suggests that intermolecular interactions involving **G2** are more likely, with several regions of the molecule displaying changes in chemical shift. However, many neighbouring signals show no detectable variation, and the only LDM signals showing any shift are again the NH signals, which increase in chemical shift by approximately 0.07 ppm. Given the magnitude of the changes observed, strong drug-gelator interactions are unlikely in either system. NMR diffusiometry studies (Diffusion Ordered Spectroscopy, DOSY) conducted in DMSO-d_6 are presented in Appendix D, Figure D9 and further support the claim that drug-gelator interactions are negligible. Strong interactions between either **G1** or **G2** and LDM in solution would result in both molecules having the same (or close) diffusion coefficients, but this was not the case.

However, the NMR titrations presented in Figure 5.6 are limited by the choice of solvent since the solubility of LDM in dioxane is approximately 8 mg/mL, meaning that only a relatively narrow range of LDM : gelator molar ratios were analysed. It is possible that binding interactions may not have been detected because the full binding curve was not sampled. The binding at 90 °C is also likely to be far weaker than at room temperature, with NMR samples in dioxane requiring considerable heating to dissolve gelatinous precipitates. While an NMR solvent such as DMSO-d_6 is less relevant for this system since neither G1 nor G2 form gels of DMSO, it would have been possible to analyse a greater range of LDM : gelator molar ratios in this solvent due to the much higher solubility of LDM. Titration in DMSO-d_6 comes with additional complications, however, since the solvent itself may compete for hydrogen bonding interactions with either solute and disrupt the drug-gelator binding.

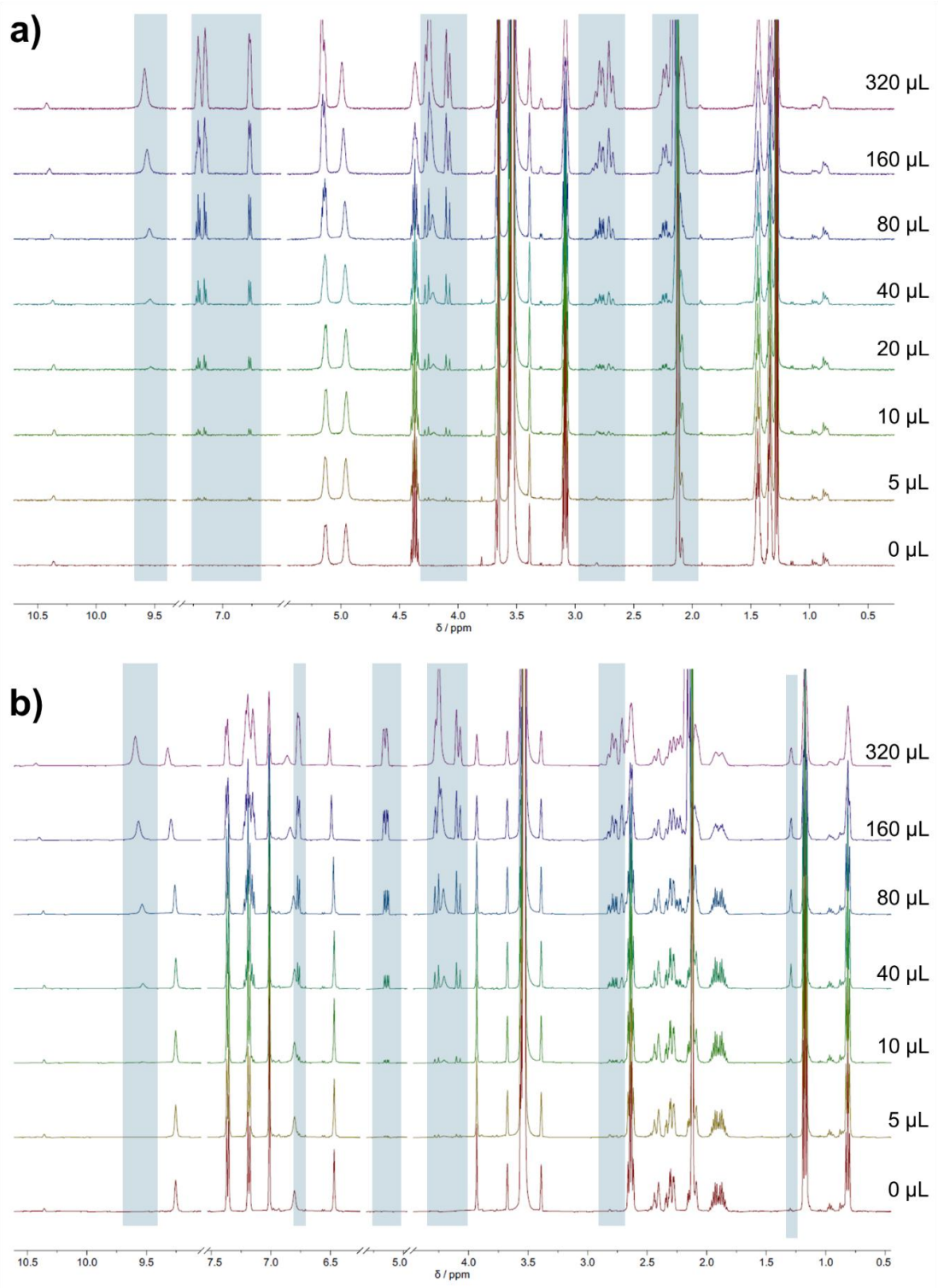

Figure 5.6. 500 MHz ^{1}H NMR titration plots for dioxane-d_8 gels of a) **G1** and b) **G2** (initially at 1.4 % w/v) as aliquots of a dioxane-d_8 solution of LDM (7 mg/mL) were added. Residual solvent peaks for dioxane and water are present as strong signals at 3.5 and 2.1 ppm respectively. The gelator-drug molar ratio increased from 1 : 0.04 up to 4.5 : 1 over 8 steps. LDM signals increase in intensity as larger aliquots are added, but there are no significant changes in chemical shift for either drug or gelator component in either titration, suggesting that no strong binding interactions are present in the solution state. Data were collected and interpreted by Dr Juan Aguilar-Malavia.

Although no strong interactions were detected, NMR titrations in solution do not reveal whether LDM molecules could become physically incorporated in the gel fibres when they form, potentially affecting the surface composition of the fibres which may link to the observed crystallisation phenomena. However, the ^{1}H NMR spectra of a **G1** gel of dioxane-d_8 at 1.5 % w/v containing a fixed 0.5 % w/v of LDM obtained at 25 °C, 50 °C and 90 °C (Appendix D, Figure D10) also show that as the gelatinous sample is warmed up and dissolves, the signals corresponding to **G1** increase in intensity while the LDM signals do not change in integral relative to the residual DMSO-d_6 solvent peak, indicating that no significant quantity of LDM molecules are incorporated into the **G1** gel fibres. This may differ in the **G1** gels of cyclopentanone and/or ethanol and therefore be linked to the observed differences in crystallisation outcome compared to the solution phase controls, however these solvents were intractable for solution state NMR studies.

Taken together, this suggests that if any drug-gelator interactions linked to the gel-phase crystallisation phenomena are present, they are too weak to detect by NMR in the solution state. This means that the observed crystallisation phenomena are likely related to general gel-phase properties such as limited molecular diffusion and/or convection, the removal of active surfaces from glass or dust to provide a homogeneous medium for nucleation, or the presence of the gel fibres as an active surface with a periodicity that can transfer to the growing API crystal through heterogeneous secondary nucleation.[10] If this is the case, then the periodicity of the **G1** fibres may be such that it can template the growth of LDM Form 2 in ethanol and LDM Form 8 in cyclopentanone, while the periodicity of the **G2** fibres does not. This is also compatible with the observation that LDM Form 8 could be grown within blended gels at a **G1** ratio as low as 20% w/w, assuming that **G1** and **G2** fibres grow orthogonally and that the presence of some **G1** fibres templates the growth of Form 8 while the remaining **G2** fibres are inert with respect to crystal growth. Alternatively, a recent discovery is that confinement can have a significant effect on polymorph crystallisation.[42–44] For example, crystallisation from a structured ternary fluid can influence polymorph nucleation by restricted diffusion locally perturbing supersaturation levels and influencing the free energy barrier for the growth of different polymorphs.[44] While the mesh size of the **G1** and **G2** gels are unknown, it is possible that they are on a comparable scale to the nano-sized domains within structured ternary fluids, and the confinement effect provided by **G1** fibrous meshes influences the crystallisation outcome.

Gel-phase crystallisation of AZ1

The gel-phase crystallisation study of LDM demonstrated that **G1** gels were capable of crystallising the metastable anhydrous Form 4 from ethanol instead of the thermodynamic anhydrous Form 1 that grows from the solution phase, and that a new cyclopentanone hemi-solvate form could be grown from **G1** gels of cyclopentanone. **G1** gels of dioxane could also potentially inhibit the concomitant growth of both Forms 1 and 2 observed in the solution phase, producing only Form 1, although the presence of Form 2 in small quantities could not be ruled out. Of the solvents that **G1** can gel, PROTAC compound AZ1 has good solubility in dioxane, nitrobenzene and cyclopentanone, however the solubility is very high (>20% w/v) in cyclopentanone making it intractable to grow crystals in this solvent given the limited quantity of AZ1 material available. Gel-phase crystallisation experiments of AZ1 were therefore conducted in **G1** gels of dioxane and nitrobenzene only, at both CGC and MGC. Oscillatory rheometry (Appendix D, Figure D11) shows that the **G1** gels containing AZ1 are stronger at MGC than CGC, although the nitrobenzene gel at CGC was very weak and collapsed upon removal from its original vial, hence its rheometry is omitted.

The drug solids grown inside the gels were powders that were difficult to observe by optical microscopy since the gels themselves were opaque. XRPD analysis (Figure 5.7) shows that crystallisation in nitrobenzene gels produced no crystalline AZ1 material and that the crystallisation in dioxane gels at CGC matches the control gel containing no AZ1. However, analysis of the dioxane gel at MGC reveals a set of unique peaks that do not match the dioxane control gel, the gelator itself nor any of the three reported crystalline forms of AZ1.[45] Unit cell determination by SC-XRD was not possible due to the poor quality and small size of the crystalline particles produced, so it is unclear whether the unique peaks correspond to an unknown crystalline phase of AZ1 or the gelator. However, the new peaks do occur at the same angles as the unique peaks identified for the analogous gel-phase crystallisation of lenalidomide, suggesting that they arise from the xerogel structure and not from the drug substance. They are therefore unlikely to correspond to a new AZ1 solid phase. However, only a small number of gel-phase recrystallisation experiments were attempted with AZ1 due to the limited sample quantity and it is possible that crystallisation within gels using other solvents or gelators may impact the solid form outcome.

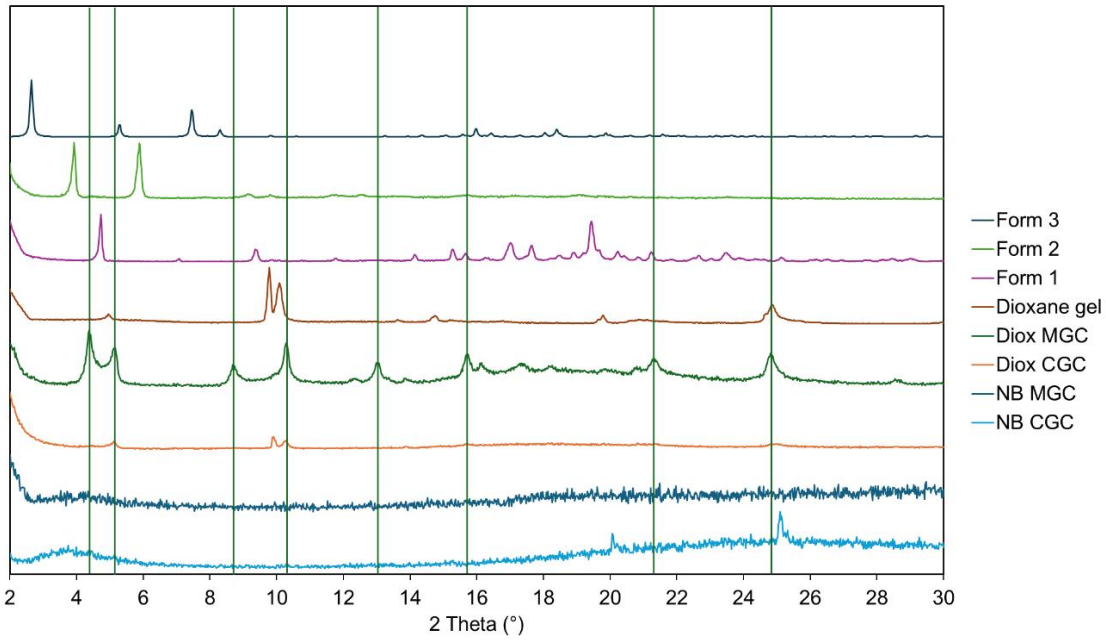

Figure 5.7. XRPD patterns of gel-crystal mixtures analysed from AZ1 recrystallisation experiments in **G1** gels of dioxane and nitrobenzene. Experiments at both CGC and MGC are compared. The dioxane gel was also analysed as a xerogel containing no AZ1. The powder pattern of AZ1 Form 3 was simulated from SC-XRD data presented in Chapter 2. While the gel-crystal mixture sampled from the dioxane gel at MGC shows peaks that do not match any of the three known forms of AZ1, they do match the new xerogel peaks observed for the dioxane xerogels previously analysed in the experiments to recrystallise LDM.

5.4 Conclusion

Crystallizing lenalidomide within gels formed with a non-mimetic bis(urea) gelator revealed a novel hemi-solvate of cyclopentanone and facilitated the direct growth of the metastable anhydrous form over the thermodynamic form in ethanol, offering an alternative route to dehydration of lenalidomide hydrates to obtain this metastable form. This demonstrates the usefulness of the gel-phase crystallisation approach in pharmaceutical solid form screening. Crystallizing lenalidomide within equivalent gels of a drug-mimetic bis(urea) gelator, however, demonstrated no such control over the polymorphic outcome nor produced the novel hemi-solvate. Crystallisation experiments in co-gels of both gelators in cyclopentanone produced the cyclopentanone hemi-solvate at all molar ratios except pure drug-mimetic gelator, suggesting that its growth is enabled simply by the presence of fibres of the non-mimetic gelator, and that by comparison, the drug-mimetic gel fibres have no effect on the crystallisation outcome. Diffusiometry and NMR studies showed the interaction between lenalidomide and either gelator was not strong, suggesting that the mechanism by which the non-mimetic gelator affects crystallisation is either via heterogenous secondary nucleation and/or the periodicity of

the gel fibres that it forms or via confinement effects, and not through specific intermolecular interactions with the drug. In the very limited number of gel-phase crystallisation experiments possible using PROTACs, no crystalline particles were detected after precipitation from non-mimetic gels of dioxane and nitrobenzene.

5.5 References

1. Q. Zhang, Y. Yan, Y. Xu, X. Zhang and J. W. Steed, *J. Colloid Interface Sci.*, 2025, **687**, 582–588.
2. R. Contreras-Montoya, L. Álvarez de Cienfuegos, J. A. Gavira, J. W. Steed, *Chem. Soc. Rev.*, 2024, **53**, 10604–10619.
3. J. A. Foster, K. K. Damodaran, A. Maurin, G. M. Day, H. P. G. Thompson, G. J. Cameron, J. C. Bernal and J. W. Steed, *Chem. Sci.*, 2016, **8**, 78–84.
4. B. Saikia, M. T. Mulvee, I. Torres-Moya, B. Sarma and J. W. Steed, *Cryst. Growth Des.*, 2020, **20**, 7989–7996.
5. A. Dawn, K. S. Andrew, D. S. Yufit, Y. Hong, J. P. Reddy, C. D. Jones, J. A. Aguilar and J. W. Steed, *Cryst. Growth Des.*, 2015, **15**, 4591–4599.
6. S. S. Jayabhavan, J. W. Steed and K. K. Damodaran, *Cryst. Growth Des.*, 2021, **21**, 5383–5393.
7. I. Torres-Moya, A. Sánchez, B. Saikia, D. S. Yufit, P. Prieto, J. R. Carrillo and J. W. Steed, *Gels*, 2023, **9**, 26.
8. J. L. Andrews, S. R. Kennedy, D. S. Yufit, J. F. McCabe and J. W. Steed, *Cryst. Growth Des.*, 2022, **22**, 6775–6785.
9. J. Buendía, E. Matesanz, D. K. Smith and L. Sánchez, *Cryst. Eng. Comm.*, 2015, **17**, 8146–8152.
10. D. Giuri, L. J. Marshall, C. Wilson, A. Seddon and D. J. Adams, *Soft Matter*, 2021, **17**, 7221–7226.
11. H. Sharma, B. K. Kalita, D. Pathak and B. Sarma, *Cryst. Growth Des.*, 2024, **24**, 17–37.
12. L. A. Estroff and A. D. Hamilton, *Chem. Rev.*, 2004, **104**, 1201–1217.
13. P. Dastidar, *Chem. Soc. Rev.*, 2008, **37**, 2699–2715.
14. M. De Loos, B. L. Feringa and J. H. Van Esch, *Eur. J. Org. Chem.*, 2005, **17**, 3615–3631.
15. F. A. F. Genio and M. C. Paderes, *ChemistrySelect*, 2021, **6**, 7906–7911.
16. B. Sravan, K. Kamalakar, M. S. L. Karuna and A. Palanisamy, *J. Solgel Sci. Technol.*, 2014, **71**, 372–379.
17. F. Piana, D. H. Case, S. M. Ramalhete, G. Pileio, M. Facciotti, G. M. Day, Y. Z. Khimyak, J. Angulo, R. C. D. Brown and P. A. Gale, *Soft Matter*, 2016, **12**, 4034–4043.
18. D. Navarro-Barreda, C. A. Angulo-Pachón, B. Bedrina, F. Galindo and J. F. Miravet, *Macromol. Chem. Phys.*, 2020, **221**, 1900419.
19. L. Wang, X. Shi and J. Wang, *Soft Matter*, 2018, **14**, 3090–3095.
20. J. Baillet, A. Gaubert, D. M. Bassani, J. Verget, L. Latxague and P. Barthélémy, *Chem. Comm.*, 2020, **56**, 9569–9569.
21. X. Li, Y. Li, G. Feng, T. Wang, J. Ren and X. Yu, *ChemistrySelect*, 2020, **5**, 4389–4392.
22. S. Debnath, S. Roy, Y. M. Abul-Haija, P. W. J. M. Frederix, S. M. Ramalhete, A. R. Hirst, N. Javid, N. T. Hunt, S. M. Kelly, J. Angulo, Y. Z. Khimyak and R. V. Ulijn, *Eur. J. Chem.*, 2019, **25**, 7881–7887.
23. G. O. Lloyd and J. W. Steed, *Nat. Chem.*, 2009, **1**, 437–442.
24. J. A. Foster, M. O. M. Piepenbrock, G. O. Lloyd, N. Clarke, J. A. K. Howard and J. W. Steed, *Nat. Chem.*, 2010, **2**, 1037–1043.

25. L. S. Reddy, S. Basavoju, V. R. Vangala and A. Nangia, *Cryst. Growth Des.*, 2006, **6**, 161–173.
26. *US Pat.*, Polymorphic forms of 3-(4-amino-1-oxo-1,3 dihydro-isoindol-2-yl)-piperidine-2,6-dione, US 7,465,800 B2, 2008.
27. R. Chennuru, P. Muthudoss, R. S. Voguri, S. Ramakrishnan, P. Vishweshwar, R. R. C. Babu and S. Mahapatra, *Cryst. Growth Des.*, 2017, **17**, 612–628.
28. *US Pat.*, Polymorphic forms of 3-(4-amino-1-oxo-1,3 dihydro-isoindol-2-yl)-piperidine-2,6-dione, US 7,977,357 B2, 2011.
29. L. Jia, Z. Li and J. Gong, *Pharm. Dev. Technol.*, 2019, **24**, 1175–1180.
30. L. Wang, Y. Yan, X. Zhang and X. Zhou, *Int. J. Pharm.*, 2022, **613**, 121394.
31. J. X. Song, Y. Yan, J. Yao, J. M. Chen and T. B. Lu, *Cryst. Growth Des.*, 2014, **14**, 3069–3077.
32. M. A. Screen, G. Tomkinson, J. F. McCabe, S. Askin, C. S. Mahon, M. R. Wilson and J. W. Steed, *New J. Chem.*, 2025, **49**, 6535–6543.
33. J. X. Song, J. M. Chen and T. B. Lu, *Cryst. Growth Des.*, 2015, **15**, 4869–4875.
34. X. Chen, D. Li, J. Wang, Z. Deng and H. Zhang, *J. Mol. Struct.*, 2019, **1175**, 852–857.
35. J. A. Foster, R. M. Edkins, G. J. Cameron, N. Colgin, K. Fucke, S. Ridgeway, A. G. Crawford, T. B. Marder, A. Beeby, S. L. Cobb and J. W. Steed, *Chem. Eur. J.*, 2014, **20**, 279–291.
36. O. V. Dolomanov, L. J. Bourhis, R. J. Gildea, J. A. K. Howard and H. Puschmann, *J. Appl. Crystallogr.*, 2009, **42**, 339–341.
37. G. M. Sheldrick, *Acta Crystallogr. C Struct. Chem.*, 2015, **71**, 3–8.
38. D. Wu, A. Chen and C. Johnson, *J. Mag. Res. Ser. A*, 1995, **115**, 2, 260–264.
39. A. Jerschow and N. Müller, *J. Mag. Res.*, 1997, **125**, 2, 372–375.
40. M. A. Connell, P. J. Bowyer, P. A. Bone, A. L. Davis, A. G. Swanson, M. Nilsson and G. A. Morris, *J. Mag. Res.*, 2009, **198**, 1, 121–131.
41. M. C. Etter, *Acc. Chem. Res.*, 1990, **23**, 120–126.
42. B. D. Hamilton, J.-M. Ha, M. A. Hillmyer and M. D. Ward, *Acc. Chem. Res.*, 2012, **45**, 3, 414–423.
43. Q. Jiang and M. D. Ward, *Chem. Soc. Rev.*, 2014, **43**, 2066–2079.
44. J. J. Maunder, J. A. Aguilar, P. Hodgkinson and S. J. Cooper, *Chem. Sci.*, 2022, **13**, 13132.
45. M. A. Screen, J. F. McCabe, S. Askin, J. L. Guest, P. Hodgkinson, A. J. Cruz-Cabeza, T. J. Blundell, D. N. Rainer, S. Coles, A. Longcake, M. R. Probert, C. S. Mahon, M. R. Wilson and J. W. Steed, Crystallising the Un-crystallizable: Insights from Extensive Screening of PROTACs, *J. Am. Chem. Soc.*, 2025, **147**, 31, 28056–28072.

6. Conclusion and Future Work

This thesis provides new insights into the solid-state and formulation challenges of PROTACs, a class of poorly soluble bRo5 molecules. Single-crystal structures of the cereblon-recruiting PROTAC 'AZ1', obtained by advanced crystallographic techniques, revealed that dispersive interactions dominate its lattice packing energy despite the presence of multiple hydrogen bonding functionalities. Differences in dissolution behaviour between amorphous forms produced via distinct routes suggest that PROTACs may exhibit *pseudo*-polyamorphism, highlighting the complexity of their solid-state landscapes and the significant experimental effort required to characterise them.

The characterisation of AZ1 solid forms was limited by sample availability and reproducibility however, particularly crystalline Form 3 and amorphous form B which was obtained by desolvation of crystalline Form 2. If the availability of the pure $AZ1_{RRS}$ sample had not been limited to approximately 150 milligrams, it may have been better to use this material for the extensive crystallisation screening rather than the much more abundant $AZ1_{mix}$ provided. In Chapter 2, it was evident that $AZ1_{RRS}$ had a greater propensity to crystallise while $AZ1_{RRR}$ only appeared to crystallise in solid solutions alongside $AZ1_{RRS}$. Using pure $AZ1_{RRS}$ may have increased the crystallinity of some samples that were determined amorphous by XRPD analysis during crystal screening, potentially leading to the discovery of more crystal forms. Many hundreds of "failed" crystallisation experiments were labelled as such after characterisation by XRPD only – however if nanoscale crystallites were present, they may have been undetectable by XRPD and only revealed by DSC analysis. With greater resources and time, DSC analysis of all crystal screening samples may have revealed other solvents capable of producing crystalline AZ1 material. CSP analysis on $AZ1_{RRS}$ may also be of interest to determine whether Form 1 is indeed the thermodynamic anhydrous form, or whether even this relatively dense form could be metastable with respect to another that may have been missed. Forms 1, 2 and 3 could be produced as solid solutions of both isomers when crystallised from $AZ1_{mix}$, but it is also worth noting that if there are crystal forms that can only be adopted by one of the two isomers, these may not have been grown using $AZ1_{mix}$ because the solution may have been undersaturated with respect to the only isomer that could adopt that form. Parallel development of high-throughput crystallisation methods which provide slower approaches to supersaturation than ENaCt could also accelerate discovery of crystalline forms of PROTACs.

It would also have been useful to measure the solubility of AZ1 in a broad range of solvents quantitatively using HPLC to produce a more accurate dataset than presented in Appendix A Table A1, ideally at two or more fixed temperatures (e.g. 0, 30 and 60 °C

depending on the solvent boiling point) and including some relevant solvent-antisolvent mixtures such as acetonitrile-water and chloroform-hexane. This may have facilitated the design of crystallisation protocols with a finer control of supersaturation, using cooling and antisolvent methods to obtain AZ1 crystals with higher crystallinity or in greater yields. While these crystallisation experiments may be equally hindered by slow crystallisation kinetics as observed in Chapter 2, the use of larger vessels may also provide benefits including lower shear forces from agitation compared to magnetic stirrer fleas (or perhaps even the roller mixer) in small vials, which were suspected of amorphising AZ1 samples. Depending on the heating method, a greater temperature difference could also be maintained between the top and bottom of the vessel, potentially allowing the replication of the unusual conditions that caused Form 3 crystals to appear in a droplet on the side of a vial, removed from the bulk suspension, as described on page 51. If crystallisation at a larger scale improved the reproducibility and/or yield of Form 2 crystals, it may have also facilitated the production of greater quantities of amorphous form B for further analysis by solid-state NMR – comparing these spectra for amorphous forms A and B may have revealed structural differences confirming the observation of pseudo-polyamorphism, explaining the differences in their dissolution profiles.

While this thesis provides a valuable deep-dive into the crystallisability of a single PROTAC compound, it is unclear whether these findings are generally applicable across more PROTACs such as those with significantly different linker or ligand chemistries, for example VHL-based PROTACs. At present there is still no literature on PROTAC crystals besides that which is presented in this thesis, and it is unclear whether the findings in Chapter 2 are exclusive to AZ1, to cereblon-based PROTACs, or whether they are general to the entire class of PROTAC compounds. PROTACs selected as candidates for development by the pharmaceutical industry are likely to be more readily crystallisable compounds due to concerns over physical and chemical stability, purity and ease of manufacture – therefore, it may be of interest to compare the chemical structure of these compounds once patented and released publicly, to better understand what structural features present in these compounds may influence their suitability for development. Features such as molecular flexibility (i.e. number of rotatable bonds) and potential for hydrogen bonding (i.e. number of donor and acceptor atoms) may be critical for crystallisability based on observations in Chapter 2.

Given PROTACs' crystallisation difficulties, formulation strategies are critical for improving their bioavailability. ASDs of AZ1 with HPMCAS achieved up to a two-fold increase in drug supersaturation compared to the neat amorphous drug, particularly when prepared by slurry conversion, which maintained dissolution enhancement at

higher loadings. Evidence indicates that these ASDs may also consist of dispersive drug–polymer interactions, in contrast to conventional drugs where drug-polymer hydrogen bonding is more common. From the limited data available, ASDs of the more acidic HPMCAS polymer appeared to be superior to those of PVPVA, but this may vary between PROTAC compounds with different pKa values (e.g. those with polyethylene glycol linkers rather than piperidine/piperazine-based linkers). By contrast, co-amorphous formulations with low molecular weight excipients offered no solubility benefit (in some cases, performing much worse than pure amorphous AZ1) despite evidence of hydrogen bonding, underscoring the unique behaviour of PROTACs. Together, these findings demonstrate that informed polymer-based ASD design, coupled with optimised preparation methods, may help the pharmaceutical industry to deliver robust and potentially commercializable oral solid forms of PROTACs in future.

With more AZ1 material available, it would be crucial to repeat the dissolution comparison of ketoglutaric acid, m-nitrobenzoic acid and oxalic acid co-amorphous salts with pure amorphous AZ1 presented in Figure 3.2 to confirm that the unexpected behaviour is reproducible using a second batch of the co-amorphous samples. If these co-amorphous salts consistently show poorer dissolution than the pure amorphous solid, the remaining six co-amorphous salts presented in section 3.3 could be scaled up and their dissolution compared to AZ1 instead to identify if this behaviour is general or only for the three salts studied. It is also worth noting that the only method used to screen for co-crystalline and co-amorphous solids of AZ1 was liquid-assisted grinding in a planetary ball mill, to screen as many potential co-formers as possible in a reasonable time using limited AZ1 material. Without these limitations, efforts to produce co-crystals or crystalline salts of AZ1 via a slurry method may have been more successful due to the propensity of AZ1 to amorphise when milled. The solubility of AZ1 and the potential co-formers in a range of solvents could be measured accurately using HPLC to identify appropriate solvent choices for each slurry such that both solid components have comparable (and limited) solubility, allowing the design of slurry experiments at targeted molar ratios of components. This method was successfully applied to the co-crystallisation of lenalidomide, a structural fragment of AZ1, with melamine in Chapter 4 as part of a complementary proof-of-principle study to produce a co-crystal with reduced solubility as a potential inhalable formulation strategy. However, it can be concluded from this thesis that successful strategies to co-crystallise lenalidomide are not easily translated to AZ1, and ultimately the co-formers that successfully produced co-amorphous solids were not easily predicted by the supramolecular synthon approach nor by using a knowledge of the co-crystals of lenalidomide as a molecular fragment.

The availability of more AZ1 material would also allow ASDs to be prepared in greater quantities by slurry conversion and solvent evaporation, allowing the dissolution profiles presented in Figure 3.5 and Figure 3.7 to be collected with more repeats, providing more precise data. ASDs could also be prepared with additional polymers such as Eudragit and Soluplus which feature in previous PROTAC ASD literature, and by additional methods such as spray-drying and hot melt extrusion which are more industrially viable and easily scaled up. With additional material available for PROTACs AZ2-4, ASDs could be produced at a much greater range of drug loading to determine if the expected LoC behaviour is eventually observed, or whether the dissolution of the PROTAC continues to improve with drug loading until the limit of drug-polymer miscibility. Studying the potential phenomenon of liquid-liquid phase separation in these dissolution studies using dynamic light scattering may also provide insight into the mechanism by which PROTAC ASDs dissolve, as discussed in sections 1.1.4 and 3.1. Complementary studies of the ASD particle surfaces may also be insightful, such as contact angle measurements to quantify wettability, and TEM or XPS to study the drug-polymer ratio present at the surfaces before and after dissolution. Future studies should also extend ASD formulation across a broader range of PROTAC compounds encompassing a greater library of ligand and linker moieties, to establish whether general design principles can be identified for this compound class given that conventional rules and features such as the LoC for conventional drug ASDs do not appear to apply in the same manner for PROTACs. As suggested in Chapter 3, exploring more advanced ASD strategies such as polymer-coated hierarchical particles prepared by slurry conversion could also be very valuable to further improve wettability and dissolution for PROTAC formulations.

Another complementary proof-of-principle study in Chapter 5 showed that crystallisation of lenalidomide within supramolecular gels enabled the discovery of a novel solvate form and the selective crystallisation of the metastable polymorph. These results illustrate how non-conventional crystallisation strategies can expand the pharmaceutical solid-form landscape of well-characterised drugs. While attempts to crystallise AZ1 inside gels the same bis(urea) gelators were unsuccessful, this study was significantly abbreviated due to sample constraints. With greater resources, a much broader range of gelators capable of gelling a broader range of solvents could be applied to the gel-phase crystallisation study of AZ1 to increase the likelihood of growing crystals and potentially observing crystallisation control. However, similarly to the co-crystallisation results, the gel-phase crystallisation control observed for lenalidomide in Chapter 5 is likely to translate poorly to AZ1 based on the initial results presented in Figure 5.7.

This work did not include the use of structured ternary fluids, metal organic frameworks or crystalline sponges to obtain crystal structures of PROTACs or influence their

crystallisation, although applying these approaches may lead to valuable structural insights needed to better predict and manipulate the physical properties of PROTAC compounds. This thesis also did not explore alternative bio-enhancement strategies such as nanocrystallisation, emulsion-based drug delivery systems or nanocarriers such as mesoporous silica, which may prove useful in developing bioavailable PROTAC drug products. Ultimately, integrating solid-state engineering with advanced formulation strategies will be essential for overcoming the solubility limitations of PROTACs and enabling their progression into viable oral medicines.

7. Appendices

Appendix A

Table **A1**. Approximate solubility data for $AZ1_{mix}$ assessed during crystallisation screening. The solubility of AZ1 was first assessed at 10 mg/mL in each solvent. If soluble without heating, the concentration was doubled by adding more AZ1 powder until heat was required to fully dissolve the powder. Solvents in which AZ1 appeared partially soluble at 10 mg/mL were halved in concentration by addition of more solvent until the powder could be fully dissolved with heating. Solvents in which AZ1 appeared completely insoluble at 10 mg/mL were not studied further.

Solvent	Solubility (mg/mL)	Solvent	Solubility (mg/mL)	Solvent	Solubility (mg/mL)
1,2-dibromoethane	10	Benzyl alcohol	5	Ethyl acetate	<1
1,2,4-trichlorobenzene	<1	Chlorobenzene	10	Hexane	<1
1,4-dioxane	62	Chloroform	114	Isopropanol	<1
1-butanol	5	Cyclohexanone	10	Mesitylene	<1
1-pentanol	5	Cyclopentanone	120	Methanol	<1
1-propanol	<1	Diethyl ether	<1	Nitrobenzene	10
2-butanol	3.3	Diethylene glycol	10	Nitromethane	5
2-butanone	5	Diisopropyl ether	<1	Pyridine	224
2-picoline	158	Dichloromethane	112	Tetrahydrofuran	170
4-ethyl pyridine	188	Dimethylacetamide	200	Toluene	<1
Acetonitrile	1.25	Dimethylformamide	84	Water	<1
Acetone	<1	Dimethylsulfoxide	104	p-xylene	<1
Benzene	<1	Ethanol	2.5		

Table **A2**. ENaCt plate layouts for $AZ1_{mix}$ crystallisation experiments. Data were collected and processed by Dr Alexandra Longcake.

Plate 1 layout:		**200 nL of oils**											
50 nL of AZ1 solution (approximate concentration/ mg mL^{-1})		**1**	**2**	**3**	**4**	**5**	**6**	**7**	**8**	**9**	**10**	**11**	**12**
DMSO (5.2 mg mL^{-1})	**A**	No oil	PDMSO					No oil	Fomblin Y				
DMSO (5.2 mg mL^{-1})	**B**	No oil	FC-40					No oil	Mineral oil				
DMF (41.7 mg mL^{-1})	**C**	No oil	PDMSO					No oil	Fomblin Y				
DMF (41.7 mg mL^{-1})	**D**	No oil	FC-40					No oil	Mineral oil				
DCM (10.4 mg mL^{-1})	**E**	No oil	PDMSO					No oil	Fomblin Y				
DCM (10.4 mg mL^{-1})	**F**	No oil	FC-40					No oil	Mineral oil				
DESO (20.8 mg mL^{-1})	**G**	No oil	PDMSO					No oil	Fomblin Y				
DESO (20.8 mg mL^{-1})	**H**	No oil	FC-40					No oil	Mineral oil				
Plate 2 layout:		**200 nL of oils**											
50 nL of AZ1 solution (approximate concentration/ mg mL^{-1})		**1**	**2**	**3**	**4**	**5**	**6**	**7**	**8**	**9**	**10**	**11**	**12**
Toluene (5.2 mg mL^{-1})	**A**	No oil	PDMSO					No oil	Fomblin Y				
Toluene (5.2 mg mL^{-1})	**B**	No oil	FC-40					No oil	Mineral oil				
DCE (5.2 mg mL^{-1})	**C**	No oil	PDMSO					No oil	Fomblin Y				
DCE (5.2 mg mL^{-1})	**D**	No oil	FC-40					No oil	Mineral oil				
2-Me THF (5.2 mg mL^{-1})	**E**	No oil	PDMSO					No oil	Fomblin Y				
2-Me THF (5.2 mg mL^{-1})	**F**	No oil	FC-40					No oil	Mineral oil				
THTP-1-oxide (20.8 mg mL^{-1})	**G**	No oil	PDMSO					No oil	Fomblin Y				
THTP-1-oxide (20.8 mg mL^{-1})	**H**	No oil	FC-40					No oil	Mineral oil				
Plate 3 layout:		**200 nL of oils**											
50 nL of AZ1 solution (approximate concentration/ mg mL^{-1})		**1**	**2**	**3**	**4**	**5**	**6**	**7**	**8**	**9**	**10**	**11**	**12**
EtOAc (5.2 mg mL^{-1})	**A**	No oil	PDMSO					No oil	Fomblin Y				
EtOAc (5.2 mg mL^{-1})	**B**	No oil	FC-40					No oil	Mineral oil				
MeCN (5.2 mg mL^{-1})	**C**	No oil	PDMSO					No oil	Fomblin Y				
MeCN (5.2 mg mL^{-1})	**D**	No oil	FC-40					No oil	Mineral oil				
4-Methyl-2-pentanone (5.2 mg mL^{-1})	**E**	No oil	PDMSO					No oil	Fomblin Y				
4-Methyl-2-pentanone (5.2 mg mL^{-1})	**F**	No oil	FC-40					No oil	Mineral oil				
Nitromethane (5.2 mg mL^{-1})	**G**	No oil	PDMSO					No oil	Fomblin Y				
Nitromethane (5.2 mg mL^{-1})	**H**	No oil	FC-40					No oil	Mineral oil				
Plate 4 layout:		**200 nL of oils**											
50 nL of AZ1 solution (approximate concentration/ mg mL^{-1})		**1**	**2**	**3**	**4**	**5**	**6**	**7**	**8**	**9**	**10**	**11**	**12**
DMAC (20.8 mg mL^{-1})	**A**	No oil	PDMSO					No oil	Fomblin Y				
DMAC (20.8 mg mL^{-1})	**B**	No oil	FC-40					No oil	Mineral oil				
1,4-dioxane (5.2 mg mL^{-1})	**C**	No oil	PDMSO					No oil	Fomblin Y				
1,4-dioxane (5.2 mg mL^{-1})	**D**	No oil	FC-40					No oil	Mineral oil				
NMI (5.2 mg mL^{-1})	**E**	No oil	PDMSO					No oil	Fomblin Y				
NMI (5.2 mg mL^{-1})	**F**	No oil	FC-40					No oil	Mineral oil				
piperidine (5.2 mg mL^{-1})	**G**	No oil	PDMSO					No oil	Fomblin Y				
piperidine (5.2 mg mL^{-1})	**H**	No oil	FC-40					No oil	Mineral oil				

Table **A3**. ENaCt results from plate readouts. F – fail; 1 – oil only or still solvated; 2 – amorphous or non-crystalline material; 3 – small single crystals or microcrystalline material. Data were collected and processed by Dr Alexandra Longcake.

Plate 1 results	**1**	**2**	**3**	**4**	**5**	**6**	**7**	**8**	**9**	**10**	**11**	**12**
A	1	2	2	2	2	1	2	1	1	1	1	1
B	1	2	2	2	2	2	2	1	1	1	1	1
C	1	2	2	2	2	2	2	1	1	1	1	1
D	1	2	2	2	2	2	2	2	1	1	1	1
E	1	2	2	2	2	2	1	1	1	1	1	1
F	1	1	2	2	2	2	1	1	2	2	2	2
G	1	1	F	1	1	1	1	1	1	1	1	1
H	1	1	F	1	1	1	1	3	1	1	1	1
Plate 2 results	**1**	**2**	**3**	**4**	**5**	**6**	**7**	**8**	**9**	**10**	**11**	**12**
A	2	2	2	2	2	2	2	2	2	2	2	2
B	2	2	2	2	2	2	2	1	1	1	2	2
C	1	2	1	1	1	1	1	1	1	1	1	1
D	1	1	1	1	1	1	1	1	1	1	1	1
E	1	1	1	1	1	1	1	1	1	1	1	1
F	1	1	1	1	1	1	1	1	1	1	1	1
G	1	1	1	1	1	1	1	1	1	1	1	1
H	1	1	1	1	1	1	1	1	1	1	1	1
Plate 3 results	**1**	**2**	**3**	**4**	**5**	**6**	**7**	**8**	**9**	**10**	**11**	**12**
A	1	1	1	1	1	1	2	2	2	1	1	1
B	2	2	2	2	2	2	2	1	1	1	1	2
C	2	2	2	2	2	2	2	2	2	2	2	2
D	2	2	2	2	2	2	2	2	2	2	2	2
E	1	1	1	1	1	1	1	1	1	1	1	1
F	1	1	1	1	1	1	1	1	1	1	1	1
G	2	2	2	2	2	2	2	2	2	2	2	2
H	2	2	2	2	2	2	2	2	2	2	2	2
Plate 4 results	**1**	**2**	**3**	**4**	**5**	**6**	**7**	**8**	**9**	**10**	**11**	**12**
A	2	1	1	1	1	1	2	1	1	1	1	1
B	2	1	1	1	1	2	2	1	1	1	1	1
C	1	1	1	1	1	1	1	F	1	1	1	1
D	1	1	1	1	1	1	1	F	1	1	1	1
E	2	2	2	2	2	2	2	1	2	2	1	1
F	1	1	1	1	1	1	1	1	1	1	1	1
G	1	1	1	1	1	1	2	1	2	3	1	1
H	1	2	2	2	1	2	2	1	1	1	1	1

Table **A4**. Crystallographic data for AZ1 Form 1. Data were collected and processed by Dr Toby J. Blundell.

Empirical formula	$C_{49}H_{63}FN_{10}O_3$	**μ/mm^{-1}**	n/a
Formula weight	859.108	**F(000)**	744.1
Temperature/K	175(5)	**Crystal size /μm^3**	1.8 × 0.65 × n/a
Crystal system	monoclinic	**Radiation**	electron (λ = 0.0251 Å)
Space group	*I*2	**2Θ range for data collection/°**	0.16 to 1.8
a/ Å	9.4516(8)	**Index ranges**	-11 ≤ h ≤ 11, -7 ≤ k ≤ 7, -85 ≤ l ≤ 85
b/ Å	6.2776(4)	**Reflections collected**	10286
c/ Å	75.233(16)	**Independent reflections**	10284
α/°	90	**Data/ restraints/ parameters**	10284/706/571
β/°	92.476(10)	**Goodness-of-fit on F^2**	1.177
γ/°	90	**Final R indexes [I >=2σ (I)]**	R_1 = 0.1539, wR_2 = 0.3464
Volume/Å^3	4459.7(10)	**Final R indexes (all data)**	R_1 = 0.2134, wR_2 = 0.3828
Z	4	**Largest diff. peak /hole (Olex2 N-beam)**	1.03/-1.16
ρ_{calc} g/cm^3	1.280	**Z-score (Olex2)**	17.40 (9.19 raw)

Table **A5**. Hydrogen bond for AZ1 Form 1.

D	**H**	**A**	**d(D-H)/Å**	**d(H-A)/Å**	**d(D-A)/Å**	**D-H-A/°**
N9	H9	O1	1.027	2.262	3.269(16)	166.2(4)

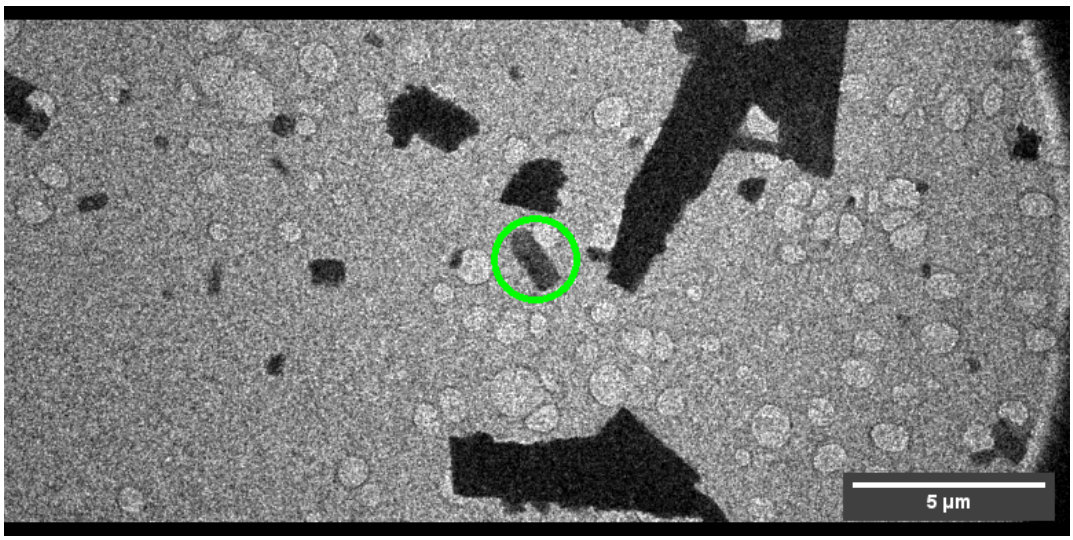

Figure **A1**. Image of crystal used for 3D ED structure determination, the green circle indicating the size and position of the selected area aperture.

Table **A6**. Crystallographic data for AZ1 Form 3. Data were collected and processed by Dr Toby J. Blundell.

Empirical formula	$C_{55}H_{70.5}FN_{10}O_3$	**μ/mm^{-1}**	0.226
Formula weight	938.71	**F(000)**	1007.0
Temperature/K	100.00	**Crystal size /mm^3**	0.089 × 0.008 × 0.002
Crystal system	monoclinic	**Radiation**	Synchrotron (λ = 1.0402)
Space group	$P2_1$	**2Θ range for data collection/°**	1.786 to 79.728
a/ Å	12.0183(5)	**Index ranges**	-14 ≤ h ≤ 14, -7 ≤ k ≤ 7, -40 ≤ l ≤ 41
b/ Å	6.2727(2)	**Reflections collected**	18586
c/ Å	33.8422(11)	**Independent reflections**	8942 [R_{int} = 0.0659, R_{sigma} = 0.1137]
α/°	90	**Data/ restraints/ parameters**	8942/1377/666
β/°	99.389(3)	**Goodness-of-fit on F^2**	0.957
γ/°	90	**Final R indexes [I >=2σ (I)]**	R_1 = 0.0492, wR_2 = 0.1094
Volume/Å^3	2517.09(16)	**Final R indexes (all data)**	R_1 = 0.0823, wR_2 = 0.1188

Z	2	Largest diff. peak /hole / e Å^{-3}	0.19/-0.25
ρ_{calc} g/cm^3	1.239	Flack parameter	0.4(4)

Table **A7**. Hydrogen bond for AZ1 Form 3.

D	H	A	d(D-H)/Å	d(H-A)/Å	d(D-A)/Å	D-H-A/°
N9	H9	O1A[2]	0.88	1.98	2.628(19)	129.7

[1]+X,1+Y,+Z; [2]1-X,-1/2+Y,1-Z

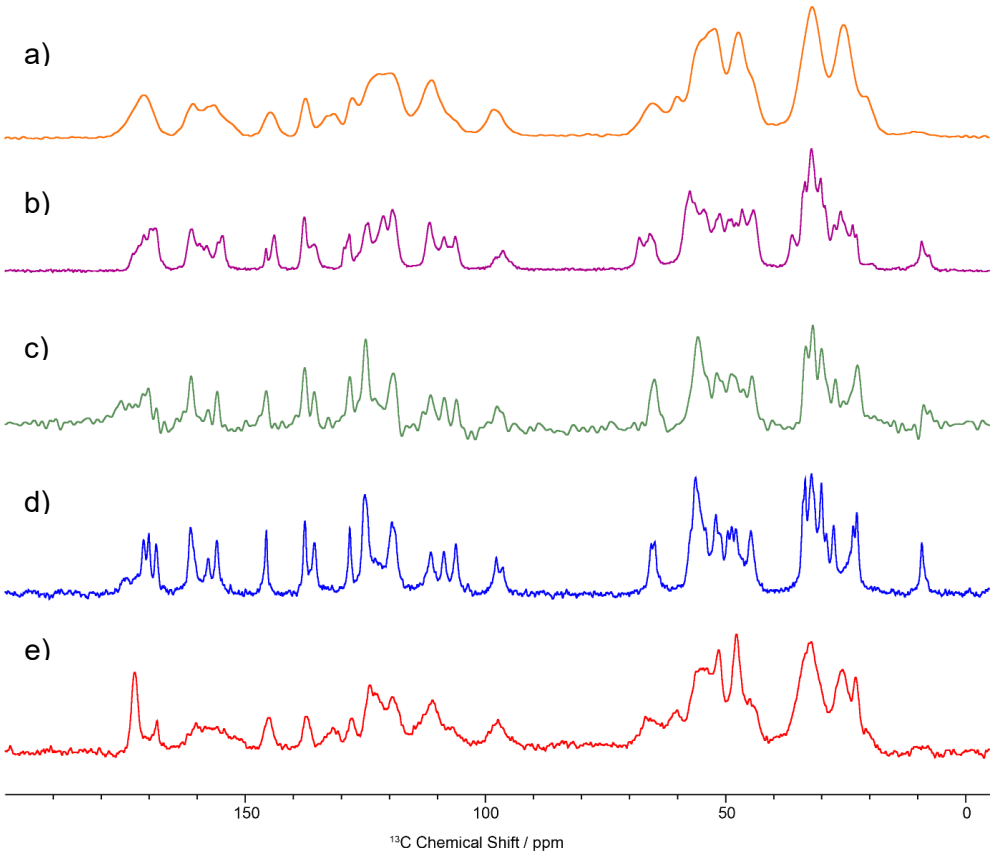

Figure **A2**. Solid-state ^{13}C NMR spectra of AZ1 samples. a) Ball milled AZ1$_{mix}$ (amorphous type A), b) AZ1$_{mix}$ as-synthesised (Form 1), c) AZ1$_{mix}$ slurried in MeCN (Form 1), d) AZ1$_{RRS}$ as-synthesised (Form 1) and e) AZ1$_{mix}$ Form 2. NMR analysis of other AZ1 samples was prevented by limited sample quantities. Spectrum c) was acquired with a relatively low sample quantity. Data were collected by Jamie L. Guest.

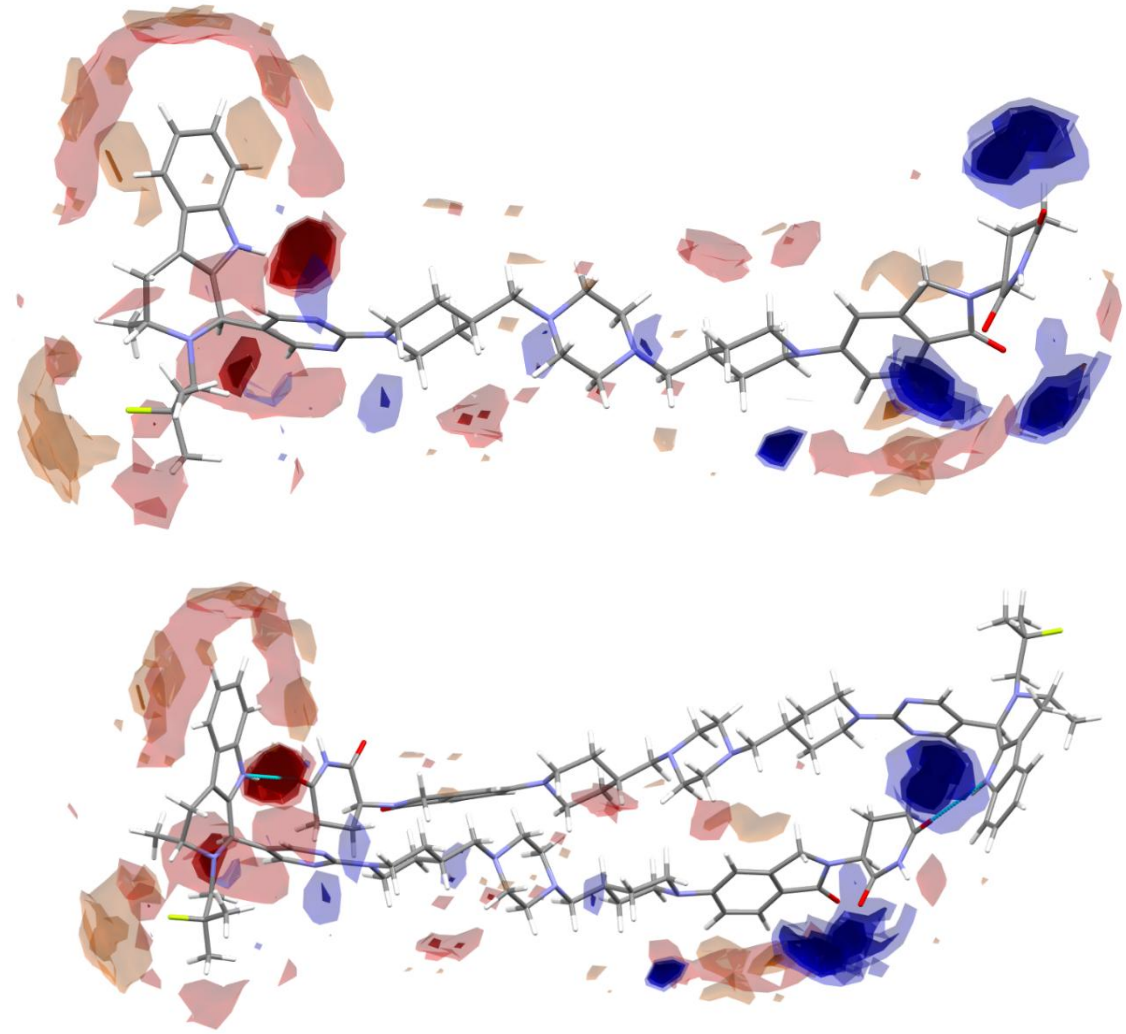

Figure **A3**. Full interaction maps of AZ1 Form 1 calculated using Mercury.[122] Red surfaces indicate a predicted probability of hydrogen bond acceptors; blue surfaces indicate a predicted probability of hydrogen bond donors; brown surfaces indicate a hydrophobic preference.

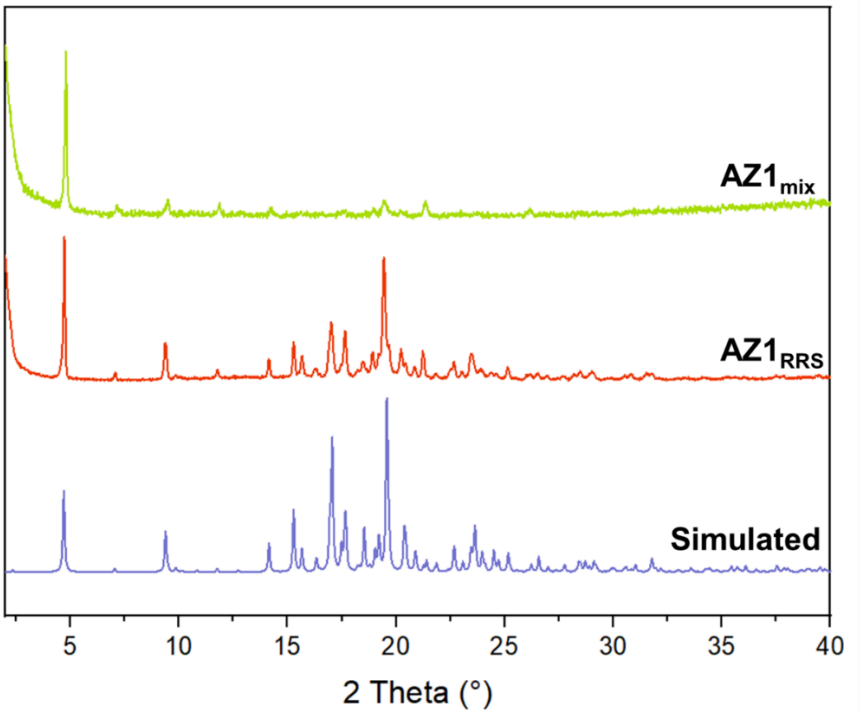

Figure **A4**. XRPD patterns for Form 1 produced using $AZ1_{mix}$ (top) and $AZ1_{RRS}$ (centre) compared to the simulated pattern from single crystal data (bottom), confirming phase purity of the bulk Form 1 samples.

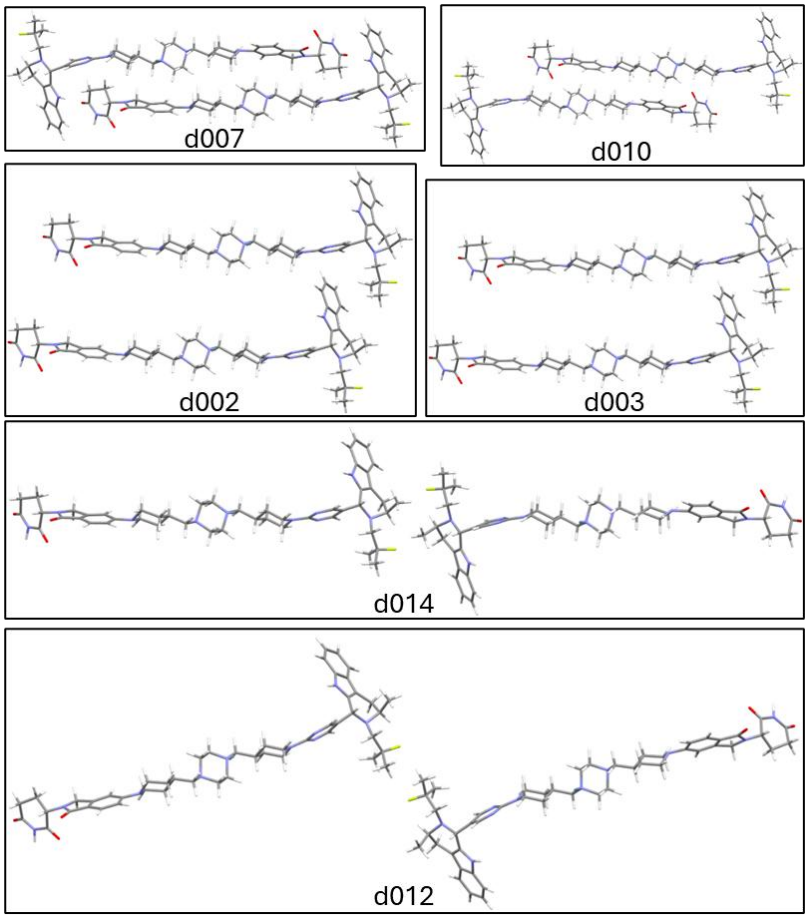

Figure **A5**. CrysIn interaction pairs for Form 1 not included in Figure 2.6.

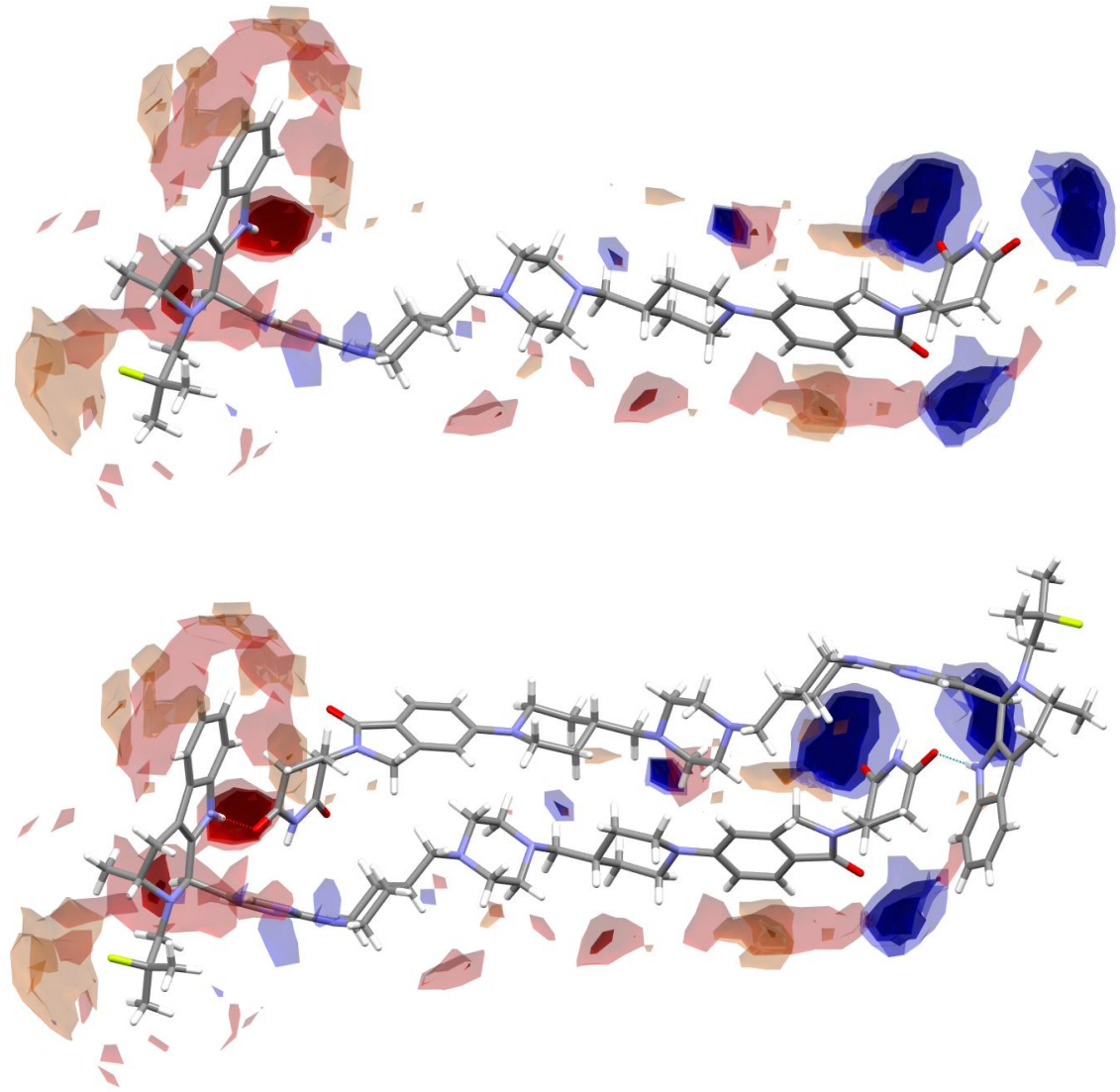

Figure **A6**. Full interaction maps of AZ1 Form 3 calculated using Mercury.[122] Red surfaces indicate a predicted probability of hydrogen bond acceptors; blue surfaces indicate a predicted probability of hydrogen bond donors; brown surfaces indicate a hydrophobic preference.

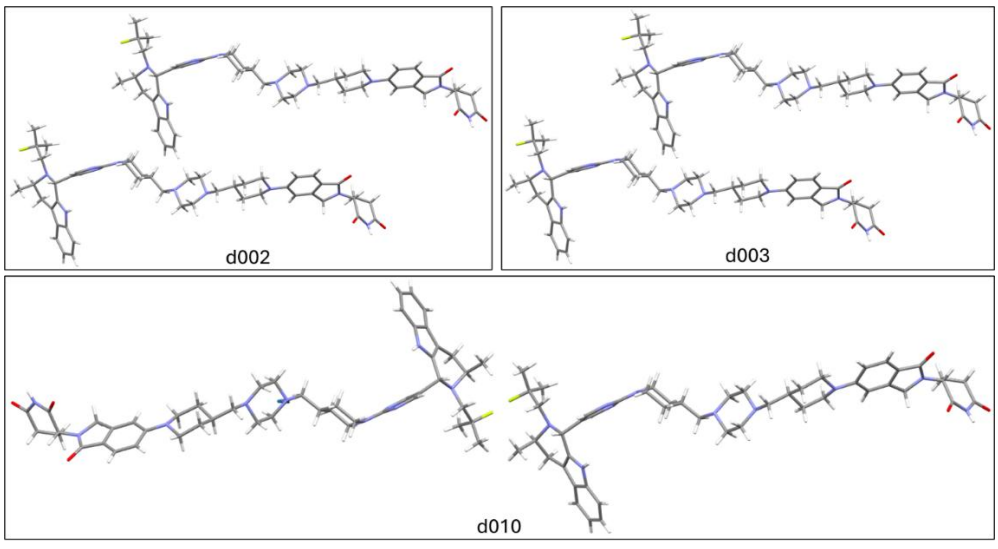

Figure **A7**. CrysIn interaction pairs for Form 3 not included in Figure 2.11.

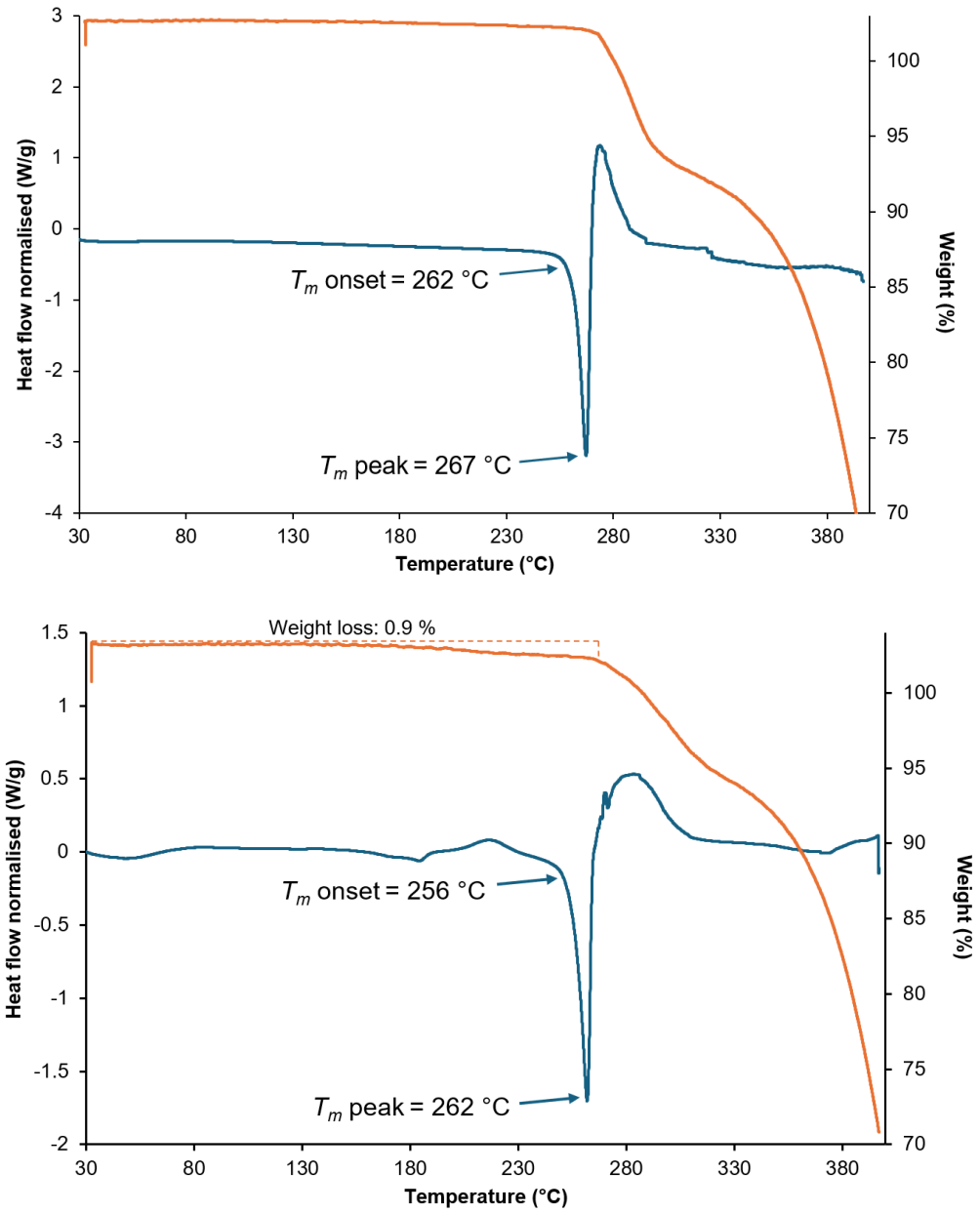

Figure **A8**. DSC and TGA of Form 1 $AZ1_{RRS}$ (top) and $AZ1_{mix}$ (bottom). Top) Melt decomposition onset at 262, peak at 267 °C. Bottom) 0.9% mass loss from ~190 up to 260 °C. Melt decomposition onset at 256, peak at 262 °C. While neither sample appears to contain any amorphous content by XRPD analysis, the DSC thermogram of Form 1 obtained with $AZ1_{mix}$ contains a broad exotherm-like feature between 150 and 200 °C that corresponds to a loss in mass of approximately 0.8 %, which could be a broad glass transition temperature (T_g) for some amorphous content dispersed through the sample. The $AZ1_{RRS}$ sample is completely dry by comparison. Since $AZ1_{mix}$ contains a 1:1 mixture of RRR- and RRS- isomers, the evidence of only a small quantity of amorphous content suggests it is highly unlikely that only one isomer crystallises as Form 1 while the remaining 50 % of the mass is the other isomer as completely amorphous solid. It is more likely that, like Form 3, both isomers are capable of packing into the same crystal structure but potentially to different extents.

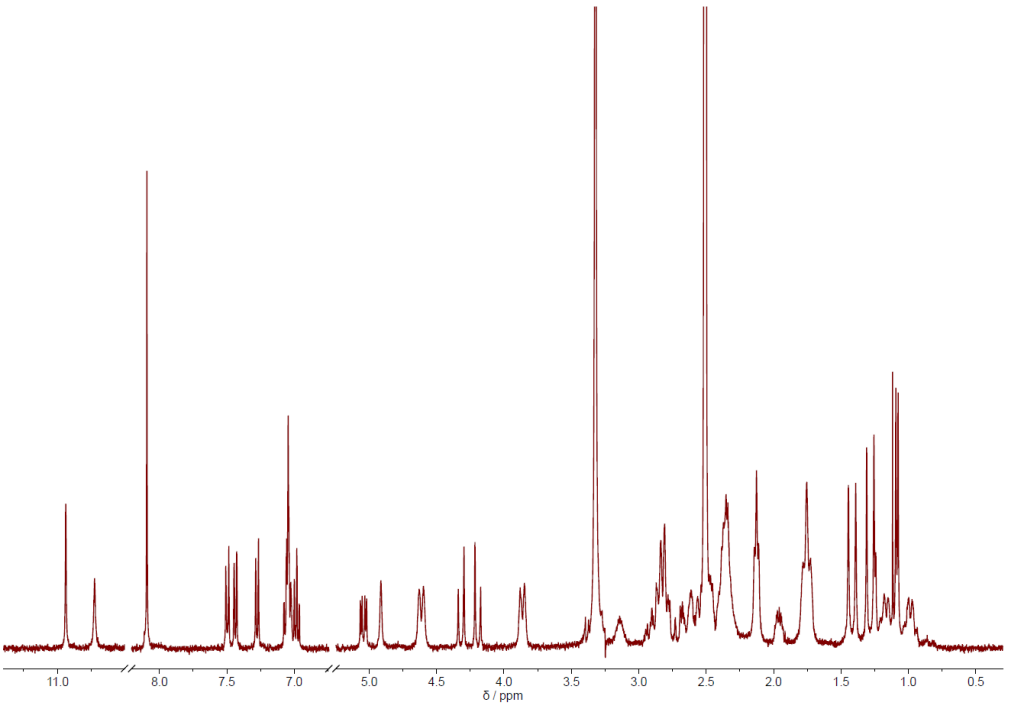

Figure **A9**. Solution-state ^{1}H NMR spectrum of Form 1 showing only residual DMSO and H2O solvent peaks.

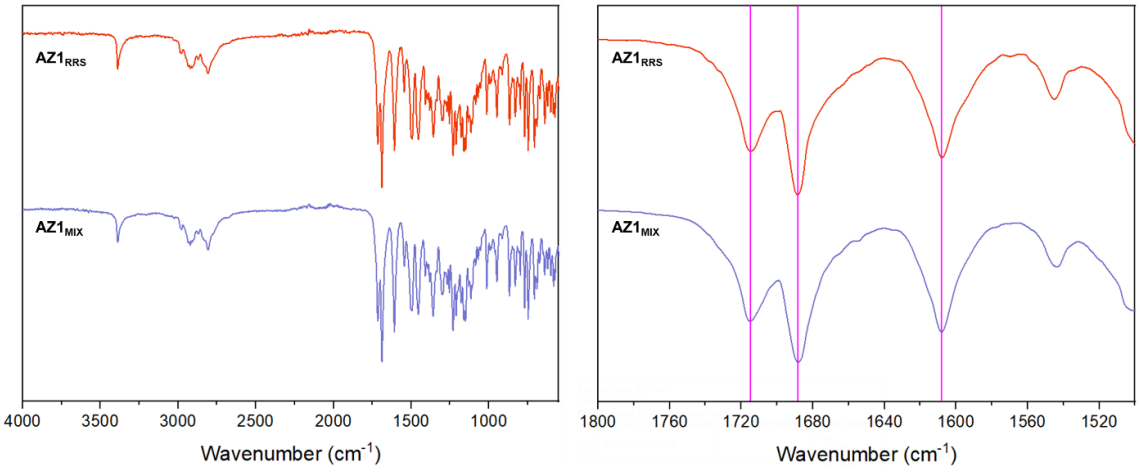

Figure **A10**. FTIR spectra of Form 1 prepared from $AZ1_{MIX}$ and $AZ1_{RRS}$, showing that both solids are indistinguishable.

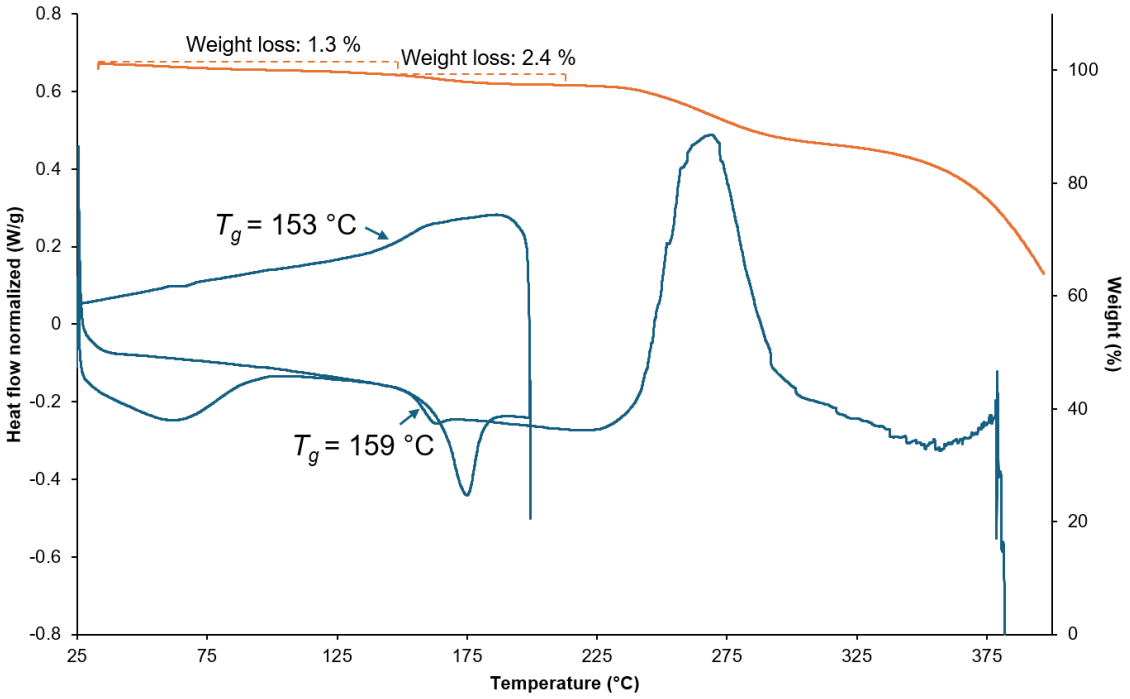

Figure **A11**. Heat-cool-heat DSC and TGA of Form 2 (DCM). Gradual loss of 1.3% mass up to 118 °C attributed to labile DCM, followed by 2.4% mass loss between ~120 and 200 °C attributed to desolvation of crystalline DCM. Desolvation leads to collapse of the crystal structure, with T_g values observed at 153 °C on cooling and 159 °C on reheating, followed by decomposition at 230 °C.

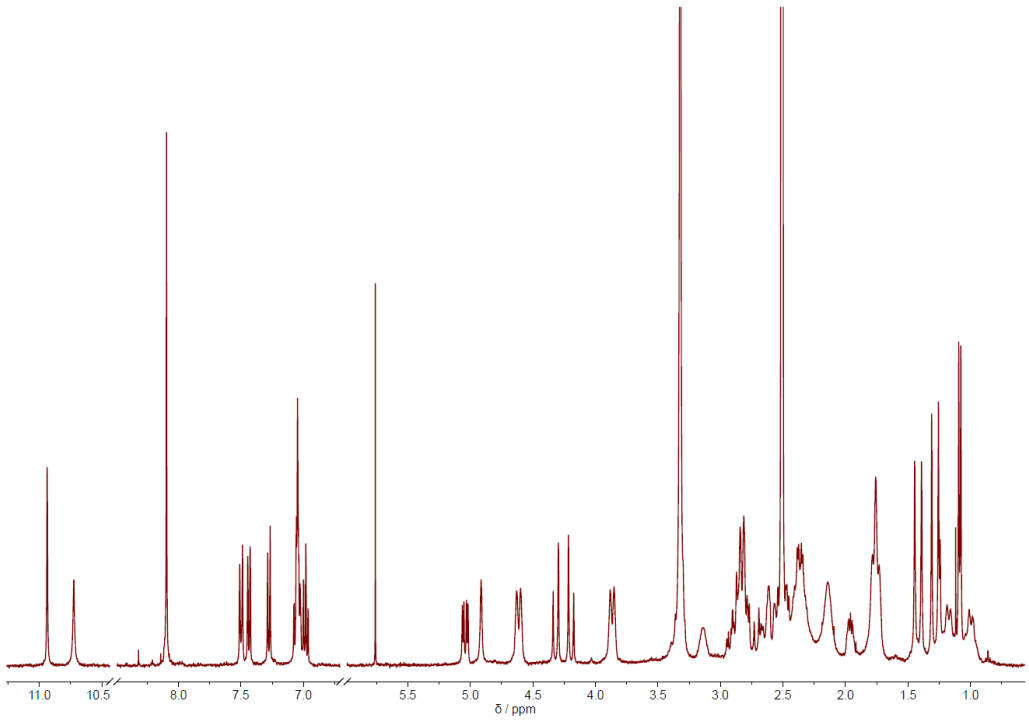

Figure **A12**. Solution-state ^{1}H NMR spectrum of Form 2 showing residual DMSO and H2O solvent peaks as well as a characteristic dichloromethane signal (singlet at 5.76 ppm).

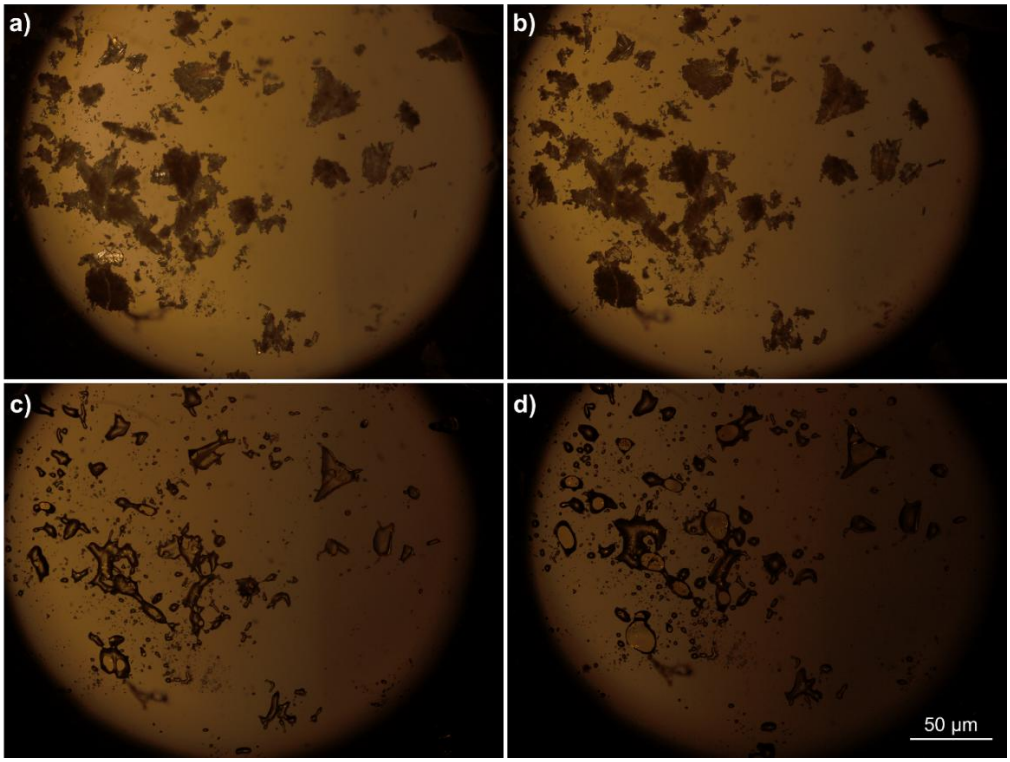

Figure **A13**. Hot-stage polarised optical microscopy (HS-POM) images of Form 2 ($AZ1_{mix}$) at a) 30 °C, b) 170 °C, c) 170 °C after holding for 10 minutes and d) 30 °C upon cooling. The sample was heated at 10 °C/min from 30 to 170 °C, held for 10 minutes and cooled back to 30 °C at 10 °C/min. The needle-like crystals appear to have been broken and clumped together during the preparation of the slide, with some shiny particles still evident at the start of the experiment. These appear to melt and/or desolvate around 170 °C and remain amorphous upon cooling.

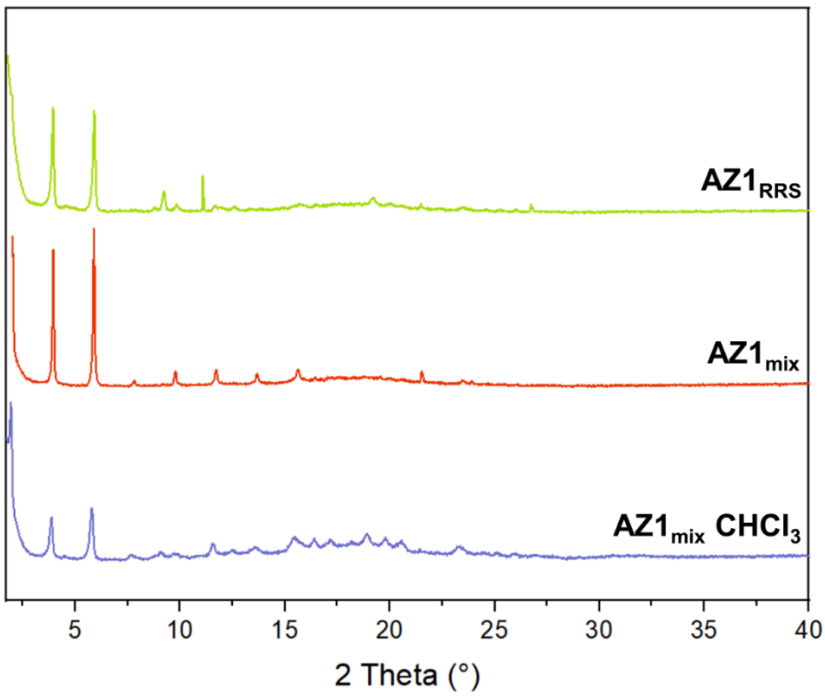

Figure **A14**. XRPD patterns for Form 2 produced using $AZ1_{RRS}$ (top) and $AZ1_{mix}$ (centre) and a sample crystallised from chloroform that appears to be isostructural.

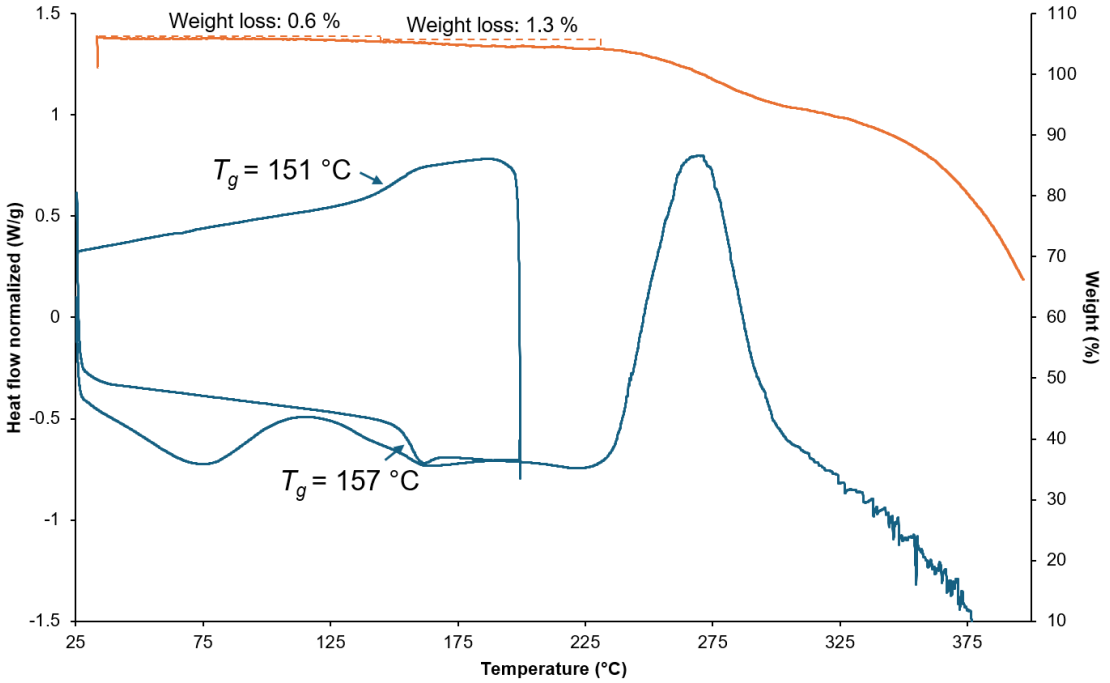

Figure **A15**. Heat-cool-heat DSC and TGA of Form 2 ($CHCl_3$). Gradual loss of 0.6% mass up to 130 °C attributed to labile chloroform, followed by 1.3% mass loss between ~155 and 225 °C attributed to desolvation of crystalline $CHCl_3$, for a combined total stoichiometry of 1 : 0.14 moles of AZ1 to $CHCl_3$. Desolvation leads to collapse of the crystal structure, with T_g values observed at 151 °C on cooling and 157 °C on reheating, followed by decomposition at 230 °C.

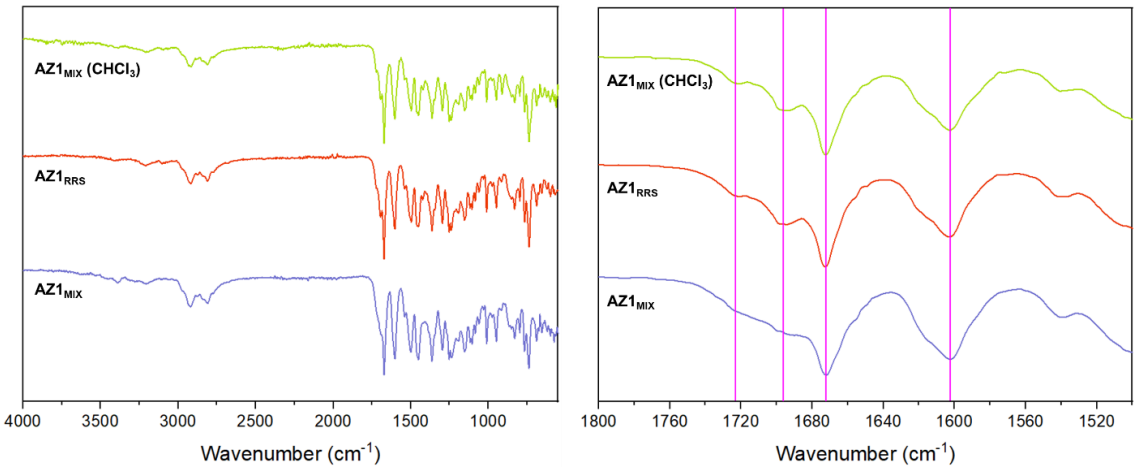

Figure **A16**. FTIR spectra for Form 2 (DCM) produced using $AZ1_{mix}$ (bottom), $AZ1_{RRS}$ (centre) and a potentially isostructural sample produced from chloroform (top). Form 2 (DCM) samples differ only in the sharpness of spectral features, with the $AZ1_{RRS}$ sample showing greater crystallinity as per Figure S11.

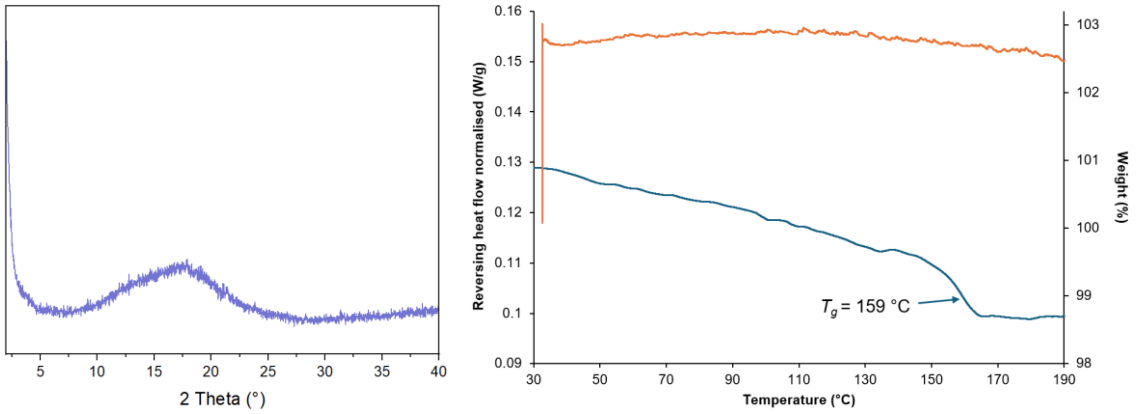

Figure **A17**. XRPD pattern and DSC/TGA of scaled-up amorphous form B, showing a T_g at 159 °C and no solvent loss up to 190 °C.

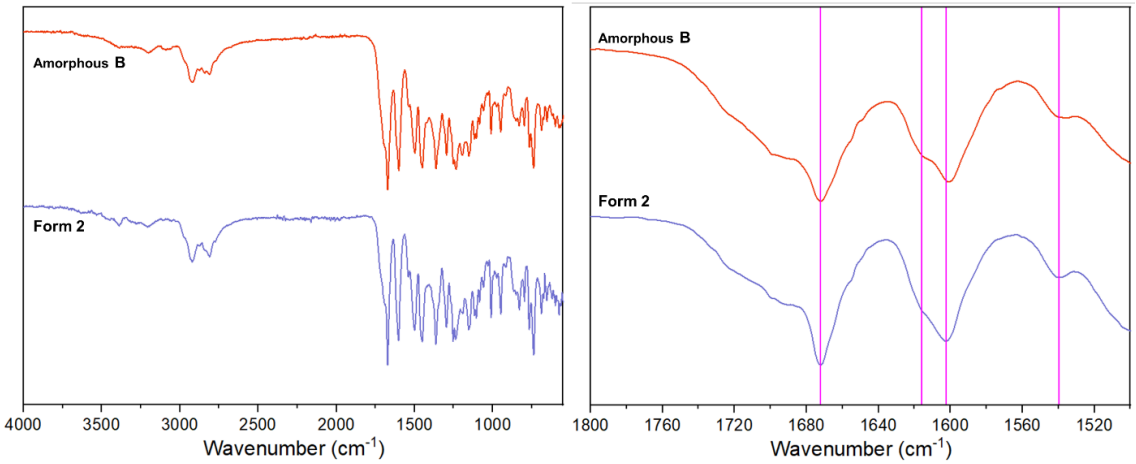

Figure **A18**. FTIR spectra comparing Form 2 and desolvated form 2 (amorphous form B). The spectra are indistinguishable.

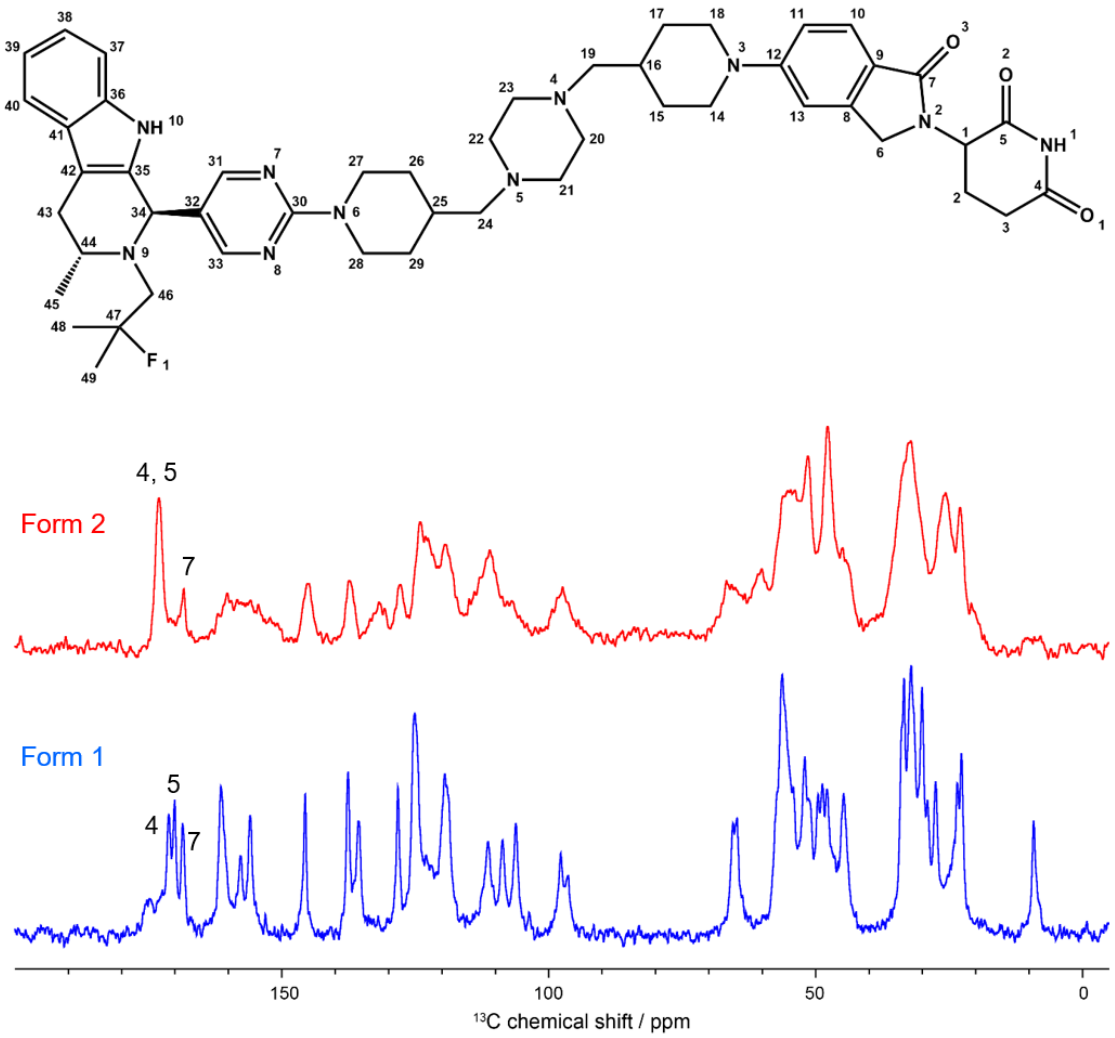

Figure **A19**. ^{13}C CPTOSS spectra of Form 1 ($AZ1_{RRS}$) and Form 2 ($AZ1_{mix}$) acquired with 512 and 3600 scans, and recycle delays of 4 s and 1 s, respectively, at a MAS rate of 10 kHz. Excitation and decoupling were achieved using a 3 μs ^{1}H 90° pulse corresponding to a nutation rate of 83.3 kHz. 25 and 40 Hz of Lorentzian line broadening was applied to Form 1 and 2 respectively. An atomic numbering scheme is shown above, indicating that carbon atoms 4, 5 and 7 correspond to carbonyl carbon atoms. These have been assigned with the aid of CASTEP DFT-predicted ^{13}C chemical shifts (see Figure S19) of the Form 1 crystal structure obtained via electron diffraction. Data were collected by Jamie L. Guest.

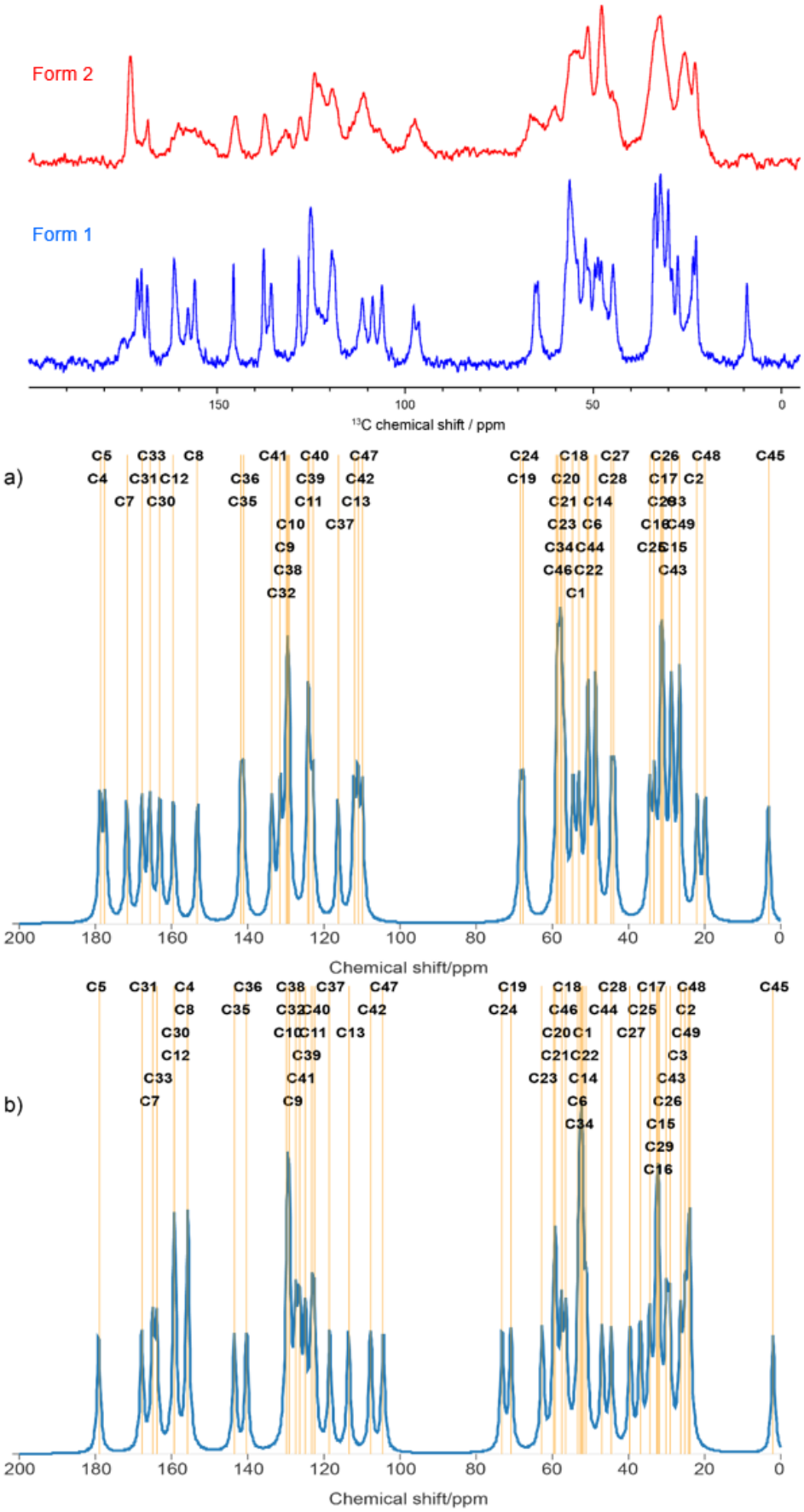

Figure **A20**. NMR prediction via CASTEP calculation of Form 1, in which all atomic positions have been geometry optimised a) and in which the heavy atoms have been frozen b). The predicted spectra have been compared versus the experimental spectra from Figure S18. There is a

noticeable difference between the resultant predicted NMR spectra in the alkyl region (15–80 ppm), with the fully geometry optimised structure (a) bearing a closer resemblance to the experimental NMR spectrum. This would be consistent with a degree of disorder / thermal motion in the linker region of structure. The 3D ED structure of Form 1 was obtained at 175 K. Data were collected and processed by Jamie L. Guest.

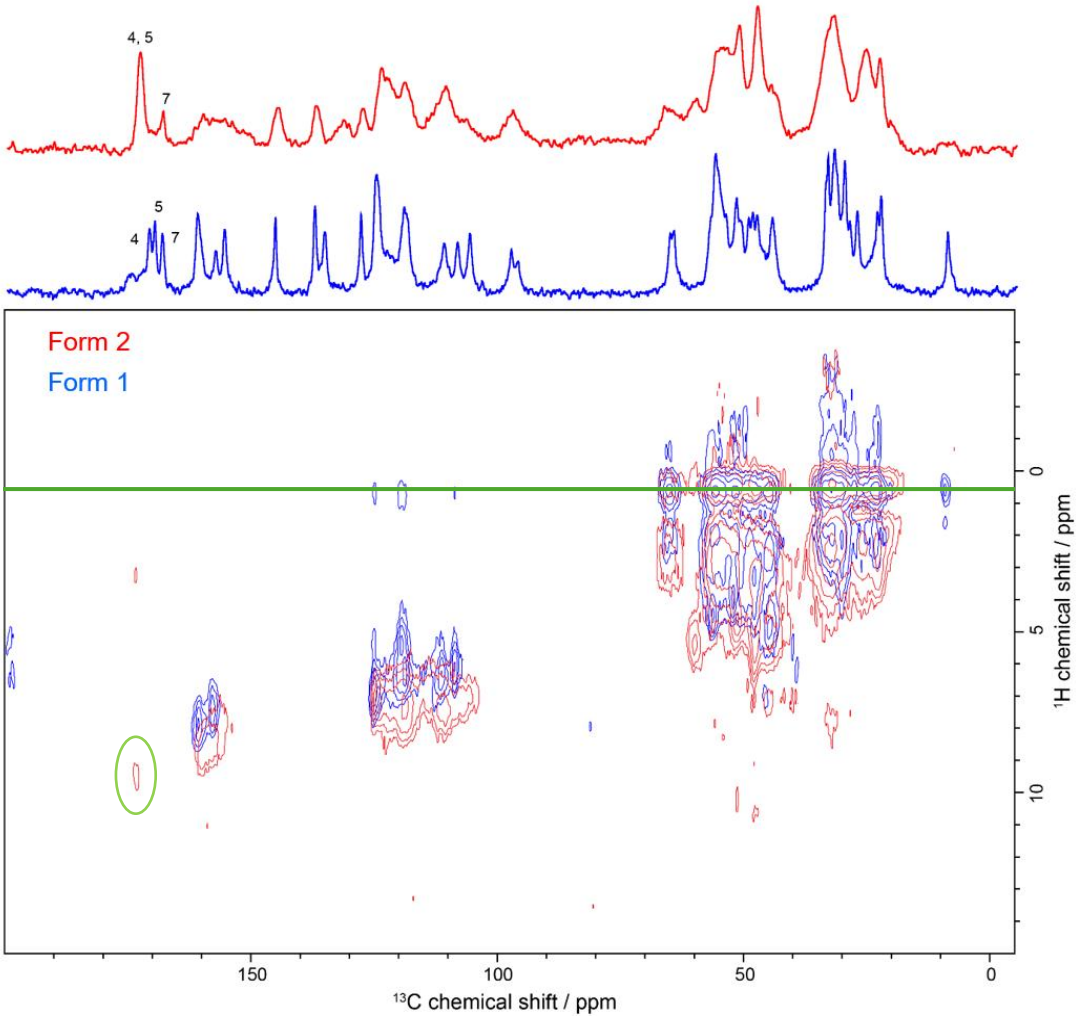

Figure **A21**. ^{1}H-^{13}C FSLG HETCOR spectra of Form 1 ($AZ1_{RRS}$) and Form 2 ($AZ1_{mix}$) acquired with a 100 µs contact pulse, 512 and 900 scans per slice, and recycle delays of 4 s and 1 s, respectively, at a MAS rate of 10 kHz. 80 slices in the indirect dimension were acquired. Excitation and decoupling were achieved using a 3 µs ^{1}H 90° pulse corresponding to a nutation rate of 83.3 kHz. 40 Hz of Lorentzian line broadening was applied to the F2 dimension and a 0.3 Hz QSINE sine bell shift of 3 was applied to the F1. The horizontal external projections are the CPTOSS spectra from Figure S18. The cross peaks denoted by the green horizontal line are an artifact resulting from the LG decoupling. The carbonyl peaks produce only a single weak contact in Form 2 at short contact times (highlighted by the green oval), corresponding to the interaction between C4 and C5 and what is most likely the N1H group, due its high chemical shift at 9.5 ppm. Data were collected and processed by Jamie L. Guest.

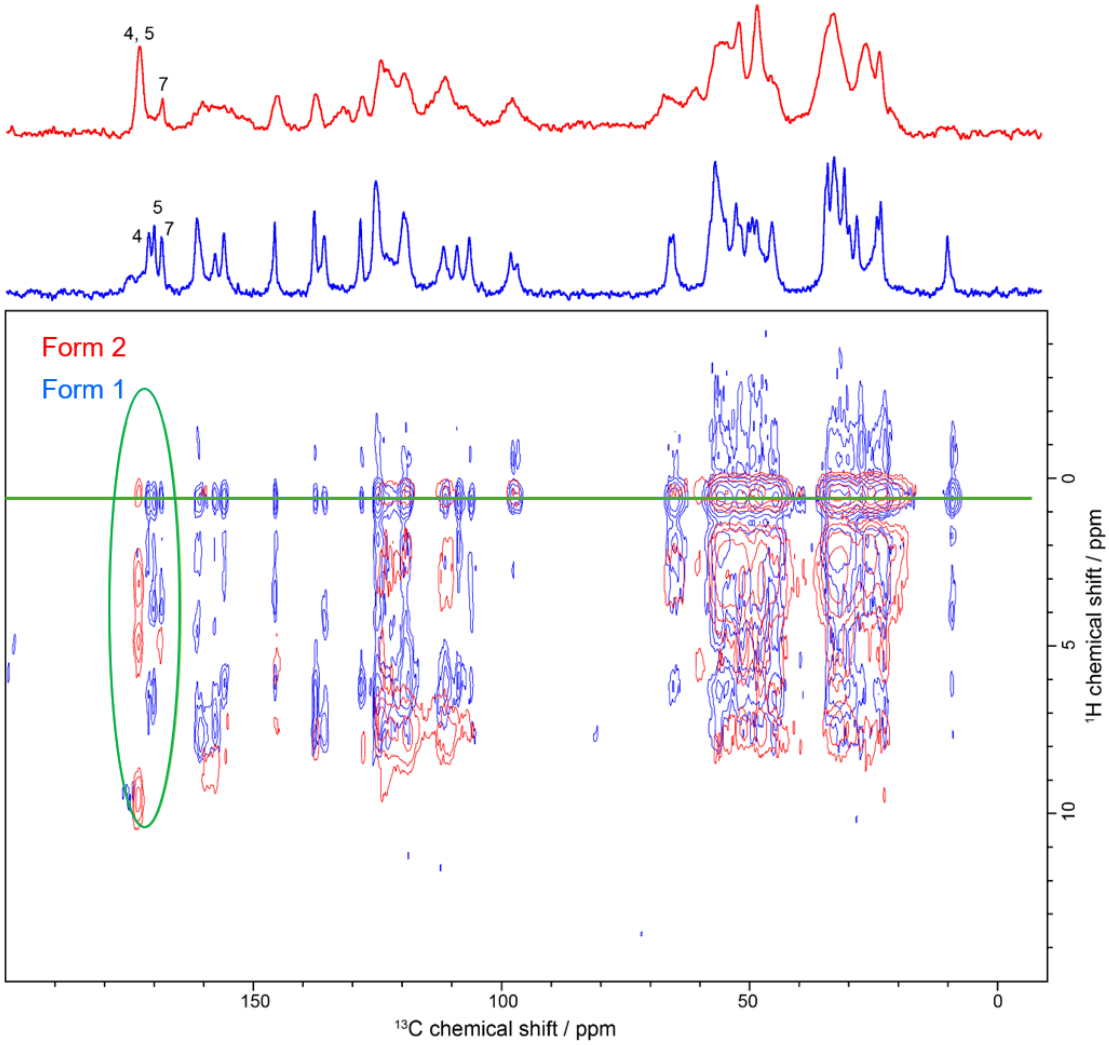

Figure **A22**. ^{1}H-^{13}C FSLG HETCOR spectra of Form 1 ($AZ1_{RRS}$) and Form 2 ($AZ1_{mix}$) acquired with a 1000 µs contact pulse, 512 and 900 scans per slice, and recycle delays of 4 s and 1 s, respectively, at a MAS rate of 10 kHz. 80 slices in the indirect dimension were acquired. Excitation and decoupling were achieved using a 3 µs ^{1}H 90° pulse corresponding to a nutation rate of 83.3 kHz. 40 Hz of Lorentzian line broadening was applied to the F2 dimension and a 0.3 Hz QSINE sine bell shift of 3 was applied to the F1. The horizontal external projections are the CPTOSS spectra from Figure S18. The cross peaks denoted by the green horizontal line are an artifact resulting from the LG decoupling. At longer contact times, the interaction between C4/C5 and N1H is much stronger, and longer distance dipolar interactions are also observed for both forms (highlighted by the green oval), which can be attributed to the interaction between the carbonyl carbon atoms and neighbouring alkyl hydrogen atoms, as the cross peaks appear at lower chemical shifts in the F1 dimension. These cross peaks likely correspond to the interaction between the carbonyl carbon atoms, C4 and C5, and protons on neighbouring carbon atoms on that same ring (such and C2 and C3), as well as the N1H group. There is also a cross peak corresponding to an interaction between the carbonyl C7 group and neighbouring protons. There does not appear to be any evidence of a long-distance interaction between the C4 and C5

carbonyl atoms and the N10H group on the other side of the molecule. Data were collected and processed by Jamie L. Guest.

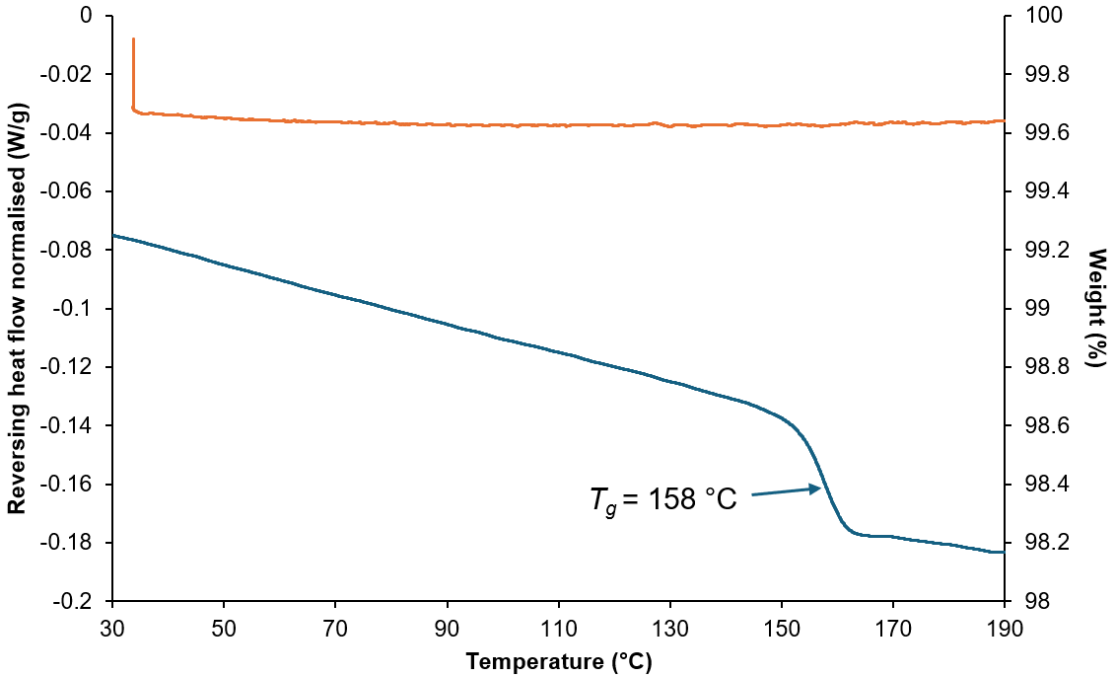

Figure **A23**. DSC/TGA of amorphous form A ($AZ1_{mix}$) showing a T_g at 158 °C and no solvent loss up to 190 °C.

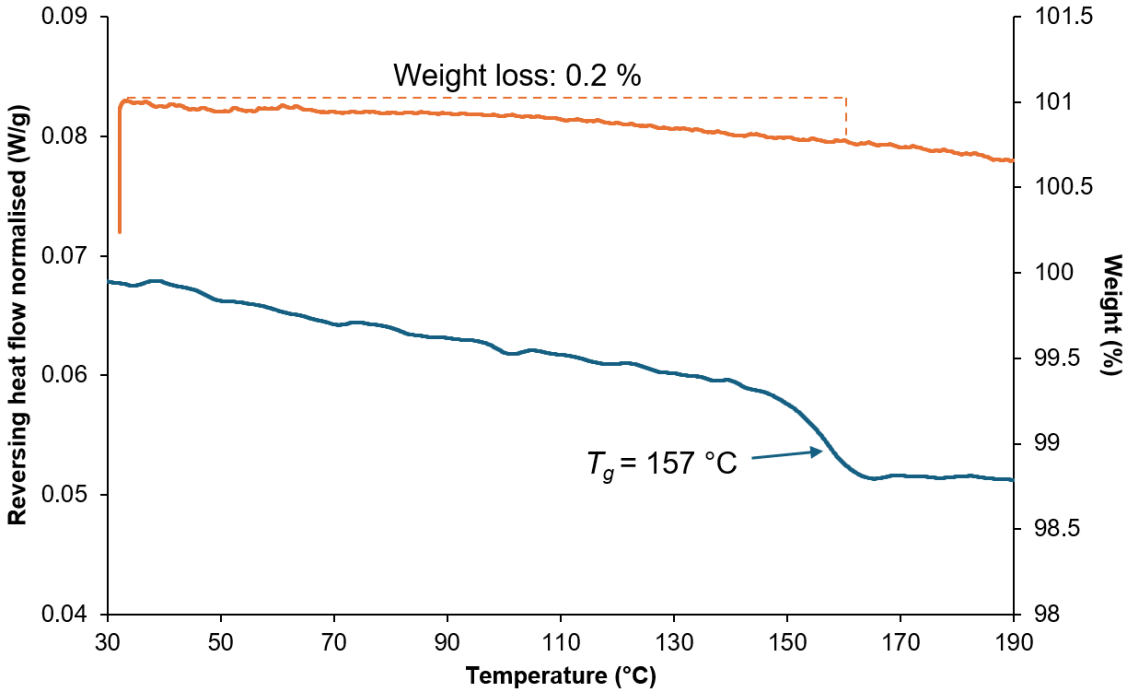

Figure **A24**. DSC/TGA of amorphous form A ($AZ1_{RRS}$) showing a T_g at 157 °C and 0.2 % weight loss up to 190 °C.

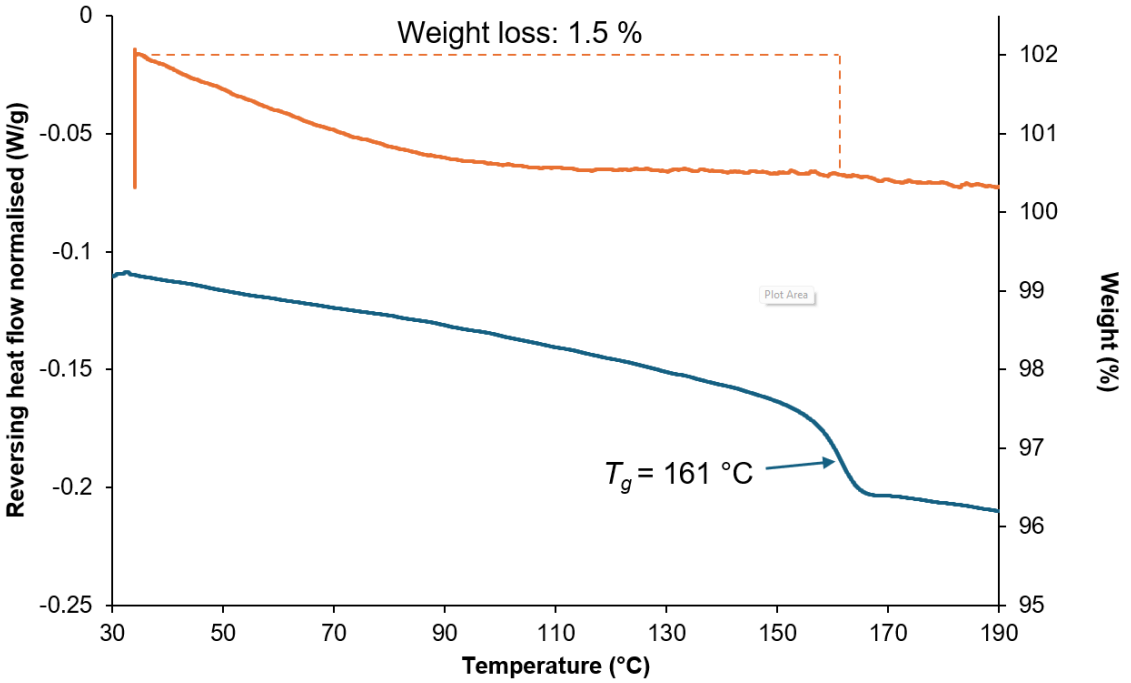

Figure **A25**. DSC/TGA of amorphous form A ($AZ1_{RRR}$) showing a T_g at 161 °C and 1.5 % weight loss up to 190 °C.

Appendix B

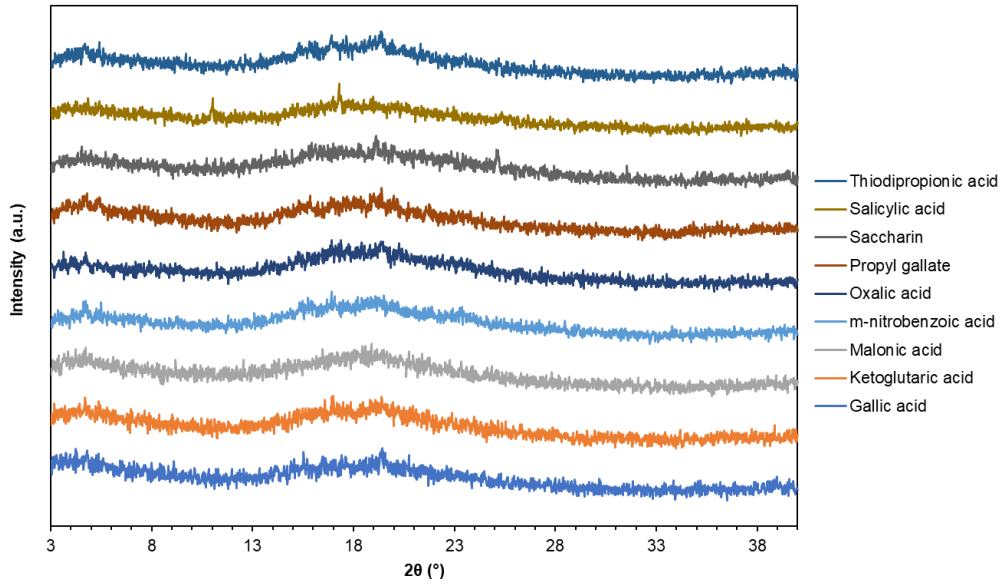

Figure **B1**. XRPD patterns of all nine potential co-amorphous solids showing a broad amorphous halo.

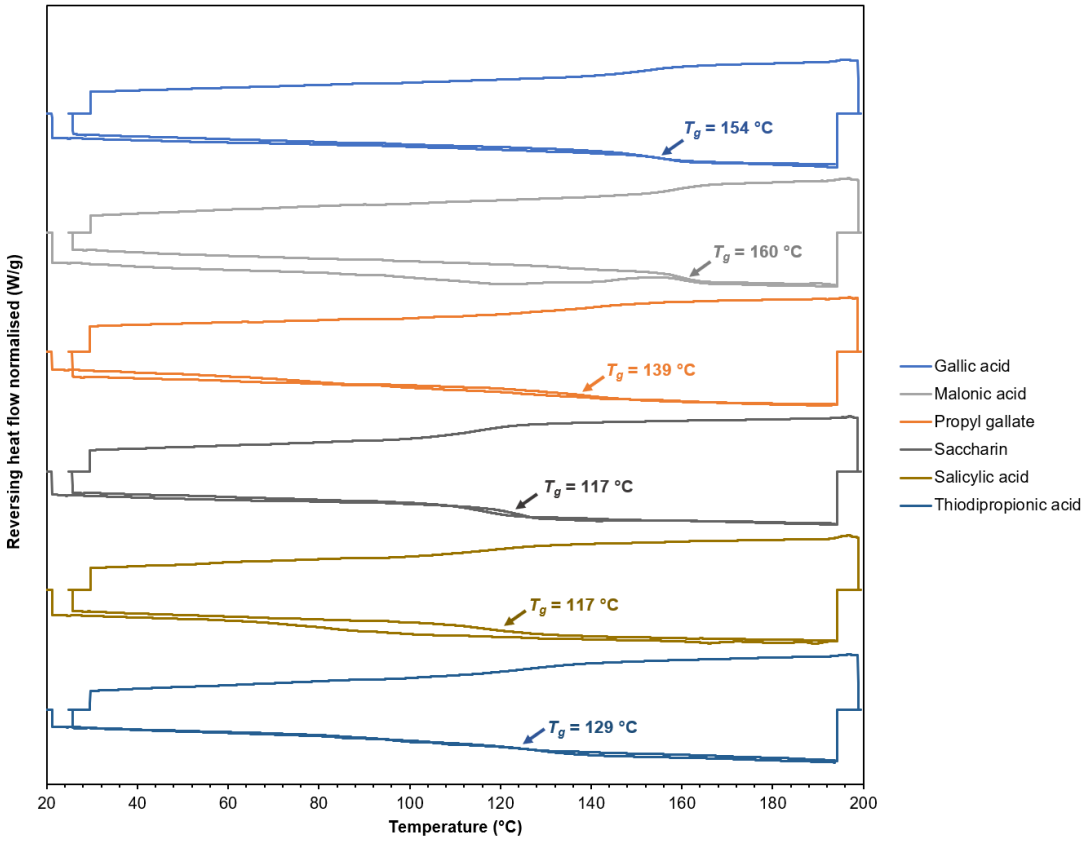

Figure **B2**. Heat-cool-heat mDSC thermograms for six of the nine potential co-amorphous solids not taken forward for dissolution studies, all showing a single T_g. The "dry" T_g values from the second heating cycle are marked on the plot.

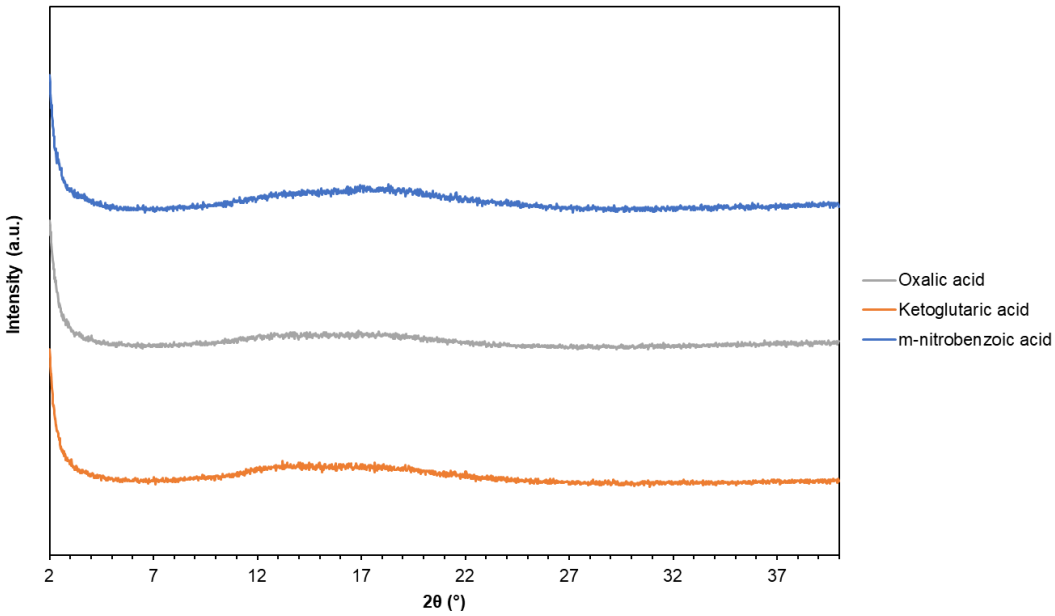

Figure **B3**. XRPD patterns of the three scaled-up co-amorphous solids of AZ1 with OXA, KGA and NBA showing physical stability of the amorphous phase after 3 months.

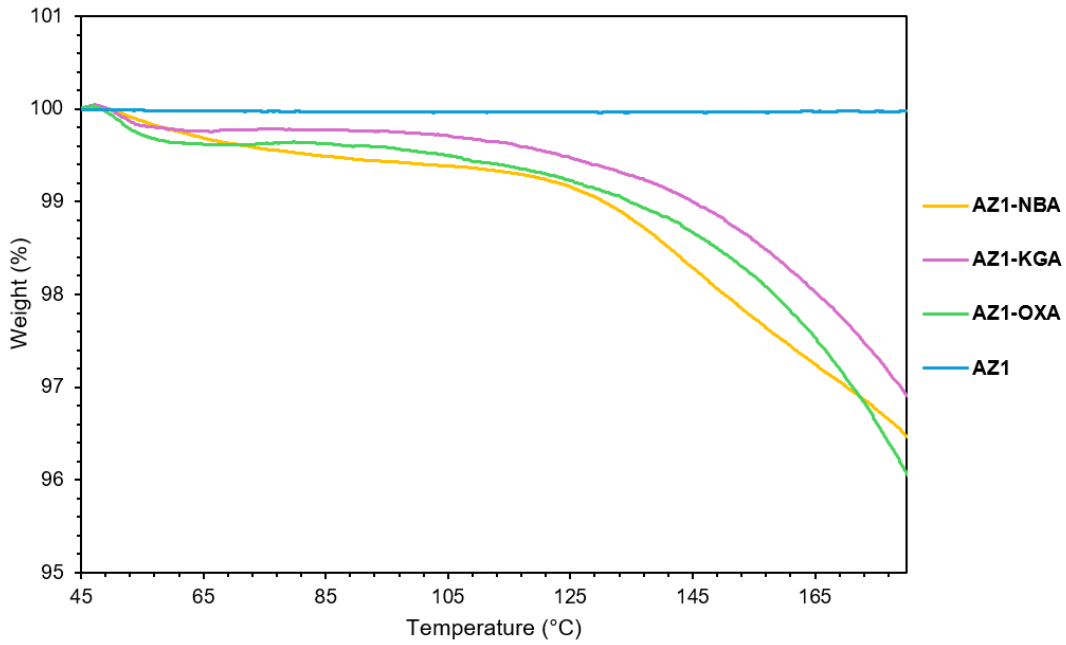

Figure **B4**. TGA thermograms for the co-amorphous solids of AZ1 with OXA, KGA and NBA.

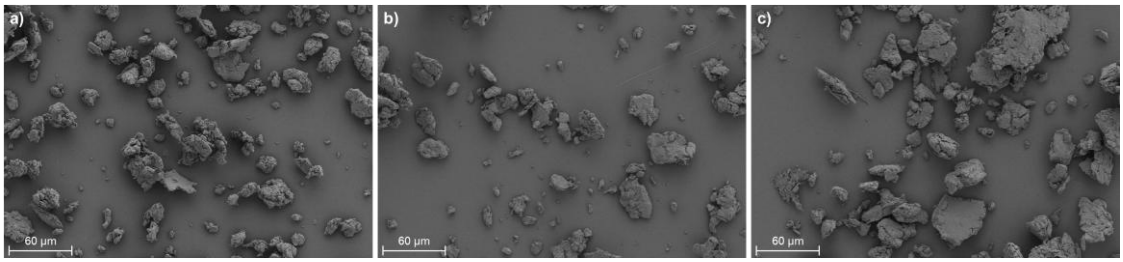

Figure **B5**. SEM images of co-amorphous solids of AZ1 with a) OXA, b) NBA and c) KGA.

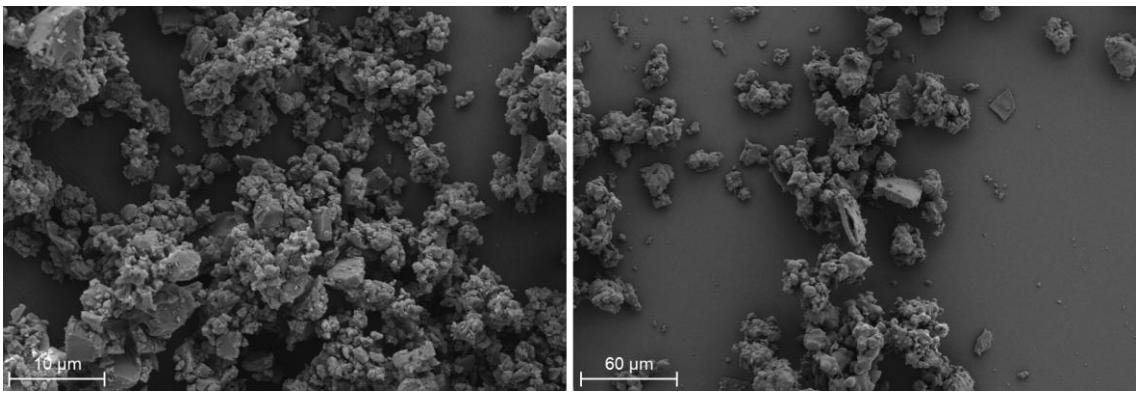

Figure **B6**. SEM images of milled amorphous AZ1 a) before and b) after 24 hours of slurry in FaSSIF.

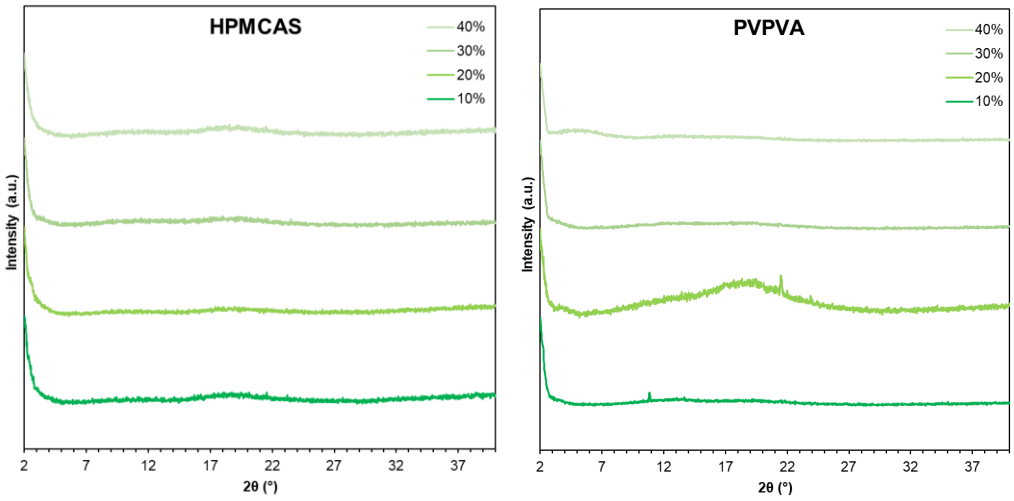

Figure **B7**. XRPD patterns of AZ1 ASDs with HPMCAS and PVPVA from 10 – 40 % DL prepared by slurry conversion, all showing a broad amorphous halo.

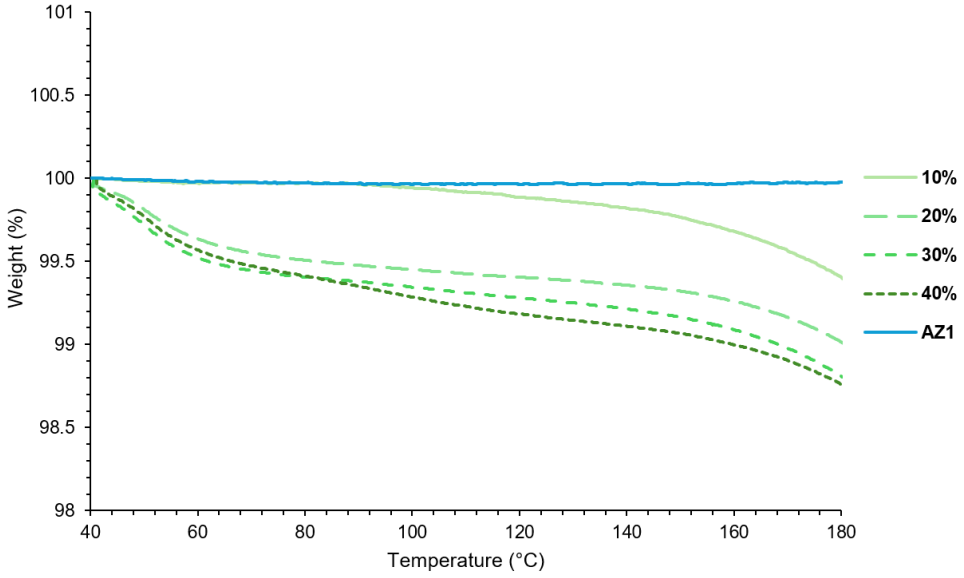

Figure **B8**. TGA thermograms of AZ1 HPMCAS ASDs prepared by slurry conversion from 10 – 40 % DL.

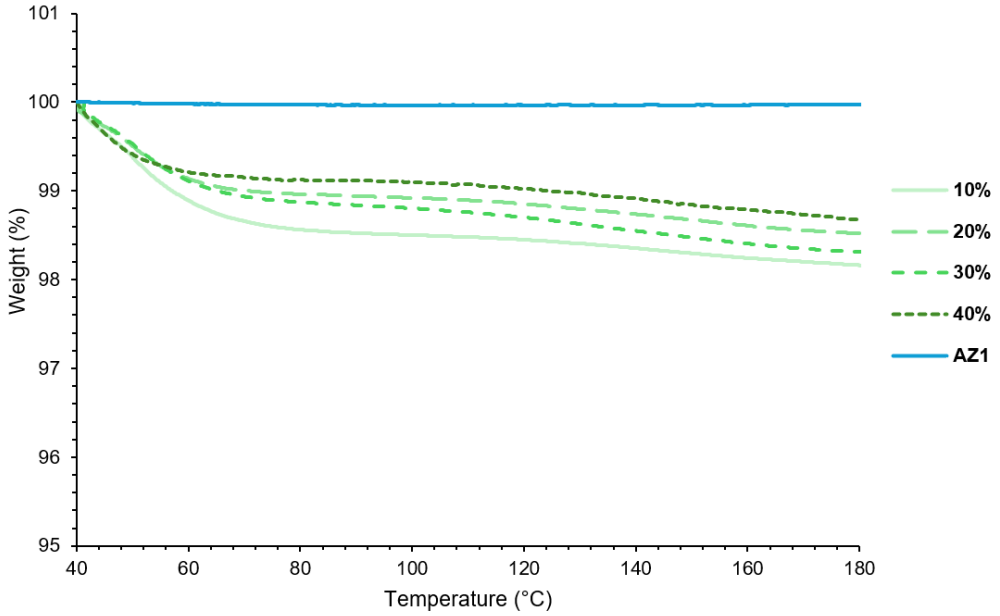

Figure **B9**. TGA thermograms of AZ1 PVPVA ASDs prepared by slurry conversion from 10 – 40 % DL.

Table **B1**. Comparison of experimental T_g values for AZ1 ASDs and predicted values from the Gordon-Taylor equation simplified to the Fox relation.

PROTAC	Polymer	Method	DL (% w/w)	Measured Tg (°C)	Predicted Tg (°C)	Difference (°C)
AZ1	HPMCAS	Slurry conversion	10	129	125	+4
			20	132	128	+4
			30	135	131	+4
			40	135	135	±0
		Solvent evaporation	10	129	125	+4
			20	135	128	+7
			30	136	131	+5
			40	139	135	+4
	PVPVA	Slurry conversion	10	115	115	±0
			20	116	118	-2
			30	121	122	-1
			40	125	126	-1
		Solvent evaporation	10	112	115	-3
			20	119	118	+1

			30	128	122	+6
			40	134	126	+8
AZ2	HPMCAS	Slurry conversion	10	131	126	+5
			20	134	129	+5
			30	147	133	+14
AZ3	HPMCAS	Slurry conversion	10	131	126	+5
			20	140	129	+11
			30	144	133	+11
AZ4	HPMCAS	Slurry conversion	10	131	126	+5
			20	140	129	+11
			30	143	133	+10

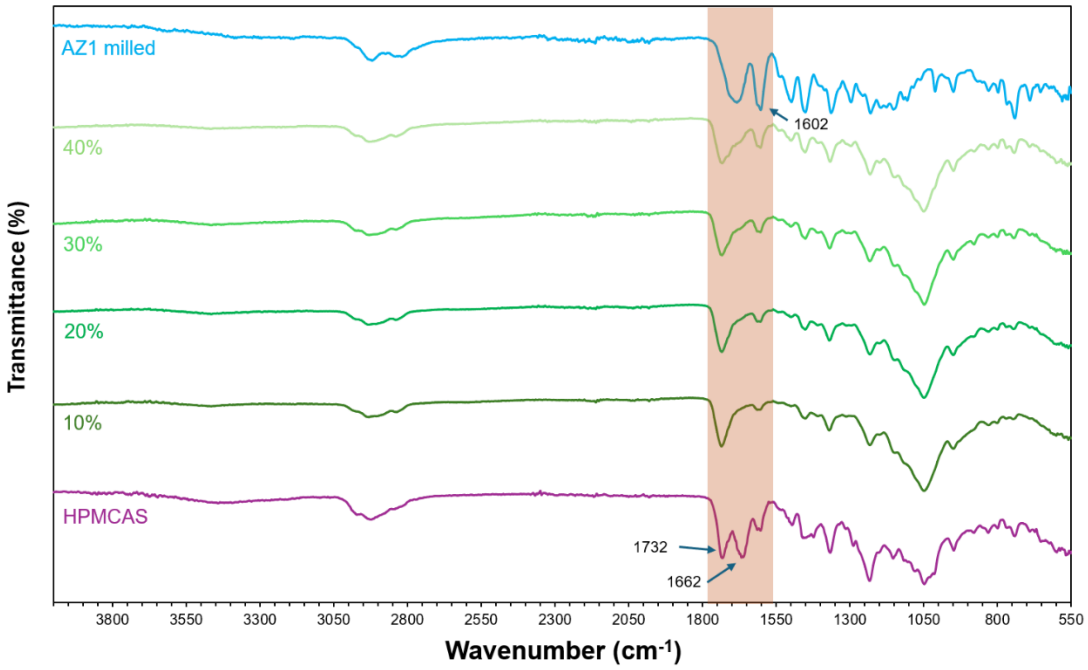

Figure **B10**. FTIR spectra of AZ1 HPMCAS ASDs prepared by slurry conversion from 10 – 40 % DL.

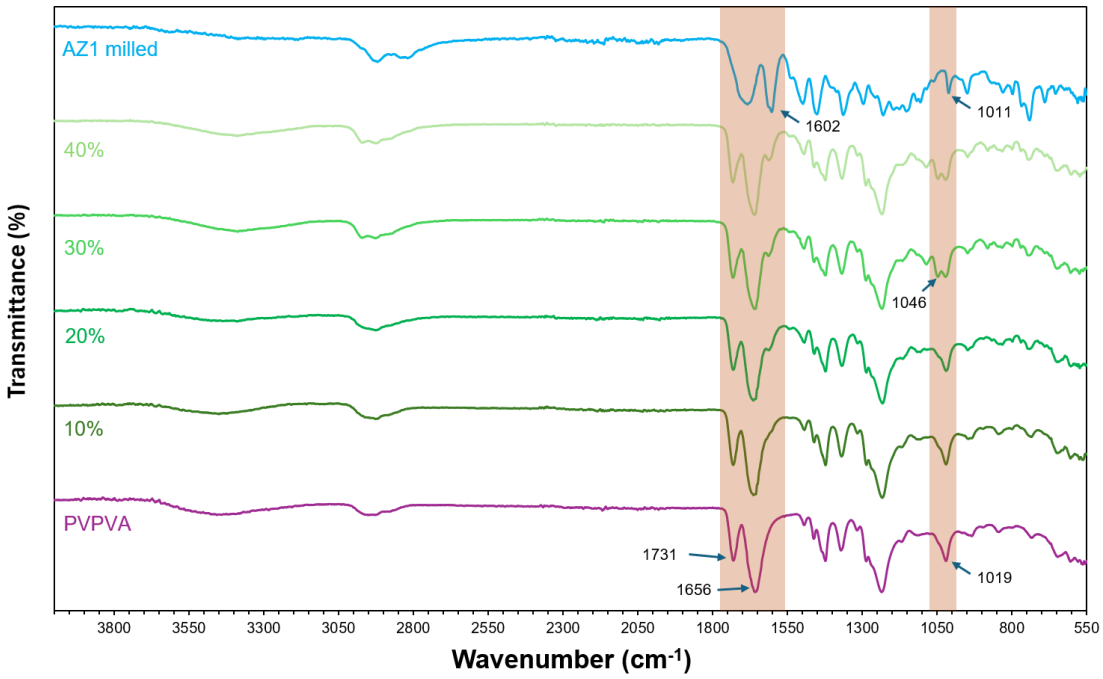

Figure **B11**. FTIR spectra of AZ1 PVPVA ASDs prepared by slurry conversion from 10 – 40 % DL.

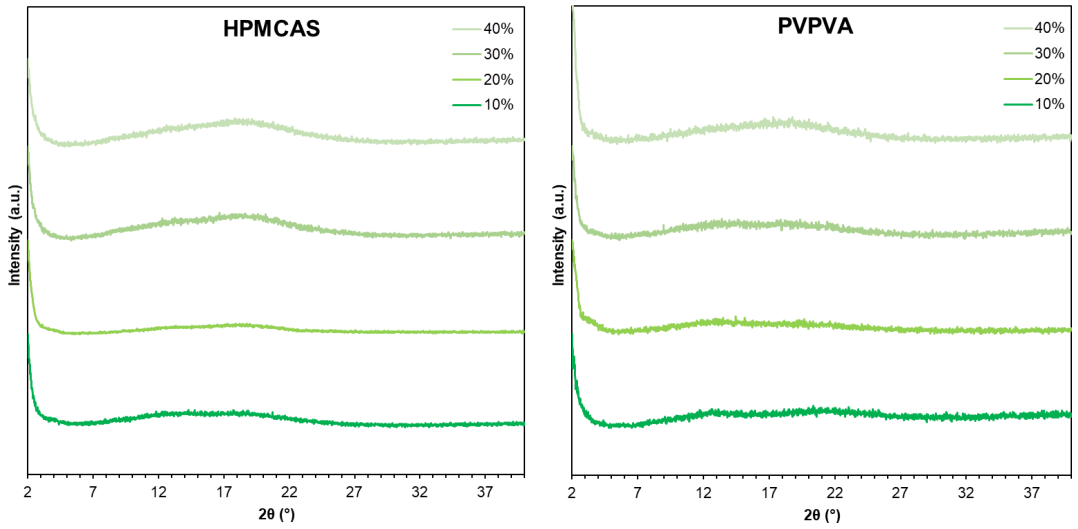

Figure **B12**. XRPD patterns of AZ1 ASDs with HPMCAS and PVPVA from 10 – 40 % DL prepared by solvent evaporation, all showing a broad amorphous halo.

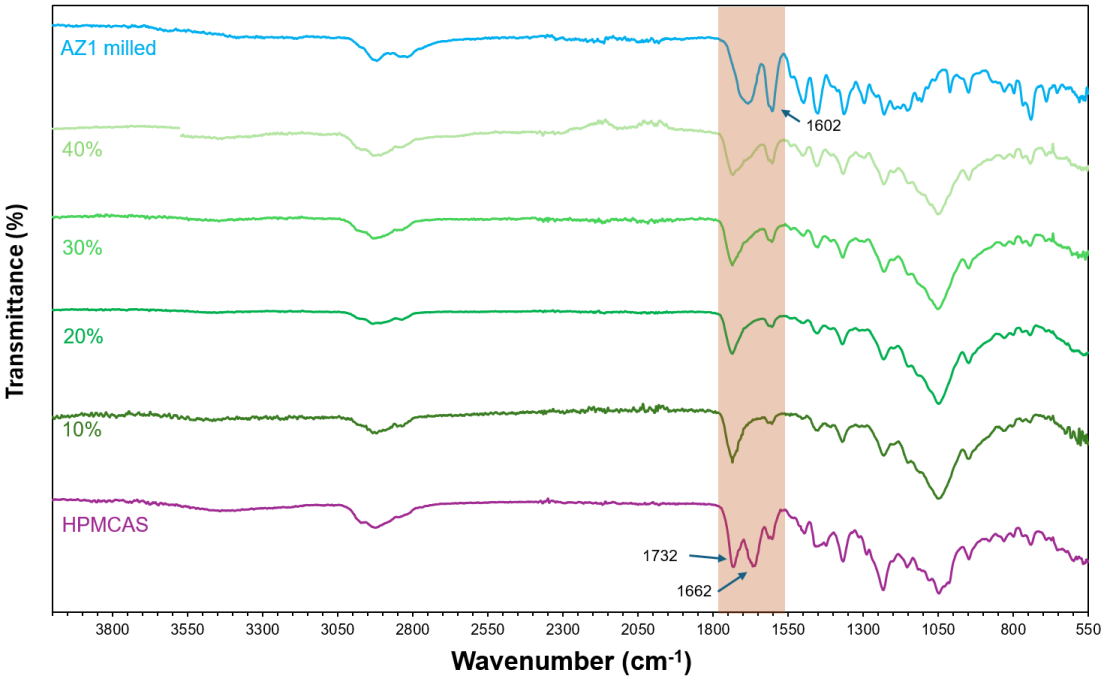

Figure **B13**. FTIR spectra of AZ1 HPMCAS ASDs prepared by solvent evaporation from 10 – 40 % DL.

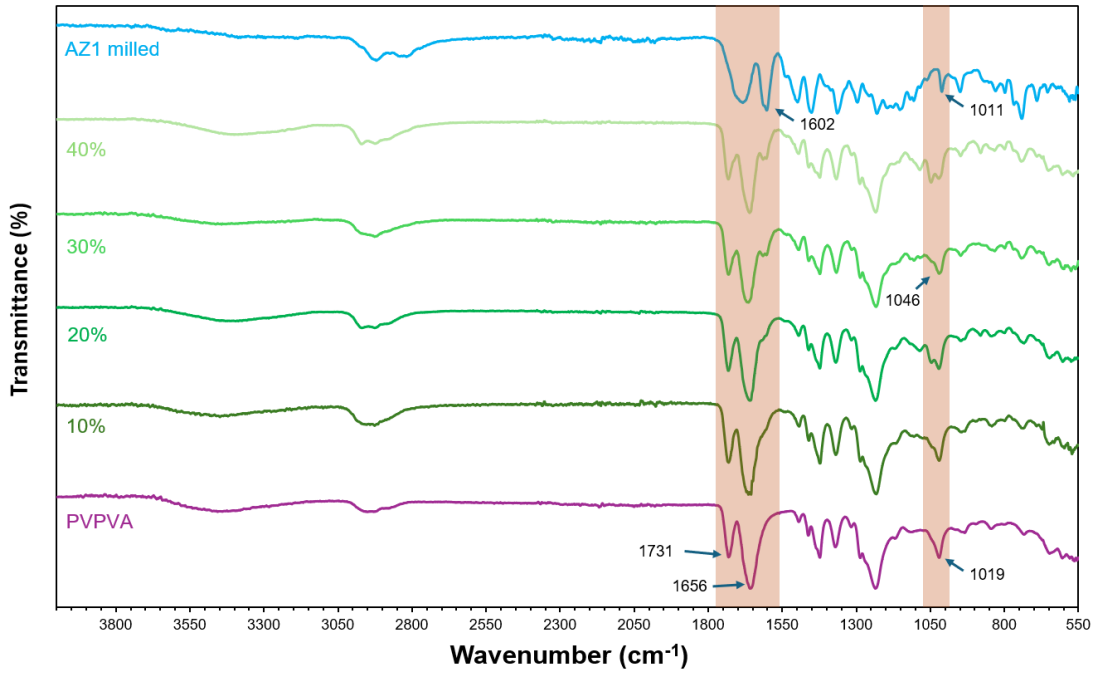

Figure **B14**. FTIR spectra of AZ1 PVPVA ASDs prepared by solvent evaporation from 10 – 40 % DL.

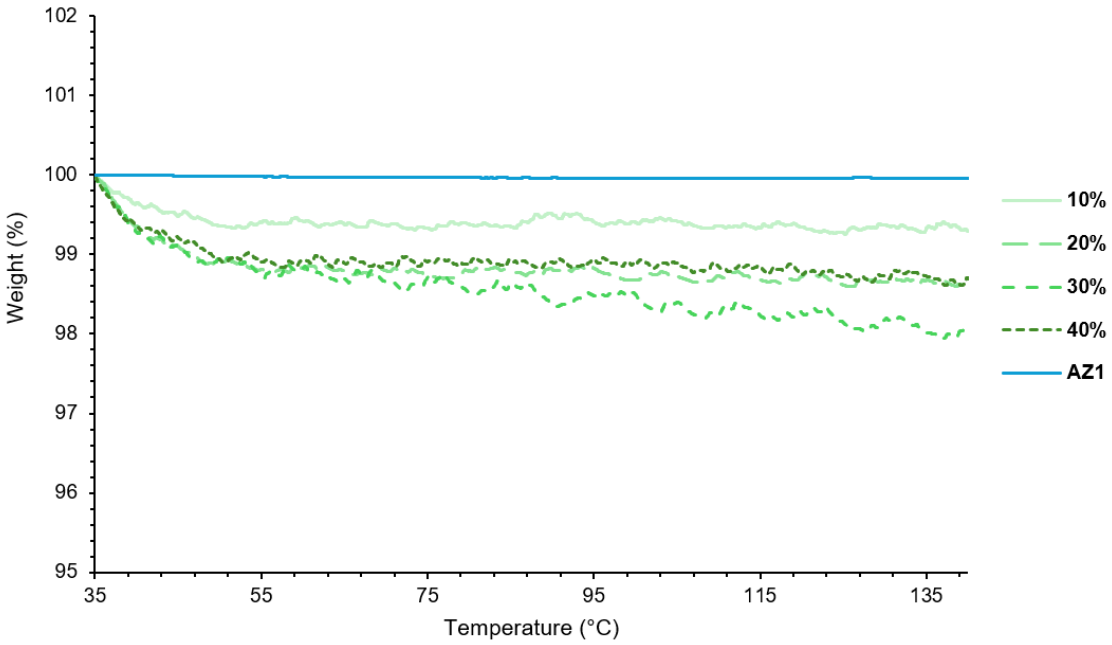

Figure **B15**. TGA thermograms of AZ1 HPMCAS ASDs prepared by solvent evaporation from 10 – 40 % DL.

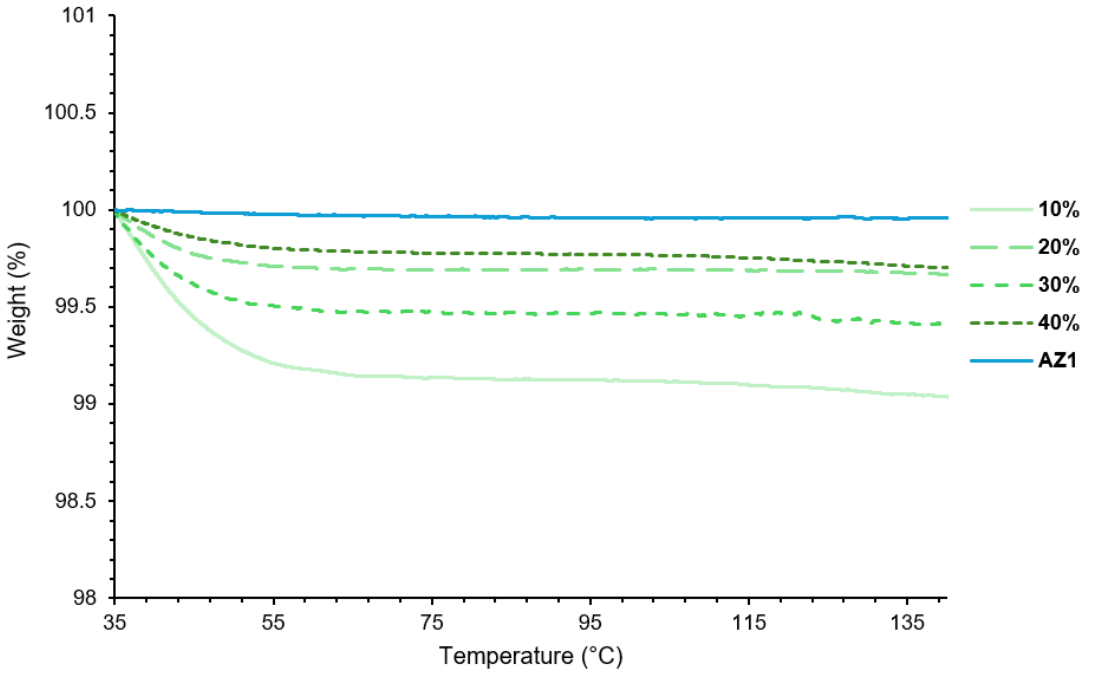

Figure **B16**. TGA thermograms of AZ1 PVPVA ASDs prepared by solvent evaporation from 10 – 40 % DL.

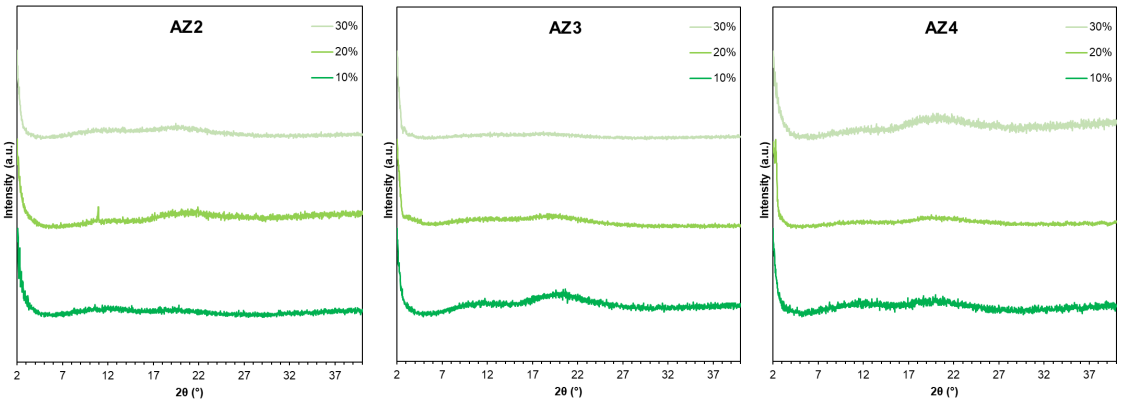

Figure **B17**. XRPD patterns for AZ2, AZ3 and AZ4 ASDs with HPMCAS from 10 – 30 % DL prepared by slurry conversion, all showing a broad amorphous halo.

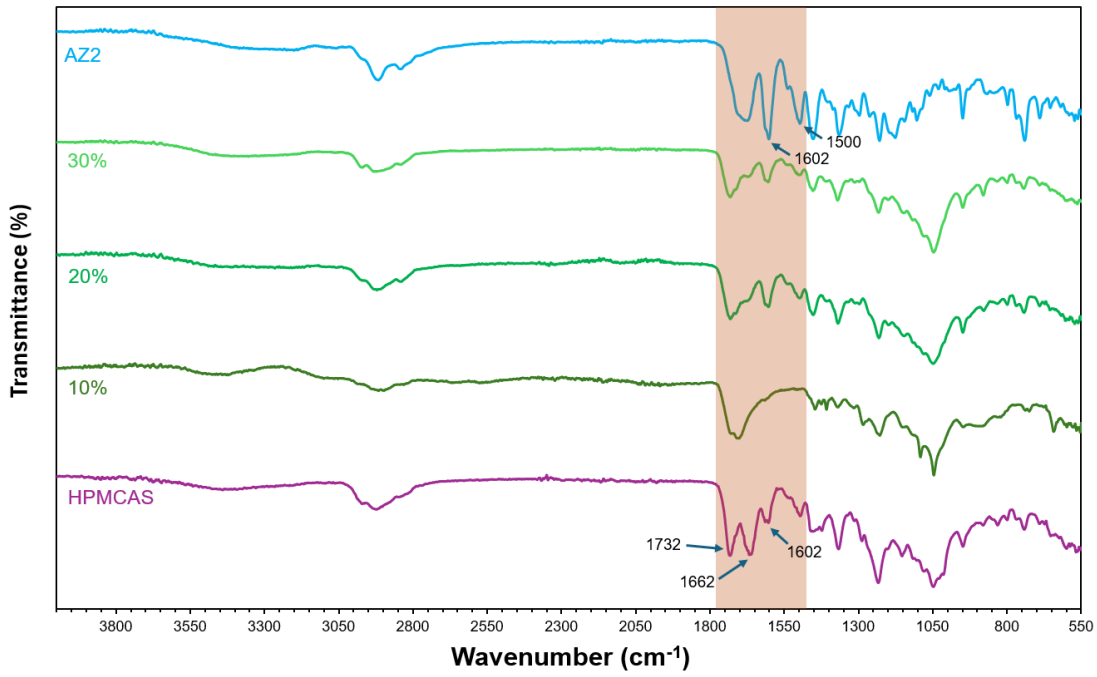

Figure **B18**. FTIR spectra of AZ2 HPMCAS ASDs from 10 – 30 % DL.

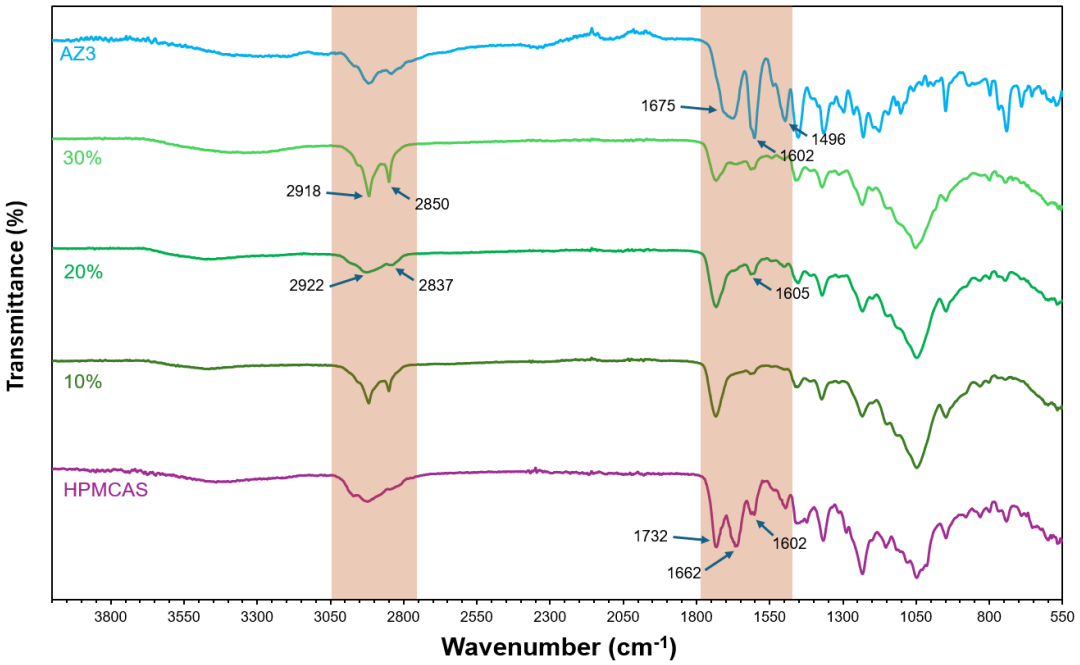

Figure **B19**. FTIR spectra of AZ3 HPMCAS ASDs from 10 – 30 % DL.

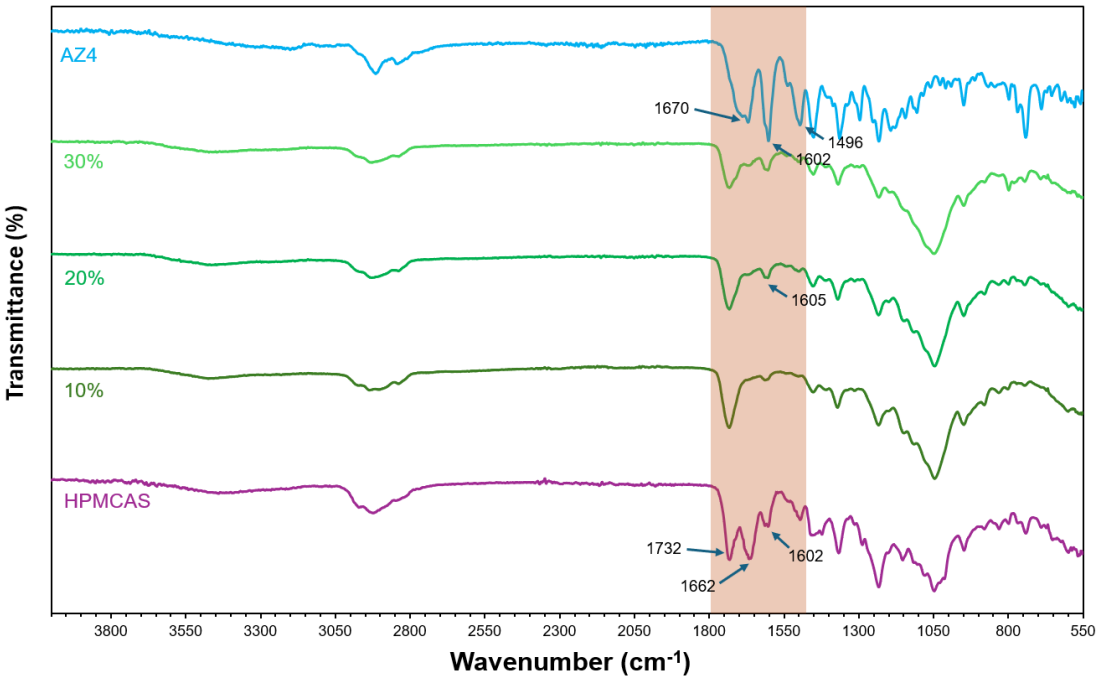

Figure **B20**. FTIR spectra of AZ4 HPMCAS ASDs from 10 – 30 % DL.

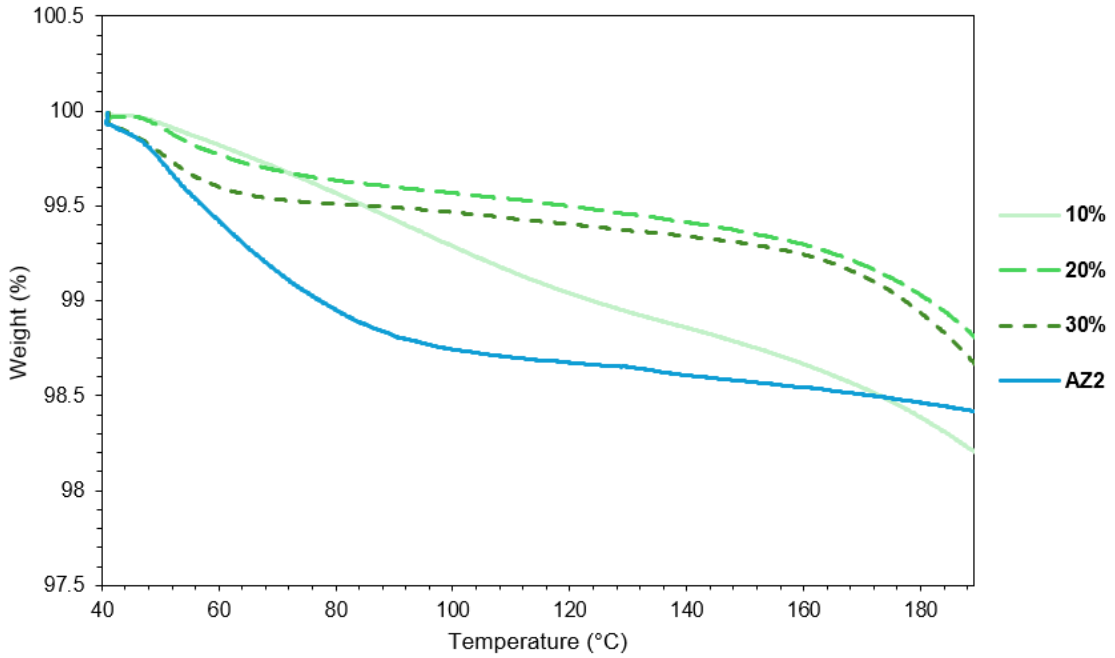

Figure **B21**. TGA thermograms of AZ2 HPMCAS ASDs from 10 – 30 % DL. AZ2 contains roughly 1.3 % w/w of water.

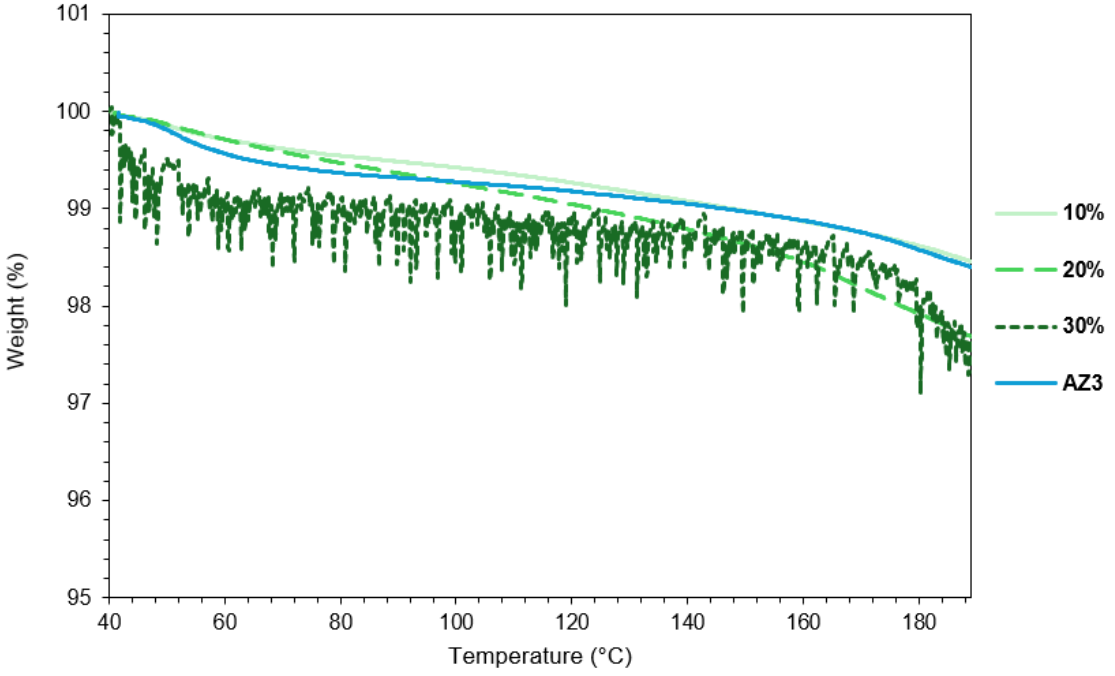

Figure **B22**. TGA thermograms of AZ3 HPMCAS ASDs from 10 – 30 % DL. AZ3 contains roughly 0.7 % w/w of water.

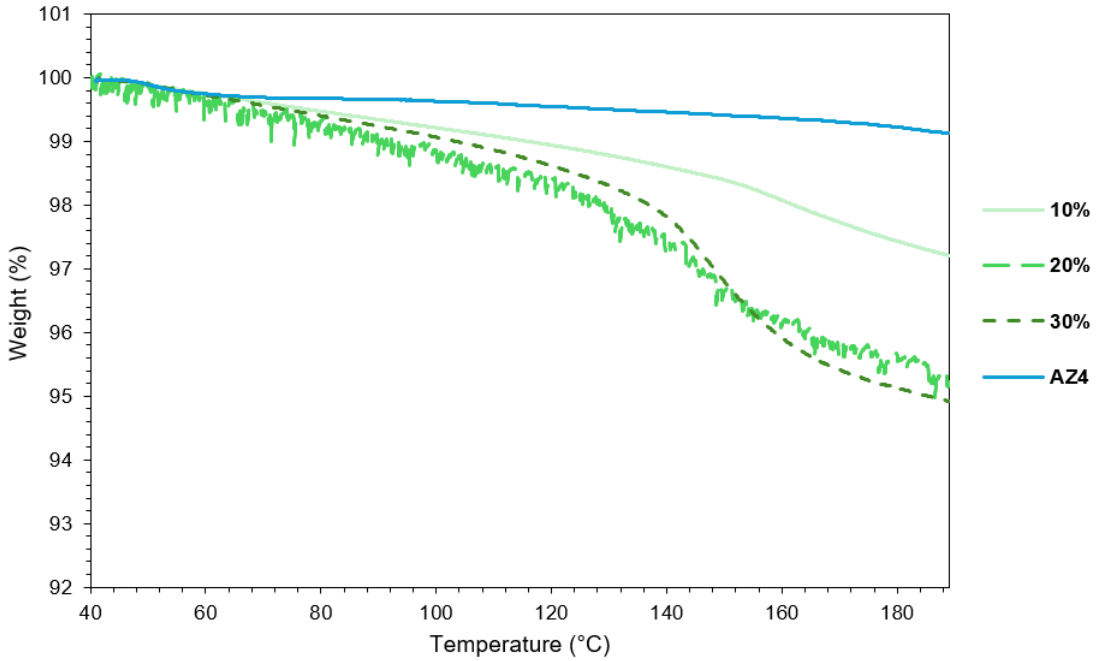

Figure **B23**. TGA thermograms of AZ4 HPMCAS ASDs from 10 – 30 % DL. AZ4 contains 0.4 % w/w of water.

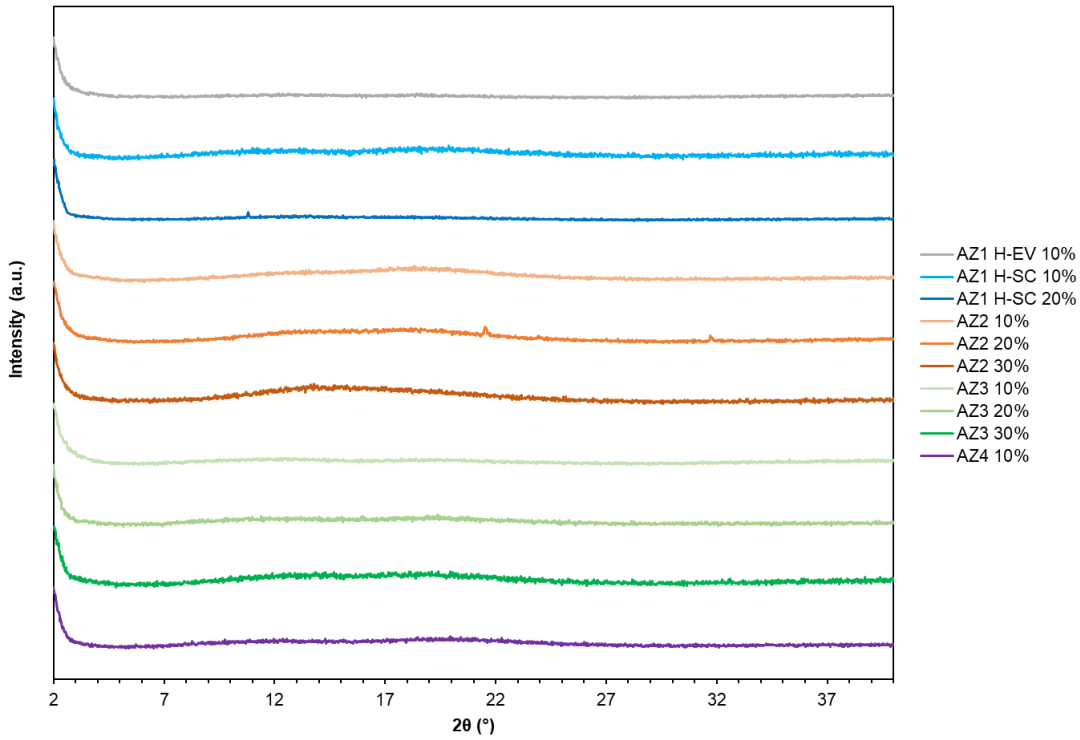

Figure **B24**. XRPD patterns for ASDs conditioned for 1 month at 75% RH and 40 °C, all showing a broad amorphous halo.

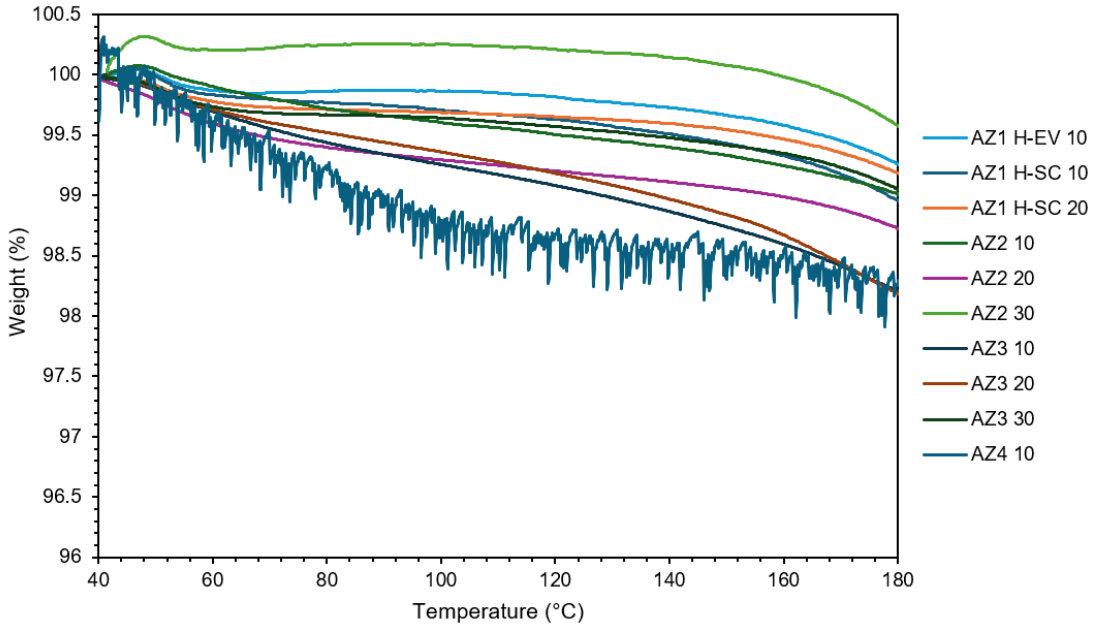

Figure **B25**. TGA thermograms for ASDs conditioned for 1 month at 75% RH and 40 °C.

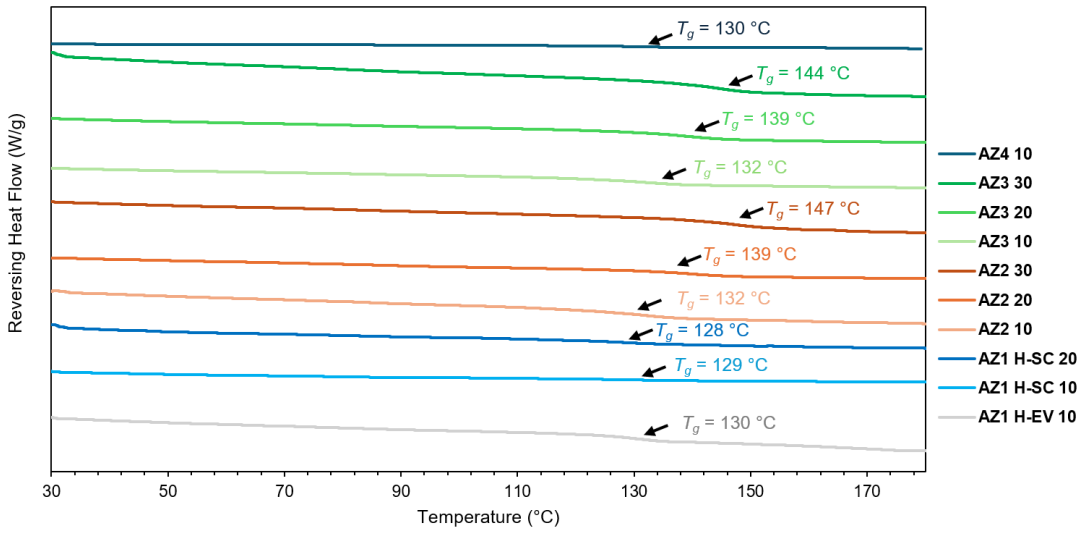

Figure **B26**. mDSC thermograms for ASDs conditioned for 1 month at 75% RH and 40 °C.

Appendix C

Table **C1**. Crystallographic data for co-crystal **2**. Data were collected and processed by Dr Toby J. Blundell.

Empirical formula	$C_{17}H_{24}N_9O_{4.5}$	**μ/mm^{-1}**	0.113
Formula weight	426.45	**F(000)**	450.0
Temperature/K	120.00	**Crystal size/mm^3**	0.38 × 0.15 × 0.02
Crystal system	triclinic	**Radiation**	Mo Kα (λ = 0.71073)
Space group	$P\bar{1}$	**2Θ range for data collection/°**	5.534 to 55.998
a/Å	7.9402(3)	**Index ranges**	-10 ≤ h ≤ 10, -13 ≤ k ≤ 13, -16 ≤ l ≤ 16
b/Å	10.2062(3)	**Reflections collected**	29232
c/Å	12.5527(4)	**Independent reflections**	4552 [R_{int} = 0.0639, R_{sigma} = 0.0424]
α/°	93.5640(10)	**Data/restraints/parameters**	4552/8/370
β/°	94.6780(10)	**Goodness-of-fit on F^2**	1.128
γ/°	111.0870(10)	**Final R indexes [I>=2σ (I)]**	R_1 = 0.0800, wR_2 = 0.1738
Volume/Å^3	941.39(5)	**Final R indexes [all data]**	R_1 = 0.0943, wR_2 = 0.1816
Z	2	**Largest diff. peak/hole / e Å^{-3}**	0.76/-0.40
ρ_{calc}g/cm^3	1.504		

Table **C2**. Hydrogen bonds for co-crystal **2**.

D	H	A	d(D-H)/Å	d(H-A)/Å	d(D-A)/Å	D-H-A/°
N2	H2	N4	0.92(4)	1.97(4)	2.887(3)	177(3)
N3	H3A	O2^1	0.78(3)	2.41(3)	3.145(4)	158(4)
N3	H3A	O5	0.78(3)	2.64(5)	3.058(9)	116(4)
N7	H7A	O3	0.89(3)	2.17(4)	3.007(3)	156(3)
N7	H7B	O4	0.88(4)	2.14(4)	2.929(4)	149(3)
N8	H8C	O2	0.87(3)	2.05(4)	2.924(3)	175(3)
N8	H8D	O1^2	0.90(4)	2.18(4)	3.063(3)	166(3)

N9	H9A	N5[3]	0.84(4)	2.18(4)	3.017(4)	172(3)
N9	H9B	O1[4]	0.82(4)	2.41(4)	3.040(3)	135(3)
O5	H5A	O1[1]	0.87	2.38	3.223(9)	164.0

[1]1-X,1-Y,-Z; [2]1+X,+Y,+Z; [3]3-X,2-Y,1-Z; [4]2-X,2-Y,1-Z

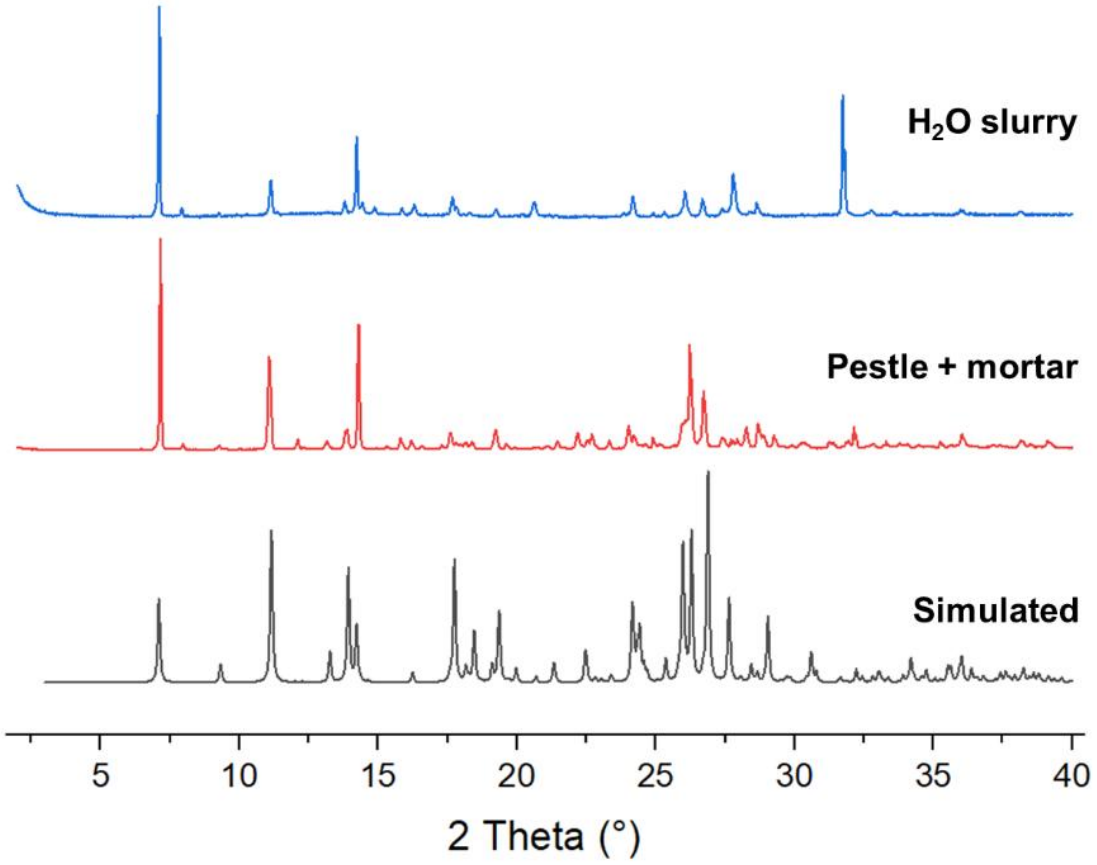

Figure **C1**. XRPD patterns of co-crystal **1** prepared by slurry in water or by grinding lenalidomide Form B and melamine in a pestle and mortar, compared to the pattern simulated from single crystal XRD data of isostructural co-crystal **2**.

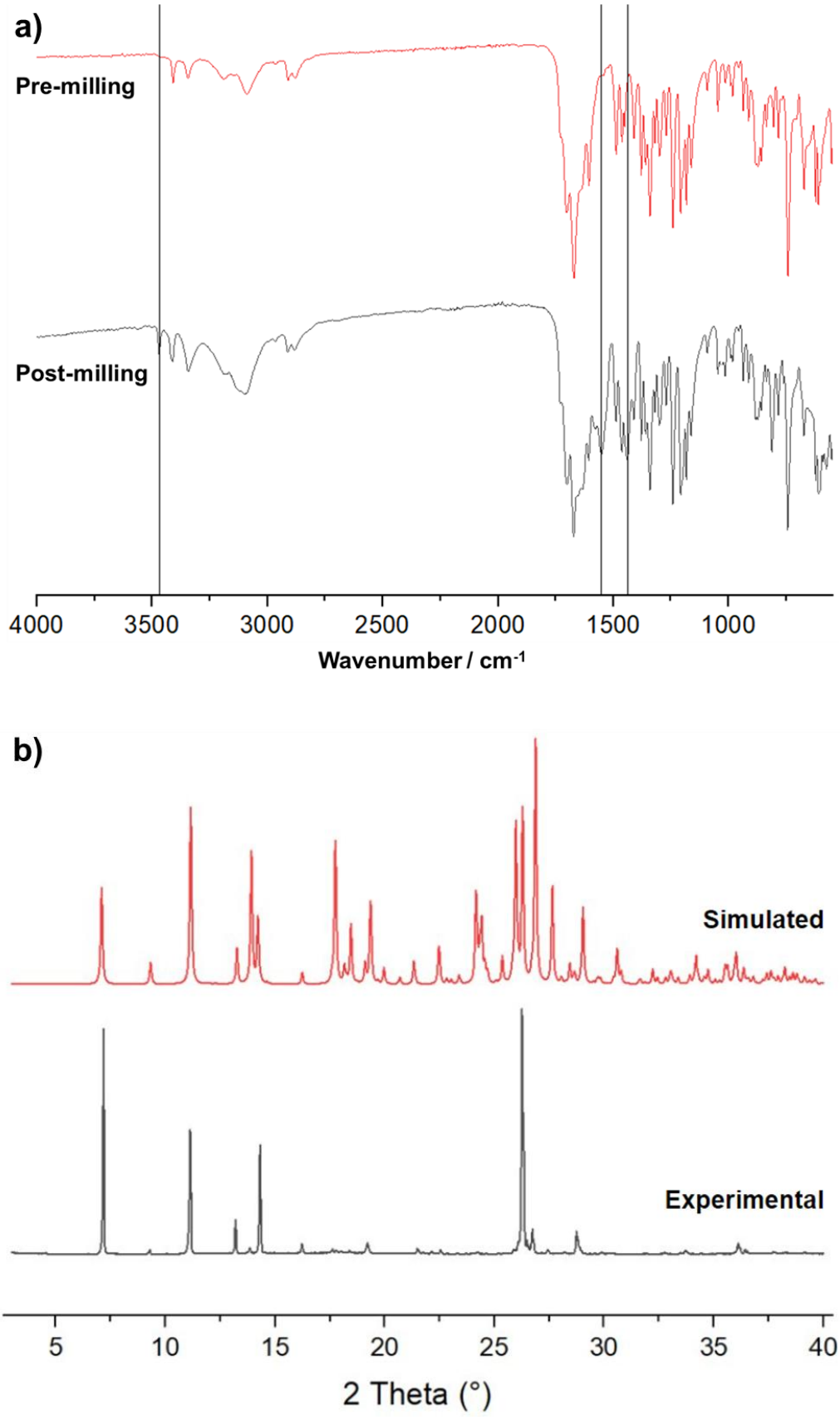

Figure **C2.** a) FTIR spectra of lenalidomide Form B and melamine before and after liquid-assisted grinding (LAG) in the presence of methanol to form co-crystal **2**. b) XRPD pattern of **2** prepared by LAG compared to the pattern simulated from single crystal XRD data.

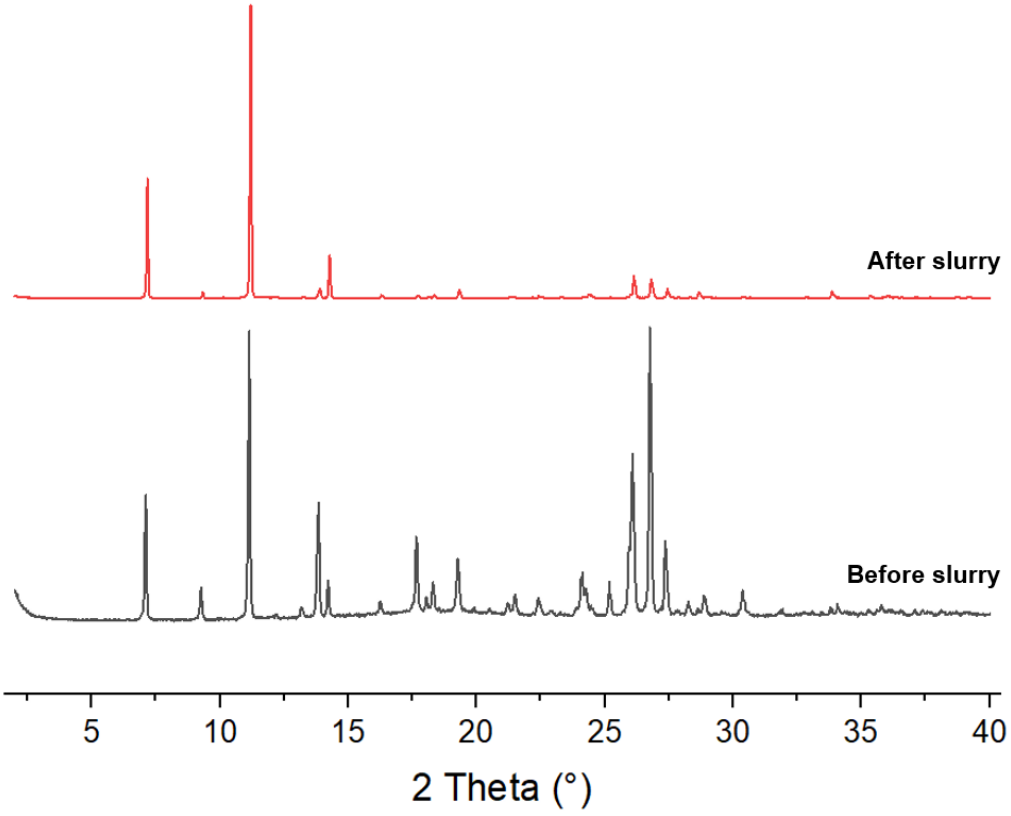

Figure **C3.** XRPD pattern of co-crystal **2** before and after 24 hours of slurry in water, showing no change in crystal structure although preferred orientation effects appear to increase.

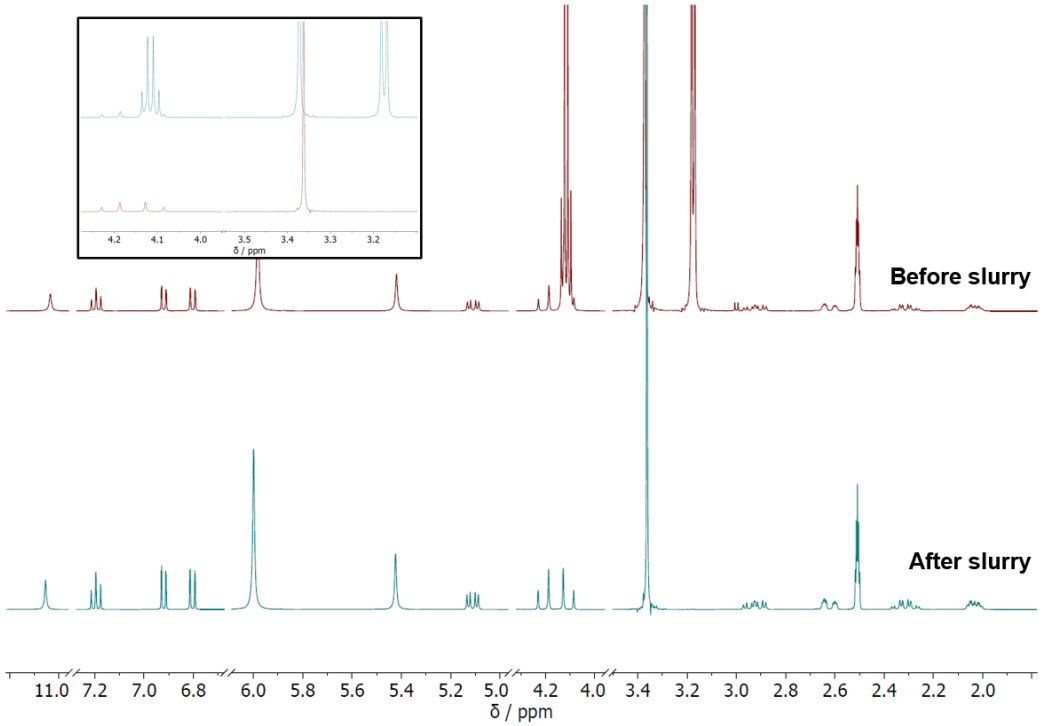

Figure **C4.** ^{1}H NMR (400 MHz, $CDCl_3$) of co-crystal **2** before and after 24 hours of slurry in water, showing the disappearance of characteristic methanol signals: δ / ppm 3.17 (3H, d, *J* = 5.3 Hz) 4.11 (1H, q, *J* = 5.3 Hz).

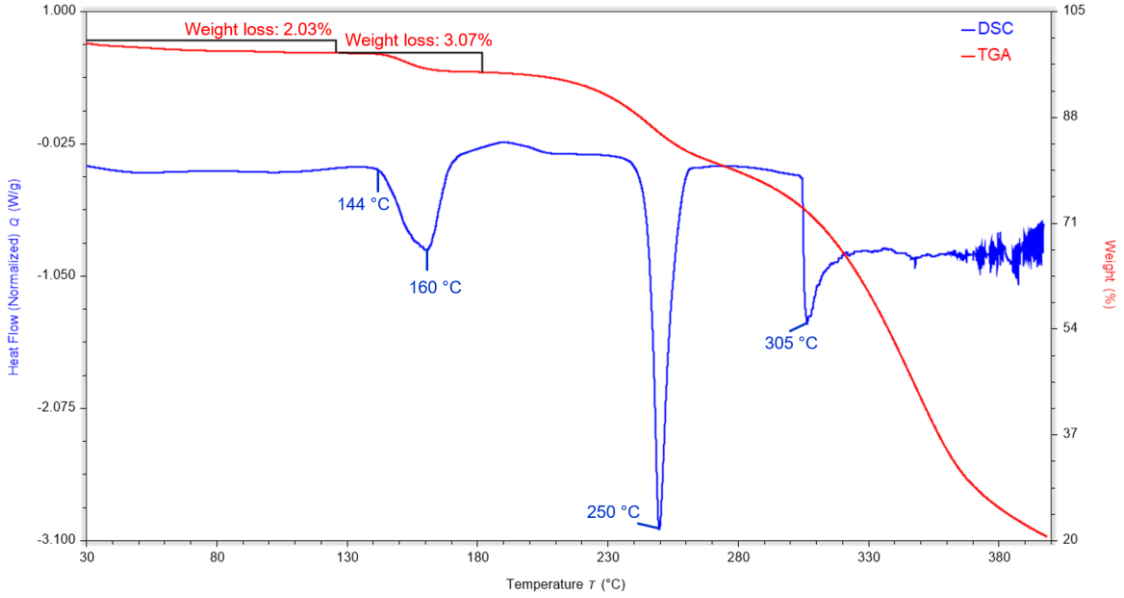

Figure **C5**. DSC and TGA thermograms for **2** showing a broad solvent loss endotherm between 30 and 130 °C, corresponding to a loss of 2.0 % mass in the TGA trace, followed by another broad solvent loss endotherm with an onset temperature of 144 °C that corresponds to a further 3.1 % mass loss by TGA. This suggests that the disordered methanol solvent is labile and is lost gradually up to 130 °C, before the water is lost between 144 and 174 °C. The relatively high temperature of this dehydration indicates that water is tightly bound in the crystalline lattice. The second solvent loss endotherm appears to be convoluted with a recrystallisation event where the dehydrated co-crystal is destabilised and recrystallises into lenalidomide and melamine, followed by a melt with an onset temperature of 246 °C and a peak at 250 °C corresponding to lenalidomide. The simultaneous mass loss around 250 °C suggests that this is a melt-decomposition event. Melamine appears to decompose at 305 °C.

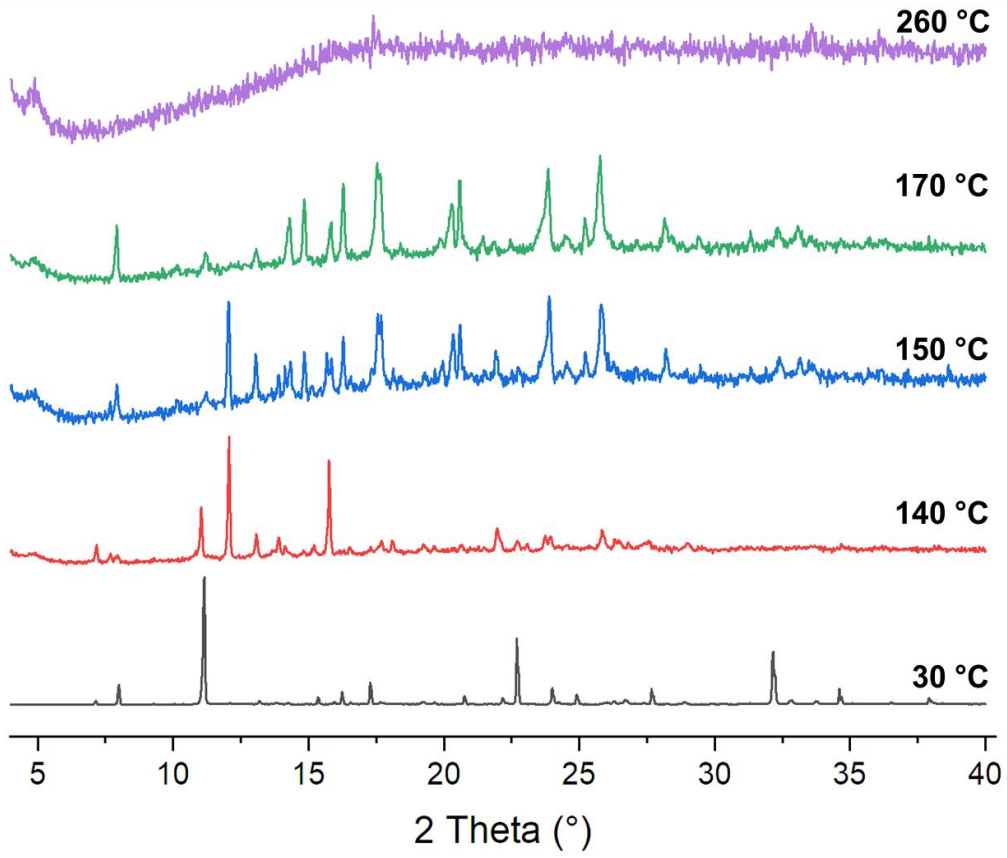

Figure **C6**. VT-XRD patterns for **2** showing recrystallisation into lenalidomide Form A above 140 °C, which melts to leave amorphous material above 260 °C.

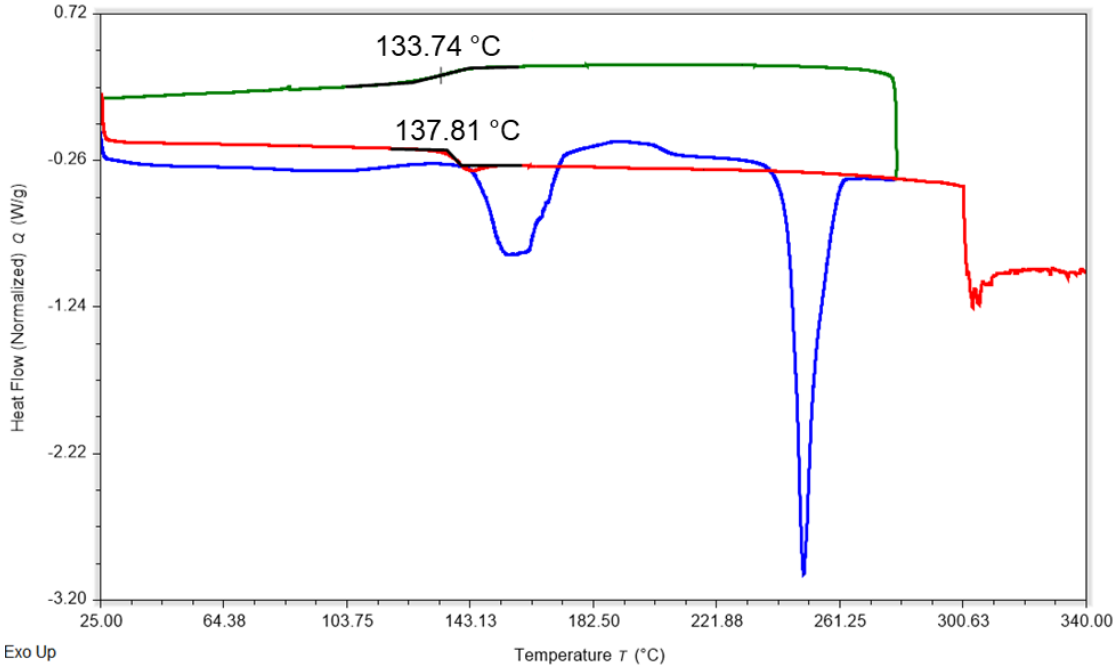

Figure **C7.** DSC thermogram of **2** showing heating from 25 °C to 280 °C (blue) followed by cooling back to 25 °C (green) and subsequent heating to 340 °C (red). Co-crystal **2** recrystallises as lenalidomide Form A upon desolvation at 142 °C and amorphous melamine is formed.

Lenalidomide melts at 260 °C and decomposes. The remaining amorphous melamine undergoes a glass transition at 134 °C upon cooling and at 138 °C upon heating, before decomposing above 300 °C.

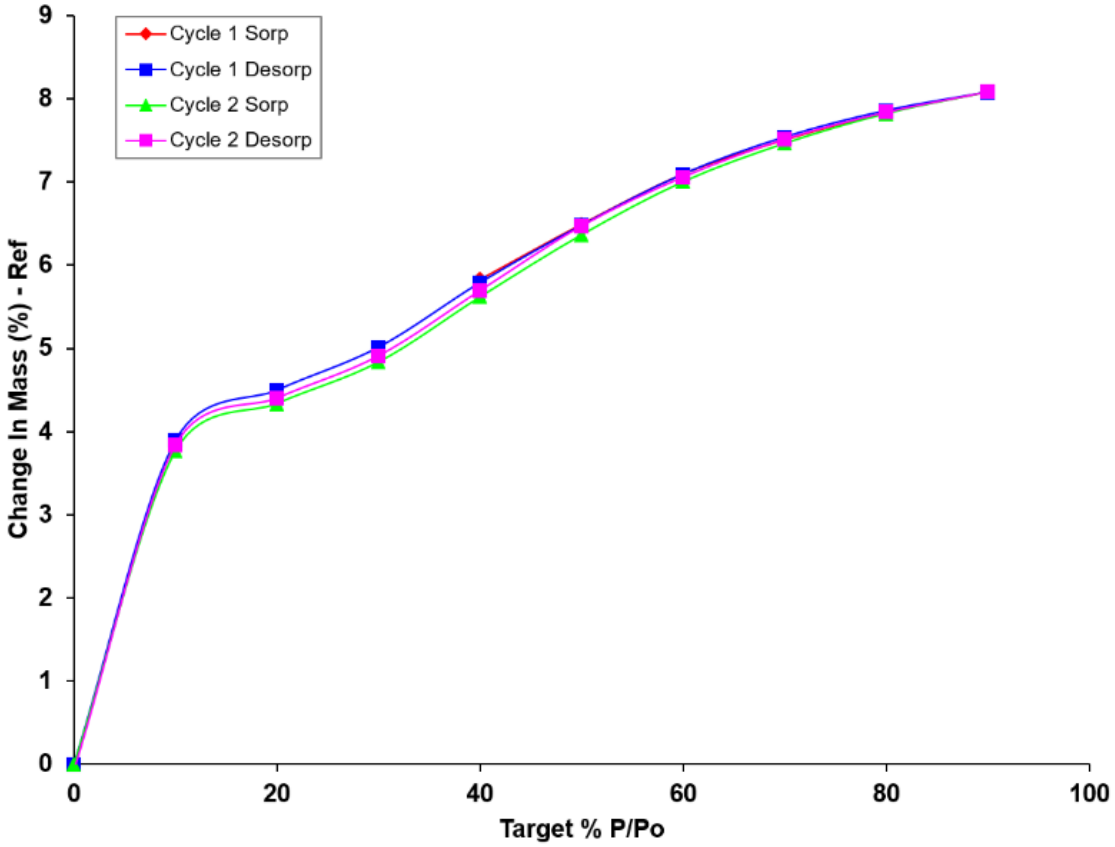

Figure **C8**. DVS isotherm of **2** with two cycles of sorption and desorption at 25 °C. The minimum equilibration time was 29 minutes and the maximum was 360 minutes (at 0% RH). The loss of 5.8 % mass when decreasing from 40 to 0 % RH is close to the 5.1 % total mass loss observed in the TGA upon heating to 180 °C, indicating the loss of all solvent from the co-crystal below 20 % RH. Upon ramping back up to 90% RH, the same mass of water is taken up again without hysteresis, indicating that the desolvated crystal retains its structure at 0% RH when all solvent is removed. This may differ from the recrystallisation event observed upon desolvation in the DSC thermogram because the DVS isotherm is acquired at 25 °C and therefore the sample has less energy to recrystallise than at approximately 160 °C in the DSC experiment. The absence of any significant hysteresis in the second cycle of sorption suggests that the labile methanol in the co-crystal sample had evaporated before the DVS experiment started, and hence the same amount of water was taken up on both cycles. The step increase from 0 to 20% RH of approximately 4.4% mass gain indicates the formation of 2 as a monohydrate. The further increase to roughly 8% mass gain at 90% RH indicates that additional water can pack into the solvent channels at high humidity, leading to an approximately dihydrate structure of 2 with a 1.9 : 1 molar ratio of water in the asymmetric unit.

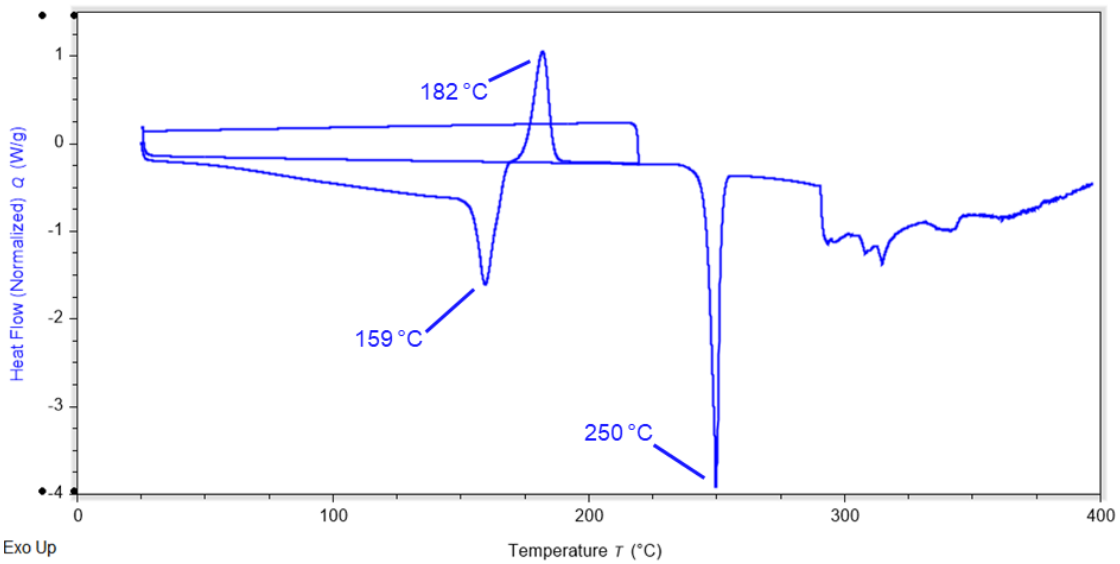

Figure **C9**. DSC thermogram of **1** showing heating from 25 °C to 220 °C, cooling back to 25 °C, and subsequent re-heating to 400 °C. No glass transition corresponding to amorphous melamine is detected in the cooling or second heating cycles.

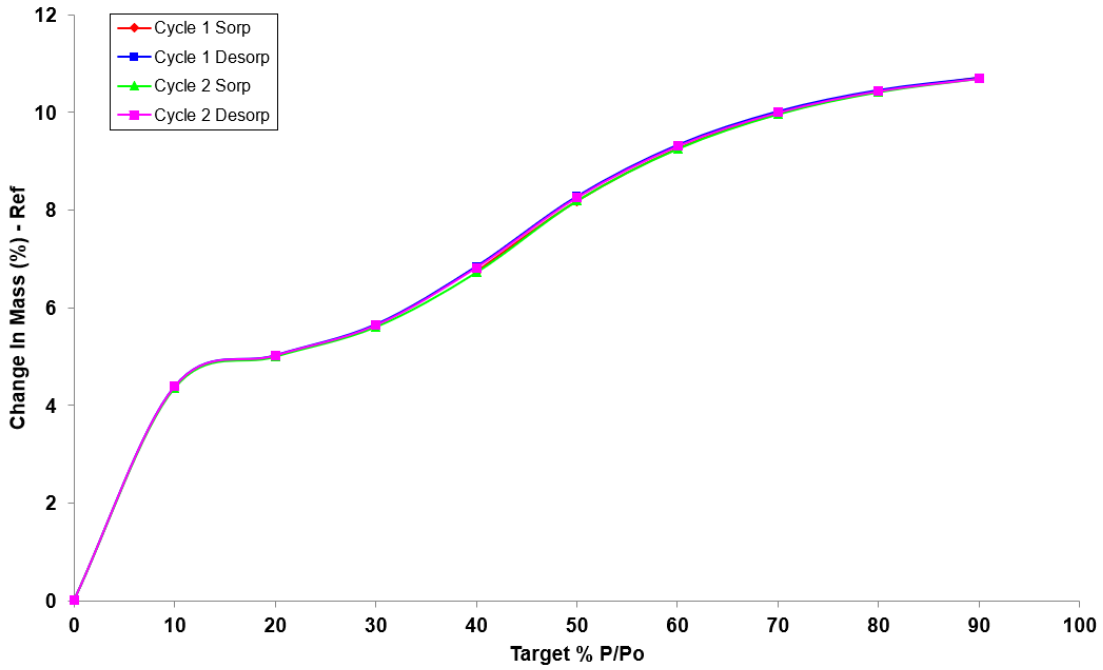

Figure **C10**. DVS isotherm of **1** with two cycles of sorption and desorption at 25 °C. The minimum equilibration time was 38 minutes and the maximum was 361 minutes (at 0% RH).

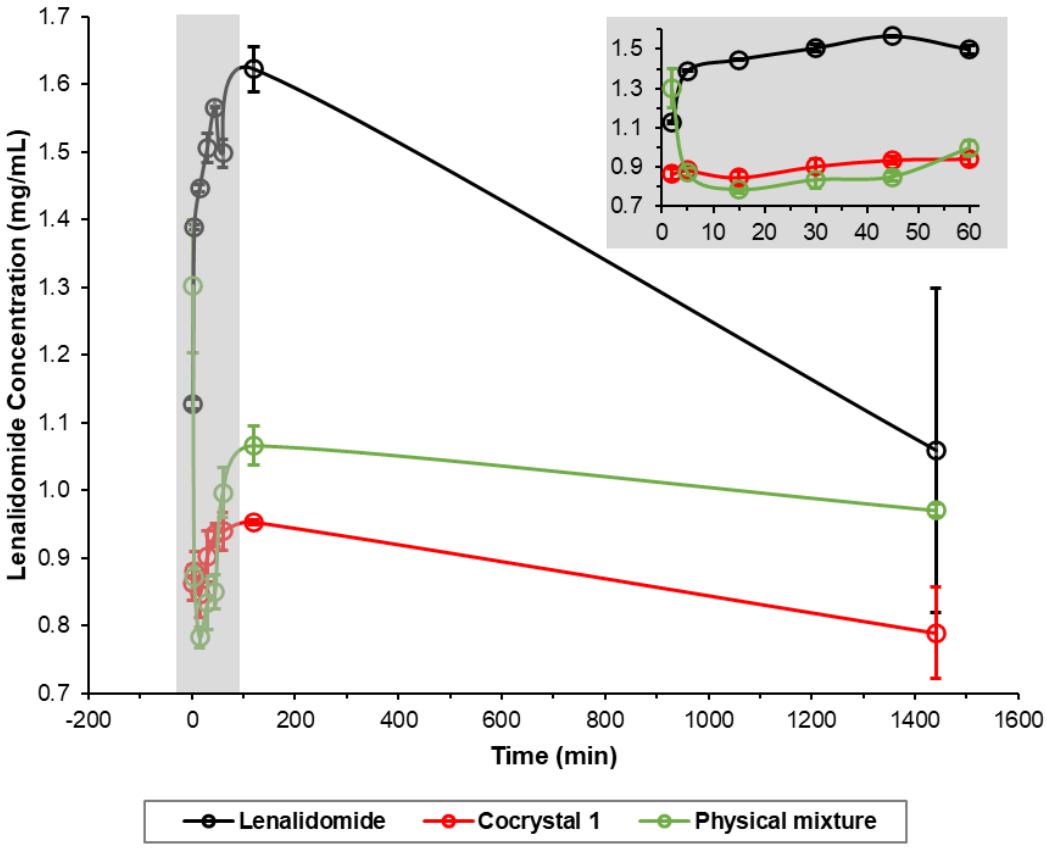

Figure **C11**. Non-sink powder dissolution profiles of lenalidomide Form A, co-crystal **1** and a physical mixture of Form A and melamine (PM) over 24 hours in FaSSIF at 37 °C. The inlaid plot shows only the first hour of the dissolution profile. Vessels were charged with approximately 5 mL of pre-warmed FaSSIF at 37 °C before accurately weighed masses of each sample were added such that all slurries were at ten times the measured solubility limit of lenalidomide. Slurries were stirred at 350 rpm for 24 hours. Aliquots of the slurries were removed at each time point, and concentrations were determined by UPLC analysis. Average concentrations and error bars indicating standard deviations of the mean are shown for time-points acquired in triplicate. Dissolution data points reflect a time constant due to 30 minutes of centrifugation as detailed in section 4.2, during which further dissolution may have occurred.

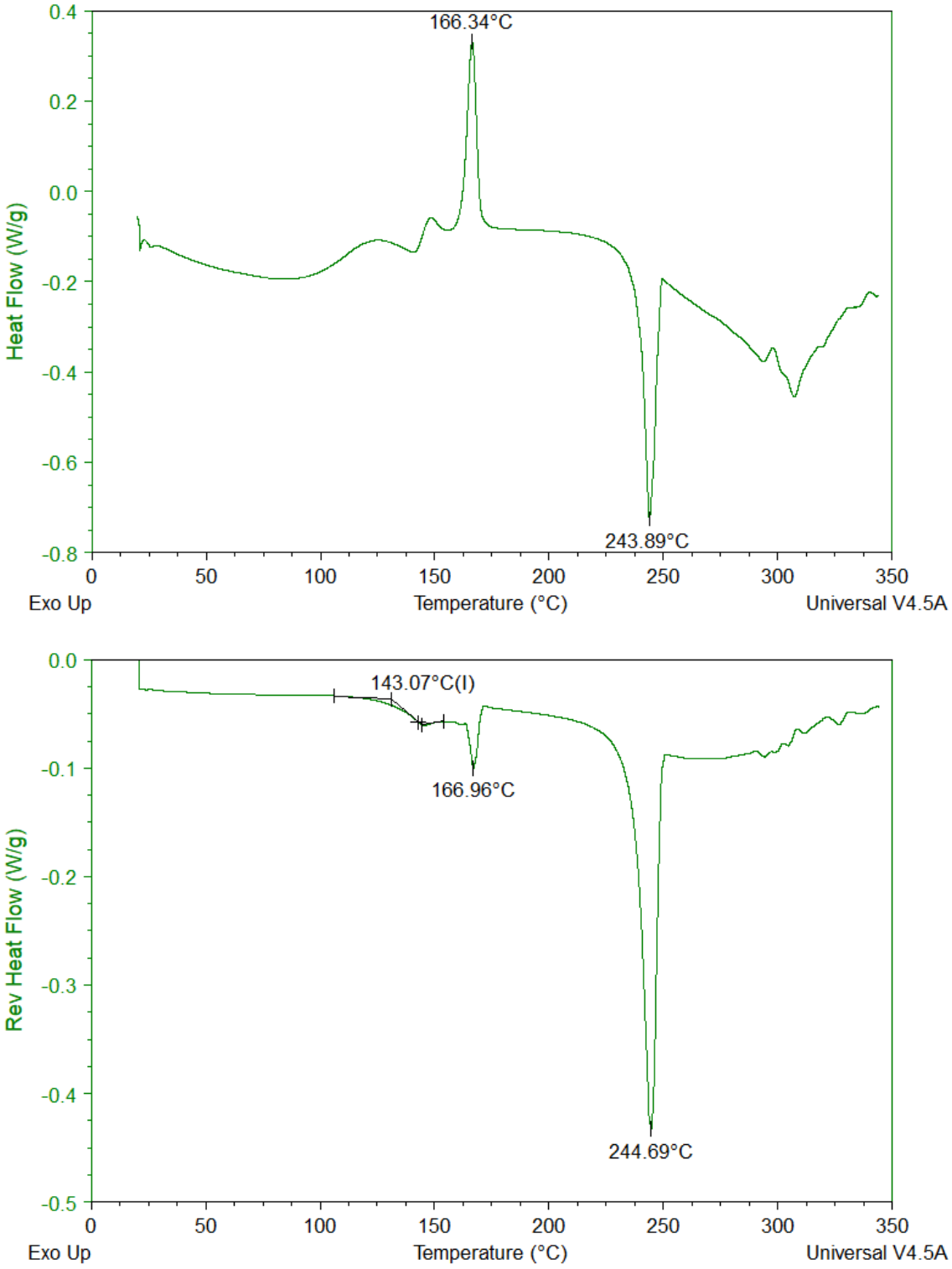

Figure **C12.** Modulated DSC thermogram of co-crystal **1** after milling for 30 minutes at 20 Hz in a ball mill and conditioning the sample for 24 h at 50 °C and 75 % RH. (a) Full DSC and (b) Reversing heat component. A glass transition temperature at 143 °C is evident in the extracted reverse heat flow thermogram, as well as a recrystallisation in combination with dehydration at 167 °C and the subsequent melt of lenalidomide at 245 °C.

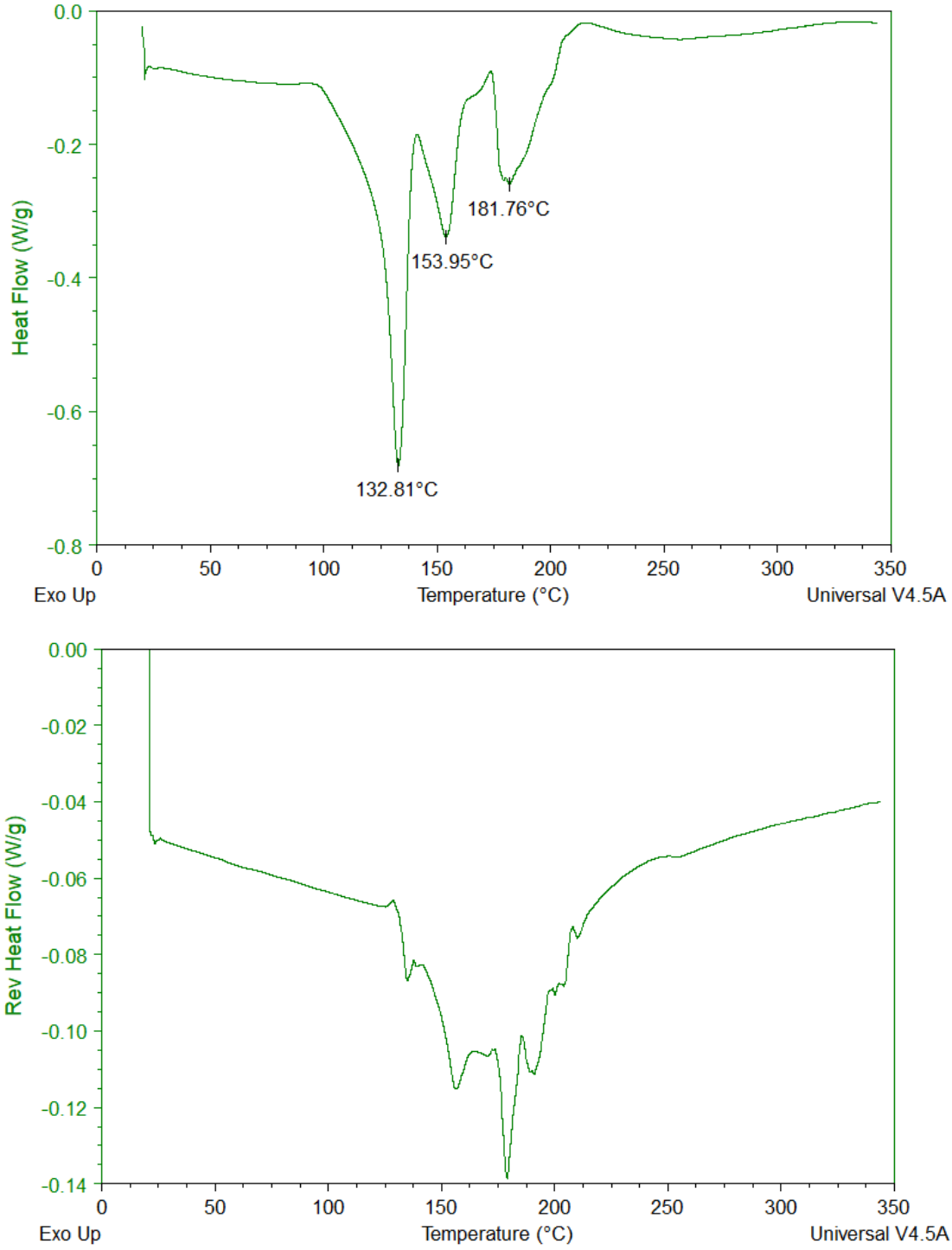

Figure **C13.** Modulated DSC thermogram of co-crystal **1** after milling with α-lactose at 20% w/w of co-crystal **1** for 30 minutes at 20 Hz in a ball mill and conditioning the sample for 24 h at 50 °C and 75 % RH. (a) Full DSC and (b) Reversing heat component. The thermogram is dominated by endotherms for the dehydration of lactose monohydrate and its degradation, and no thermal events for co-crystal **1** can be observed even in the extracted reverse heat flow thermogram.

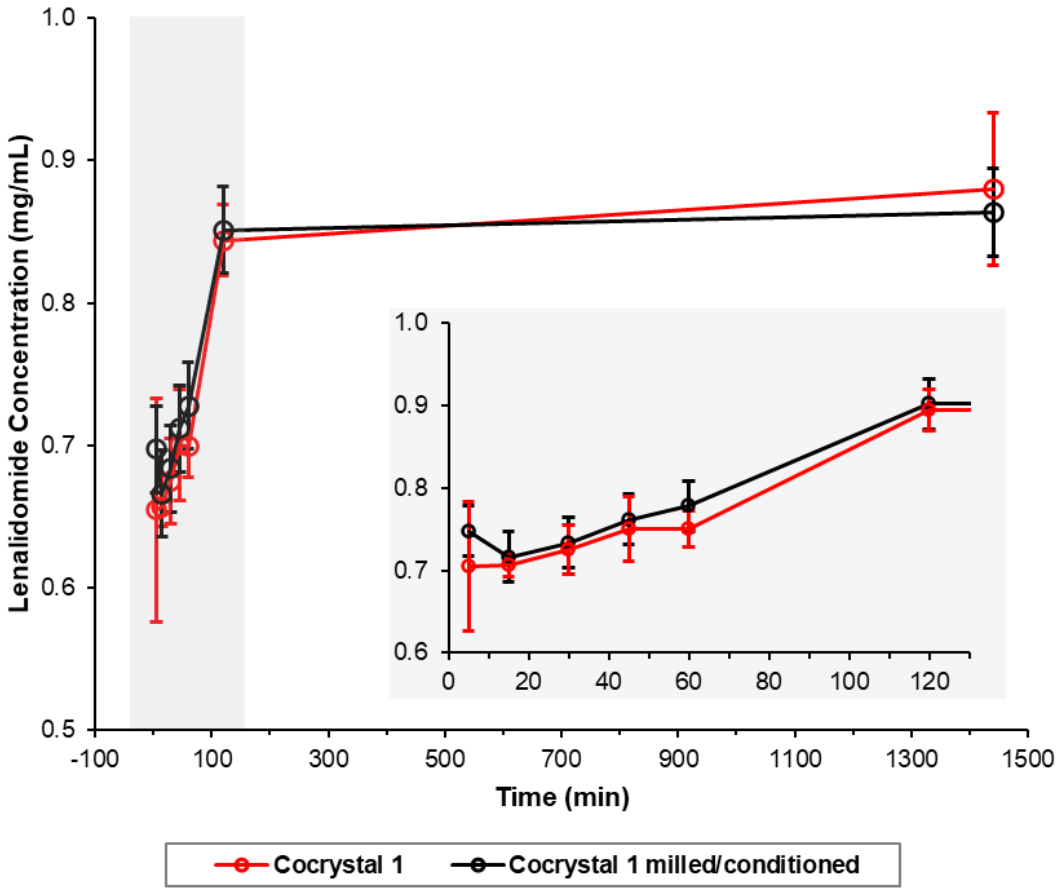

Figure **C14.** Non-sink powder dissolution profiles of co-crystal **1** and the micronised/conditioned co-crystal **1** at 37 °C in PBS. The inlaid plot shows only the first 2 hours of the dissolution profile. Vessels were charged with approximately 5 mL of pre-warmed PBS at 37 °C before accurately weighed masses of each sample were added such that all slurries were at ten times the measured solubility limit of lenalidomide. Slurries were stirred at 350 rpm for 24 hours. Aliquots of the slurries were removed at each time point, and concentrations were determined by UPLC analysis. Average concentrations and error bars indicating standard deviations of the mean are shown for time-points acquired in triplicate. Dissolution data points reflect a time constant due to 30 minutes of centrifugation as detailed in section 4.2, during which further dissolution may have occurred.

Appendix D

Gelator G1 synthesis and characterisation. L-alanine methyl ester hydrochloride (1.594 g, 11.42 mmol) was dissolved in chloroform (40 mL) and triethylamine (1600 µL, 11.47 mmol) was added. 1,6-Diisocyanatohexane (910 µL, 5.67 mmol) was added dropwise then the solution was heated under reflux. After 1 h, the solution was cooled to room temperature and the gelatinous precipitate was filtered and washed with dichloromethane (2×10 mL) and then diethyl ether (10 mL). The resulting solid was sonicated in warm water (40 °C) for 30 min then filtered, recrystallised from methanol, filtered again and washed with diethyl ether. The compound was dried in a drying pistol for 6 h and the product was obtained as a white powder (1.074 g, 2.400 mmol, 42 % yield). ^{1}H NMR (400.20 MHz, DMSO-d_6): δ=6.16 (2 H, d, J=7.7 Hz, N(10,19)H), 5.93 (2 H, t, J=5.6 Hz, N(5,8)H), 4.11 (2 H, p, J=7.3 Hz, NHC(12,21)H), 3.58 (6 H, s, OC(16,26)H_3), 2.99–2.86 (4 H, m, NHC(1,7)H_2), 1.30 (6 H, d, J=6.4 Hz, C(13,22)H_3), 1.23–1.17 ppm (8 H, m, C(2,3,4,6)H_2). ^{13}C{^{1}H}-NMR (100.63 MHz, DMSO-d_6): δ=174.75 (COO), 157.79 (NCO), 52.09 (OCH$_3$), 48.55 (NHCHCH$_3$), 40.7–39.7 (NCH$_2$CH$_2$ under DMSO residual solvent peak), 30.36 (NCH$_2$$CH_2$), 26.51 (CH$_2CH_2$$CH_2$), 18.45 ppm (CH$CH_3$). m/z (ES$^+$-MS): 375 ([M+H]$^+$, 79 %), 397 ([M+Na]$^+$, 100 %), 771 ([2 M+Na]$^+$, 10 %). Elemental analysis calculated (%) for $C_{16}H_{30}N_4O_6$: C 51.32, H 8.08, N 14.96; found: C 50.59, H 8.06, N 14.84.

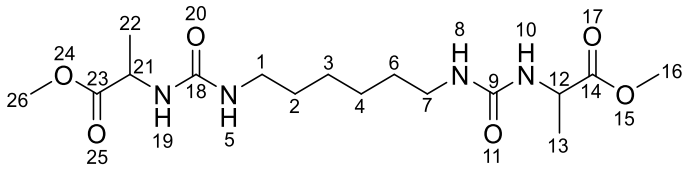

Gelator G2 synthesis and characterisation. DL-aminoglutethimide (0.7392 g, 3.186 mmol) was dissolved in chloroform (45 mL) and an excess of triethylamine (0.6 mL) added dropwise with continuous stirring. A solution of 4,4′-methylenebis(2,6-diethylphenyl isocyanate) (0.6150 g, 1.699 mmol) in chloroform (30 mL) was added dropwise and the reaction mixture stirred at 70 °C for 24 h. The resulting white precipitate was isolated by filtration, washed with chloroform (2×15 mL) and dried in a drying pistol for 4 h. The product was obtained as a white powder (0.4662 g, 0.5642 mmol, 35% yield). ^{1}H NMR (400.20 MHz, DMSO-d_6): δ=10.82 (2H, s, N(47,50)H), 8.80 (2H, s, NH), 7.55 (2H, s, NH), 7.45 (4H, d, J=8.82 Hz, H-Ph), 7.16 (4H, d, J=8.7 Hz, H-Ph), 7.00 (4H, s, C(4,6,9,13)H), 3.86 (2H, s, C(7)H_2), 2.59-2.38 (10H, m, CH_2), 2.36-2.26 (2H, m, CH_2), 2.23-2.10 (4H, m, CH_2), 1.82 (4H, dtt, J=21.1, 14.3, 7.3 Hz, CH$_3$-CH_2), 1.11 (12H, t, J=7.5 Hz, Ph-CH$_2$-CH_3), 0.76 (6H, t, J=7.4 Hz, CH$_2$-CH_3). ^{13}C{^{1}H}-NMR (100.63 MHz, DMSO-d_6): δ=176.3, 173.2, 154.3, 142.3, 140.1, 139.7, 132.6, 132.2, 127.0, 126.7, 118.2, 50.0, 32.6, 29.5, 26.4, 24.9, 15.1, 9.3 ppm. m/z (ES$^+$-MS): 827 ([M+H]$^+$, 20 %), 849 ([M+Na]$^+$,

100 %). Elemental analysis calculated (%) for $C_{49}H_{58}N_6O_6$: C 71.16, H 7.07, N 10.16; found: C 70.31, H 6.80, N 9.97.

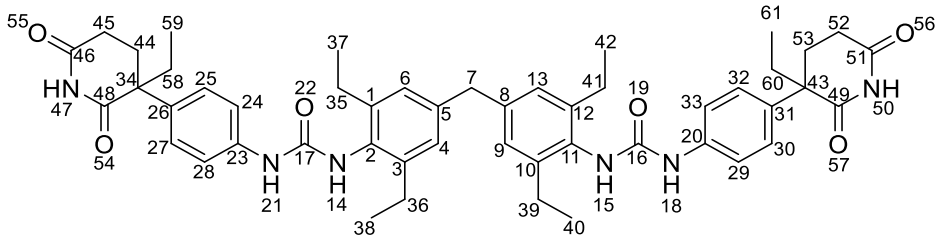

Table **D1**. Solubilities of LDM in a range of solvents at room temperature, determined via the gravimetric method.

Solvent	Solubility (mg/mL)	Solvent	Solubility (mg/mL)	Solvent	Solubility (mg/mL)
Chloroform	0.4	Cyclohexane	0.0	1-butanol	1.4
Toluene	0.0	p-xylene	2.0	2-butanol	1.4
Tetrahydrofuran	4.2	Nitromethane	5.4	1-propanol	0.4
Acetone	1.8	Nitrobenzene	1.2	1,4-butanediol	0.0
Dichloromethane	0.8	Cyclohexanone	8.9	Ethanol	1.7
DMSO-H_2O (1:1)	8.8	Cyclopentanone	9.4	Methanol	3.1
MeOH-H_2O (1:1)	3.0	Pentanol	0.2	Acetonitrile	3.1
THF-H_2O (1:1)	7.6	1,4-dioxane	7.8	Ethyl acetate	2.1

Table **D2**. Crystallographic data for LDM Form 8 (cyclopentanone hemi-solvate). Data were collected and processed by Dr Toby J. Blundell.

Empirical formula	$C_{15.5}H_{17}N_3O_{3.5}$	**μ / mm^{-1}**	0.104
Formula weight	301.32	**F(000)**	636.0
Temperature / K	120.00	**Crystal size / mm**	0.076 × 0.049 × 0.025
Crystal system	triclinic	**Radiation**	Mo Kα (λ = 0.71073)
Space group	$P\bar{1}$	**2Θ range for data collection / °**	3.968 to 51.398

a / Å	11.1851(7)	**Index ranges**	-13 ≤ h ≤ 13, -14 ≤ k ≤ 14, -15 ≤ l ≤ 15
b / Å	12.1666(8)	**Reflections collected**	38307
c / Å	12.6313(8)	**Independent reflections**	5315 [R_{int} = 0.1340, R_{sigma} = 0.0937]
α / °	62.187(2)	**Data/ restraints/ parameters**	5315/0/421
β / °	78.555(2)	**Goodness-of-fit on F^2**	1.006
γ / °	66.633(2)	**Final R indexes [I >=2σ (I)]**	R_1 = 0.0574, wR_2 = 0.1020
Volume / $Å^3$	1395.46(16)	**Final R indexes (all data)**	R_1 = 0.1231, wR_2 = 0.1243
Z	4	**Largest diff. peak /hole**	0.45/-0.24
ρ_{calc} g/cm^3	1.434		

Table **D3**. Hydrogen bonds for LDM Form 8 (cyclopentanone hemi-solvate).

D	H	A	d(D-H)/Å	d(H-A)/Å	d(D-A)/Å	D-H-A/°
N103	H103	O103[1]	0.87(3)	2.05(3)	2.919(3)	174(3)
N202	H20A	O101	0.90(4)	2.07(4)	2.976(4)	176(3)
N203	H203	O202[2]	0.90(3)	1.93(3)	2.826(3)	174(3)

[1]2-X,1-Y,-Z; [2]1-X,2-Y,-Z

Table **D4**. Crystallographic data for **G1** Form B. Data were collected and processed by Dr Toby J. Blundell.

Empirical formula	$C_{16}H_{30}N_4O_6$	**μ / mm^{-1}**	0.101
Formula weight	374.44	**F(000)**	202.0
Temperature/K	120	**Crystal size / mm**	0.191 × 0.077 × 0.019
Crystal system	triclinic	**Radiation**	Mo Kα (λ = 0.71073)
Space group	*P*1	**2Θ range for data collection/°**	4.6 to 54.712

a / Å	4.6439(4)	**Index ranges**	-5 ≤ h ≤ 5, -7 ≤ k ≤ 7, -22 ≤ l ≤ 23
b / Å	6.0527(5)	**Reflections collected**	13159
c / Å	17.9322(15)	**Independent reflections**	4128 [R_{int} = 0.0399, R_{sigma} = 0.0469]
α / °	95.476(3)	**Data/ restraints/ parameters**	4128/178/264
β / °	94.920(3)	**Goodness-of-fit on F^2**	1.066
γ / °	108.854(3)	**Final R indexes [I >=2σ (I)]**	R_1 = 0.0521, wR_2 = 0.1186
Volume / Å^3	471.17(7)	**Final R indexes (all data)**	R_1 = 0.0620, wR_2 = 0.1231
Z	1	**Largest diff. peak /hole**	0.29/-0.25
ρ_{calc} g/cm^3	1.320	**Flack parameter**	0.5(7)

Table **D5**. Hydrogen bonds for **G1** Form B.

D	H	A	d(D-H)/Å	d(H-A)/Å	d(D-A)/Å	D-H-A/°
N1	H1	O3[1]	0.81(5)	2.09(5)	2.845(5)	156(4)
N3	H3	O4[2]	0.93(5)	2.02(5)	2.899(4)	156(4)
N4	H4	O4[2]	0.97(7)	2.04(7)	2.947(4)	154(6)

[1]1+X,+Y,+Z; [2]-1+X,+Y,+Z

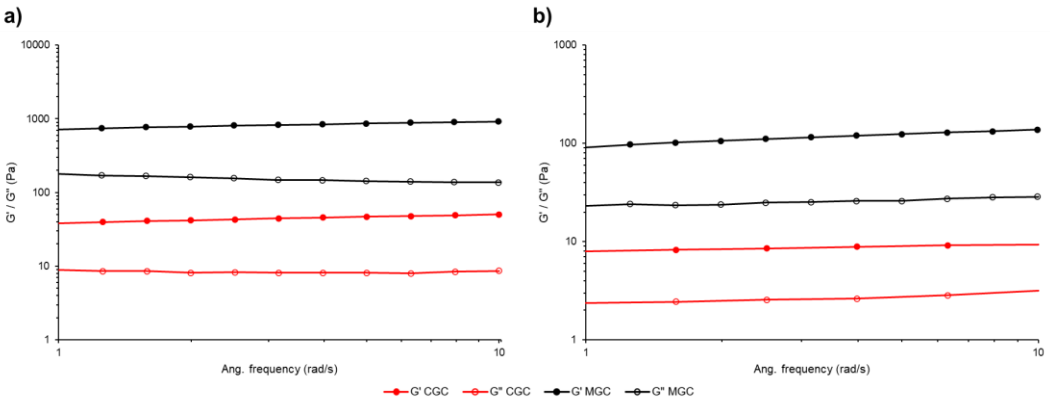

Figure **D1**. Frequency sweep rheology for a) **G1** and b) **G2** gels of cyclopentanone at both CGC and MGC, measured at a constant oscillatory stress of 0.5 Pa. Gels are characterised by a viscosity (slope of G' or G") that is invariant with angular frequency while at a constant oscillatory stress within the linear viscoelastic region (LVR).

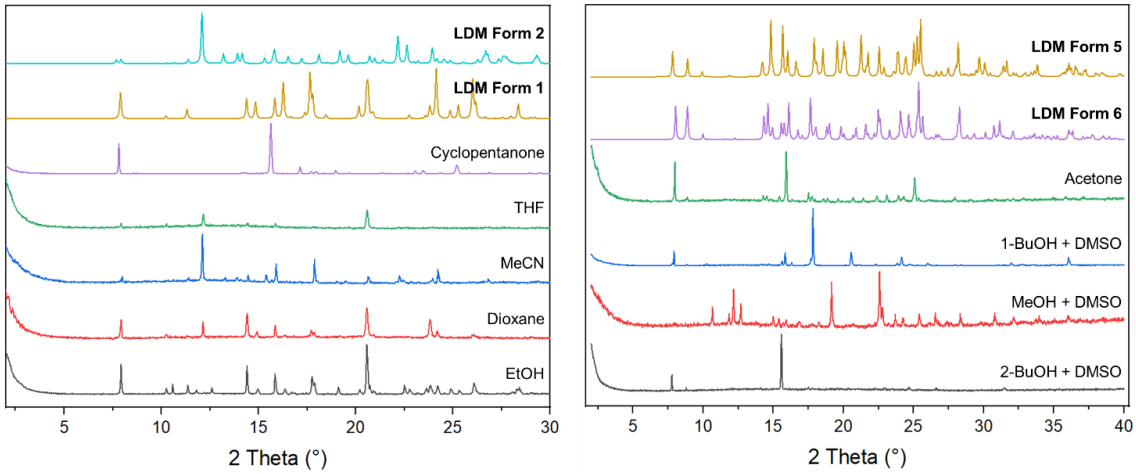

Figure **D2**. XRPD diffractograms for LDM recrystallisation experiments in solvents that can be gelled by gelator **G1** and/or **G2**. Powder patterns of known LDM polymorphs and solvates were simulated from SC-XRD data and shown in bold. This data was used in combination with single-crystal XRD to determine the polymorphic outcome from crystallisation in the absence of gelators **G1** and **G2**. The results are listed in Table 5.2.

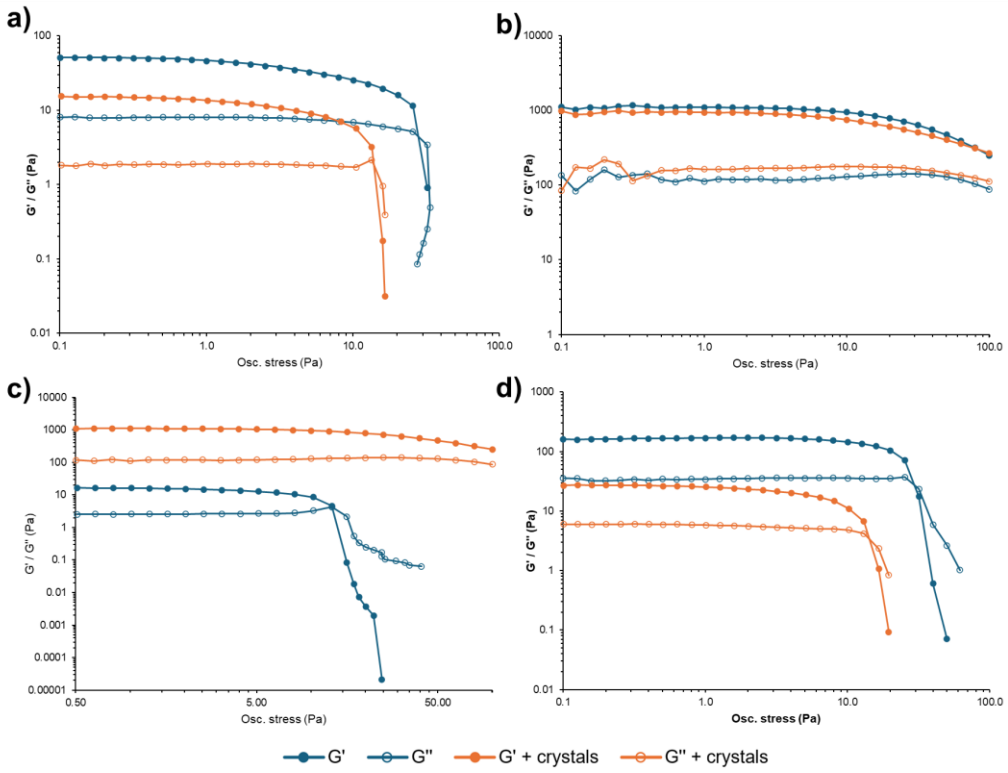

Figure **D3**. Oscillatory stress sweeps for cyclopentanone gels prepared with a) **G1** at CGC, b) **G1** at MGC, c) **G2** at CGC and d) **G2** at MGC, with and without the presence of LDM crystals. The presence of LDM crystals appears to weaken the gels produced with **G1** at CGC and **G2** at MGC, with a reduction in storage and loss moduli as well as a reduction in yield stress. By contrast, the

gel produced with **G2** at CGC became stronger with a greater yield stress when LDM crystals were present. The **G1** gel at MGC appeared relatively unaffected by the presence of LDM crystals.

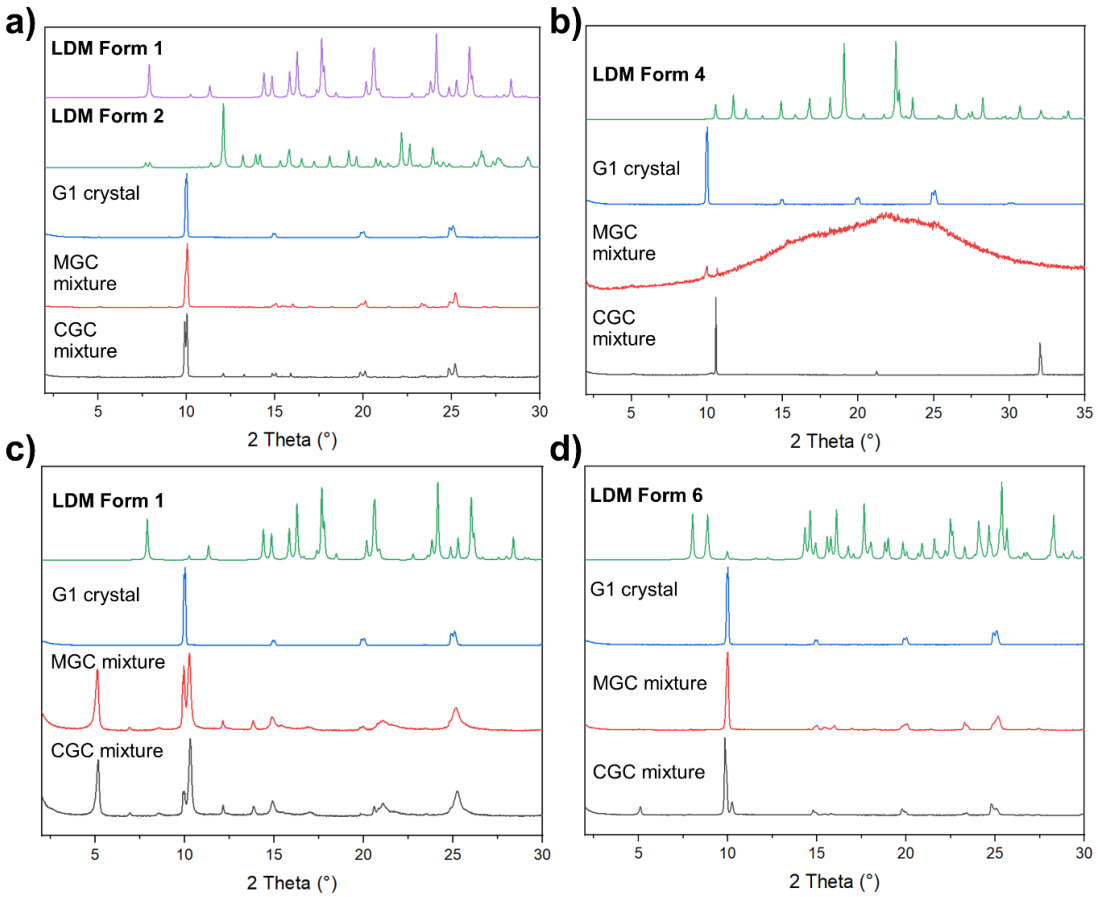

Figure **D4**. XRPD patterns of gel-crystal mixtures analysed from LDM recrystallisation experiments in **G1** gels of a) acetonitrile, b) nitrobenzene, c) tetrahydrofuran and d) acetone. Experiments at both CGC and MGC are compared. This data was used in combination with single-crystal XRD to determine the polymorphic outcome from crystallisation within **G1** gels. The powder pattern for LDM polymorphs and solvates were simulated from the SC-XRD data and shown in bold.

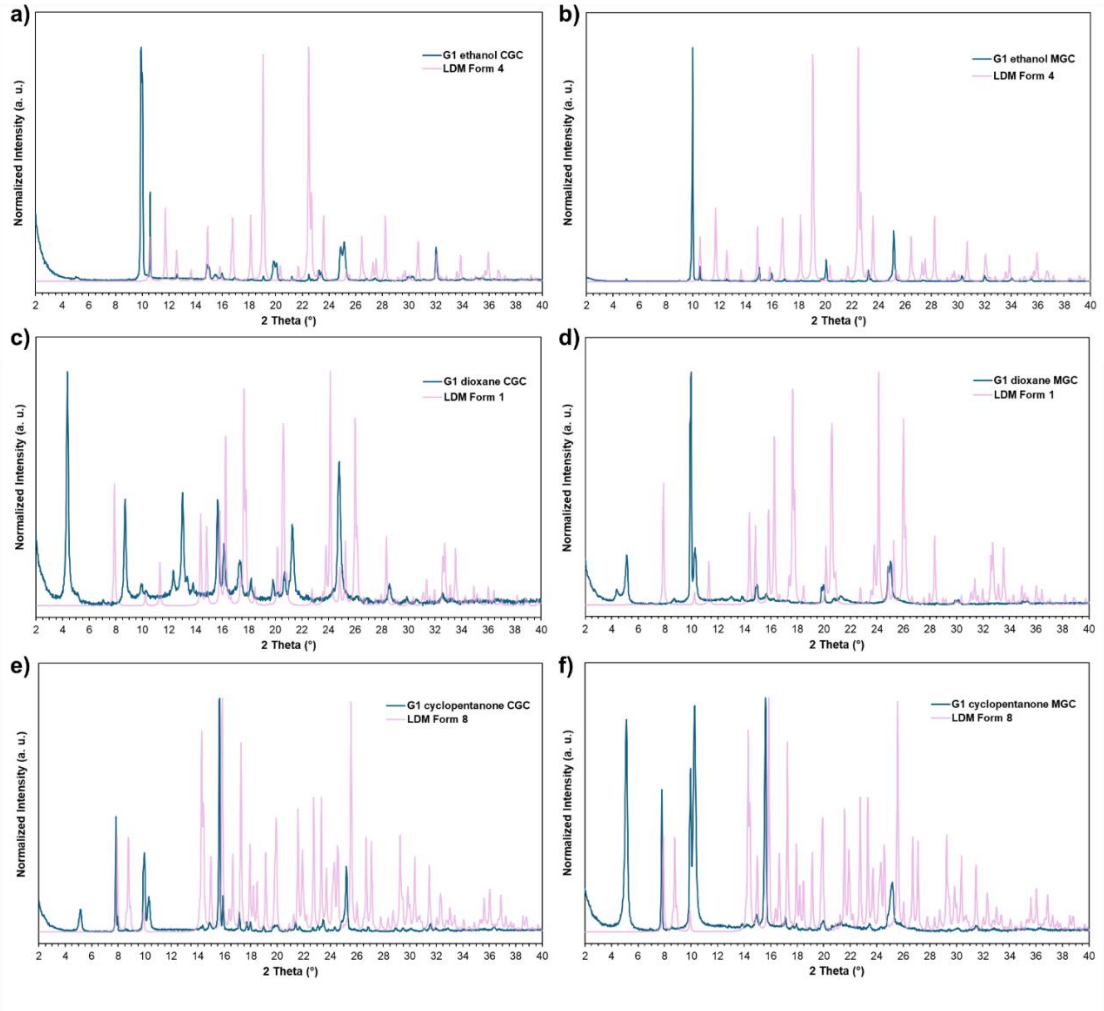

Figure **D5**. Overlays comparing experimental XRPD patterns (blue) of gel-crystal mixtures from LDM recrystallisation experiments in **G1** gels of a-b) ethanol, c-d) dioxane and e-f) cyclopentanone with the patterns simulated from SC-XRD data (pink) of the LDM solid form identified in each recrystallisation experiment via unit cell determination. Both experiments at CGC and MGC are shown for each solvent. Peaks from the simulated patterns may be missing in the experimental patterns due to preferred orientation effects, or because the LDM crystal peaks are obscured or drowned out by the **G1** xerogel peaks.

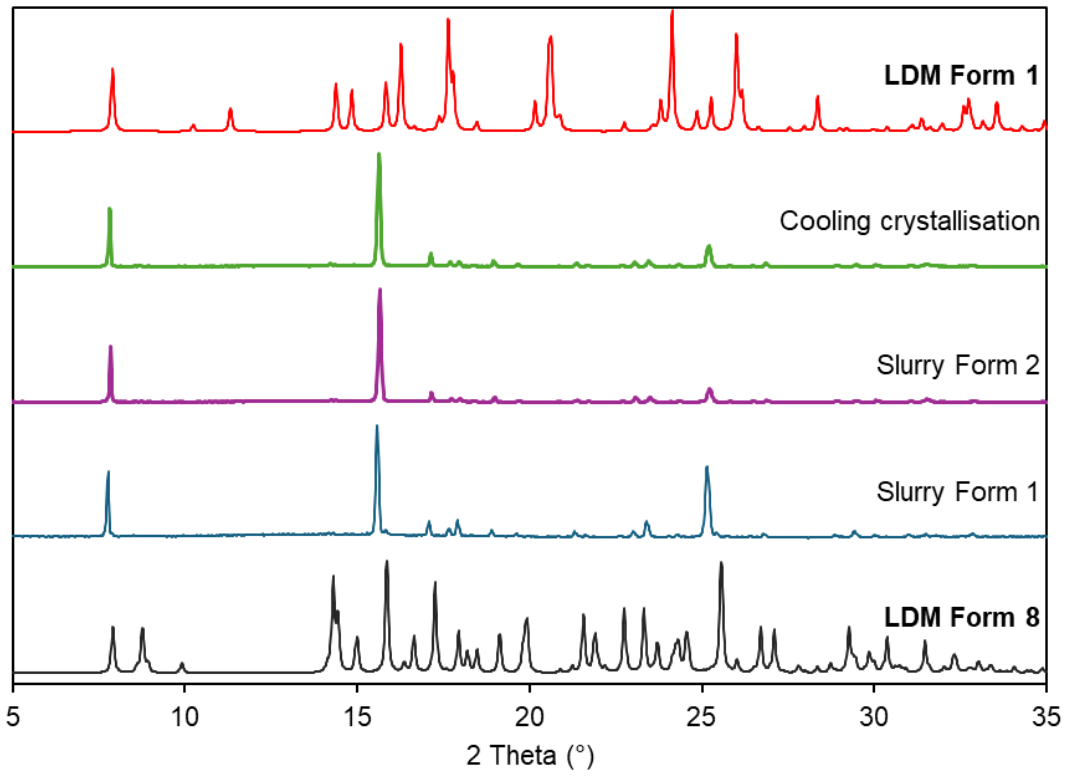

Figure **D6**. XPRD patterns for cooling and slurry crystallisation experiments of LDM in cyclopentanone compared to the powder patterns of LDM Forms 1 and 8 simulated from SC-XRD data. Slurry experiments were conducted for 2 weeks starting from LDM Forms 1 and 2. Unit cell determination by SC-XRD confirmed that all three samples contained LDM Form 1.

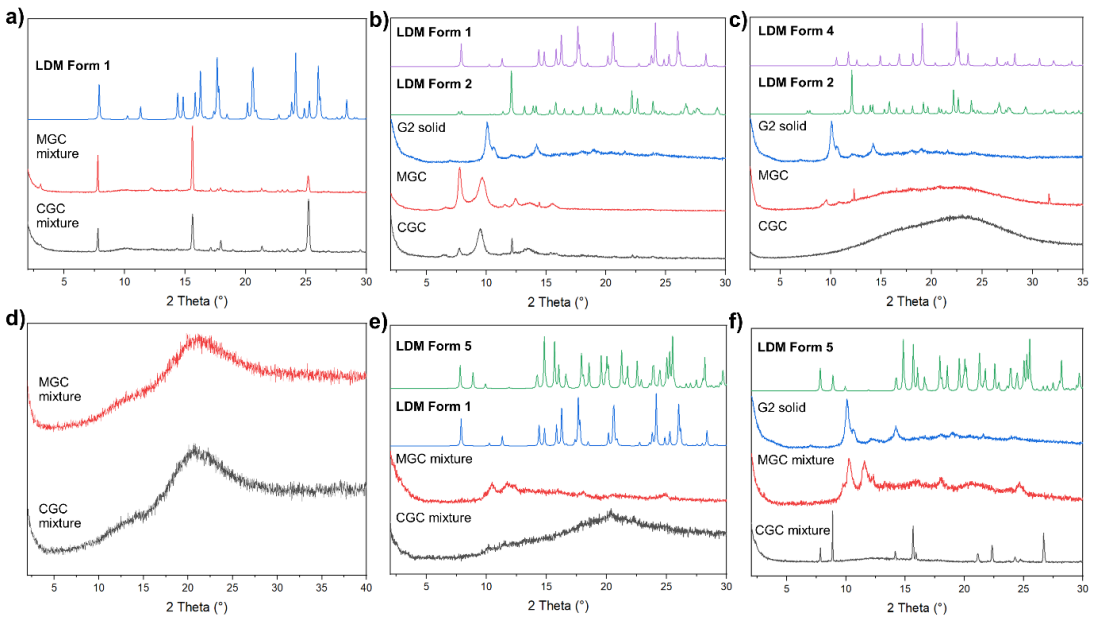

Figure **D7**. XRPD patterns of gel-crystal mixtures analysed from LDM recrystallisation experiments in **G2** gels of a) cyclopentanone, b) dioxane, c) nitrobenzene, d) methanol + DMSO, e) 1-butanol + DMSO and f) 2-butanol + DMSO. Experiments at both CGC and MGC are compared. This data was used in combination with single-crystal XRD to determine the

polymorphic outcome from crystallisation within **G2** gels. The powder pattern for LDM polymorphs and solvates were simulated from the SC-XRD data and shown in bold.

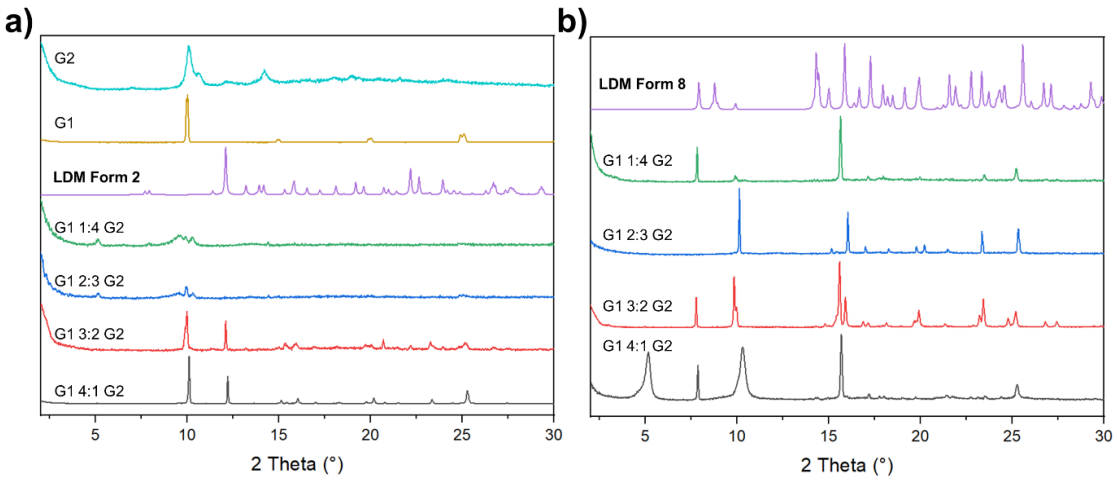

Figure **D8**. XRPD patterns of gel-crystal mixtures analysed from LDM recrystallisation experiments in gel blends of **G1** and **G2** at varying molar ratios in a) dioxane and b) cyclopentanone.

Table **D6**. Polymorphic outcome of LDM from recrystallisation experiments in gel blends of **G1** and **G2** at varying molar ratios in dioxane and cyclopentanone, determined by a combination of XRPD and SC-XRD.

Dioxane		**Cyclopentanone**	
Molar ratio G1:G2	LDM polymorphic outcome	Molar ratio G1:G2	LDM polymorphic outcome
1:4	Poor crystals	1:4	Form 8
2:3	Poor crystals	2:3	Form 8
3:2	Form 2	3:2	Form 8
4:1	Form 2	4:1	Form 8

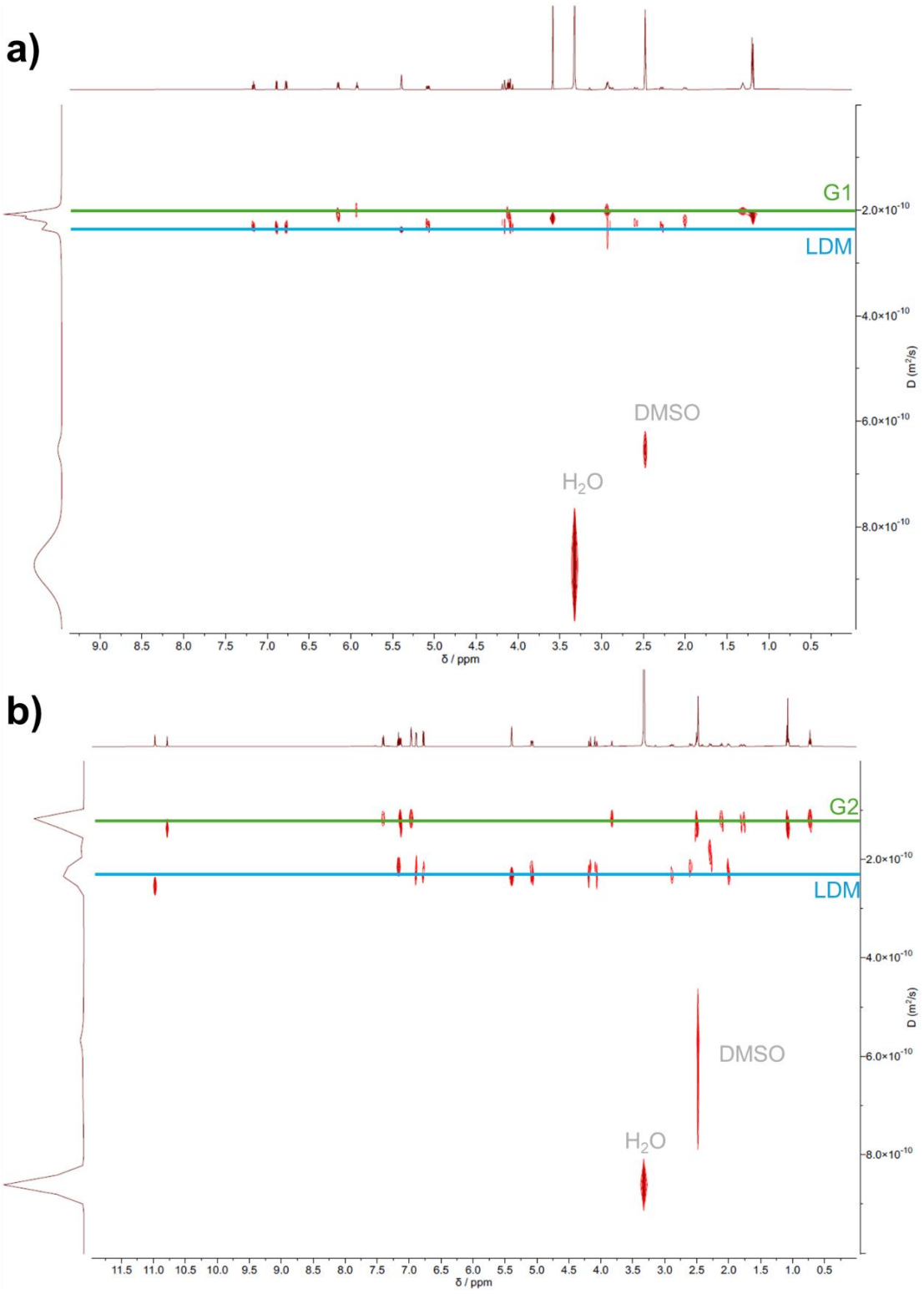

Figure **D9**. DOSY NMR spectra for LDM and a) **G1** or b) **G2** at a 1:1 molar ratio in DMSO-d_6, in which both drug and gelator components are fully soluble. In both cases, the drug and gelator signals have different diffusion constants, indicating that they are not strongly interacting in solution in DMSO. Data were collected by Dr Juan Aguilar-Malavia.

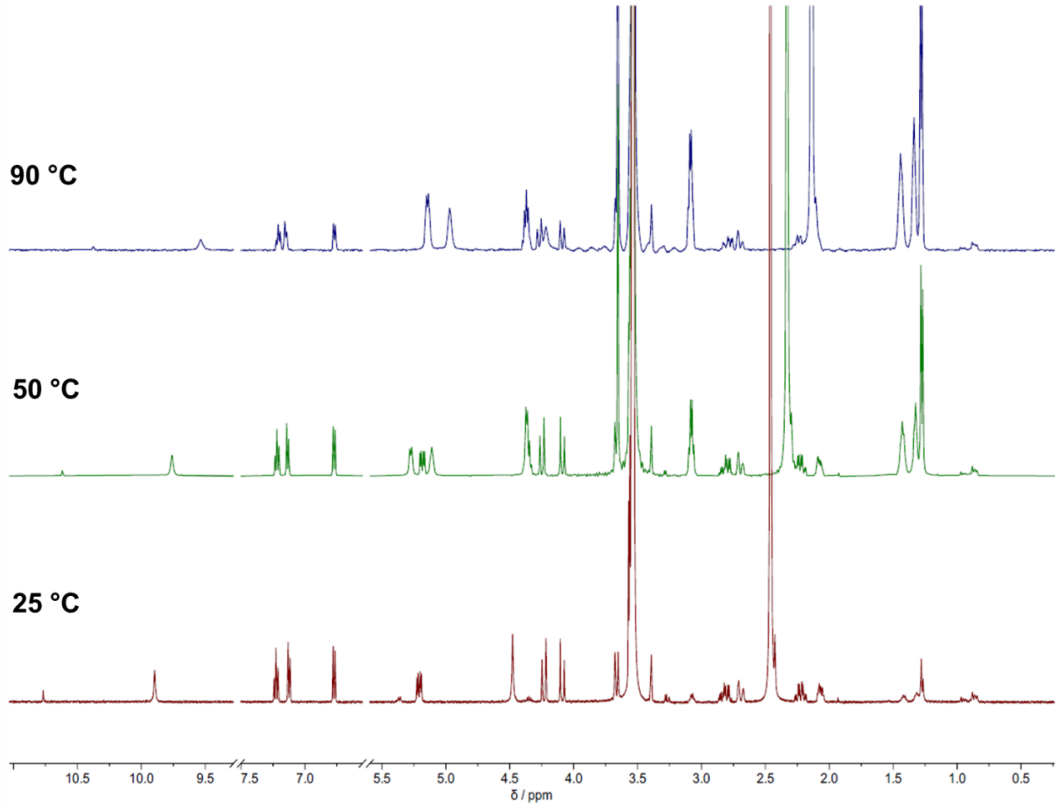

Figure **D10**. The ^{1}H NMR spectrum of a **G1** gel of dioxane-d8 at 1.5 % w/v containing 0.9 % w/v of LDM at 25 °C, 50 °C and 90 °C. As the gelatinous sample is warmed up and dissolves, the signals corresponding to **G1** increase in intensity while the LDM signals do not change in integral relative to the residual DMSO-d_5 solvent peak, indicating that no significant quantity of LDM molecules are incorporated into the **G1** gel fibres. Data were collected and processed by Dr Juan Aguilar-Malavia.

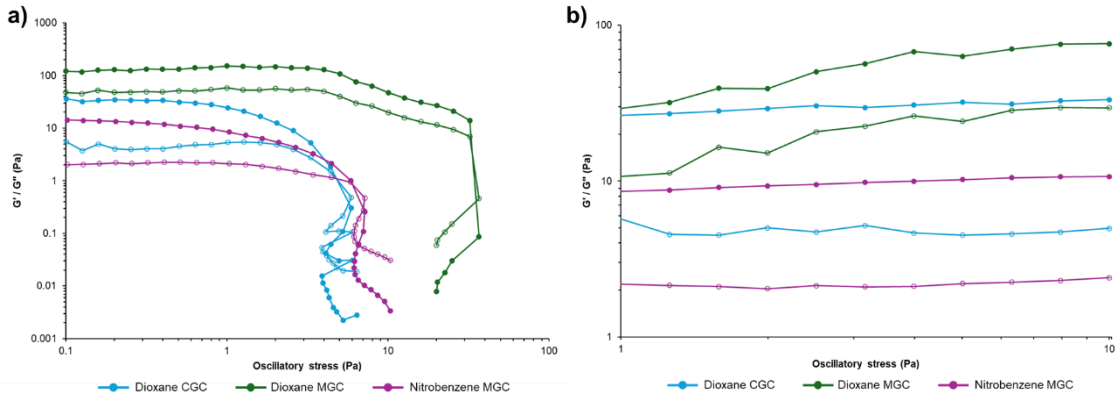

Figure **D11**. a) Oscillatory stress sweeps and b) frequency sweeps for **G1** gels of dioxane (CGC and MGC) and nitrobenzene (MGC) containing AZ1. The **G1** gel of nitrobenzene at CGC was very loose and collapsed upon removal from its original vial; hence its rheometry is omitted. Frequency sweeps were measured at a constant oscillatory stress of 0.5 Pa. Gels are characterised by a viscosity (slope of G' or G") that is invariant with angular frequency while at a constant oscillatory stress within the linear viscoelastic region (LVR).